College of Engineering, Mathematics and Physical Sciences

Optimisation of ocean-powered turbines for seawater desalination

Submitted by

Mohammad Hassan Khanjanpour

to the University of Exeter as a thesis for the degree of

Doctor of Philosophy in Engineering

April 2021

I certify that all material in this thesis which is not my own work has been identified and that no material has previously been submitted and approved for the award of a degree by this or any other University.

Signature:

Abstract

In this research, a novel conceptual desalination system was introduced which can be powered by Horizontal Axis Tidal (HAT) and Vertical Axis Tidal (VAT) turbines. Since in the proposed design, the most important part is the tidal turbine, the focus has been placed on optimisation of the turbines. The energy required for desalinating 1 m^3/h was determined. Accordingly, a VAT turbine and a HAT turbine were separately designed to fulfil this amount of energy. The greatest weakness of these turbines is the high price of design, development, and manufacturing. Traditionally, optimisation of turbine geometry can be achieved by running several numerical models of the turbine which can become computationally expensive. In this work, a combination of the Taguchi method and CFD modelling was used as a straightforward solution for optimisation of geometry of tidal turbines.

Although improving the hydrodynamic performance is a key objective in the design of ocean-powered turbines, some factors affect the efficiency of the device during its operation. In this study, the impacts of a wide range of surface roughness, as a tribological parameter, on stream flow around a hydro turbine and its power loss were studied. A comprehensive program of 3D Computational Fluid Dynamics (CFD) modelling, as well as an extensive range of experiments were carried out on a tidal turbine in order to measure reduction in hydrodynamic performance due to surface roughness. The results showed that surface roughness of turbine blades plays an important role in the hydrodynamics of the flow around the turbine. The surface roughness increases turbulence and decreases the active fluid energy that is required for rotating the turbine, thereby reducing the performance of the turbine.

The geometry of the HAT turbine was optimised with combination of only 16 CFD simulations using the Taguchi method. The effects of blade size, number of blades, hub

radius, and hub shape were studied and optimised. The results revealed that the most important parameters influencing the power output of HAT turbine are the number of blades, size of blade, hub radius, and hub shape. Moreover, the superposition model showed that the minimum signal-to-noise (S/N) ratio was 5% less than the amount achieved in the Taguchi approach. The power coefficient (C_p) of the optimised HAT turbine was 0.44 according to the results of CFD simulations, which was 10% higher than that of the baseline model (0.40) at tip speed ratio (TSR) of 5. The weight of the optimised model was less than the baseline model by 17%.

Moreover, a number of CFD simulations were carried out using the mixed-level modified Taguchi technique to determine the optimal hydrodynamic performance of a VAT turbine. The effects of four parameters: twist angle, camber position, maximum camber, and chord/radius ratio were studied. The interaction of these parameters was investigated using the Variance of Analysis (ANOVA) approach. The Taguchi analysis showed that the most significant parameter affecting hydrodynamic performance of the turbine is the twist angle and the least effective parameter is chord/radius ratio. The ANOVA interaction analysis showed that the twist angle, camber position and maximum camber have significant interaction with each other. Moreover, the results showed that the power coefficient (C_p) for the optimised VAT turbine was improved by 26% compared to the baseline design. In addition, the flow separation in the optimised model was greatly reduced in comparison with the baseline model, signifying that the twisted and cambered blade could be effective in normalising the spraying vortices over blades due to suppressing dynamic-stall. The findings of this thesis can provide guidelines for optimisation of tidal turbines.

To Fatemeh and Hoshang, my mum and dad.

بیرون ز تو نیست هرچه در عالم هست

در خود بطلب هر آنچه خواهی که تویی

(مولوی، دیوان شمس)

The Universe is Not Outside of You. Look Inside Yourself;

Everything That You Want, You Already Are.

Jalal ad-Din Muhammad Balkhi (Iranian poet)

November 2020

Mohammad Hassan Khanjanpour

ACKNOWLEDGEMENTS

First, I am very grateful to Professor Akbar A. Javadi, my supervisor, for supporting this research and for his tremendous encouragement and advice during my PhD. Accomplishing the complex projects has many hardships and during this time, Professor Javadi, managed the project with unique kindness and patience. I was lucky to study under his supervision and I would like to express my infinite thanks to him for his guidance, support and his miracle intuition.

I would like to thank all staffs of hydraulics laboratory of University of Exeter, especially Julian Yates, Roger Perrett and Siobhan Kelley for supporting me in experimental work. I am also thankful to Robert O'Neale as well, for his help in providing me with high quality IT support. I am grateful to Dave Gregory, Russ Edge, and Martin Guille who helped me in the Mechanical workshop to overcome all experimental challenges as well. At the same time, I want to thank all of my friends and colleagues in the engineering department of University of Exeter.

I would also like to thank my family for always being there for me. I especially thank my mom for her sincere love and support during every stage of my life. A warm gratitude is deserved for my father who opened a new horizon and made a huge influence on my vision. Moreover, I would like to express my warmest appreciations to my dear brother, Mohammad Sadra, for his endless supports.

At the end, I would like to thank all staffs of the University of Exeter.

Publications

The major body of this thesis contains the following papers:

Journal papers:

- Khanjanpour, M. H. and Javadi, A. A. (2020). "Experimental and CFD Analysis of Impact of Surface Roughness on Hydrodynamic Performance of a Darrieus Hydro (DH) Turbine." Energies **13**(4): 928, doi.org/10.3390/en13040928.

- Khanjanpour, M. H. and Javadi, A. A. (2020). "Optimisation of the hydrodynamic performance of a vertical Axis tidal (VAT) turbine using CFD-Taguchi approach." Energy Conversion and Management 222: 113235 (Elsevier), doi: 10.1016/j.enconman.2020.113235.

- M. H. Khanjanpour and Javadi, A. A. (2020), Optimisation of a Horizontal Axis Tidal (HAT) turbine for powering a Reverse Osmosis (RO) desalination system using Computational Fluid Dynamics (CFD) and Taguchi method." Energy Conversion and Management 222: 113235 (Elsevier), https://doi.org/10.1016/j.enconman.2021.113833.

Conference paper:

- Khanjanpour, M. H., Javadi, A. A., and Akrami, M. (2020), CFD analyses of a tidal hydro-turbine (THT) for utilising in sea water desalination, International Conference on Science, Technology, Engineering and Management (ICSTEM), London, 7th - 8th July (2019).

Table of Contents

List of Figures

List of Tables

List of Symbols and Abbreviations

WHO	World Health Organisetion
UNICEF	United Nations Children's Fund
WRI	World Resources Institute
GWI	Global Water Intelligence
DT	Desalination technologies
MED	Multi-effect distillation
MSF	Multi stage flash
VC	Vapour compression
ED	Electrodialysis
RO	Reverse osmosis
TDS	Total dissolved solids
PPM	Parts per million
OPT	Ocean power technologies
OWC	Oscillating water column
WO	Wave overtopping
PA	Point Absorber
TB	Tidal barrages
VAT	Vertical axis tidal
HAT	Horizontal axis tidal
HAW	Horizontal axis wind
AS	Archimedes screw
TK	Tidal kite
CFD	Computational fluid dynamic
OA	Orthogonal Arrays
Π	Number of experiments
Ω	Number of levels
Φ	Number of factors
S/N	Signal-to-noise
TPRO	Tidal power reverse osmosis
DH	Darrieus Hydro
FH	Francis Hydro
H_r	Roughness height
NACA	National advisory committee for aeronautics
CAD	Computer-aided design
SST	Shear stress transport
PISO	Pressure implicit with splitting of operator
GS	Grid sensitivity
y^+	Non-dimensional wall distance
C_m	Moment coefficient
RSD	Relative standard deviation
T_m	Average torque
T	Torque
ρ	Density of water
U	Velocity of water
A	Area of the turbine blades
z	Number of data points
TSR	Tip speed ratio

Δt	Time steps
ADV	Acoustic Doppler Velocimeter
C_p	Power coefficient
P	Power output
R	Radius of vertical turbine's hub
ω	Angular velocity of turbine
C_r	Roughness constant
U_q	Velocity at the wall near cell at centre point q
y_q	Height at the centre point q of the cells near the wall
μ	Viscosity of water
ΔG	Roughness function
τ_W	Wall shear stress
K_r	Karman constant
u_1	Wall friction velocity
k_q	Turbulent kinetic energy near the wall at point q
H_s^+	Non-dimensional roughness height
DOF	Degrees of freedom
μm	Micrometer
Q_p	Pressure coefficient
p	Pressure
A_v	Area of the vertical turbine blades
p_w	Pressure of water
C_d	Drag coefficient
P_l	Power loss
P_c	Power of clean turbine
P_r	Power of roughed turbine
T_m	Mean torque
VATRO	Vertical Axis Tidal Reverse Osmosis
ANOVA	Variance of Analysis
TSS	Total sum of squares
n_v	Number of measurements
T_i	i_{th} measurements
$\overline{T}$	mean of the n_y measurements
ERD	Energy recovery device
PV	Photovoltaic
P_n	Nominal power output
H	Height of vertical turbine blade
R	Vertical turbine radius
D_1	Chord length of vertical turbine blade
QL	Quality Loss
V_e	Calculated response
V_t	Target quality
LTB	Larger the better
NTB	Nominal the best
STB	Smaller the better
σ	Solidity ratio
N_b	Number of blades
θ	Difference between the maximum and minimum responses
η^o	Estimated S/N ratio
η	Average of total mean S/N ratios

η_{Ai}	S/N ratios with the factor A at level i
η_{Bj}	S/N ratios with the factor B at level j
η_{Ck}	S/N ratios with the factor C at level k
η_{Dl}	S/N ratios with the factor D at level l
η^*	Interaction term
η_{AiBj}	Average of total mean S/N ratios including both A_i and B_j
p_i	Freestream pressure
W	Wake
IB	Indicated blade
HATRO	Horizontal axis tidal turbine reverse osmosis
r	HAT turbine radius
A_h	Area of the HAT turbine
α	Solidity ratio of HAT turbine
n_b	Number of HAT turbine blades
b	Initial size of the HAT Turbine blade
Ah	Area of a blade
OF	Objective function
β	Indicator

Chapter One: Introduction

1.1 Overview

Freshwater is at the heart of sustainable development and is vital for socio-economic development, energy and food production, healthy ecosystems and for human survival itself. Water is also at the core of adaptation to climate change, serving as the essential link between the society and the environment. According to a new report by WHO and UNICEF, by 2025, 1.8 billion people will be living in countries or regions with absolute water scarcity. Because of changing climate, population growth, industrial development and rising patterns of water demand, the global water consumption has been ascending at a rate of 1% per year over the previous decades, and it will continue to grow dramatically in the future (Van dam, 2003). Water crisis is a problem from which many societies and the environment around the world are suffering and it is expected to get worse in the future. According to the World Resources Institute (WRI), most of the regions of the world will face sever water shortage. Almost half the world's population will be living in areas of high water stress by 2040 and water scarcity in some arid and semi-arid places will displace 700 million people by 2030 (Figure 1.1). Even countries that are currently rich in water resources will face water shortage in future. Several policies should be adopted to mitigate water resource challenges, including water recycling, drainage maintenance, and enhanced catchment and distribution networks (Elimelech & Phillip, 2011). Although these efforts are essential, they can only enhance the existing water supplies, not expand new resources. Desalination is the best way to expand the availability of water above what is available in the hydrological cycle (Esmaeilion, 2020). Turning seawater into freshwater must be on the highest priority for addressing this problem in the strategic roadmaps in all countries (Xu et al., 2020). Therefore, desalination systems have been developed significantly over the past 5 decades, along with rising water consumption (Ang et al. 2019). As water sources are

increasingly depleted, the desalination of saline water is receiving more and more attention, Most of existing desalination technologies require huge amounts of energy, which is expensive in terms of environmental effects as well as money (Ibrahim et al., 2020; Karagiannis & Soldatos, 2008; Lourenço & Carvalho, 2020). While desalination is already deemed an essential source of fresh water globally, its high cost is one of the key challenges of expanding it (Schallenberg et al., 2014). An average of £73519 million is anticipated to be invested in desalination schemes in the coming four years, according to the Global Water Intelligence (GWI) (Nassrullah et al., 2020). About £40486 million is allocated to operational expenses (Al-Karaghouli & Kazmerski, 2013). As illustrated in Figure 1.2, running costs of desalination system are split into four major categories including energy, labour, replacements, and chemicals. Thermal and electrical energy will account for about 50 percent of the operational budget. Therefore, reducing energy consumption of desalination system would be very important.

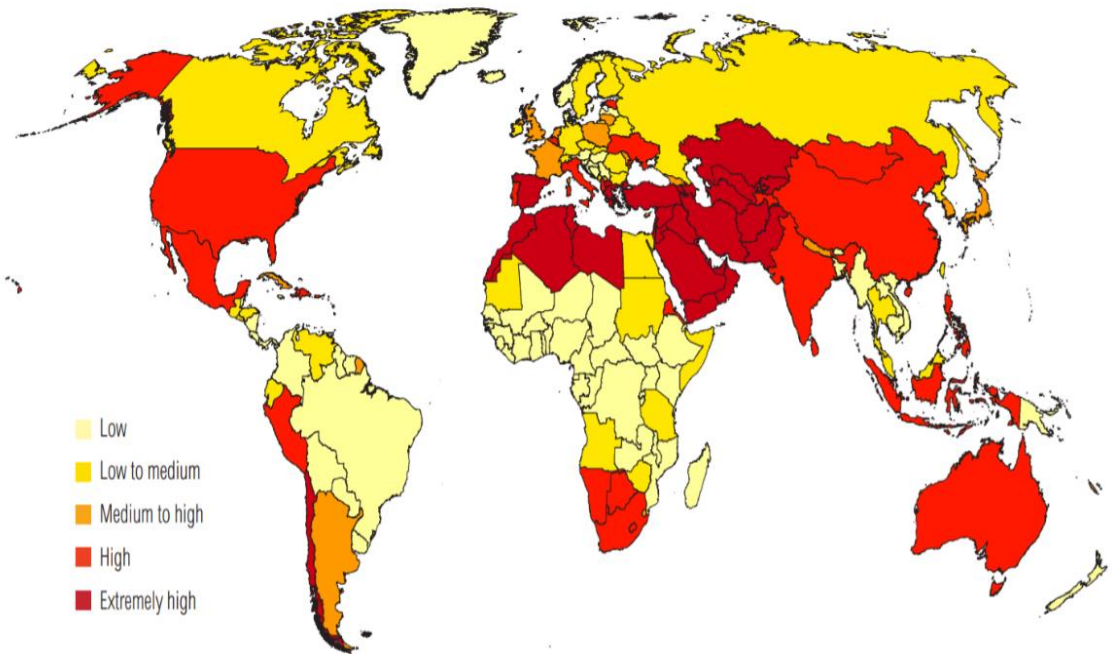

Figure 1.1 Country-level water stress in 2040 (Khan et al., 2009).

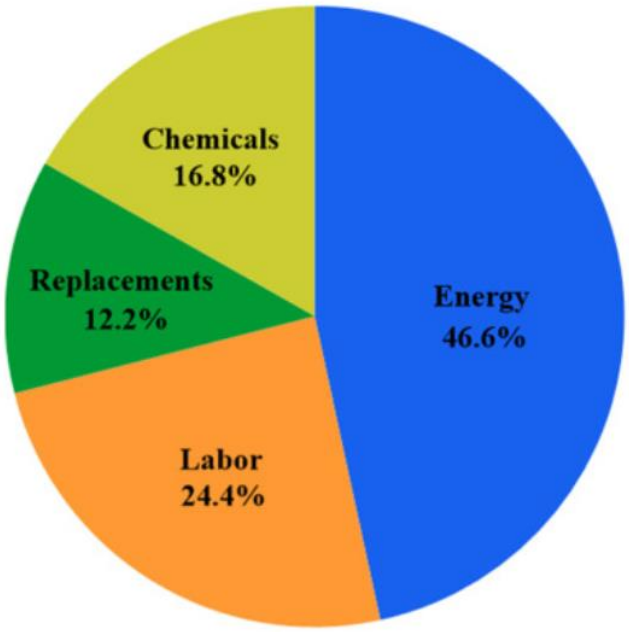

Figure 1.2 Percentage of running costs of desalination (Shahzad et al. , 2017).

1.2 Desalination technologies (DT)

Desalination is a water treatment process that removes salts from saline water to produce freshwater. Technologies for desalination systems are classified as membrane and thermal (phase-change) desalination technologies. Multi-effect distillation (MED), multi stage flash (MSF), and vapour compression (VC) are the main thermal distillation technologies, while electrodialysis (ED) and reverse osmosis (RO) are the main membrane technologies (Al-Karaghouli & Kazmerski, 2013; Mohsen et al., 2016). The selection of technologies is affected by the nature of the water source, the amount of collected water, and most importantly, the total energy consumption (Burn et al., 2015). Based on water salinity, the water source can be classified as seawater and brackish water. The amount of total dissolved solids (TDS) of brackish water is higher than drinking water and smaller than seawater (Youssef et al., 2014). Drinking water must have TDS below 1000 ppm. Brackish water has TDS in the range of 1,000 to 25,000

ppm, whilst mean TDS of seawater is about 35,000 ppm (El-Dessouky & Ettouney, 2002).

1.2.1 Multi-effect distillation (MED)

A schematic of Multi-effect distillation (MED) system is illustrated in Figure 1.3. The distillation of MED is an energy-intensive process involving both electric and thermal energy. The heating system for the feed-brine is in the form of low-pressure bleed steam (1 to 3 bars) and medium-pressure steam for the ejectors to produce the necessary vacuum in the various parts of the device. Electrical power is needed for running the system's numerous pumps, which power recycling, water-cooling, distillate liquid, brine roll down, condensation, and chemical pumps. Usually, the capacity of MED is from 10,000 to 35,000 m^3/day and comprises a set of processes, varying from 4 to 40 each, with minimal levels of temperature and pressure that allow the hot brine to flash evaporation followed by fresh water condensation (Al-Karaghouli & Kazmerski, 2013).

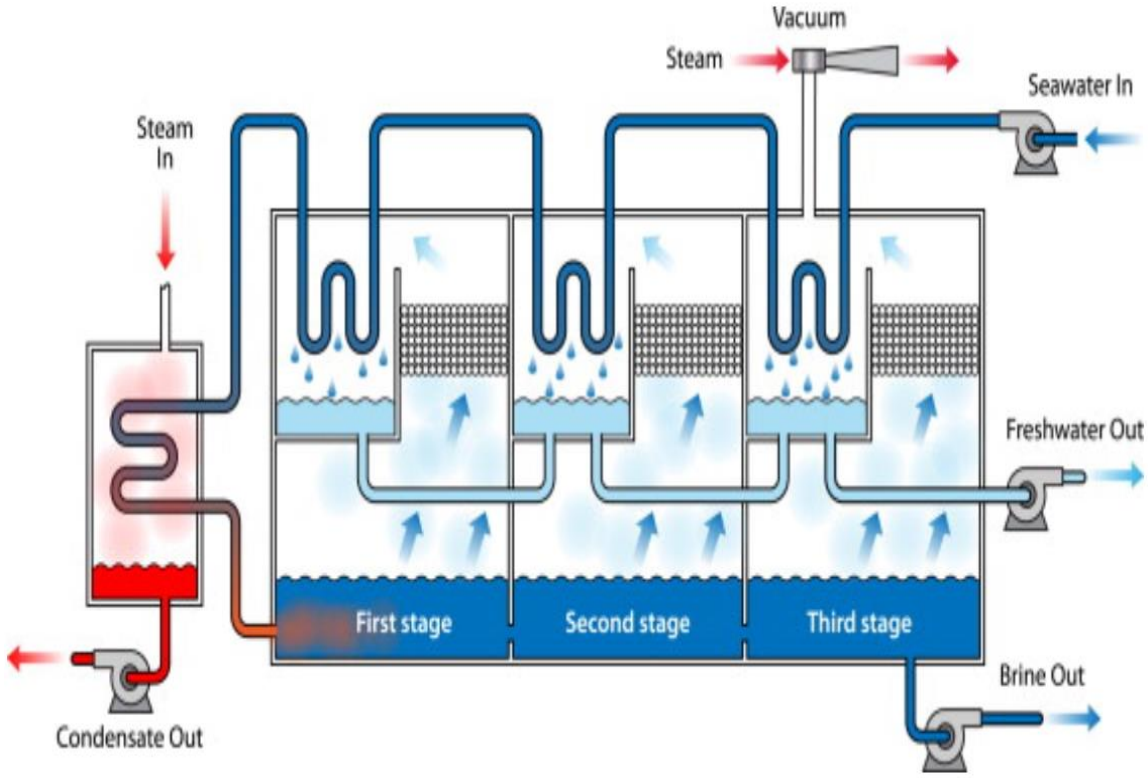

Figure 1.3 Schematic of Multi-effect distillation (MED) system (Al-Karaghouli & Kazmerski, 2013).

1.2.2 Multi stage flash (MSF)

A schematic diagram of the multi stage flash (MSF) unit can be seen in Figure 1.4. The MSF system has a series of phases (typically 2 to 16) which are sustained at reducing pressure levels. To raise the salt-water temperature of the first phase to about 70 °C, external heat from a fossil-fuel boiler, power plant waste heat, solar, or other sources is supplied to evaporate a part of the salt water within the process that is held at low pressure. The water vapour generated from this phase is moved to the next heating stage within a tube for boiling extra seawater, which generates water vapour in a number of forms. In general, multi stage flash systems are constructed at volumes of 600 to 30,000 m3 / day. The system is made up of two structures:

1) A vertical pipe through which the saline water boils through a thin film and condenses on the heat-transfer tubes.

2) A horizontal pipe in which the saline water feed is sprayed on the tubes' outer surface, and vapour flows within the horizontal pipe, where it condenses to create fresh water (Al-Karaghouli & Kazmerski, 2013).

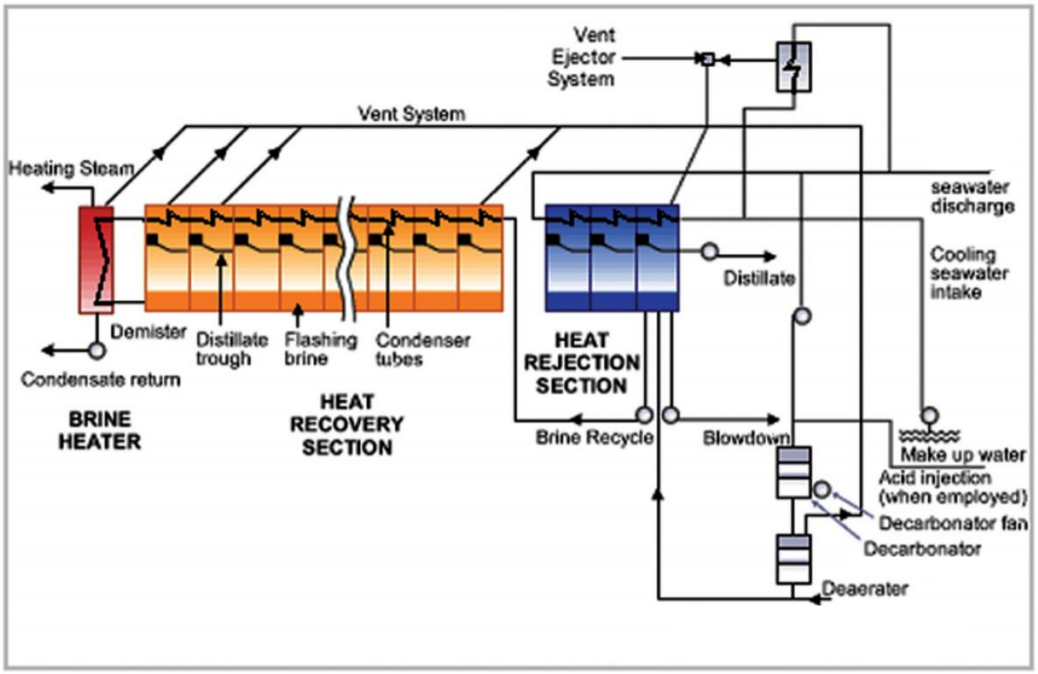

Figure 1.4 Schematic of Multi stage flash (MSF) system (Elragei et al., 2010).

1.2.3 Mechanical vapour compression (MVC)

The schematic diagram of mechanical vapour compression (MVC) system is shown in Figure 1.5. MVC is a desalination system which utilises a compressor to pressurise and heat water vapour, and then uses a heat exchanger with the incoming seawater to condense the vapour into pure distillate. The feed-water is first preheated and then sprayed over a set of evaporation tubes, where the water is evaporated. The vapour

flows through a demister and to the compressor where it is partially superheated. By spraying on the hot evaporator heat exchanger, the preheated seawater is then partially evaporated. This water vapour flows into the compressor, in which it is heated by adiabatic pressurisation. This vapour then moves into the heat exchanger of the evaporator, and when adequate heat is provided, it cools down and becomes a perfect distillate (Warsinger et al., 2015). The MVC procedure requires energy, mainly to run the compressor, the fire up heaters, and the pumps.

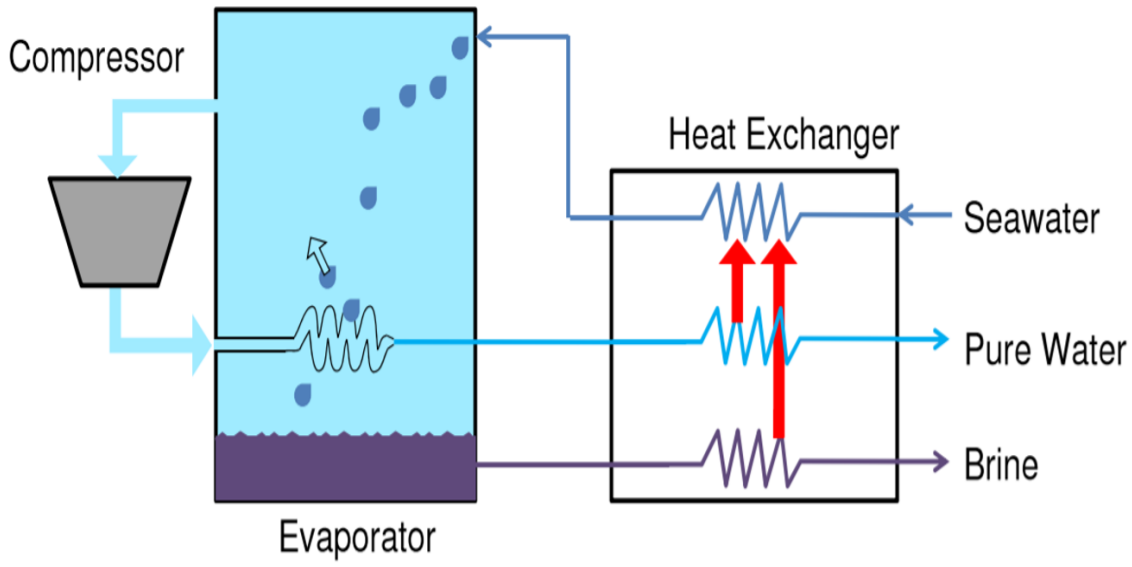

Figure 1.5 Schematic of Mechanical vapour compression system (Warsinger et al., 2015).

1.2.4 Electrodialysis (ED)

A schematic diagram of the electrodialysis (ED) system can be seen in Figure 1.6. Seawater contains salt in the form of ions. It is possible to remove the salt ions from water by adding an electric field. This is the basis of the electrodialysis (ED) desalination system (Sadrzadeh & Mohammadi, 2008). Ion exchange membranes are positioned between anodes and cathodes (Figure 1.6). The positive and negative ions relocate to the anodes and cathodes, under an electric field, generating brine and freshwater in two different platforms. By using ED, the salinity of freshwater can be different. In order to

run the ED process, the processing of ion exchange membranes produces significant water recovery and It does not require chemicals, reaction, or phase change (Al-Amshawee et al., 2020).

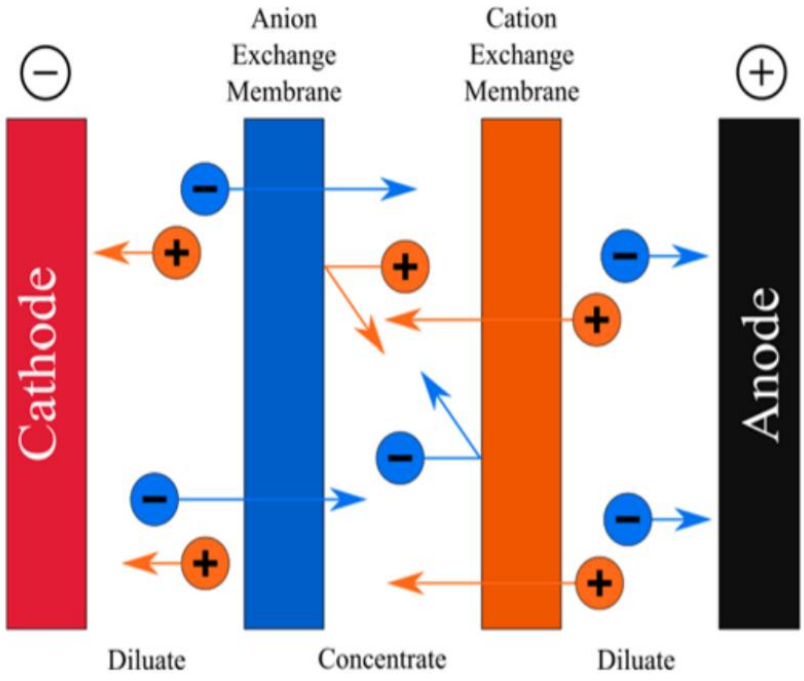

Figure 1.6 Electrodialysis desalination system (Nayar et al., 2017).

1.2.5 Reverse osmosis (RO)

Figure 1.7 shows a schematic of a membrane of a RO unit. RO is a process where pressurised seawater flows through a semipermeable membrane, separating freshwater from saline water. The chemical potential of the solute, depending on temperature, salinity and pressure, is to be equal on both sides of the membrane. By adding an external pressure to one side of the membrane, clean water will flow to the other side to restore the chemical potential. The products of the RO process are freshwater and the residue (concentrate or brine) of high salinity. The RO method has unique advantages such as adjustable size and low price (almost 25% less than thermal options) (Alkaisi et al., 2017). Recently, there has been significant research on the use of RO system for

sustainable water production (Alsarayreh et al., 2020; Atallah et al., 2020; Ruiz-García et al., 2018; Shekari et al., 2020). The characteristics of the membrane enable water to be preferentially transported over the solute. To ensure that water passes through the membrane, the pressure difference between the feed part and the membrane permeate side should be considerably higher than the osmotic pressure. This working pressure of RO must be about 3-5 bar according to existing studies (Wilf & Awerbuch, 2007), however, several qualified RO industries are designing innovative products which could be utilised with much less pressure (Qi et al., 2016).

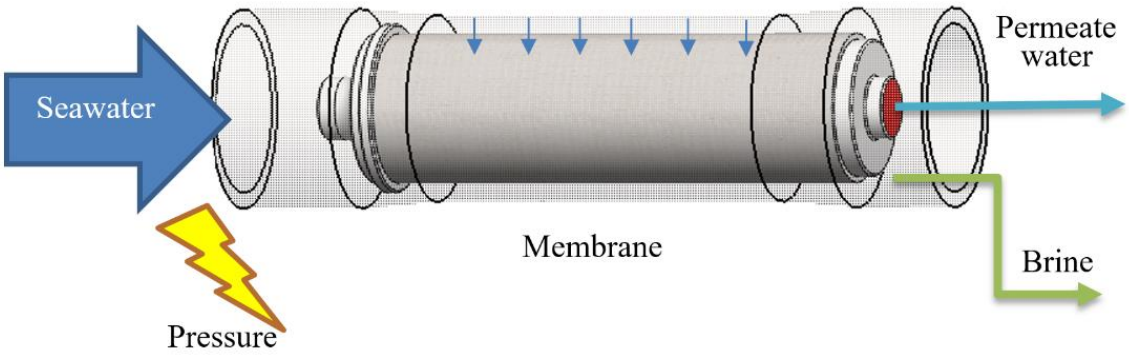

Figure 1.7 Schematic of a membrane of an RO unit.

1.3 Energy consumption of desalination systems

Generally, the supply network of a desalination system which consume energy can be categorised into four stages: intake of seawater and pre-treatment, desalination, storage of water and distribution (Al-Nory & Graves, 2013; Balfaqih et al., 2017). For instance, energy consumption for modern RO desalination systems is between 2000-4000 Wh/m3 (Amy et al., 2017; Kim et al., 2019; Park et al., 2020). By using a more efficient ERD, the energy consumption inside the RO unit can be around 2400 Wh/m^3 for seawater with salinity of 30 ppt (Karabelas et al., 2018). The energy usage for transferring seawater to

RO unit and the storage tank in a standard desalination system is about 200 Wh/m^3 (Fritzmann et al., 2007). Moreover, desalination is a quick way to produce potable water, but it has a significant effect on the environment. Therefore, it is essential to find more sustainable solutions for all stages of the network. Some researchers studied the sustainability of desalination processes (Gude & Nirmalakhandan, 2010; Singh et al., 2020; Wang et al. , 2019). Desalination facilities vary in size from small-scale machines to gigantic plants (Lim et al., 2020; Liponi et al., 2020). Some rural and remote locations use small-scale independent desalination unit, providing just few cubic metres of water every day, adjusted in size to the needs of local residents (Herold et al., 1998; Mathioulakis et al., 2007). The required amount of energy to operate a desalination system is one of the major barriers in sustainable desalination (Elsaid et al., 2020; Im et al., 2012). The appropriate source of energy for the desalination system depends on the energy source available and the characteristics of the saline water at the particular location (Busch & Mickols, 2004; Miller et al., 2015). A large number of current desalination systems use fossil fuels, or electricity generated from fossil fuels, as the main source of energy (Forstmeier et al., 2007; Ghermandi & Messalem, 2009). Recently, due to the increase in price of energy produced from fossil fuels, as well as their harmful effects on the environment, there has been growing interest worldwide in the use of renewable energy for desalination systems. In the last decade, more than 130 desalination plants have been built that operate using renewable energy (Hasan, 2015). The major renewable sources of energy are wind, solar, geothermal, tidal and wave energy (Leijon et al., 2020). Figure 1.8 shows the percentage of renewable energy-based desalination plants around the world. Among the above options, oceans and seas provide a renewable resource with the advantage of being predictable many days in advance, stable during day and night, and significantly greater in energy density compared to wind and solar energies (Gunn & Stock-Williams, 2012). This clean energy can be used either directly or for electricity generation (Dunnett & Wallace, 2009).

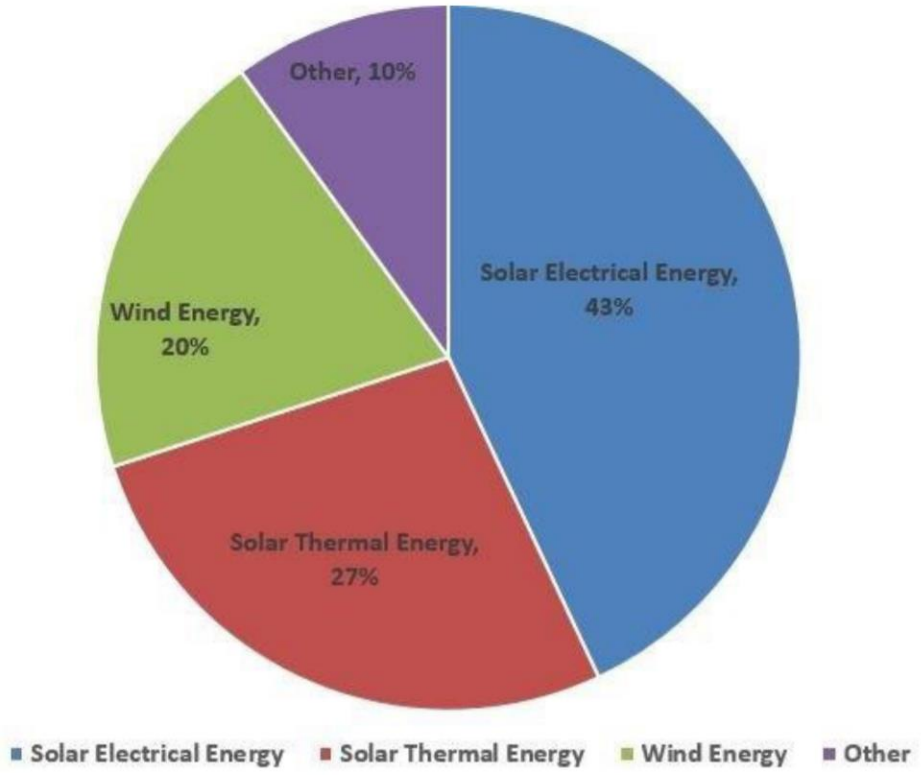

Figure 0.8 Worldwide renewable energy sources for desalination systems (Alkaisi et al., 2017).

1.4 Ocean power technologies (OPT)

Oceans cover approximately 75% of the Earth's surface. These sources of sustainable energy have enormous potential for providing the energy required by humans (Akinyele & Rayudu, 2014). Compared to other forms of green energy, the stability and predictability of ocean energy makes it much more desirable (Ponta & Jacovkis, 2008). Numerous researches have carried out research to establish feasible tools for harnessing energy with maximum efficiency (OECD, 2007). Power that can be produced from ocean can provide a significant part of world's energy needs; however, only a limited portion of the world's energy demand is currently provided by ocean resources. A wide range of ocean-powered devices is available for producing electricity from movements of the ocean. Although, ocean-powered devices can be

made commercially, most of them are in the early stage of research and development. In order to enhance the use of ocean energy, many projects have aimed to reduce the price of ocean-powered convertors as well as improving their efficiency. Also, a significant amount of research has been carried out to evaluate the best locations for utilising ocean power, the performance of advanced ocean energy systems, the quantity of electricity produced and the environmental effects of these systems. Ocean energy can be divided into two major forms: wave and tidal energies (Soleimani et al., 2015).

1.4.1 Tidal energy

One of the most reliable and predictable sources of renewable energy is tidal energy (Finnegan et al., 2020; Rourke et al., 2010). Tidal energy takes advantage of the natural ebb and current of marine tidal waters induced mainly by the interaction of earth, sun and moon gravity fields (Hammons, 1993; Mazumder & Arima, 2005). Tidal energy is estimated to have a global potential of 120 *GW* and could generate up to 150 *TWh* annually (Abuan & Howell, 2019; Finnegan et al., 2020; Zhu, Ding, Huang, Bao, & Liu, 2020). Latest attempts have been focused on the kinetic energy of tidal currents to harness this predictable source of energy (Watchorn & Trapp, 2000; Owen, 2008). The force of gravity of the moon is 2.2 times greater than the gravitational force of the sun because it is closer to the earth (Hay et al., 2020). In coastal regions and in environments in which the seafloor causes the water to pass into narrow channels, tidal currents are observed. These channel flows are categorised as two types of current; the current flowing in the direction of the ocean is referred to as the flood current and the current receding from the ocean is referred to as the ebb current (Boyle, 2004). Figure 1.9 shows the estimated tidal current speeds around the world. The velocity ranges from zero to maximum in both directions. Tidal energy systems can be divided into two major types: tidal barrages which utilise the tides' potential energy and tidal turbines that use kinetic energy (Lemonis & Cutler, 2004).

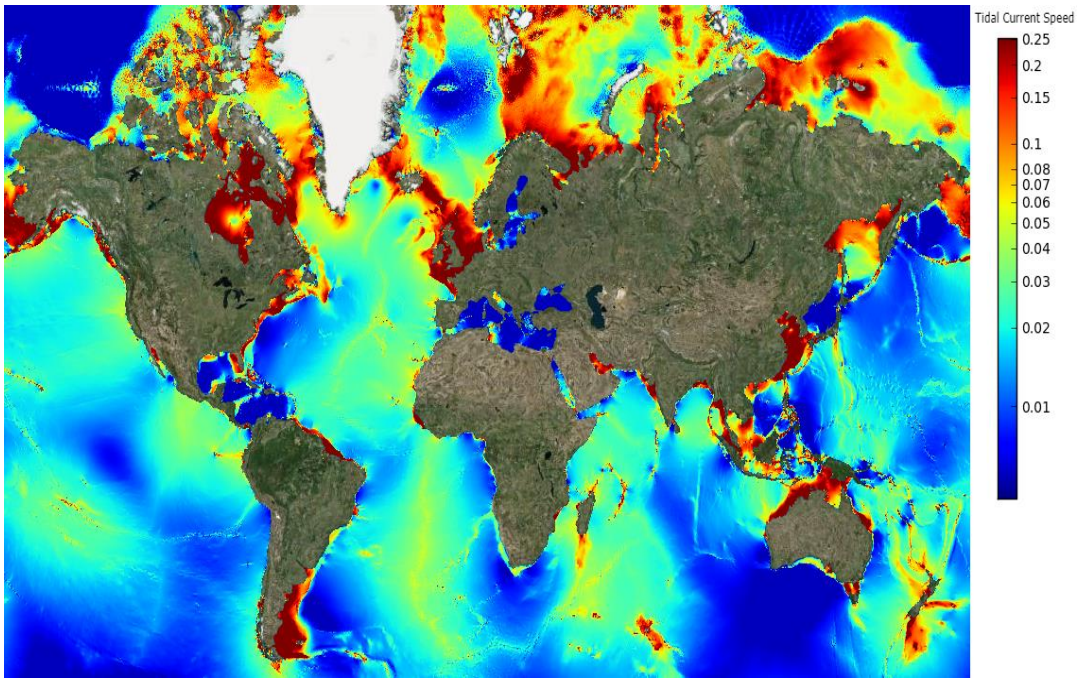

Figure 1.9 Estimated tidal current speed of the world in m/s ("https://tips.noveltis.com/," 2020).

1.4.1.1 *Tidal barrages (TB)*

Tidal barrages (TB) work based on the tides' potential energy. Usually, a TB is a dam constructed through a harbour or canal that has a tidal level over 5 m (Etemadi et al., 2011). The tidal barrages are built across the estuary of the sea. A standard tidal barrage includes turbines, sluice gates, embankments and ship locks. The turbines which are used in tidal dams can be either unidirectional or bidirectional. TB separates the input and output tides and then constructs a water head (Samo et al., 2017). When the pressures are applied to the turbine, the water level will flow in and out into the channel by which the turbine rotates. Figure 1.10 shows a schematic of a tidal barrage.

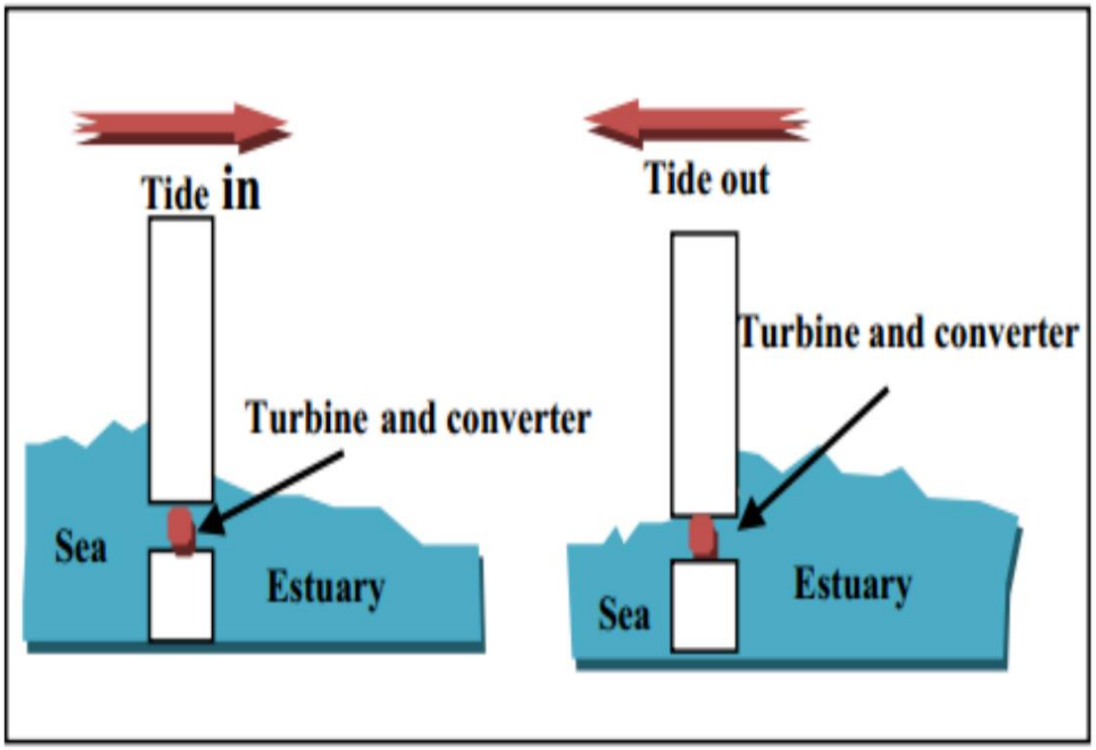

Figure 1.10 Schematic of a tidal barrage (Samo et al., 2017).

1.4.1.2 *Vertical axis tidal (VAT) turbine*

A vertical axis tidal (VAT) turbine implies that the blades of the turbine spin in the vertical plane (Li & Calisal, 2010). Because of its basic construction, the ease of realisation and indifference to the flow path, the VAT turbine is one of the main elements of the tidal energy generation technologies (Zhang et al., 2012). Figure 1.11 shows some of the common arrangements in vertical axis tidal turbines. VAT turbines can be used in coastal regions with appropriate tides (Derakhshan et al., 2017). The most popular choices in the vertical axis categories are Darrieus turbines. It is also very common to use H-Darrieus or Squirrel-cage Darrieus turbines, and there are many reports of Darrieus turbines used in tidal technology (Kumar & Saini, 2017; Sornes, 2010).

According to Tidal power Co. (http://tidalpower.co.uk, 2020), the major weakness of tidal turbines is the high price of design and manufacturing. Traditionally, optimisation of

turbine geometry can be achieved by running numerous numerical models of the turbine which can become computationally expensive. Using combination of the Taguchi method and CFD modelling is a straightforward solution for optimisation of geometry of tidal turbines. As the efficiency of these turbines increases, their cost of manufacturing becomes more economically justified.

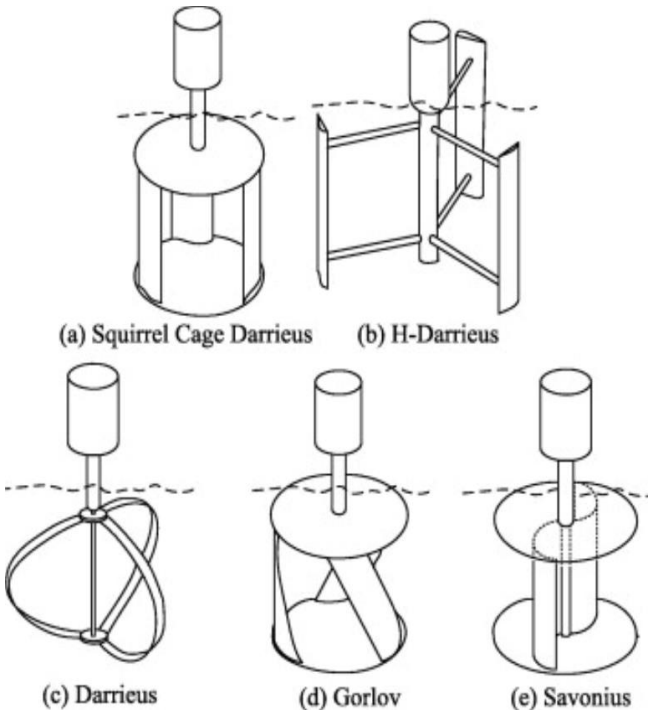

Figure 1.11 Vertical axis tidal (VAT) turbines (Khan et al., 2009).

1.4.1.3 *Horizontal axis tidal (HAT) turbine*

A schematic of a Horizontal axis tidal (HAT) turbine is illustrated in Figure 1.12. The HAT turbines run similarly to horizontal axis wind (HAW) turbines. In fact, their comparatively advanced state of production is primarily attributed to the technical achievements and sophistication of the wind industry (Nicholls-Lee, 2011). In a HAT turbine, relative passes over the spinning blades formed by the airfoil, causing a pressure gradient, thus lifting, and dragging forces. The lift force is much stronger than the drag force and this results in turbine's complete rotation along the rotational axis. The HAT turbine blades convert the kinetic energy of the tidal power to the

mechanical power of the shaft, and a generator transforms this mechanical energy into electricity.

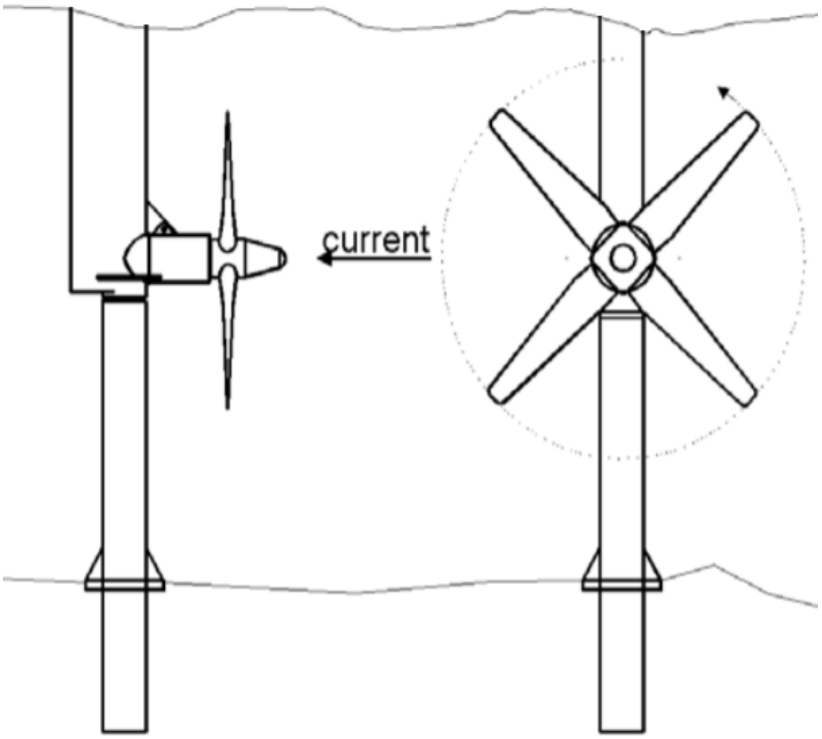

Figure 1.12 Schematic of a horizontal axis tidal (HAT) turbine (Kirke & Lazauskas, 2008).

1.4.1.4 *Oscillating hydrofoil (OH)*

An oscillating hydrofoil, illustrated in Figure 1.13, converts the tidal energy to mechanical energy, in a similar way to a turbine. An OH contains a hydrofoil wing connected to a lever arm (Roberts et al., 2016). As water passes over the hydrofoil, it produces lift, allowing the lever to move up and down. The generated oscillations can be used to push the water to a system to generate electricity or/and desalinate water.

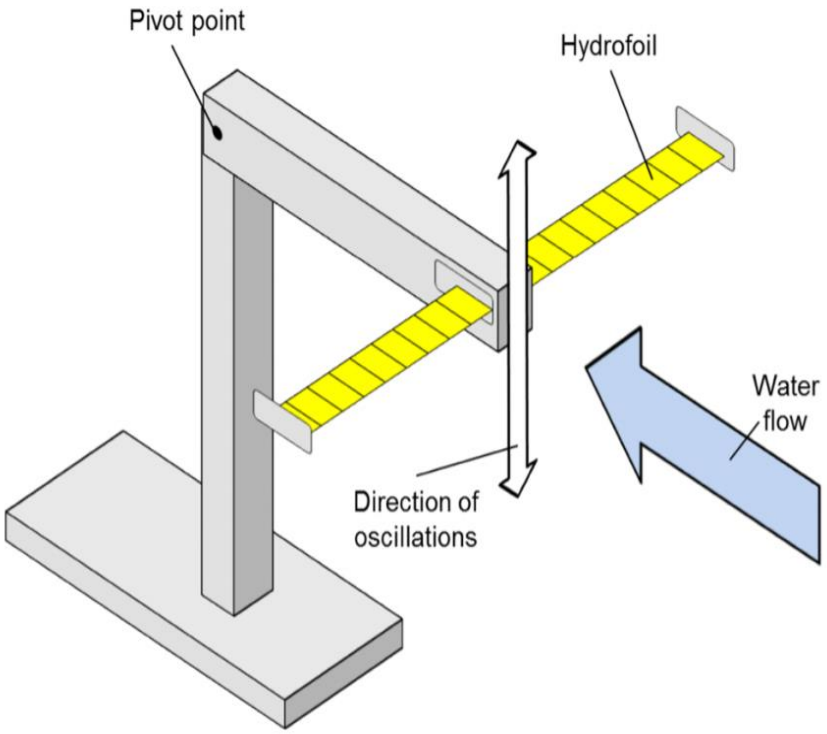

Figure 1.13 A schematic of an Oscillating hydrofoil (Roberts et al., 2016).

1.4.1.5 *Archimedes screw (AS)*

The Archimedes screw (AS) is a device, which was used since ancient times in a number of applications (Waters, 2015). Throughout the 3rd century BC, the Greek mathematician, Archimedes, is known to have created the screw pump, hence it is known as the "Archimedes screw" (Lashofer et al., 2012). According to one hypothesis, the King of Egypt ordered Archimedes to find a method to extract water from his vessels, while others state that the system was invented hundreds of years before Archimedes was born and he only modified it and made it well known in the world (Koetsier & Blauwendraat, 2004). This device (Figure 1.14) is a helical set of basic blades wrapped, like a woodscrew, around a central cylinder. There may be a single blade, or numerous blades on the AS device. It is most common for screws utilised as turbines to have three or four paths of blades. An attached gearbox and generator produce energy during the torque transmission. The momentum of the flow and the hydrostatic force generate the

torque. Due to the comparatively low rotational values of Archimedes screw turbines, a complex gearbox is required for link with a generator.

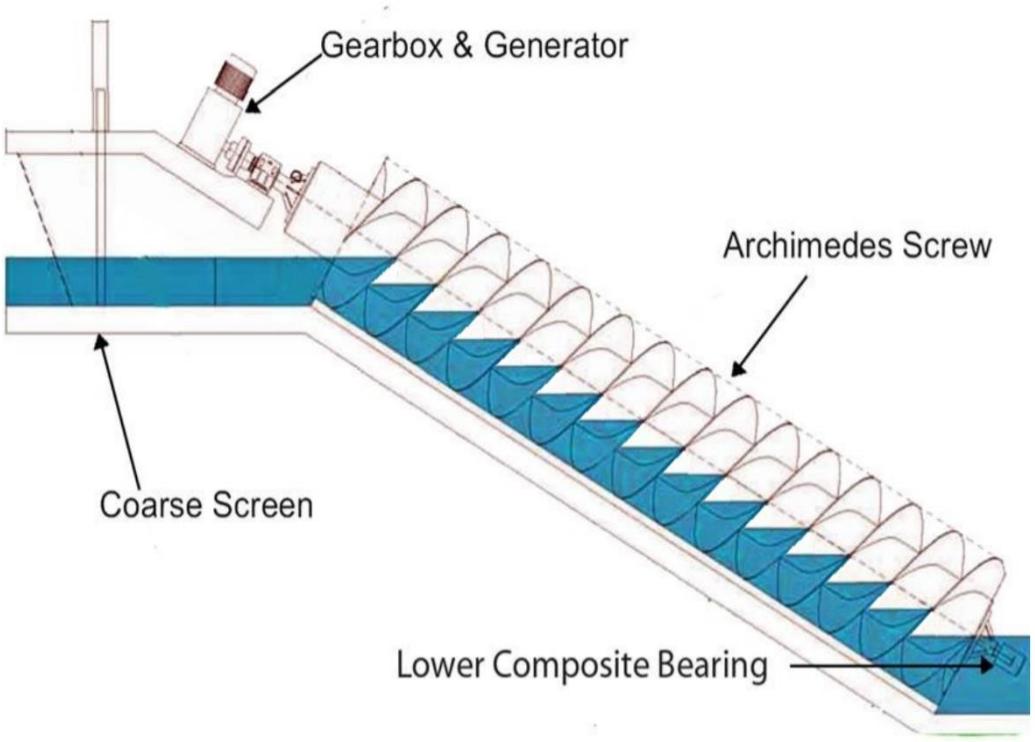

Figure 1.14 A schematic of an Oscillating hydrofoil (Simmons & Lubitz, 2017).

1.4.1.6 *Tidal kite (TK)*

A tidal kite (Figure 1.15) is a tied paravane flying underwater, turning the kinetic energy of current to electricity. This system consists of a turbine connected to a wing that travels through the water in circles like a kite, while it is bound to the sea floor by means of a flying cable (Khan & Bhuyan, 2009). The tidal kite is theoretically very effective by adopting a figure-eight vector, and works in water depths of 60-120 m at currents as low as 1.2 m/s.

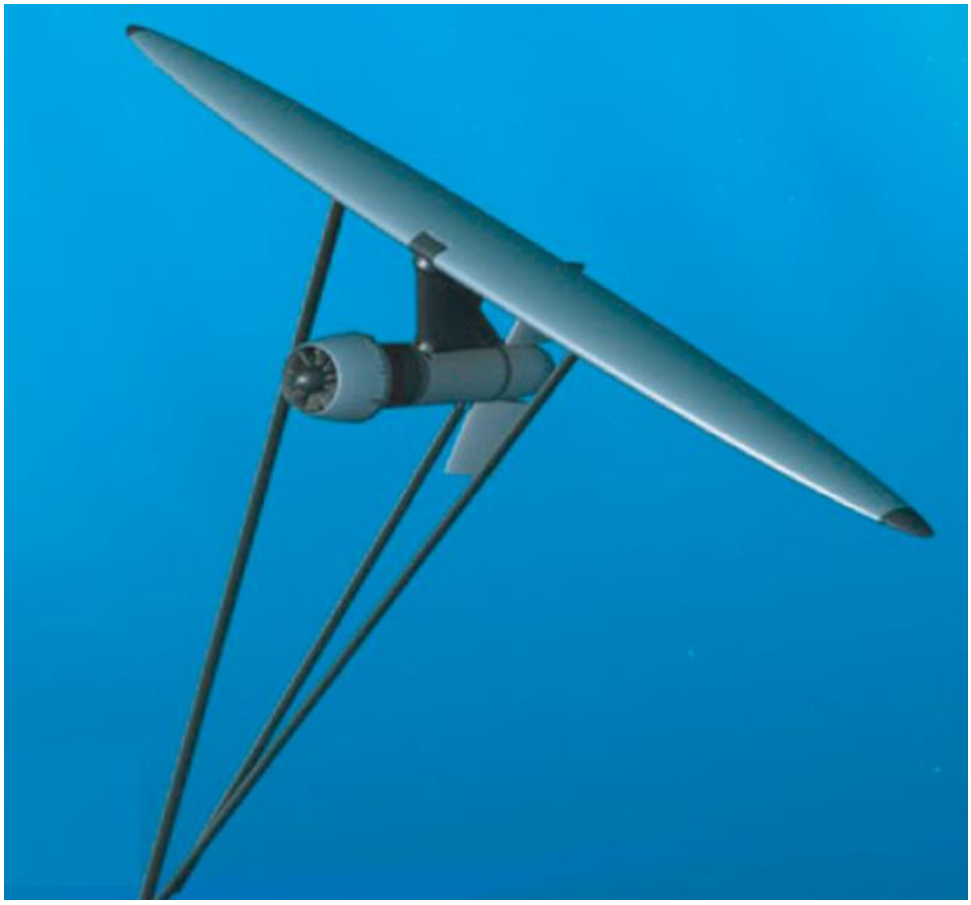

Figure 1.15 Tidal kite (Segura et al., 2017).

1.5 Ocean-powered desalination technologies

All possible combinations of desalination technologies and ocean power concepts are surmised in Table 1.1. Among these combinations, some have been studied and some may be far-fetched. Most studies of ocean-powered desalination have focused on the use of wave energy converters (Li et al., 2018). These typically involve the use of oscillating systems to pressurise air or water to drive a turbine or hydraulic system. Such systems have been tested in terms of electricity production, but their application to desalination systems has also been studied and tested. However, wave energy is highly variable and not suitable for more sheltered coastlines where there is insufficient fetch for waves to develop except in extreme conditions. Where appropriate tidal resources exist,

current-driven desalination plants may provide a more reliable alternative. The best desalination method which can be combined with tidal energy is RO (Delgado-Torres et al., 2020; Ling et al., 2018). Therefore, in this current study, the combinations of VAT and HAT turbines with RO desalination system are investigated.

Table 1.1 All possible combinations of ocean power concepts and desalination technologies

Desalination technology (DT)	Ocean power technology (OPT)	OPT/DT system
Multi-effect distillation (MED)	Oscillating Water Column (OWC)	OWCMED
Multi-effect distillation (MED)	Wave Overtopping (WO)	WOMED
Multi-effect distillation (MED)	Point Absorber (PA)	PAMED
Multi-effect distillation (MED)	Tidal barrages (TB)	TBMED
Multi-effect distillation (MED)	Vertical axis tidal (VAT) turbine	VATMED
Multi-effect distillation (MED)	Horizontal axis tidal (HAT) turbine	HATMED
Multi-effect distillation (MED)	Oscillating hydrofoil (OH)	OHMED
Multi-effect distillation (MED)	Archimedes screw (AS)	ASMED
Multi-effect distillation (MED)	Tidal kite (TK)	TKMED
Multi stage flash (MSF)	Oscillating Water Column (OWC)	OWCMSF
Multi stage flash (MSF)	Wave Overtopping (WO)	WOMSF
Multi stage flash (MSF)	Point Absorber (PA)	PAMSF
Multi stage flash (MSF)	Tidal barrages (TB)	TBMSF
Multi stage flash (MSF)	Vertical axis tidal (VAT) turbine	VATMSF
Multi stage flash (MSF)	Horizontal axis tidal (HAT) turbine	HATMSF
Multi stage flash (MSF)	Oscillating hydrofoil (OH)	OHMSF
Multi stage flash (MSF)	Archimedes screw (AS)	ASMSF
Multi stage flash (MSF)	Tidal kite (TK)	TKMSF
Mechanical Vapour compression (MVC)	Oscillating Water Column (OWC)	OWCMVC
Mechanical Vapour compression (MVC)	Wave Overtopping (WO)	WOMVC
Mechanical Vapour compression (MVC)	Point Absorber (PA)	PAMVC
Mechanical Vapour compression (MVC)	Tidal barrages (TB)	TBMVC
Mechanical Vapour compression (MVC)	Vertical axis tidal (VAT) turbine	VATMVC
Mechanical Vapour compression (MVC)	Horizontal axis tidal (HAT) turbine	HATMVC
Mechanical Vapour compression (MVC)	Oscillating hydrofoil (OH)	OHMVC
Mechanical Vapour compression (MVC)	Archimedes screw (AS)	ASMVC
Mechanical Vapour compression (MVC)	Tidal kite (TK)	TKMVC
Electrodialysis (ED)	Oscillating Water Column (OWC)	OWCED
Electrodialysis (ED)	Wave Overtopping (WO)	WOED
Electrodialysis (ED)	Point Absorber (PA)	PAED
Electrodialysis (ED)	Tidal barrages (TB)	TBED
Electrodialysis (ED)	Vertical axis tidal (VAT) turbine	VATED
Electrodialysis (ED)	Horizontal axis tidal (HAT) turbine	HATED
Electrodialysis (ED)	Oscillating hydrofoil (OH)	OHED
Electrodialysis (ED)	Archimedes screw (AS)	ASED
Electrodialysis (ED)	Tidal kite (TK)	TKED
Reverse osmosis (RO)	Oscillating Water Column (OWC)	OWCRO
Reverse osmosis (RO)	Wave Overtopping (WO)	WORO
Reverse osmosis (RO)	Point Absorber (PA)	PARO
Reverse osmosis (RO)	Tidal barrages (TB)	TBRO
Reverse osmosis (RO)	Vertical axis tidal (VAT) turbine	**VATRO**
Reverse osmosis (RO)	Horizontal axis tidal (HAT) turbine	**HATRO**
Reverse osmosis (RO)	Oscillating hydrofoil (OH)	OHRO
Reverse osmosis (RO)	Archimedes screw (AS)	ASRO
Reverse osmosis (RO)	Tidal kite (TK)	TKRO

1.6 Research objectives

Seawater desalination is an important option for solving the world's water crisis and this process requires a significant amount of energy. Renewable energy can be utilised to power desalination devices. The major advantage renewable energy sources is that they are infinite and cannot be depleted. Renewable energy options, mostly solar, wind and geothermal systems, have been studied in detail to supply the energy needed for water desalination. Ocean energy provides a renewable resource with the advantage of being predictable many days in advance, stable during day and night, and significantly greater in its energy density compared to wind and solar energies. Although advantages of energy generated from the ocean for powering desalination processes is appealing, the potential of ocean power for desalination systems has not been researched in detail. The development of ocean-powered systems has been limited due to technological limitations of energy harvesting and transportation. In recent years, several sea energy devices have been designed and deployed, converting the motion of sea waves to electricity. The potential exists to use similar technology, utilising the sea waves and tides, to drive desalination systems. However, due to the high pressure required for desalination, it is necessary to develop an innovative design to use energy from movement of the sea effectively to desalinate saline water. In this work, a novel ocean-powered RO seawater desalination system is introduced and the most expensive part of the system, which are tidal turbines, is optimised. Tidal turbines can be used for the entire desalination process to derive energy for the intake of feed water, pre-treatment, and producing pressure required by the system. The turbines will extract energy from the tidal movement and run the water pump in order to provide the hydraulic pressure needed for the desalination unit. In this concept, there is no need to convert the kinetic energy to electricity in a generator, and then electricity to kinetic energy in a motor, and finally kinetic energy to pressurised water in a pump. In this study, the converted kinetic energy is used to pressurise water in a pump, which is more cost effective. Since converting kinetic energy

to pressurised water leads to variable load, a water storage tank will be used to stabilise the driving energy. Because the tidal energy changes during day and night and is not always constant, the provided energy should be stored to supply the energy required in the RO desalination system. Storing electricity requires expensive batteries compared to the proposed model, which only needs a large water storage tank.

A key focus of this work is to optimise one vertical axis tidal turbine and one horizontal axis turbine, which can be used for water desalination.

1.7 Organisation of the thesis

In what follows, a literature review of ocean-powered desalination systems and optimisation of tidal turbines is presented in Chapter 2. Chapter 3 presents design of the RO desalination possess. In Chapter 4, the details of effects of surface roughness on hydrodynamic performance of a tidal turbine are investigated. Chapter 5 presents optimisation of a VAT turbine for powering a RO desalination system. In Chapter 6, optimisation of a HAT turbine for powering a RO desalination system is presented. Finally, Chapter 7 presents the conclusions and some recommendations for future work.

Chapter Two: Literature Review

2.1 Ocean-powered desalination system

The use of ocean kinetic power for desalination has been the subject of active research since the 1990s (Maratos, 2003). However the research in this field has been intensified throughout the last decade (Amy et al., 2017; Chen, 2015; Davies, 2005; Leijon et al., 2018; Nadel, 2008; Ng & Shahzad, 2018). A number of review papers have been published on the ocean-powered desalination technologies (Westwood, 2004; López et al., 2013). However, the development of ocean-powered seawater desalination technology is still at its infancy and more investigation is needed before operational systems are deployed and implemented. One of the earliest papers about wave powered desalination was published by Crerar et al. (1987). In their work, a novel desalination system, powered directly by wave energy, was implemented. However, the cost of water in their system was very high compared to the cost of drinking water obtained in other ways. Sawyer & Maratos (2001) studied the technological and economic potential of wave energy with a water hammer for desalination. The unit is equivalent to the commonly used hydraulic-ram to raise water from the sea. In order to achieve the hydraulic pressure for the RO desalination system, a water hammer creates unsteady incompressible pipe flow by using wave motion. The findings revealed that the introduced device can, in theory, produce direct pressure necessary to power the RO desalination system, however, it was just an investigation into the economic feasibility of RO desalination. Zhao & Liu (2009) carried out a theoretical study on a tidal-powered solar distillation system. In their innovative design, instead of running pumps with electricity, tidal energy was used to produce energy for vacuum extraction as well as water intake. They performed hydrodynamic and thermal analysis for the water intake and drainage system powered by tidal energy. Their proposed system can only work efficiently in locations with a tidal level

greater than 2 m, however, using storage tank can stabilise energy requirement when tidal energy is used for powering water pump. A wave-powered RO desalination system was developed by Sharmila et al. (2004) in India. Since waves are transient and irregular source of energy throughout the year (this is the main weakness of wave energy for use in desalination system), it is essential to predict the behaviour of the system at various wave energy rates. Thus, they theoretically simulated the wave energy profile and based on the obtained profile, they designed and developed a wave converter that was suitable for the desalination system. Unlike wave energy which is influenced by speed of the wind, the strength of tidal energy is influenced by the location and shape of the Earth which makes tidal energy quite predictable (Ullman, 2002). Ling et al. (2018) carried out an economic analysis of a tidal power RO desalination system where the productivity of the desalination system and cost of freshwater were compared with the previous methods. It was concluded that the TPRO desalination system could save water costs between 30-40% compared to the traditional RO system.

2.2 Effect of surface roughness on hydrodynamic performance of tidal turbine

Solid particles, marine animals, and cavitation erosion can increase the surface roughness of blades which could affect turbine's efficiency (Rasool et al., 2016). As the surface roughness of turbine increases, its power output greatly decreases (Walker et al., 2014). Maruzewski et al. (2009) carried out experimental and numerical investigation into the impacts of surface roughness on the performance of Francis Hydro (FH) turbine. They showed that, in a severe case of roughness, the performance could decrease to 15%. Although, this work provided valuable data for DH turbine, because of its configuration, the results cannot be generalised for DH turbine. (Walker et al.) studied, experimentally and numerically, the effects of blade roughness on the performance of a two-blade horizontal hydro turbine. Their results showed about 18% reduction in power output with roughness height (H_r) of 625 μm. Recently, Priegue & Stoesser (2017) carried out an experimental study to investigate the effects of surface roughness on the performance of

a vertical hydro turbine. They reported negative effect of blade roughness on the performance of the tidal turbine. Although this research is another useful contribution in this field, it was limited to an experimental work involving only 3 different roughness values and they did not study the physics of the flow around the turbine.

2.3 Optimisation of vertical and horizontal axis tidal turbines

Tidal turbines are used as sea-powered convertors to produce electricity or desalinate saline water (Ling, et al., 2018). Similar to wind turbines, tidal turbines are divided into Vertical Axis Tidal (VAT) turbines and Horizontal Axis Tidal (HAT) turbines (Baratchi et al., 2019). Over the last two decades, a range of tidal stream devices have been designed and developed to convert the kinetic energy of tidal currents into electrical energy and extensively tested in real-sea conditions (Singh, 2020). The tidal energy industry saw the deployment of the first arrays of devices in 2016 (Carrel, 2016), and is considered close to the point of commercial viability. Although these devices have been designed for the generation of electricity, the same design principles can be used in desalination application to produce high-pressure water directly. This would minimise energy losses that would otherwise occur through producing electricity to supply electrically powered desalination plants.

According to Kumar et al. (2019), the number of published papers on optimisation of tidal turbines is significantly less than wind turbines (see Figure 2.1).

Here a review of the notable optimisation procedures conducted on VAT and HAT turbines, in terms of optimisation methods, objective functions, optimised parameters, and results, is presented. (Ma et al., 2016) optimised the blade of a VAT turbine to increase the efficiency of the turbine. First, a genetic algorithm was used to optimise the vertical axis turbine's blade pitch motion (compared with the fixed pitch turbine), with maximum energy efficiency as the objective function and blade pitch motion as the optimised

parameter. The data were then fitted into a cosine-like curve using a particular data processing method. Following that, a general pattern for calculating blade motion was developed. Finally, the blade pitch motion formula was validated using 2D CFD simulation. The results indicated that after improving blade pitch motion, the turbine's performance was improved by 14%. It should be noted that in Ma et al.'s work, CFD was used only to validate the optimisation and was not combined with the genetic algorithm. Combining a 3D CFD simulation with a genetic algorithm would take a significant amount of time because only one 3D CFD simulation with a fixed geometry (without changing any parameters) could take a few days to obtain convergence and acceptable solutions. Alidadi (2009) studied duct optimisation of a ducted VAT turbine. They used a discrete vortex method to analyse the performance of unducted and ducted VAT turbines. The power coefficient (C_p) of a VAT turbine is greatly increased by ducting, according to a study of unducted and ducted turbines (Alidadi, 2009). Furthermore, the findings revealed that ducting significantly reduces moment variability, especially at high TSRs. A new method for calculating the influence of the towing tank wall on experimental findings was introduced based on the method designed for ducted turbines. Their findings revealed that when a turbine runs in a tank, its power coefficient increases (Alidadi, 2009). This is particularly true in the ducted turbine that has a higher blockage ratio than the unducted turbine. The findings also revealed that, as the tank width decreases, the amount of increase in power coefficient increases. An optimisation analysis was carried out in order to define the duct shape as the optimal parameter for increasing the output power of a VAT turbine. Similar to the findings of experimentally tested ducts, the results of optimised ducts showed a higher power coefficient for the turbine by 10%. An optimisation of solidity ratio of a VAT turbine was carried out by Mannion et al. (2020). They used blade element momentum theory models rather than CFD simulations. In their publication, they introduced a blade element momentum theory model for high solidity VAT turbine which traditional blade element momentum theory models are unable of modelling. Instead of the iterative approach used in conventional blade element momentum theory models, the

stream-tube model offers a dynamic approach to determine axial induction factors. The design also contains corrective methods to account for complex stall, flow expansion, and finite aspect ratios. To evaluate model performance, the power output results of the model were evaluated against experimental results for both low and high solidity ratios. In a confined flow, the model accurately predicted peak performance values for a low solidity wind turbine to within 2.5 percent, a high solidity wind turbine to within 8%, and a high solidity tidal turbine to within 10%. Huang and Kanemoto (2015) optimised the front blade pitch angle distribution in a HAT turbine numerically. In order to exploit renewable energies from tidal stream, they designed tandem propellers of a unique counter-rotating HAT turbine according to the blade element momentum theory. Then, to achieve desirable blade profiles, a multi-objective optimization approach that combined the response surface method with a genetic algorithm was used. In their publication, the front blade pitch angle distribution was used as an optimisation parameter since it has a major effect on the rear blade inlet conditions. The findings illustrated that both the power coefficient and thrust coefficient optimization goals can be greatly increased. It was also shown that the power coefficient thrust increased by 1 %. The output of the optimised counter-rotating style HAT turbine was evaluated using 3D CFD analysis to validate the optimisation approach. As can be seen in this work, they only used the CFD to validate the optimisation approach since it takes several days to do a single 3D CFD simulation of a turbine and they were not able to use CFD simulations which would provide more accurate data points based on their optimisation. Zhang et al. (2019) optimised the pitch angle and chord length distribution of a HAT turbine using blade element momentum and CFD simulations. This publication suggested a multi-objective optimisation model to improve the efficiency of HAT turbines. A proposed methodology for horizontal tidal turbines was developed, combining blade element momentum theory and CFD simulations. Then to achieve the optimum blade profiles, they used a multi-objective optimisation approach combining the response surface method with the multi-objective genetic algorithm NSGA-II. The design variables were the pitch angle and chord length

distribution, while the objective functions were the mean power coefficient and variance of power coefficient. Both objective functions were improved, as the mean power coefficient improved by 4.1 % and the variance of power coefficient decreased by 46.7 %. In this publication, the CFD was combined with another method to provide suitable data points for optimisation, since simulating a turbine with a CFD would take several days. Kumara et al. (2019) carried out an optimisation of thickness of blade of HAT turbine. Surrogate models and CFD simulations were used to optimise the cross-sectional geometry of a HAT turbine blade. The blade thickness parameters of a HAT turbine were varied to investigate changes of power coefficient of turbine. Multiple surrogates were added to the CFD results with design parameter variance to find the appropriate design. The surrogate models included response surface approximation, radial base function, Kriging, and weighted average surrogates. The optimised design increased the power coefficient by 17.9%. In this publication, the effects of type of hubs which greatly affects the turbine output efficiency were ignored.

For optimisation of a turbine with genetic algorithm or similar optimisation algorithms, hundreds of basic numerical simulations are needed. One of the limitations of 3D CFD is that it is time consuming, since for obtaining reliable results, different parameters must converge simultaneously. Computational time of combination of the genetic algorithm with the 3D CFD would be prohibitively expensive. However, the Taguchi method and superposition approach can provide a reasonable estimate of optimised parameters with a few number of simulations, and current PhD thesis is a valid example of this claim. It should be mentioned that superposition model is a kind of simple of surrogate model and was used in this work.

A review of research on VAT turbines also indicates that three parameters, namely twist angle (Pongduang et al., 2015), camber (Zhang et al., 2020), and chord/radius ratio (Heavey et al., 2018) could have significant effect on turbine performance. The impacts of these three parameters on performance of VAT turbines have not been investigated in

detail and their combined effects are unknown thus far. In this research, the effects of these three parameters on turbine performance are studied simultaneously.

A horizontal turbine consists of two main parts: the hub and the blades. The solidity ratio, which is the ratio of the total turbine blade area over the swept area, is the most important factor affecting turbine performance. The solidity ratio varies greatly with the blade size and the number of blades. Thus, optimisation of this ratio is accomplished by changing these two factors. On the other hand, the type of hub can be changed based on the hub radius and shape of the hub. In this work, four factors are considered to be optimised including size of blade, number of blades, hub radius, and hub shape.

The Taguchi method is one of the powerful optimisation methods in product design. The method, also known as the Robust Design method, significantly improves the performance and quality of engineering products (Hong et al., 2018). The basic concept of the Taguchi theory is to improve a product's quality by minimising the number of needed experiments without removing the parameters (Jahanshahi et al., 2008). The Taguchi method offers Orthogonal Arrays (OA) or matrix of experiments (as a mathematical tool) in order to implement minimum experiments for providing wide range of variables to make better decision. The term of L_{Π} (Ω^{Φ}) is used to show the number of experiments. Where Π is the number of experiments, Ω is the number of levels, and Φ is the number of factors. For constructing OA, equal-level or mixed-level pattern can be used depending on the problem to be investigated. Mix-level Taguchi method provides a wider range of levels for significant factors (Wang & Huang, 2015). Moreover, the Taguchi method introduces the signal-to-noise (S/N) ratio, which can be used to calculate the quality of the output in terms of deviation from the desired values. In other words, the S/N ratio is an indicator for measuring the quality and Orthogonal Arrays (OA) provide minimum design parameters concurrently (Sapakal & Telsang, 2012). The target quality of output is a key factor in the Taguchi method and should be defined for every application. The Taguchi method can be combined with numerical simulation (e.g.,

Computational Fluid Dynamic, CFD) models (Chan et al., 2019) in order to estimate optimised parameters. In this work, the objective is to maximise the performance of a tidal turbine. The power coefficient (C_p) which is an indicator of output, can be calculated from CFD simulations. Recently, the Taguchi technique has been used for optimising turbine parameters. Rao (2015) optimised a Vertical Axis Wind (VAW) turbine by using the Taguchi method. In their work, the impacts of wake revolution and tip loss were considered when calculating the performance of the VAW turbine. They defined two different sets of parameters and levels, called inner and outer loops, and analysed each one separately. They used a standard L_{27} (3^{10}) OA for the inner loop and a standard L_{12} (2^9) OA for each outer loop. In the design phase, the performance of the turbine was maximised by focusing on blade size and twist angle as the design parameters. The results showed an increase of 52.7% in the efficiency of the turbine. Although they considered blade size, the effects of cambered airfoil was overlooked.

Wang et al. (2018) optimised the efficiency of VAW turbine by using CFD and Taguchi technique. They considered amplitude, wavelength, and twist angle as the design parameters and power coefficient (C_P) as the objective function. They used a standard L9 (3^4) OA for the Taguchi technique. Although, they improved the VAW turbine efficiency by 18% and provided valuable information about using the Taguchi technique for optimising turbines, there was a significant gap in the selected levels for twist angle of blade, which has significant effect on the performance of turbine.

Permanasari et al. (2019) used the Taguchi method to optimise a water wheel turbine. They considered flow rate, number of buckets, and blade size as design variables and a standard L_{16} (4^3) OA for the Taguchi method. The optimised parameters achieved 4% higher efficiency. In their work, the effects of hydrofoil (i.e., the cross section of a blade which controls the hydrodynamic efficiency of a turbine for a specific flow environment) were not considered (Nandagopal & Narasimalu, 2020).

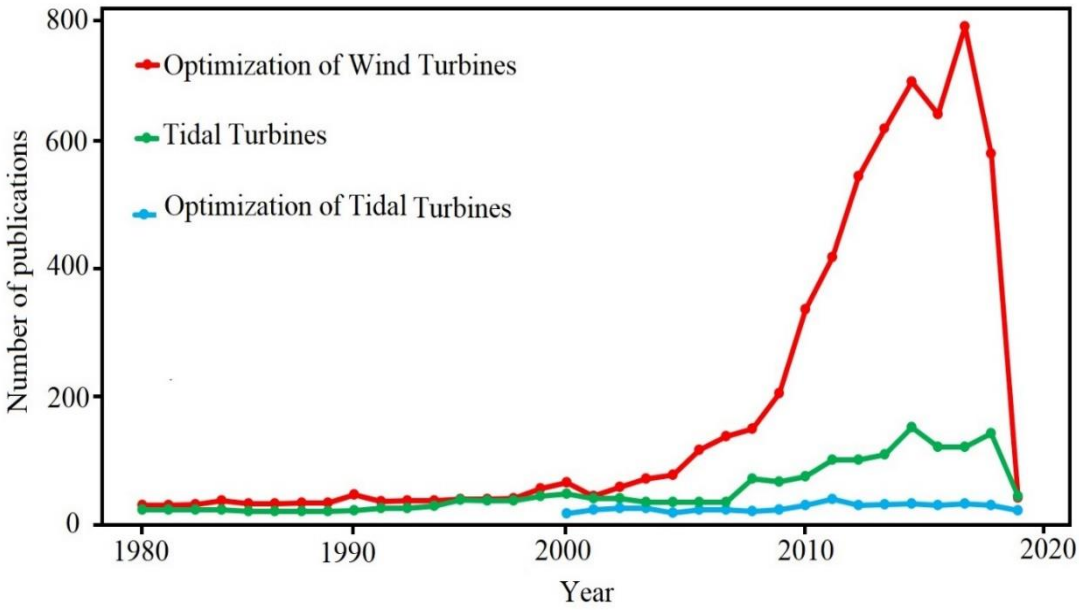

Figure 2.1 Publications on tidal turbines, optimisation of tidal turbines, and optimisation of wind turbines (Kumar et al., 2019).

2.4 Original contributions of the research

Most studies of ocean-powered desalination systems have focused on the use of wave energy converters (Leijon, 2020). These typically involve the use of oscillating systems to pressurise air or water to drive a turbine or hydraulic system. Such systems have been tested in terms of electricity production and their application to desalination systems has been studied and tested at scale (Leijon et al., 2020). However, wave energy is highly variable and is not suitable for more sheltered coastlines where there is insufficient fetch for waves to develop. Where appropriate tidal resources exist, current-driven desalination system may provide a more reliable alternative.

In this research, a new desalination system design is introduced (by adding a water storage tank for stabilising the driving energy and a PV panel for powering the booster pump), which can be powered by HAT or VAT turbines. Since in the proposed design, the

most important part is the tidal turbine, the focus has been placed on optimisation of the turbines.

There are several papers (see Figure 2.1), which offer effective and inexpensive methods for optimising wind turbines. On the other hand, for optimising tidal turbines, which are at the infancy stage of development, there is no complete guidelines, as the behaviour and interaction of materials with water is very different from air. Despite the similarities to wind turbines, the engineering of a tidal turbine differs significantly. The blades of tidal turbines are narrower and thicker than wind turbines. This is to resist the higher stresses caused by the density of the water, which is 800 times higher than air. Because of the massive difference in density, a smaller blade size and a much slower rotational speed is required for tidal turbines for equivalent performance. Greater density also brings with it some challenges, such as turbulence, which creates a huge strain on the turbine. Even a small increase in flow velocity can significantly increase the blade load. The blades of a tidal turbine must be strong enough to resist much higher forces. Some prototype devices have been found to have blade failures or fractures (Thomas, 2017). Moreover, the blade roughness of tidal turbine, which is caused by erosion or/and dogged marine animals, is far higher than the blade roughness of wind turbine, which is normally caused by pollution.

A comprehensive review of the literature shows that there are no appropriate guidelines for optimisation of tidal turbines and hence, there is a research gap in this area, including:

1) The impact of surface roughness on hydrodynamic performance of a tidal turbine is not well understood and it has not been investigated in detail.
2) The impacts of combinations of design parameters such as twist angle, camber position, maximum camber, and chord/radius on performance of VAT turbines has not been studied.

3) The influence of combinations of design parameters such as size of blade, number of blades, hub radius, and hub shape on the power output of HAT turbines has not been investigated.

In this work, a comprehensive 3D CFD simulation and a number of laboratory experiments are carried out, covering a wide range of roughness values for a vertical hydro turbine, in order to quantify the impacts of roughness on the hydrodynamic performance of hydro turbines. Moreover, an inexpensive method is developed and used to optimise a VAT turbine in order to maximise its hydrodynamic performance. The combined effects of twist angle, cambered blades, and solidity on performance of the VAT turbine is investigated. Using the mixed-level modified Taguchi approach and comprehensive 3D CFD simulations, a new set of optimised factors are identified and tested. Finally, the Taguchi method is used to optimise a HAT turbine in order to identify a cost-effective geometry for use in a RO desalination system. The effects of size of blades, number of blades, hub radius, and hub shape on power output of HAT turbine are studied.

Chapter Three: Design of the RO desalination system

3.1 Summary

Desalination is a salt (or dissolved solids) removal method that uses distillation, multiple effect thermal processes, evaporation, or membrane filtration like electrodialysis reversal, nanofiltration, and RO, to reduce the amount of dissolved salts in seawater or brackish water to a safe or drinkable level (Sobana & Panda, 2011). A RO seawater desalination method offers numerous benefits including energy savings as well as reduced installation space and has become a common process for producing freshwater either from seawater or brackish water (Kurihara et al., 2001). The required amount of energy to operate a desalination system is one of the major barriers in sustainable desalination (Vakili-Nezhaad et al., 2021). Combination of RO desalination system with clean energy sources decreases the environmental effect of carbon emissions by fossil fuels. The general objective of optimising the renewable energy powered RO desalination system is to reduce overall system costs and energy needs while still maintaining system performance (Okampo & Nwulu, 2021). In this work, by adding a storage tank and a PV panel to previous design of RO desalination system, a new design is introduced which can be powered with tidal turbines.

3.2 Conventional RO desalination system

A reverse osmotic (RO) desalination system consists of 4 main parts including, high-pressure pump, membranes, energy recovery device and booster pump as shown in Figure 3.1. High-pressure pump of the system consumes most of the energy required in RO desalination system and at least one high-pressure pump is needed in every desalination plant (www.pumpsandsystems.com). Membrane filters act as a barrier to

keep particles out of the water, and they filter the contaminants from the water. RO works by applying pressure to a semi - permeable membrane, which enables water to move through while flushing out dissolved solids. As a result, it divides the water into two channels (www.freshwatersystems.com). In this system, a booster pump is used to pump water from the energy recovery device (ERD) to the RO unit. The energy in the concentrate (or brine) residual waste is harnessed and transferred to the feed side through various methods by an ERD used in the RO desalination system. Energy consumption for modern RO desalination systems is between 2-4 kWh/m^3 (Amy et al., 2017; Kim et al., 2019; Park et al., 2020). As it can be seen, significant amount of energy is needed to desalinate the seawater. Therefore, not only the use of renewable energies should be expanded in this field, but also optimisation methods should be employed to find the maximum efficiency at reduced cost.

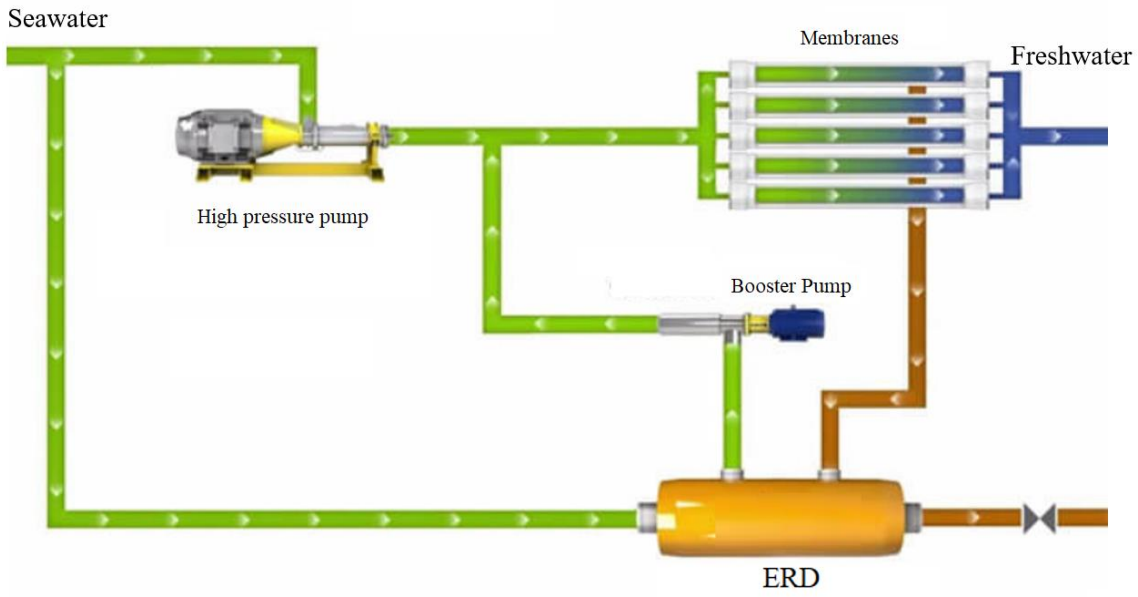

Figure 3.1 A reverse osmotic (RO) desalination system using ERD (Kadaj & Bosleman, 2018).

The total energy consumption in a RO desalination plant is determined by a number of factors including feedwater quality, RO technology implementation, plant capability, and other local conditions. There is general consensus in many publications in this field (Shrivastava et al., 2015; Voutchkov et al., 2012; Wilf et al., 2007) that, for the most energy consuming cases of desalination processes, energy consumption ranges between 2 and 4 kWh/m^3 for medium-scale plants. On the basis of the data collected from 20 RO plants, Voutchkov et al. (2012) reported the abovementioned range and presents a detailed contribution to energy consumption by the main parts of the RO plant, as shown in Figure 3.2. The item identified as "other facilities" approximately corresponds to energy consumed for discharging effluents (Karabelas et al., 2017).

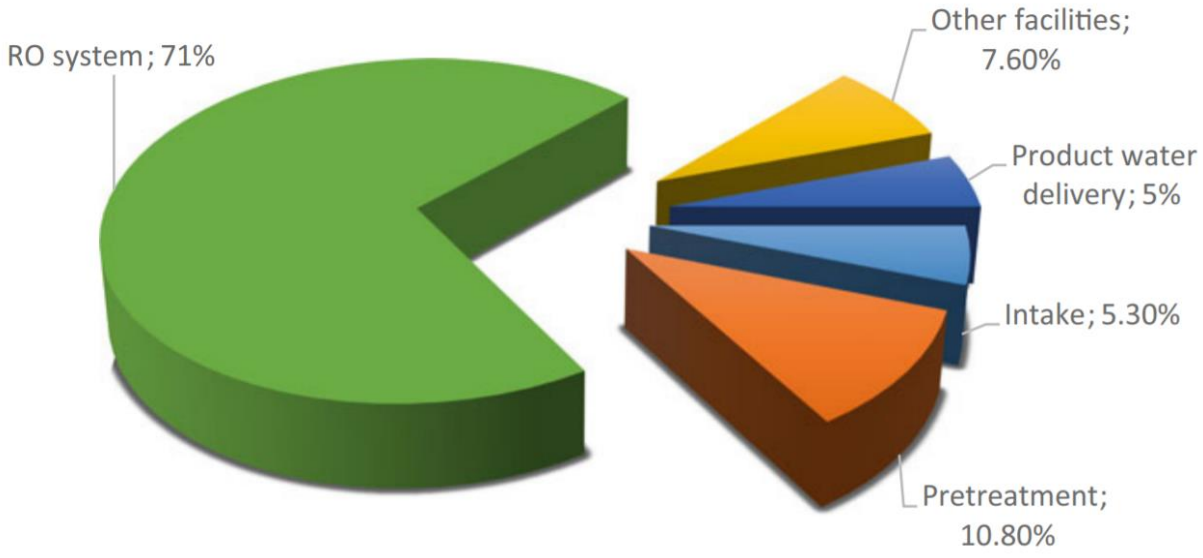

Figure 3.2 Percentage contribution to overall energy consumption of a standard RO desalination plant by each component (Karabelas et al., 2017).

3.3 Powering RO desalination system using tidal energy

(Ling et al., 2018) studied a RO desalination system coupled with tidal energy. In their publication, they provided a design of RO desalination system which can be powered by tidal energy. In this section this design is described and in the next section a new design will be introduced by adding some additional components. The designed RO desalination system is based upon the fact that it is directly powered by the mechanical energy produced by tidal energy through a hydraulic turbine, as illustrated in Figure 3.3. Since the system does not need external power or generators to work, the tidal energy RO desalination system has a lower cost of water production (Ling et al., 2018). The working pressure of the RO system varies depending on the tidal energy. Therefore, a pressure stabiliser is used to keep the pressure constant. As illustrated in Fig. 1, the pressure stabiliser is mounted before the RO pressure vessels set (Ling et al., 2018).

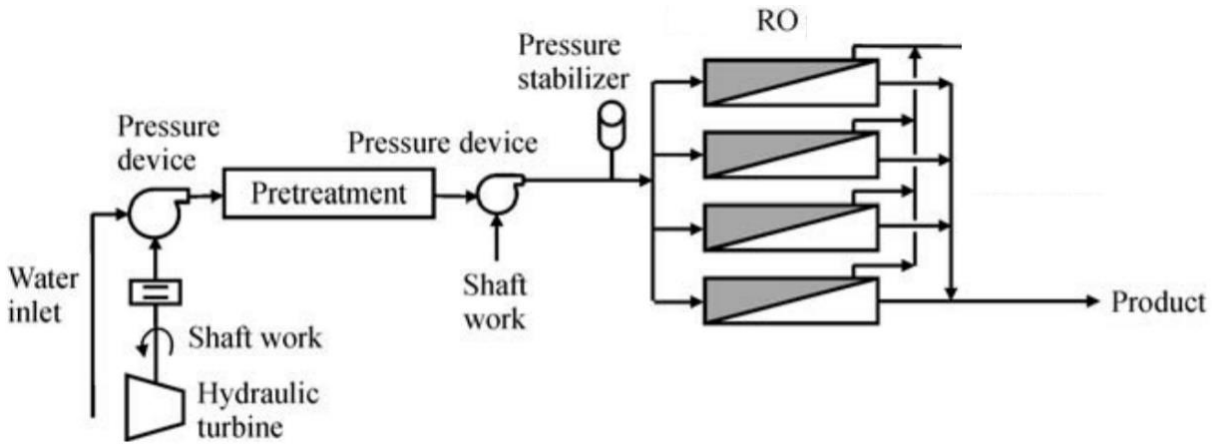

Figure 3.3 RO desalination system coupled with tidal energy (Ling et al., 2018).

3.4 The new design of tidal energy RO desalination system

As shown in Figure 3.4, (Ling et al., 2018) used a pressure stabiliser which has 2 major shortcomings. First, the pressure stabiliser can only be used when more energy is available and it cannot help when there is a shortage of the required energy. The second

problem is that, when the pressure is reduced, a part of the produced energy is wasted. However, in the proposed new design, considering the challenges of energy storage systems with expensive batteries to store the unused energy (Siti Khodijah et al., 2021), a water storage tank is introduced which can store the extra energy coming into the system as well as stabilising the required energy. Another problem of the design presented in section 3.3, is that they use another turbine to power the booster pump which is in the low-pressure line. In reality, we need very low energy to power the booster pump. In the new design, a PV panel is used for powering the booster pump. Therefore, the proposed design can solve the problems of previous designs. A schematic of the conceptual design of VATRO desalination system using HAT turbine is illustrated in Figure 3.4. Some parts of the general idea about the RO desalination system were adapted from (Gude, 2018). The main components of the design and their functions are as follows:

(1) Tidal turbine: powers the high-pressure pump and fills the water storage tank,

(2) Water storage tank: stabilises the driving energy,

(3) High-pressure pump: moves and pressurises water from the sea to the RO unit and the water tank,

(4) RO unit: desalinates saline water,

(5) Booster pump: pumps output water from energy recovery device (ERD) to the RO unit,
(6) ERD: recovers the energy of water output of RO unit, and

(7) PV (Photovoltaic) panel and battery: provide the required electricity for the booster pump.

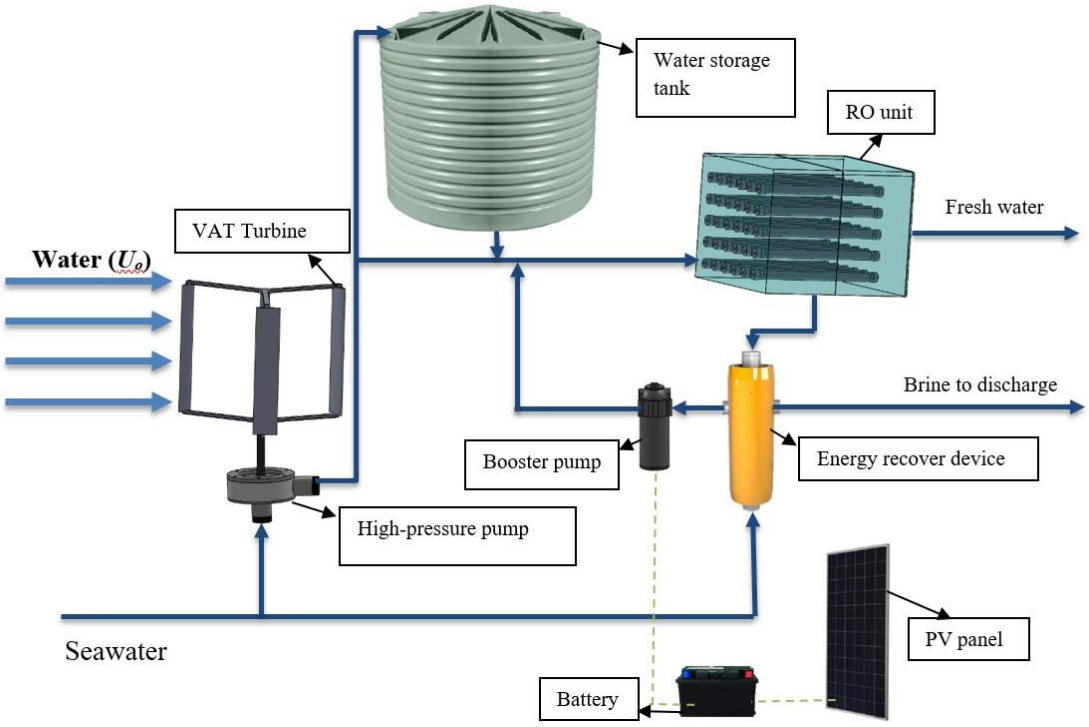

Figure 3.4 Schematic of the RO desalination system using a tidal turbine.

The tidal turbine extracts energy from the sea and runs the high-pressure water pump in order to provide the hydraulic pressure needed for the RO unit. In the proposed conceptual design, there is no need to convert kinetic energy to electricity in a generator, and then electricity to kinetic energy in an electric motor and finally use the kinetic energy to pressurise water in a pump. The kinetic energy is used directly to pressurise the water in the RO system. Moreover, the electricity harnessed from tidal power is usually wasted due to limited consumption during off-peak hours. With the proposed conceptual design, the turbine uses tidal energy to run a water pump and when the system has adequate pressurised water, the energy of the movement can be stored in the water storage tank to stabilise the driving energy.

3.5 Location of the desalination system

Figure 3.5 shows the water availability indicators due to climate change and population growth in the UK for 2050s (Boorman, 2012). The indicator of water availability, which

varies from -1 to 1, identifies the ratio of excess water consumption over water supply of the most challenging months during the estimated duration. It can be seen from this figure that, even a country like UK will experience water scarcity in the coming decades. Fortunately, since about 71% of the Earth's surface is covered with water (Thompson, 2017), one of the solutions for world's water crisis can be seawater desalination. However, seawater desalination requires a significant amount of energy (Ang et al., 2015; El-Ghonemy, 2012; Han et al., 2017; Laborde et al., 2001). Most of the existing desalination systems are powered by energy from combustion of fossil fuels (Peñate & García-Rodríguez, 2012; Tong et al., 2020). Renewable energy, in many cases, can be utilised to power desalination devices (Turek & Bandura, 2007; Tzen & Morris, 2003). Using clean energy sources for desalination has many advantages. The main advantage is that they are infinite and cannot be depleted. Tidal energy, utilising ocean tidal currents, provides a reliable renewable resource with the advantage of being highly predictable many years into the future, albeit intermittent on a daily or twice-daily time-scale, and significantly greater in its energy density compared to wind and solar energies (Pelc & Fujita, 2002).

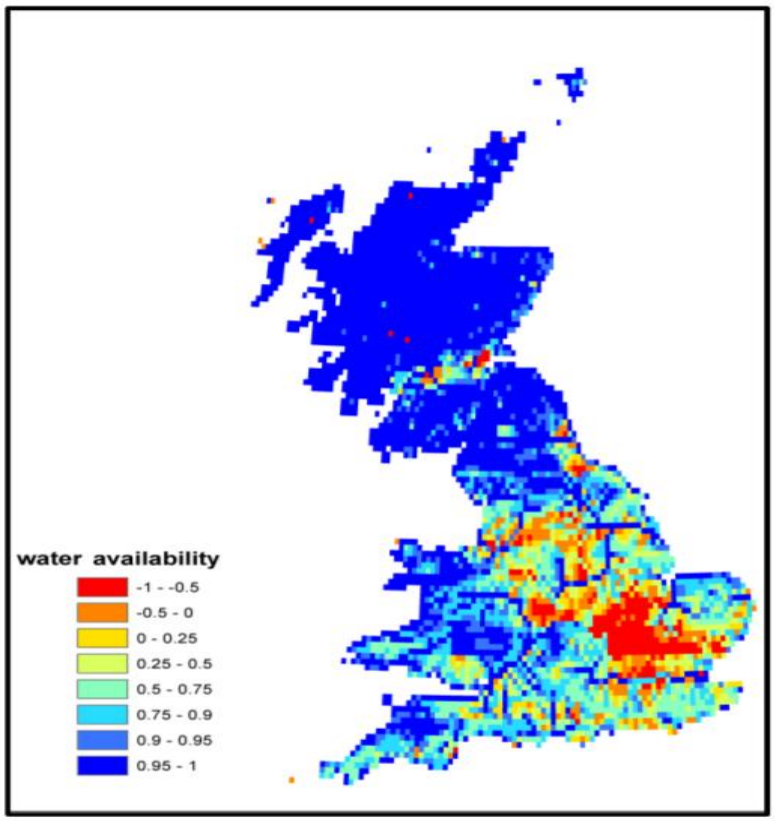

Figure 3.5 Water availability indicator for 2050s in the UK (Boorman, 2012).

One of the prerequisites of development of a tidal seawater desalination system is to find coastal areas with high-speed current, particularly in regions with low salinity as salinity can effect of energy consumption of RO unit (Koutsou et al., 2020). Figure 3.6 illustrates the current speed and seawater surface salinity around the UK. From this figure, it can be seen that there are numerous locations, which are suitable for tidal-powered desalination system, especially in the straits and in narrow places that have an appropriate space for harnessing tidal energy. According to Figure 3.6, the coastline of South East England is suitable for installation of a tidal power RO desalination system; not only it has low salinity and high current speed, but also in future it will have a higher demand for water (see Figure 3.5). Accordingly, for the rest of this research, the mean tidal current velocity and salinity of water are assumed as 1 m/s and 30 ppt respectively.

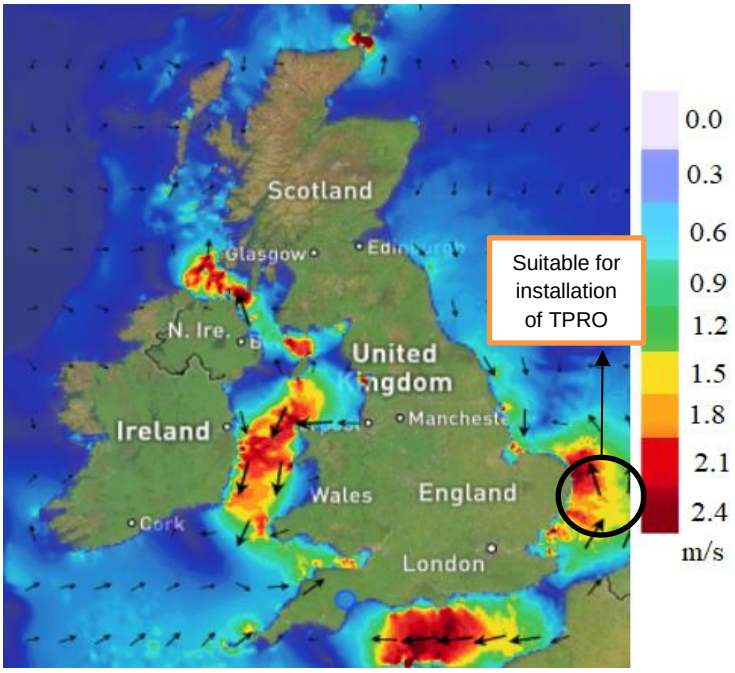

(a)

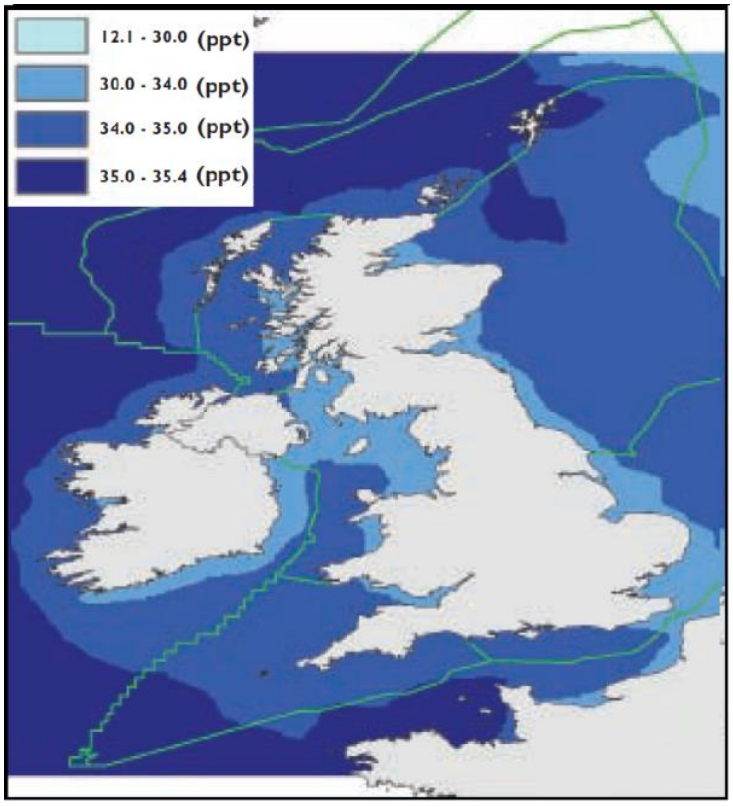

(b)

Figure 3.6 (a) The current speed (www.maps.tidetech.org, 2020) and (b) seawater surface salinity around UK (Connor et al., 2006)

3.6 Energy required for desalination

According to previous literature, energy consumption for desalinating 1 m^3/h using RO desalination systems is between 2-4 kWh/m^3 (Amy et al., 2017; Kim et al., 2019; Park et al., 2020). The proposed conceptual desalination system has three major energy requirements: (1) energy for the RO unit, which has the highest energy consumption in all RO desalination systems (Alsarayreh et al., 2020; Busch & Mickols, 2004; Chu et al., 2020; Mohamed et al., 2005; Setiawan et al., 2009), (2) energy for pumping of the seawater from the nearshore to the system, and (3) electricity consumption in the booster pump, which is used after ERD to pump water to the RO unit. According to Figure 3.6 (b) and the specified location for the desalination system in Figure 3.6 (a), the amount of salinity in the specified area is 30 ppt. The energy consumption inside the RO unit can be assumed as 2.4 kWh/m^3 for seawater with salinity of 30 ppt (Karabelas et al., 2018). The energy usage for transferring seawater to RO unit and the storage tank in a standard desalination system is about 0.3 kWh/m^3 (Fritzmann et al., 2007). Therefore, the total energy required for the RO desalination system for desalinating 1 m^3/h freshwater system is 2.7 kWh/m^3.

To determine the capacity of PV panels, first the energy consumption of a proper booster pump needs to be determined. According to Mistry & Lienhard (2013), 0.121 kWh energy is needed to power the booster pump in the RO desalination system. The closest capacity of PV panels in the market to this amount of energy is 120 Wh, which is suitable for this system.

As mentioned in section 3.2, the energy plays an important role in desalination systems, and finding the optimal turbine can help justify real world applications of these systems. Therefore, in this study a tidal turbine is selected to be optimised in terms of the amount of material and hydrodynamic performance.

3.7 Conclusion

In this work, by adding a storage tank and a PV panel to conventional RO desalination system, a new design is introduced which can be powered with tidal turbines. Since a significant amount of energy is needed to desalinate seawater, not only the use of renewable energies should be expanded in this field, but also optimisation methods should be employed to find the maximum efficiency at minimum cost. In this study, a water storage tank was introduced to store the extra energy coming into the system as well as stabilising the required energy. Moreover, a PV panel was used for powering the booster pump. The propose design can solve the problems of previous designs. The tidal turbine extracts energy from the sea and runs the high-pressure water pump in order to provide the hydraulic pressure needed for the RO unit. In the proposed conceptual design, there is no need to convert kinetic energy to electricity in a generator, and then electricity to kinetic energy in an electric motor and finally use the kinetic energy to pressurise water in a pump. The kinetic energy is used directly to pressurise the water in the RO system. Moreover, the electricity harnessed from tidal power is usually wasted due to limited consumption during off-peak hours. With the proposed conceptual design, the turbine uses tidal energy to run a water pump and when the system has adequate pressurised water, the energy of the movement can be stored in the water storage tank to stabilise the driving energy. Therefore, in this study a tidal turbine is selected to be optimised in terms of the amount of material and hydrodynamic performance. The energy required for desalinating 1 m^3/h is determined based on information from the literature. It should be noted that some assumptions are necessary to estimate this amount. The designed RO desalination system requires 2.6 kW/h for producing 1 m^3/h freshwater.

Chapter Four: Impact of Surface Roughness on Hydrodynamic Performance of a Tidal Turbine

4.1 Summary

Although improving the hydrodynamic performance is a key objective in the design of ocean-powered turbines, some factors affect the efficiency of the device during its operation. In this study, the impacts of a wide range of surface roughness as a tribological parameter on stream flow around a hydro turbine and its power loss were studied. A comprehensive program of 3D Computational Fluid Dynamics (CFD) modelling, as well as an extensive range of experiments were carried out on a tidal turbine in order to measure reduction in hydrodynamic performance due to surface roughness. The results show that surface roughness of turbine blades plays an important role in the hydrodynamics of the flow around the turbine. The surface roughness increases turbulence and decreases the active fluid energy that is required for rotating the turbine, thereby reducing the performance of the turbine.

4.2 Introduction

Tidal convertors can be utilised for converting the kinetic energy of water to mechanical energy of shafts, similar to wind turbines (Antonio, 2010). Several turbines have been developed that can use hydrodynamic lift effectively (Batten et al., 2006; Batten et al., 2007; Mohamed, 2012; Polagye, 2009; Thiébot et al., 2015). In particular, a special design suggested by French engineer Georges J. Darrieus (Mahmud et al., 2017) in 1925 has been regarded as a promising idea for contemporary wind turbines. The main benefits of Darrieus turbines are (i) their design is relatively easy, (ii) their different parts can be adjusted at ground level, and (iii) they do not need a yaw system which is an auxiliary part

of the wind turbine for orientation (Shaheen & Abdallah, 2017). Attempts have been made, particularly in the UK, the US and Germany, to develop this design for efficient wind turbines (Hau, 2013). Japanese researchers were pioneers in using Darrieus type turbine as tidal convertors (DH turbine) (Kiho et al., 1996). Parametric analysis of Darrieus turbines is necessary to find the best way to reduce the cost of manufacturing as well as their maintenance.

One obvious weakness of tidal turbine is the price of manufacturing. These turbines require to be submerged in the seawater which is quite costly, thus there have been attempts by designers to reduce the price of the turbine (Joubert, 2013). Nevertheless, there should be a trade-off between reducing the price and improving or maintaining the performance of the turbine.

There are some secondary factors in the design of hydro turbines, which affect the performance of the system during its operation. A review of the literature shows that there is a research gap in the study of these overshadowed aspects of hydro turbines. In this chapter, a comprehensive CFD simulation and a number of laboratory experiments are carried out, covering a wide range of roughness values for a vertical hydro turbine, in order to quantify the impacts of roughness on the hydrodynamic performance of hydro turbines. The results show that these factors could have a significance effect on the performance of hydro turbines and hence should be considered in the design of these turbines. In due following sections the results of the numerical and experimental models are presented and discussed.

4.3 Numerical modelling

4.3.1 Model geometry

Some key parameters of DH turbine are presented in Table 4.1. In previous literature reports (Mehmood, 2012; Coiro et al., 2005; Xiao & Zhu, 2014) NACA 0015 airfoil has

been proposed for turbines. The National Advisory Committee for Aeronautics (NACA) devised airfoil shapes for aircraft wings. The NACA 0015 airfoil is symmetrical, with no camber indicated by the 00. The number 15 means that the airfoil's thickness to chord length ratio is 15%. Therefore, in the current study NACA 0015 is selected for the experiments and numerical simulations. The water velocity is set at 1.0 m/s and height of blade and length of chord are selected as 0.45 m and 0.3 m respectively. The normal speed range of costal tides near the UK is 0.3 – 2.4 m/s (www.maps.tidetech.org, 2020).

Table 4.1 Turbine geometrical and stream specifications

Parameter	Value
Height of blade	0.45 m
Length of chord	0.3 m
Number of blades	3
Type of airfoil	NACA 0015
Velocity of water	1 m/s

Figure 4.1 shows a CAD design of a three-blade DH turbine subject to a horizontal flow of water. The interaction of DH turbine with water is complex and various parameters are needed for their complete analysis.

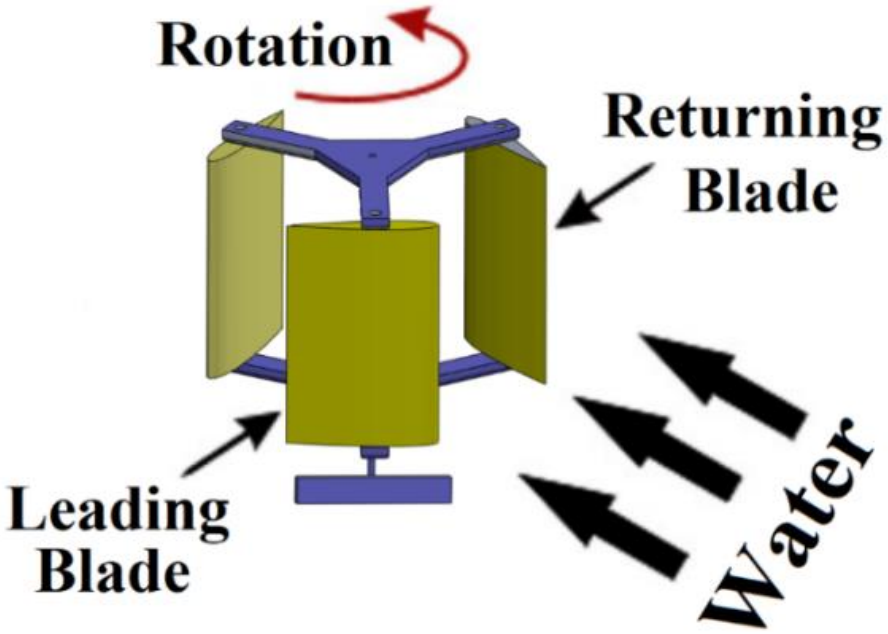

Figure 4.1 Schematic of the DH turbine.

The selection of a suitable computational domain is a key factor for the CFD model to be representative of the reality (Lanzafame et al., 2013). The domain should be optimised in order to reduce the time of computational runs and also provide enough space for appropriate meshing. Furthermore, the CFD domain should be suitable for reproducing DH turbine rotation without the effects of the walls. The domain sizes are selected based on Navabi's (Nabavi, 2008) analysis of the domain size independence. To analyse the performance of the turbine, a 3D transient time-accurate and dynamic mesh CFD model is developed using the ANSYS Fluent 19 code. The geometry of the domain used is shown in Figure 4.2. Designing of the geometry is done in the SOLIDWORKS software. Mesh generation is done in the ANSYS ICEM CFD software. Figure 4.3 shows a circular domain and intensive mesh on wall of the NACA 0015 airfoil. The distances between the centre of the turbine blades and the input and output of the domain are 2.4 m and 4.35 m respectively, and the distance between the blades and the upper and lower levels is 0.90 m. The height of the turbine blades is 0.45 m. An unstructured mesh is created around the blades while a structured mesh is used for the rest of the domain. The total number

of cells in this simulation is 1,249,795 (after grid sensitivity study). The k-ω (SST) (Shear Stress Transport) turbulence model is used to simulate the problem, and the coupling of the speed and pressure equations is performed with the PISO algorithm (Yang et al., 2011). Water velocity at the entrance is 1 m/s. For the entry, the velocity inlet and for the exit the pressure outlet are used as boundary conditions. The bottom, top and side boundaries of the domain are specified as the wall boundary condition. The simulation is done as transient, and the time step selected (after time dependence test) is 0.0001s.

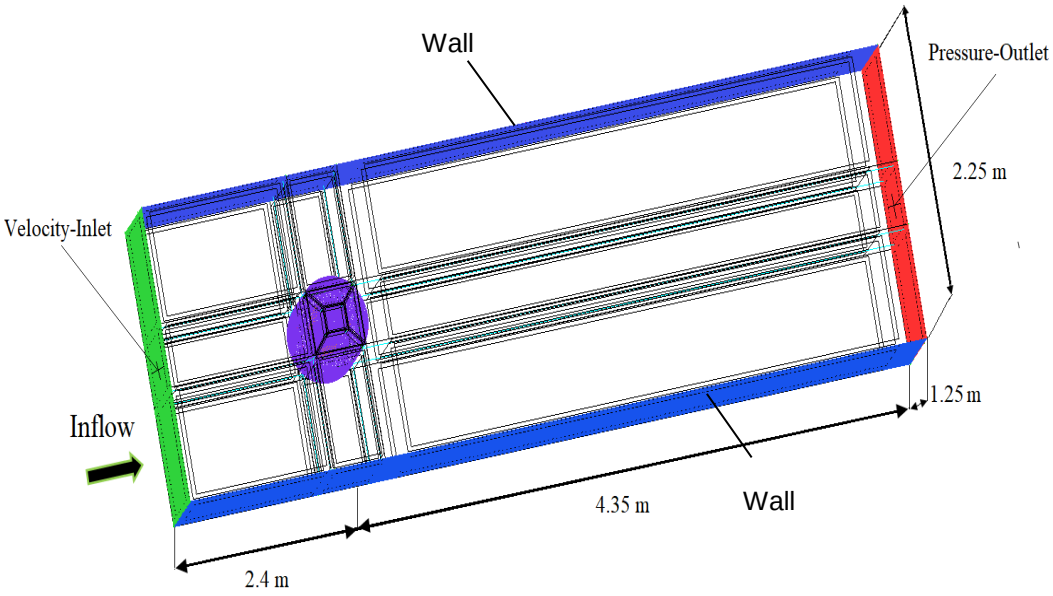

Figure 4.2 Computational domain and mesh blocks.

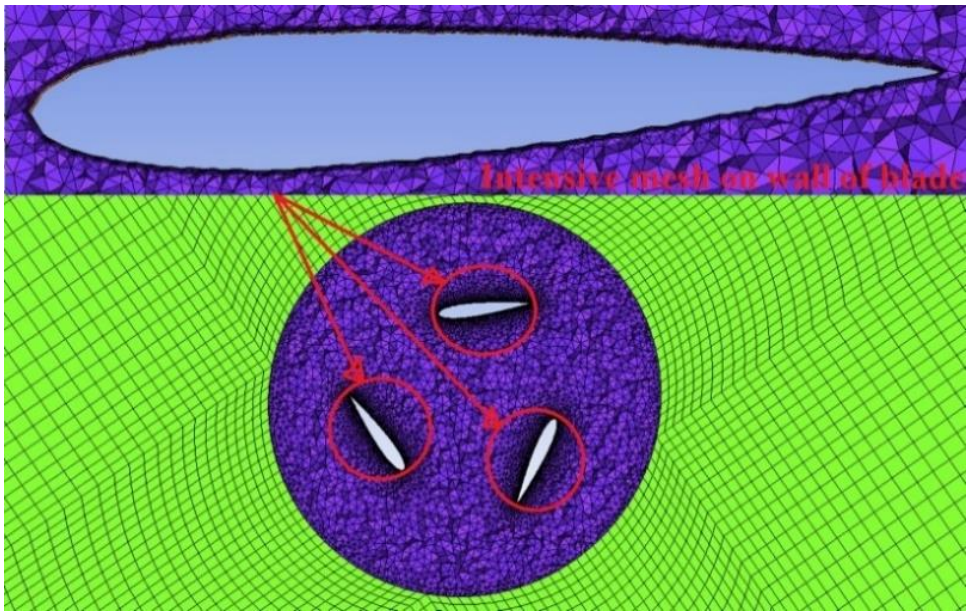

Figure 4.3 Circular domain and intensive mesh on walls of the blades of NACA 0015.

4.3.2 Grid sensitivity (GS) test

A grid sensitivity (GS) test is carried out by generating ten different meshes for the DH turbine with NACA 0015 airfoil. The results of the GS test as the variation of average moment coefficient (C_m) with the number of cells are presented in Figure 4.4. The number of cells is increased uniformly from 123,598 cells to 3,832,670 whilst y+ (non-dimensional wall distance) is 1 (Castelli et al., 2012) in all the tested meshes. Since the turbine's torque is not constant, the mean output torque is used to calculate the mean C_m. By using Eq. 3.1 and Eq. 4.2 (Lain & Osorio, 2010) average moment coefficient of each case with different number of cells is calculated (Figure 4.4). The results showed that beyond 1249795 cells, the relative standard deviation (RSD) of C_m is about 1.3%. Since the computational cost of CFD analysis increases rapidly with the number of cells and RSD ≈ 1.3% is considered acceptable for similar works on Darrieus turbines (e.g., (M. Mohamed, 2012)), 1249795 cells is chosen for numerical analysis.

$$T_m = \frac{1}{z}\sum_{i=1}^{z} T_i \qquad (4.1)$$

$$C_m = \frac{T_m}{\frac{1}{2}\rho A_v U^3} \tag{4.2}$$

where T_m is the average torque, T is the Torque, C_m is the moment coefficient, ρ *is the* density of water, U is the velocity of water, A_v is the area of the turbine blades, z is the number of data points.

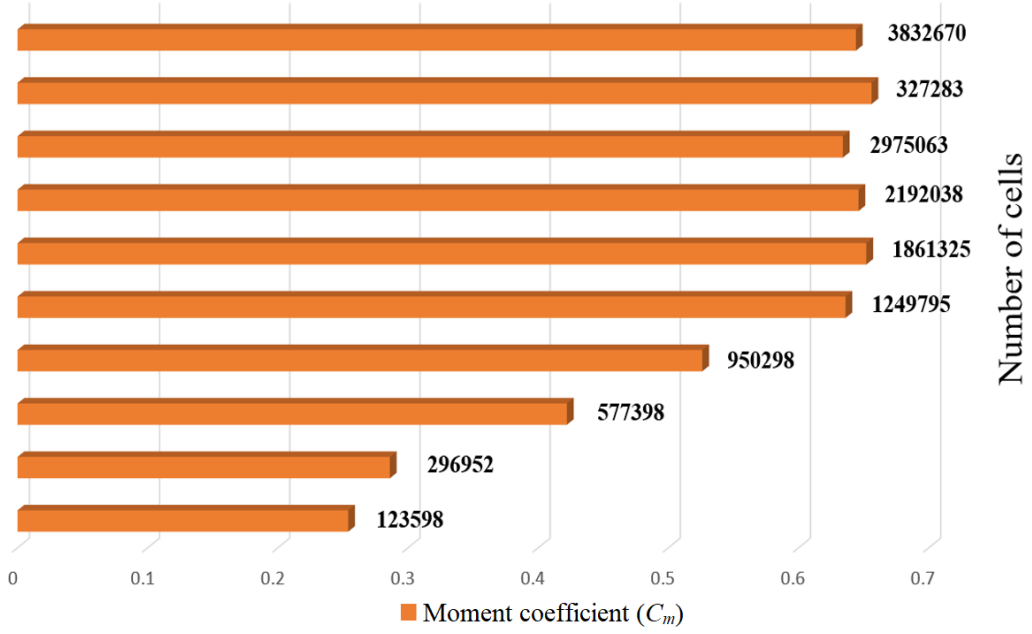

Figure 4.4 Average moment coefficient VS number of cells for grid sensitivity test.

4.3.3 Time sensitivity test

Time step is amongst the most important factors in unsteady simulations. It should be small enough to guarantee temporally independent results (Balduzzi et al. In order to understand the sensitivity of the solution to time step, a subsequent study at tip speed ratio (TSR) of 1.5 and water velocity (U) of 1 m/s is carried out. To obtain a successful convergence in the final results, the time step used for each simulation must be carefully selected (Nobile et al., 2014). In the time sensitivity test, I seek to use a large time step

that assures the minimum computational time without losing accuracy of the results. Five different simulations with time steps of Δt=0.0125, Δt=0.0025, Δt=0.0005, Δt=0.0002 and Δt=0.00008 are carried out to determine how the time step affects the torque of DH turbine with NACA 0015 airfoil. For these different time steps, the variations of torque with azimuth angle are plotted in Figure 4.5. The results show that, among the five different time step sizes, there is little difference in moment coefficient between Δt=0.0005 and Δt=0.00008. Therefore, a time step of 0.0005 is chosen for the rest of the CFD simulations in order to reduce computational time to a minimum.

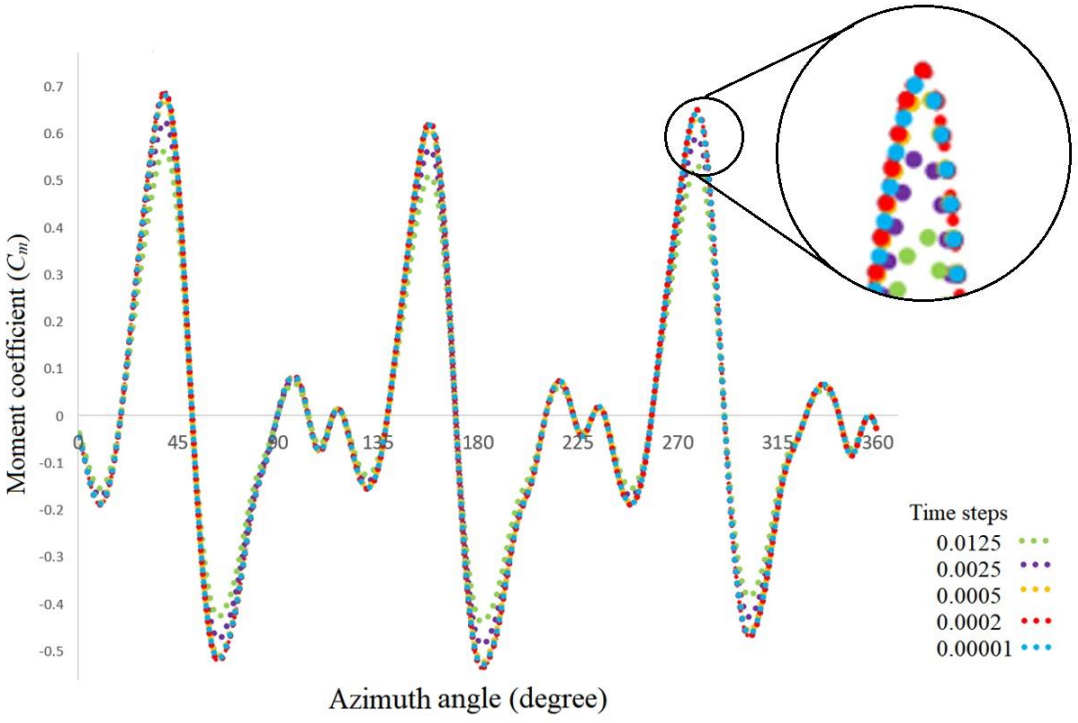

Figure 4.5 Moment coefficient (C_m) verses azimuth angle for five different time steps.

4.4 Experimental set up

An experimental setup is designed and prepared for measuring power output of the DH turbine (Figure 4.6). A three-blade DH turbine is made from Perspex with 3D printing at the Mechanical Workshop of the University of Exeter, using a NACA 0015 airfoil profile

with a chord length of 300 mm. The manufactured DH turbine is submerged in a flume (see Figure 4.7) in order to measure the output energy of the turbine. An energymeter, a resistance box and a small electromotor are employed to measure the power output of the DH turbine. The accuracy of the energymeter is approximately ±1% for voltage and current. In addition, an Acoustic Doppler Velocimeter (ADV) is used to measures the characteristics of the upstream flow of the flume.

A comprehensive set of laboratory experiments is designed and carried out to measure energy losses due to surface roughness. Rolled waterproof sandpapers with uniform roughness are used in the experiments. Five different sandpapers with roughness values of 50, 100, 250, 500 and 1000 μm are used to study the effects of surface roughness on the flow and energy output. The experimental results will be presented and compared with the CFD results in the following sections.

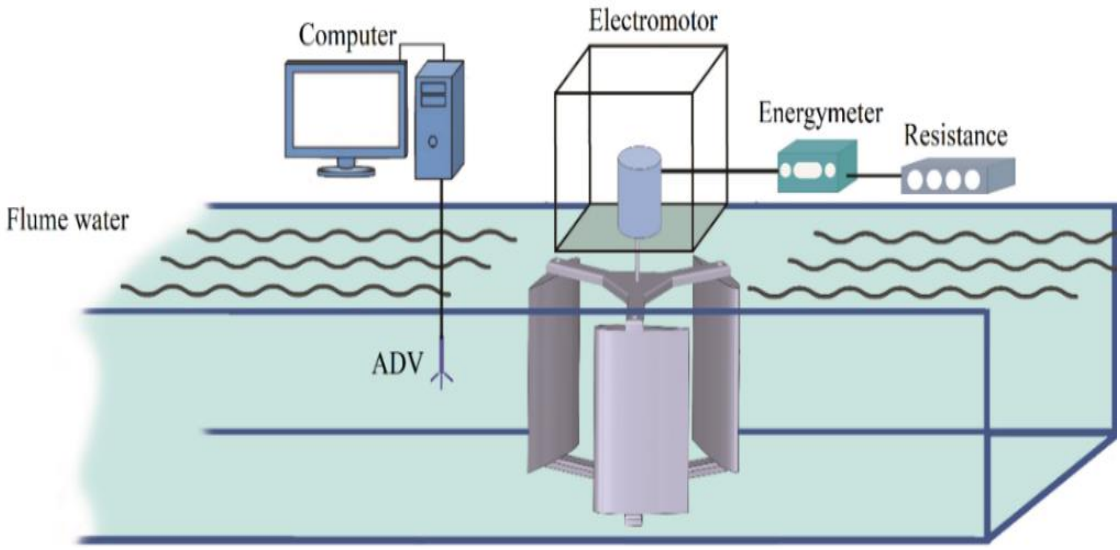

Figure 4.6 Measurement system for the DH turbine.

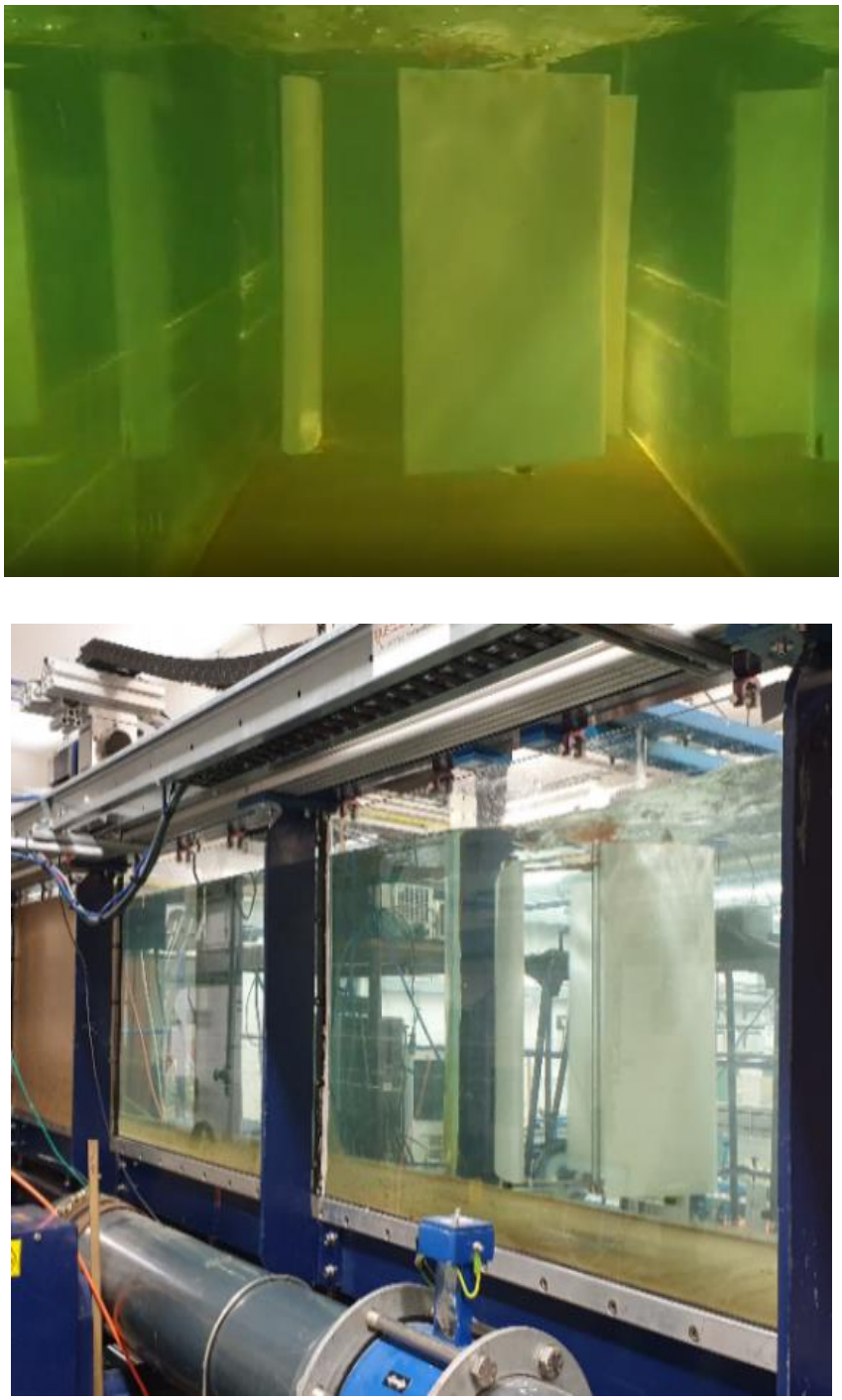

Figure 4.7 Experiments in hydraulic laboratory of University of Exeter.

4.5 Validation of the CFD model

In this section, the experimental results and outcomes from some other studies from literature will be compared with the results of the CFD simulations of the DH turbine to examine the validity of the CFD model. For this purpose, power coefficient (C_p) is calculated at different tip speed ratios (*TSR*) both experimentally and computationally. Power coefficient can be calculated as (Dai & Lam, 2009):

$$C_p = \frac{P}{0.5\rho A U^3} \tag{4.3}$$

where C_p is power coefficient, and P is power output.

Also Tip Speed Ratio (*TSR*) can be calculated as (Liu et al., 2016):

$$TSR = \frac{\omega R}{U} \tag{4.4}$$

where ω is the angular velocity of turbine and R is the radius of turbine's hub.

The calculated values of C_p at different values of *TSR* are plotted in Figure 4.8. It can be seen that the numerical results are in good agreement with the experimental results. There is, nevertheless, a difference between the CFD and measured results. The main reason for this difference is that the CFD simulations are based on rigid body geometries that ignore the turbine blade's hydroelastic behaviour. Vibration and deformation can adversely influence the performance of the turbines. In reality, the blades of the tidal turbine bend due to the pressure of the edge. The power output of the deforming blade is lower than the rigid blade. The power reduction is because of the change of the pressure distribution on the blade caused by twisted blade sections. In addition, vibration causes increasing vorticity generated in blade tip which reduces the torque of turbine (Park et al., 2016).

The general trend of the present experimental and CFD results is also consistent with some results reported in the literature (Liu et al., 2016) on the performance of three-blade NACA type DH turbines.

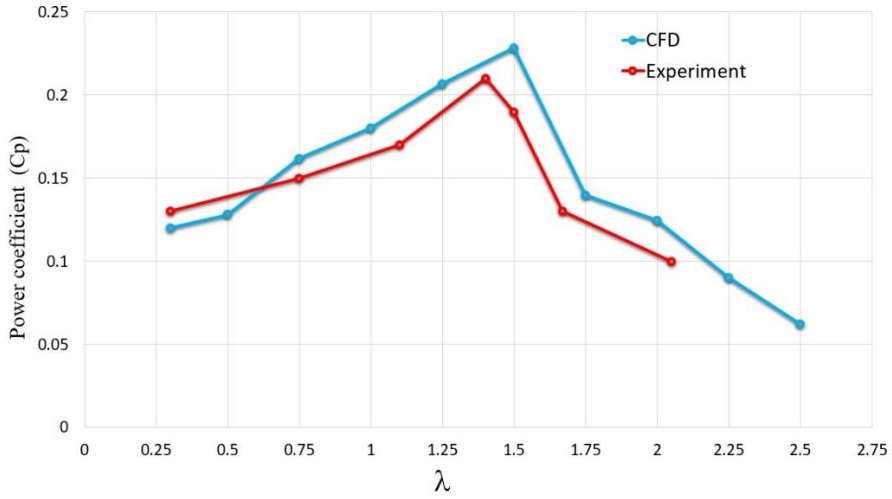

Figure 4.8 Power coefficient (C_P) VS tip speed ratio (TSR) for validation of the CFD model with the experimental work.

4.6 Modelling of roughness in ANSYS Fluent

For modelling surface roughness, the rough wall model is available in ANSYS Fluent (Adedeji et al., 2019) which is adapted from Sommerfeld and Huber's work (1999). To implement surface roughness in ANSYS Fluent, the roughness height (H_r) and the roughness constant (C_r) should be defined (Fluent). These two parameters are explained here. The effects of surface roughness can be duly accounted for in CFD codes by modified wall law as follows (Pattanapol et al., 2008):

$$\frac{\rho U_q U^1}{\tau_W} = \frac{1}{k_r} \ln\left[9.793 \frac{U^1 y_q}{\mu} \right] - \Delta G \tag{4.7}$$

where U_q is the velocity at the wall near cell at centre point q, y_q is the height at the centre point q of the cells near the wall, μ is the viscosity of water, ΔG is the roughness function, τ_W is the wall shear stress, k_r is the Karman constant, and u^1 is the wall friction velocity.

The wall friction velocity can be defined as (Menter, 2002):

$$u^1 = 0.55 k_q^{0.5} \tag{4.8}$$

where k_q is the turbulent kinetic energy near the wall at point q of the cell.

According to Cebeci et al., ΔG for fully rough regime can be defined as (Cebeci & Bradshaw, 1977):

$$\Delta G = \frac{1}{k}(1 + C_r H_s^+) \tag{4.9}$$

where H_s^+ is the non-dimensional roughness height, and C_r is the roughness constant.

The range of roughness constant is 0-1 and according to Tan et al. (2011), who worked on impacts of roughness on the numerical centrifugal pumps using Fluent, the roughness constant has a small effect on the numerical prediction of centrifugal pump performance. In this chapter, the value of C_r is taken as 0.5. In addition, the non-dimensional roughness height is defined as:

$$H_s^+ = \frac{\partial u^1 H_r}{\mu} \tag{4.10}$$

4.7 Results and discussion

4.7.1 Numerical results

4.7.1.1 *Effects of surface roughness on flow pattern*

The DH turbine with NACA 0015 airfoil is simulated using the CFD model in 6 different average roughness heights (H_r) of 0, 50, 100, 250, 500 and 1000 μm at *TSR*= 1.5. One of the most important factors for simulation of roughness is that turbulence model should be proven and validated. The k-ω (SST) model is used as the turbulence model the capabilities of which have been verified the by Sagol et al. (Sagol et al., 2013) and Villalpand et al. (Villalpando et al., 2012) for impacts of roughness. To analyse and understand the phenomenon of flow across a structure like DH turbine, the distribution of velocity and velocity vectors can be useful. The data obtained from the 3D CFD analysis are presented in Figs. 9 - 12. To better understand the effect of roughness height on the flow, the velocity distribution is presented in a cross-section (Figure 4.9) and the velocity vectors are shown in 3D (Figure 4.10). In order to obtain a comparison between the turbines with different roughness heights, I select a reference angle (180°) in the 6DOF (dynamic mesh) and then the turbine set up is simulated with different roughness heights. By using the CFD Post software at an angle of 60° related to the chosen reference, the velocity contours in a given plane and the velocity vectors are obtained in Figure 4.9 and Figure 4.10 respectively. It can be seen that the turbines with various surface roughness heights can make turbulence in the stream flow. This turbulence is not like passing fluid through the body of an airplane or an airfoil. The perturbations of all three blades accumulate and interact and cause the stream flow to change. Fluid turbulence always reduces the kinetic energy, which in turn, reduces the total turbine efficiency. It can be seen that at lower roughness heights (less than 100 μm) the hydraulic effects of roughness are negligible (see Figures. 4.9 and 4.10). At high roughness values, the velocity of the fluid flow is higher and this has a significant effect on the fluid flow

(especially for roughness heights greater than 500 μm). This effect will be discussed and quantified numerically in the following sections.

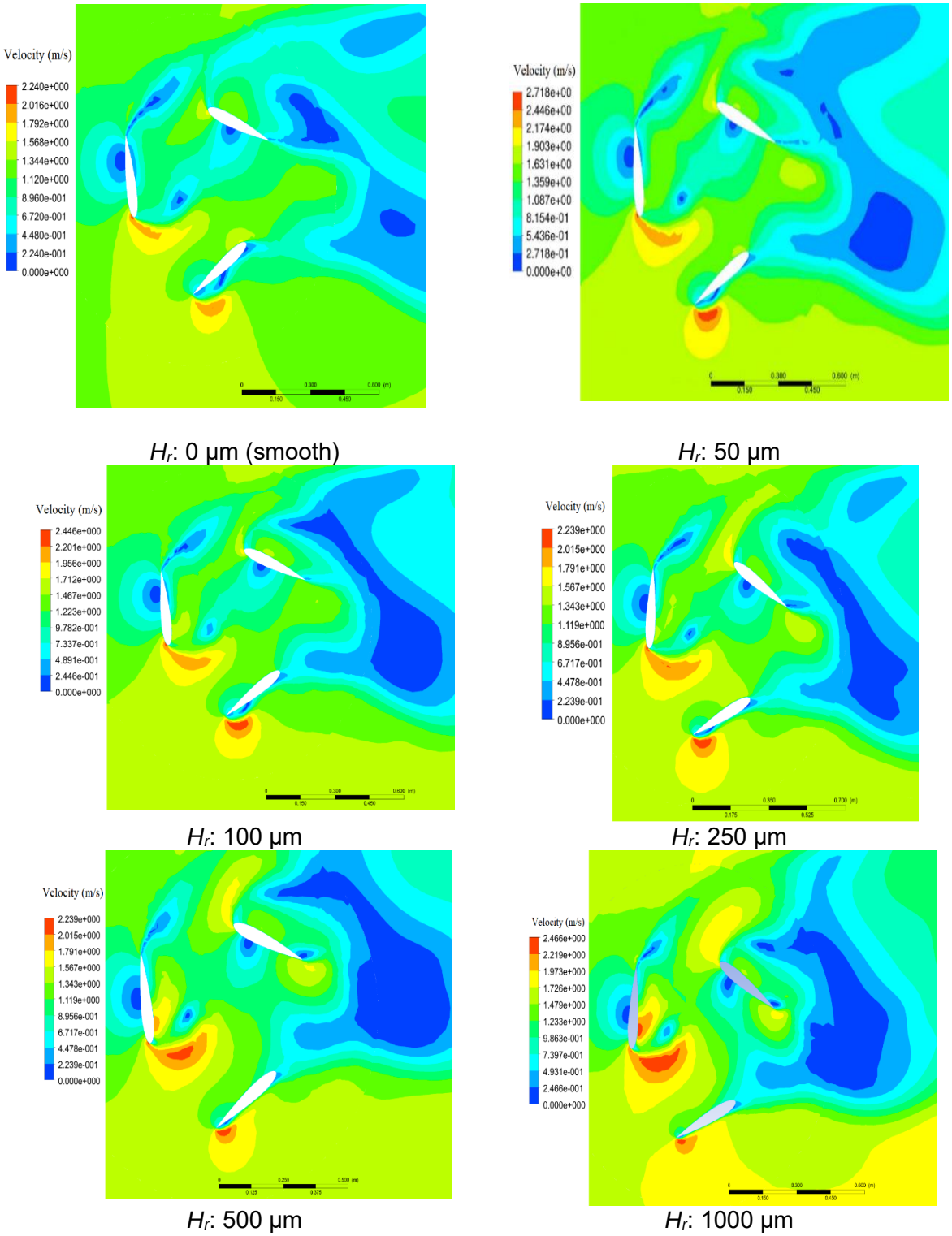

Figure 4.9 Distribution of velocity for various roughness heights on NACA 0015 airfoil at *TSR*= 1.5.

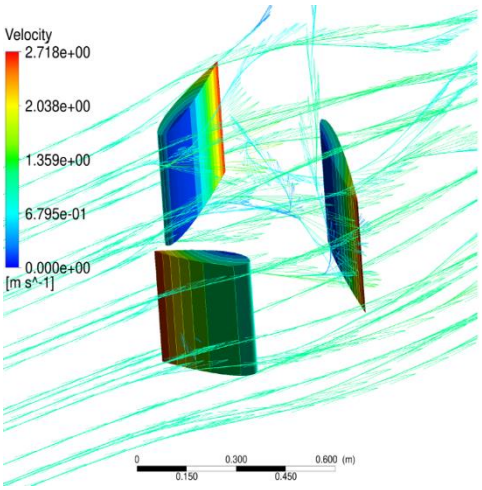

H_r: 0 μm (smooth)

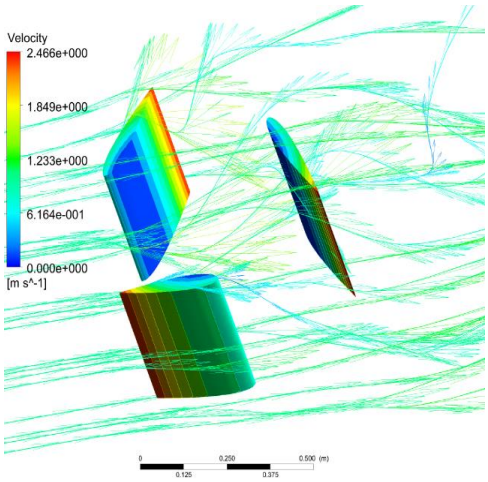

H_r: 50 μm

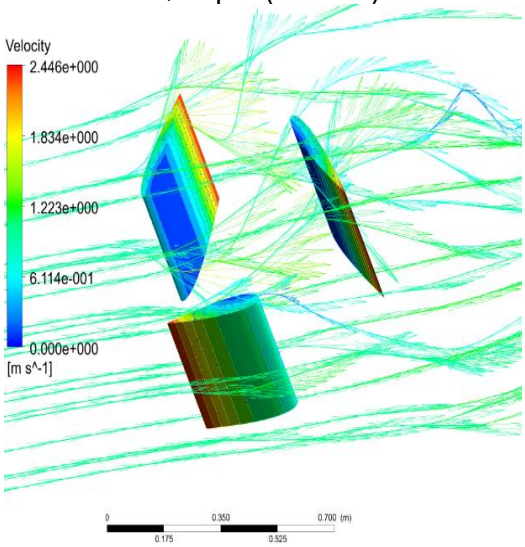

H_r: 100 μm

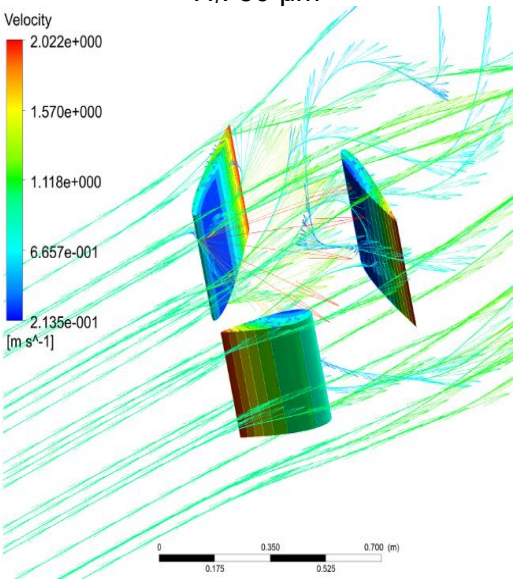

H_r: 250 μm

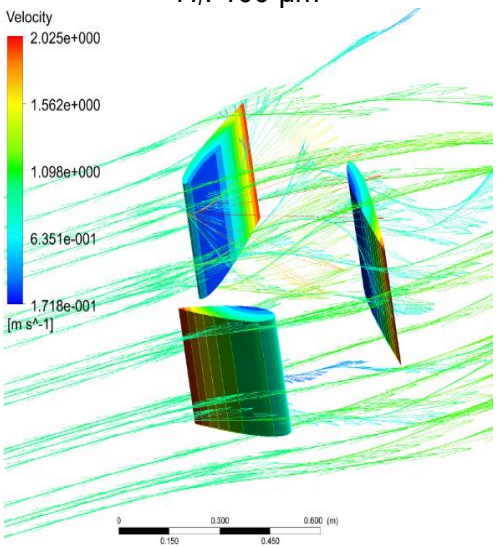

H_r: 500 μm

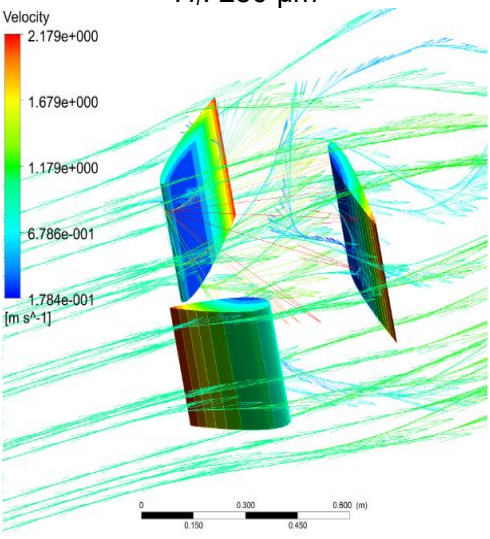

H_r: 1000 μm

Figure 4.10 Velocity vectors in various roughness heights at *TSR*= 1.5 and angle of 60°.

4.7.1.2 *Effects of surface roughness on pressure coefficient (Q_p) and drag coefficient (C_d)*

The performance of a tidal turbine is very sensitive to the pressure and drag coefficients of the specific hydrofoil section used (Walker et al., 2014). The pressure coefficient is defined as (Ehrmann, 2014):

$$Q_p = \frac{p_r - p_w}{\frac{1}{2}(\rho A_v U^3)} \tag{4.11}$$

where P_r is the pressure, A_v is the area of the blades, and p_w is the pressure of water.

The gradient of pressure between the suction surface and the pressure surface leads to a rotational torque for the shaft of the turbine (Hodson & Dominy, 1987). To analyse this, the pressure coefficient (Q_p) is calculated using the CFD model results and Eq. 4.11 at various roughness heights and the results are presented in Figure 4.11.

It can bee seen that the pressure coefficient is very sensitive to surface roughness. The margin of the pressure coefficient (Q_p) between the top and bottom surfaces of the airfoil decreased with the roughness height increasing from 0 to 1000 μm, particularly for the front location of 30% of the chord length. In addition, at the leading edge, the pressure difference between the top and bottom surfaces is greater relative to the other positions. This reduction of the pressure coefficient will reduce the torque as well as power output which will be explained in following section. These results are consistent with those presented in Li et al (2010) who also reported that the margin of variation of the pressure coefficient decreases with increasing roughness.

Drag coefficient (C_d) is one of the most important flow parameters which has influence on the performance of tidal turbines (Ahmed, 2012). In this section, the amount of change in

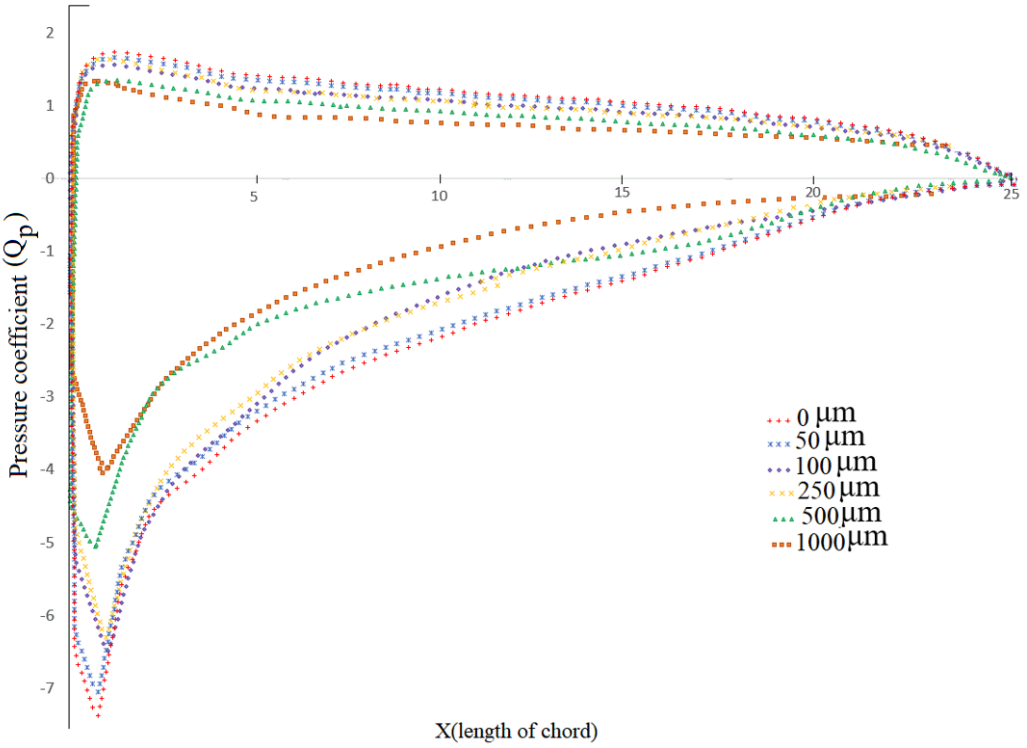

Figure 4.11 Pressure coefficient (Q_p) curves on a single NACA 0015 blade at different roughness heights.

drag coefficient due to the roughness height in DH turbine with NACA 0015 airfoil is quantified. Similar to Q_p, C_d Cruz et al. (2008) is calculated using the CFD model for different roughness heights and the results are presented in Figure 4.12. The results show that C_d increases gradually (following a second order polynomial function) with incrasing roughness. The value of C_d at H_r=1000 µm is 20% higher than the smooth blade. This trend of variation is generally consistent with the results reported by Ren & Ou (2009) for a wind turbine with a NACA 63-430 airfoil.

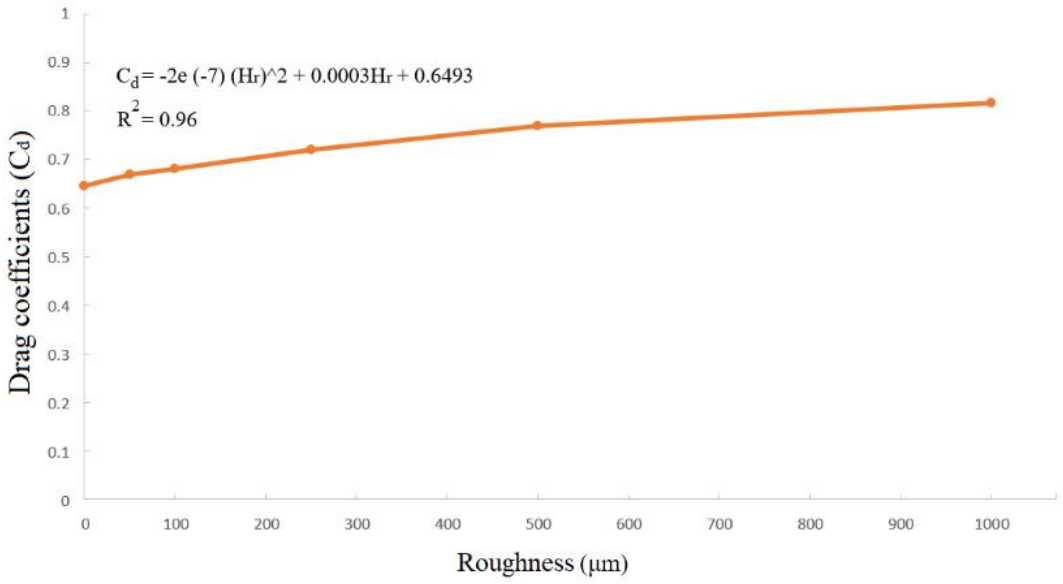

Figure 4.12 Variations of drag coefficient (C_d) at different roughness heights.

4.7.1.3 *Effects of surface roughness on torque (T)*

As mentioned above, surface roughness causes increase in the drag coefficient and decrease in pressure coefficient, both of which reduce the output torque of the turbine. To evaluate this effect, the torque (T) of the DH turbine is calculated in 6 different average roughness heights of 0, 50, 100, 250, 500 and 1000 μm. Furthermore, in order to determine which range of velocity inlet (which is representative of Reynolds number) has greater influence on the turbine, CFD simulations are carried out with U of 0.25, 0.5 and 1.0 m/s. The results of torque versus azimuth angle for 6 different roughness heights for 3 different inlet velocities are presented in Figure 4.13. As it can be seen, amongst the 3 inlet velocities, the range of 0-250 μm roughness height has a negligible impact on output torque of the turbine. On the other hand, H_r between 250-1000 μm has a significant effect on the turbine and it is the worst at velocity of 1.0 m/s. The results indicate that the effect of roughness is much greater at high Reynolds numbers. This finding is in agreement with the results reported in previous research (Blair, 1991; Freudenreich et al., 2004; Montomoli et al., 2010; Timmer & Schaffarczyk, 2004). Since a lower torque usually

produces a lower energy output (Virk et al., 2010), it can be concluded that energy losses are caused by increase in the roughness to the DH turbine blade.

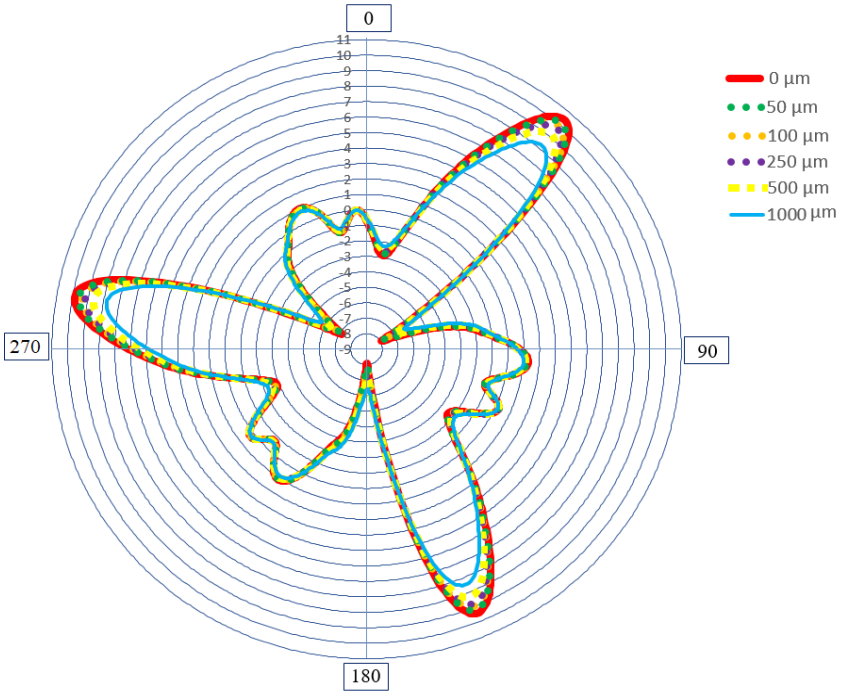

Velocity of flow= 1.0 m/s

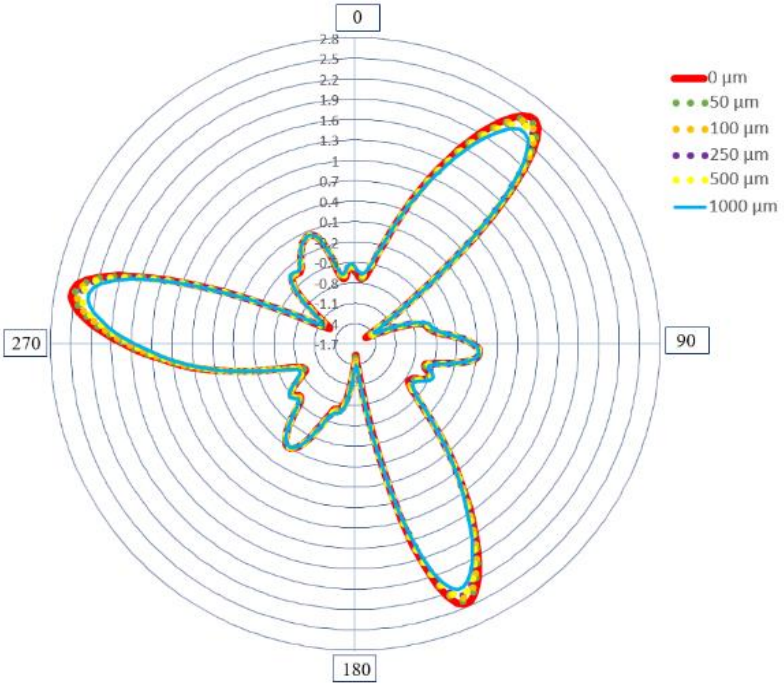

Velocity of flow= 0.5 m/s

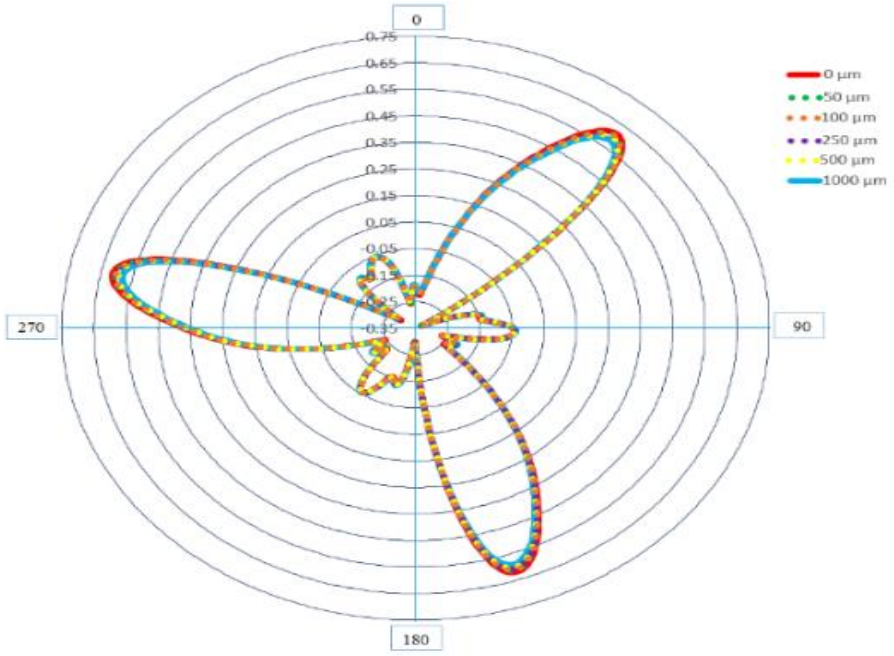

Velocity of flow=0.25 m/s

Figure 4.13 Torque (*T*) versus azimuth angle for 6 different roughness heights at *TSR*= 1.5.

4.7.1.4 *Effects of surface roughness on power loss (P_l)*

Roughness on blades almost always reduces power output of wind turbines, and the loss usually varies from 20% to 50% (Laakso et al., 2005; Dalili et al., 2009). In the same way that insects reduce the power output of wind turbines (Corten & Veldkamp, 2001; Lachmann, 1960), dogged marine animals and erosion can reduce the efficiency of hydro turbines by increasing roughness on blades. Equations 12 and 13, together with the CFD model results are used to calculate the power loss of the DH turbine in different roughness heights at velocity of 1 m/s (Zhang et al., 2011).

$$P = T_m \omega \tag{4.12}$$

$$P_l\% = \frac{P_c - P_r}{P} * 100\% \tag{4.13}$$

where P is the power, P_l is the power loss, P_c is the power of clean turbine, P_r is the power of roughed turbine, T_m is the mean torque, and ω is the angular velocity.

The turbine's power output is equal to its angular velocity (ω) times the torque (T) that acts on it (Eq. 4.13). Since the torque and angular velocity of DH turbine are not constant, the power output is also not constant. Thus, the average power output is calculated. Percentage of power loss of the DH turbine under 6 different roughness heights at U=1.0 m/s is shown in Figure 4.14.

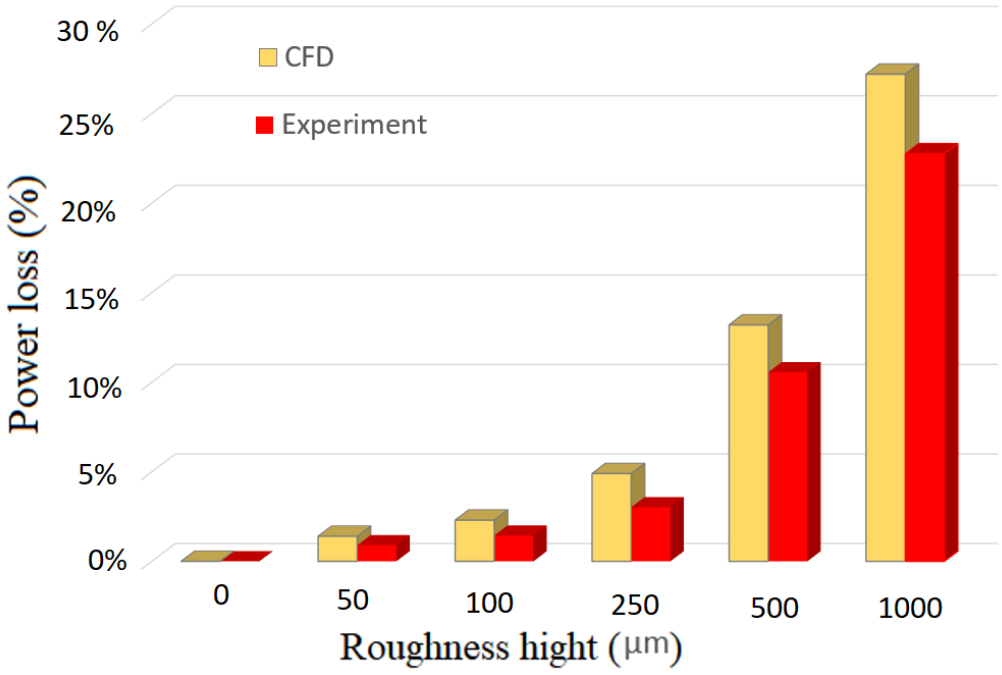

Figure 4.14 Percentage of power loss of the DH turbine with NACA 0015 airfoil for 6 different roughness heights (U=1.0 m/s).

4.8 Experimental results

The results of the laboratory experiments on the effects of surface roughness on the flow and energy loss are presented in this section. Appendix A shows the DH turbine blades

with 6 different surface roughness values created by rolled waterproof sandpapers with different surface roughness. Using the surface profiler device (model: TALYSCAN 150) in the department of Engineering of the University of Exeter, roughness of 2 of the used sandpapers are examined and their micro images are shown in Figure 4.15. The experimental results are shown in Figure 4.14. There is a difference between the CFD and measured results. The main reason for this difference is that the CFD simulations are based on rigid body geometries that ignore the turbine blade's hydroelastic behaviour. The power output of the deforming blade is lower than the rigid blade. The power reduction is because of the change of the pressure distribution on the blade caused by twisted blade sections. In addition, vibration causes increasing vorticity generated in blade tip which reduces the torque of turbine (Park et al., 2016). The results show that the energy loss increases nonlinearly with increase in the surface roughness. Amongst the roughness heights used, the maximum percentage of power loss could reach up to 27 % (numerical) and 22 % (experimentally) for 1000 μm roughness. The amount of reduction in power for $H_r \leq$ 100 μm is less than about 3%.

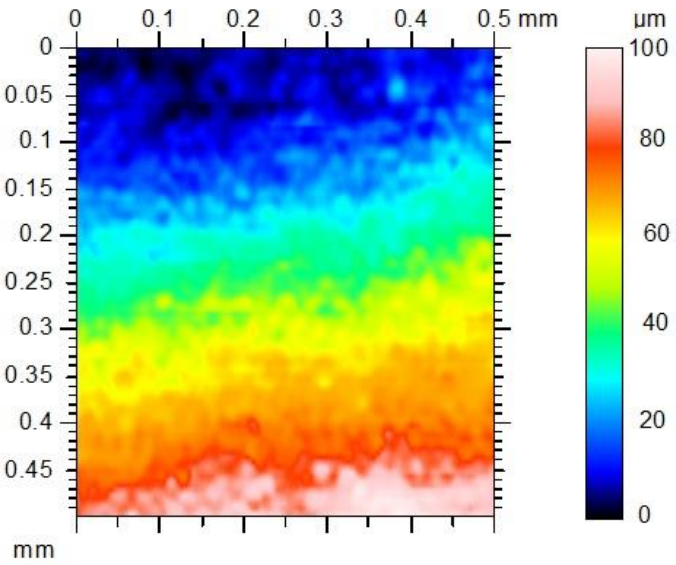
0
0.1
0.2
0.3
0.4
0.5 mm
0
0.05
0.1
0.15
0.2
0.25
0.3
0.35
0.4
0.45
mm
µm
100
80
60
40
20
0

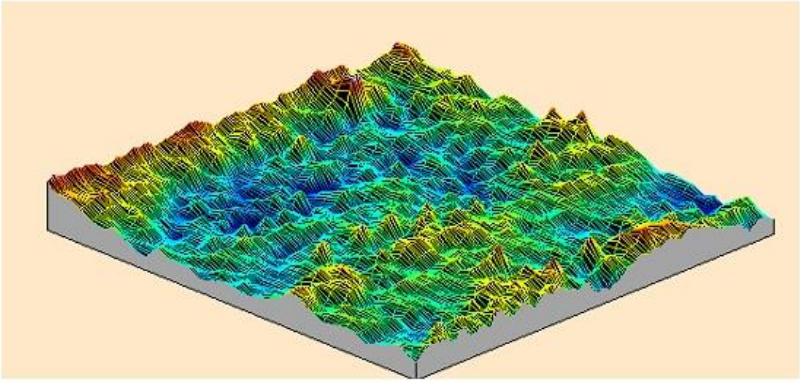

H_r: 100 µm

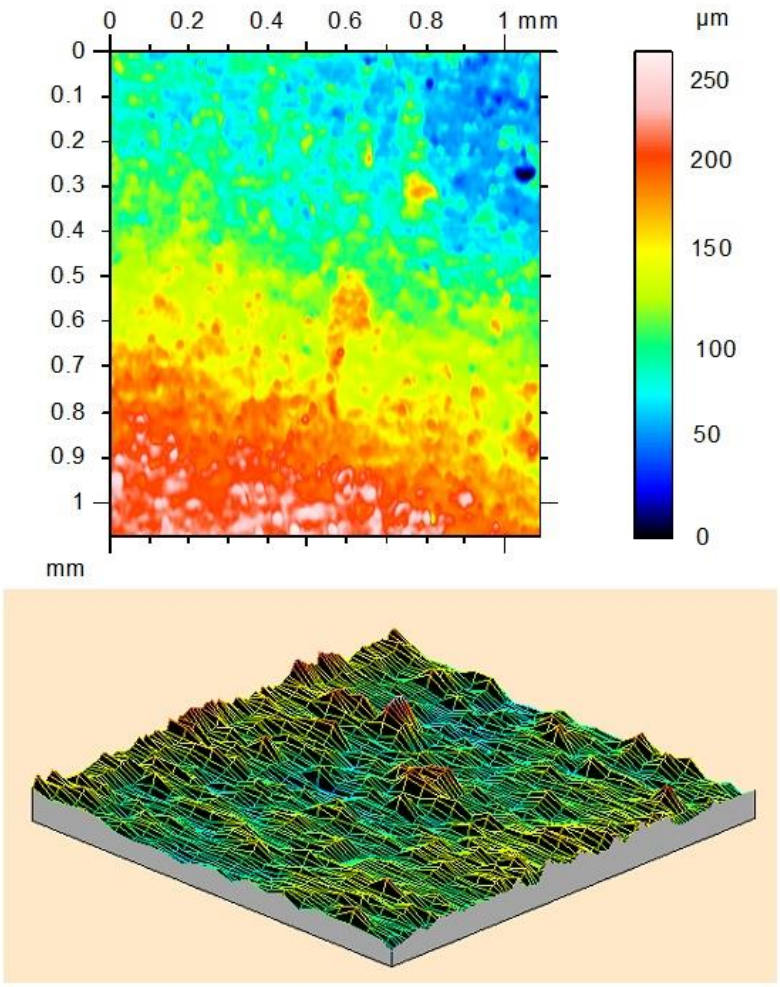

H_r: 250 µm

Figure 4.15 Micro images of sandpapers (100 and 250 µm)

4.9 Conclusion

Modifying the power output is a key objective in the development of the tidal turbines. Therefore, the study of surface roughness arising either in the manufacturing process or/and marine environment is important. The main goal of this chapter was to study the adverse effects of roughness on a tidal turbine both numerically and experimentally and use the results for next chapter. It was shown that surface roughness is a crucial factor in designing a hydro turbine, which should be considered as an initial design parameter like the number of blades, size of blades, tip speed ratio (*TSR*), water velocity and shape of

airfoils. The higher the roughness of the blade of DH turbine, the lower is the turbine performance. In order to quantify the effects of roughness on stream flow and performance of the turbine, ANSYS Fluent 19 code was used for CFD simulations. The turbine was simulated in using dynamic mesh and k-ω (SST) turbulent model. Furthermore, in a comprehensive laboratory works, six different cases with different roughness heights were developed and tested. The following conclusions can be drawn from the results obtained in this chapter:

1) Velocity distributions showed that turbulence will increase with increasing the surface roughness of DH turbine. Turbulence reduces the kinetic energy, which in turn, reduces the total turbine efficiency.
2) The surface roughness degraded the margin of pressure coefficient, especially at high values of roughness.
3) The drag coefficient increased as a second order polynomial function of H_r. When NACA 0015 airfoil was used in DH turbine, the drag coefficient is very sensitive to the variations of H_r. The drag coefficient of roughed turbine (with H_r=1000 μm) studied in this chapter was 20% higher than the smooth blade.
4) The average torque shows small changes at low flow velocities. The adverse impact of surface roughness was significantly greater at high inlet velocities (i.e., high Reynold numbers). In the CFD simulation, all parameters in the Re equation were constant except the velocity of water. It was shown that the negative impacts of roughness are much greater at high Reynolds numbers.
5) The decrease in torque due to surface roughness reduced the power output of the turbine. For the turbine studied in this chapter, the maximum reductions in power output numerically and experimentally were about 27% and 22% for H_r=1000 μm respectively.

6) The results of this chapter would be useful for manufacturers and operators of DH turbines in decisions about practical measures (e.g., coating or cleaning of blades) to reduce roughness of the turbine blades.

Chapter Five: Optimisation of a Vertical Axis Tidal turbine for powering a RO desalination system

5.1 Summary

Vertical Axis Tidal (VAT) turbines can be used as ocean-powered devices to power the RO desalination systems from movements in ocean as a renewable source of energy. In this chapter, a conceptual design of the Vertical Axis Tidal RO (VATRO) desalination system was introduced. The energy required for desalinating 1 m^3/h is determined. Accordingly, a VAT turbine was designed to fulfil this amount of energy. Consequently, a number of CFD simulations carried out using the mixed-level modified Taguchi technique to determine the optimal hydrodynamic performance of a VAT turbine. The influence of four parameters: twist angle, camber position, maximum camber, and chord/radius ratio were studied. The interaction of these parameters was investigated using the Variance of Analysis (ANOVA) approach. The Taguchi analysis showed that the most significant parameter affecting hydrodynamic performance of the turbine is the twist angle and the least effective parameter is chord/radius ratio. The ANOVA interaction analysis showed that the twist angle, camber position and maximum camber have significant interaction with each other. Moreover, the results showed that the power coefficient (C_p) for the optimised VAT turbine is improved by 26% compared to the baseline design. Analysis of the pressure coefficient (Q_p) indicates that the hydrodynamic performance of VAT turbine was sensitive to cambered blade. In addition, the flow separation in the optimised model was greatly reduced in comparison with the baseline model, signifying that the twisted and cambered blade could be effective in normalising the spraying vortices over blades due to suppressing dynamic-stall. The findings of this chapter can provide guidelines for optimisation of vertical turbines.

5.2 Introduction

Tidal turbines, including the Vertical Axis Tidal (VAT) turbine and Horizontal Axis Tidal (HAT) turbine, can be used to power desalination systems. A HAT turbine contains a radial axis rotor, which is parallel to the water stream. With its drag or lift style blades, which are usually perpendicular to the rotational axis, it can convert the kinetic energy of water to mechanical energy (Ahmadi & Yang, 2019). In VAT turbines, the radial axis rotor is perpendicular to the water stream and, similar to HAT turbines, their blades can be either drag or lift style (Bouhal et al., 2018). Since the greatest weakness of tidal turbines is the high cost of development and fabrication, using an inexpensive Taguchi method can be helpful for turbine developers to reduce design costs.

The Taguchi method is one of the powerful optimisation techniques in product design. The method, also known as the Robust Design method, significantly improves the efficiency and quality of engineering manufactured goods (Hong & Satriani, 2020). The fundamental principle of the Taguchi method is to increase the efficiency of a product by reducing the number of tests required without eliminating any parameters. The Taguchi approach provides Orthogonal Arrays (OA) for the execution of minimal tests to include a wide variety of variables for improved decision-making. It also uses the signal-to-noise (S/N) ratio to measure the output level, which is diverged from the target value. The S/N ratio is a criterion for quality assessment, and the OA is to provide minimal design parameters simultaneously (Sapakal & Telsang, 2012). The target quality of performance is a key factor in the Taguchi approach and must be indicated for each optimisation procedure. It is possible to integrate the Taguchi method with Computational Fluid Dynamic (CFD) models (the same way as other optimisation models have been combined with CFD to predict optimised factors.

Review of the literature indicates that the impacts of combinations of twist angle, camber position, maximum camber, and chord/radius on performance of VAT turbines has not been studied. Moreover, the greatest weakness of these turbines is the high price of

design and manufacturing. Traditionally, optimisation of turbine efficiency is achieved by running several numerical models of the turbine which could become time consuming and expensive. In this work, an inexpensive method is developed and used to optimise a VAT turbine in order to maximise its hydrodynamic performance. The combined effects of twist angle, cambered blades, and solidity on performance of the VAT turbine is investigated. Using the mixed-level modified Taguchi approach and comprehensive 3D CFD simulations, a new set of optimised factors are identified and tested. The mean of the signal-to-noise (S/N) ratio is used to analyse how the selected factors affect the hydrodynamic performance of the VAT turbine, whilst ANOVA is used to evaluate the interaction of each factor with the others. Moreover, the physics of flow around the optimised and baseline turbines is evaluated and discussed.

5.3 Preliminary design of the baseline VAT turbine

HAT or VAT turbines can provide the energy required by the RO desalination system. HAT turbines consist of a radial axis rotor, which is parallel to the inlet water flow. With its drag or lift style blades, which are usually perpendicular to the rotational axis, it can convert the kinetic energy of water to mechanical energy (Ahmadi & Yang, 2019). On the other hand, in VAT turbines, the radial axis rotor is perpendicular to the inlet water flow and, similar to HAT turbines, their blades can be either drag or lift style (Bouhal et al., 2018). VAT turbines have advantages of simple structure and independency to stream path in comparison to HAT turbines, and have been commonly used in both small and medium scales (Zhang et al., 2014). To design these turbines, the energy required to desalinate 1 m^3/h of water in this section was calculated based on previous work, which is 2.6 kW/h. This power was set as the initial parameter of both turbines. Geometry has been designed using the equations governing the power output and dimensions of HAT and VAT turbines and it was found the specific geometry that can provide 2.6 kW/h to power the RO desalination system.

According to the Chapter four, changes in roughness of the blades due to sticky sea animals and corrosion can decrease the performance of tidal turbines by about 20%. Considering this amount of power reduction, the turbine should provide 3.24 kWh/m^3 of energy. Finally, to minimise the effects of uncertainties, 0.2 kWh/m^3 was added to this 3.24 kW/h as a confidence factor. Therefore, in the end, the turbine should provide 3.44 kWh/m^3.

As mention above, the VAT turbine must provide 3.44 kWh/m^3 to power RO desalination system for producing 1 m^3/h freshwater. The well-known equations of vertical turbines are used to estimate this power. The real power output is described as the power coefficient (C_p) multiplied by nominal power output (P_n) (Eq. 5.1) (Meng et al., 2020). This nominal power output can be calculated by the turbine geometry as well as the flow characteristics based on the particular application (Li, 2014). For initial design of the baseline VAT turbine, some basic assumptions are considered based on the literature. According to the work by Li et al. (2010) the maximum amount of C_p of 0.35 is considered for the tidal turbine, as a safe estimate, to determine the baseline turbine geometry.

$$P = P_n C_p \tag{5.1}$$

where P is the power output, P_n is the nominal power, and C_p is the power coefficient.

The nominal power can be calculated as (De Lellis et al., 2018):

$$P_n = \rho R H U^3 \tag{5.2}$$

where H is the height of turbine blade, and R is the turbine radius (distance between the centre of hub to the blade tip).

With the mentioned values for the power output and maximum power coefficient, and considering the inlet water velocity as 1 m/s, the initial parameters of the baseline HAT turbine (1:100 scale) are determined as summarised in Table 5.1.

5.4 Initial design, CFD modelling and validation

Initial design parameters of a VAT turbine are listed in Table 5.1. The blade height, chord length, and radius of the turbine are chosen as 0.4 m, 0.06 m, and 0.20 m respectively. In this section, the twist angle is zero and the blades are completely straight, and the number of turbine blades is three. For the hydrofoil, NACA 4-digit (XYZW) airfoils is chosen as they can be parameterised and also this type of airfoil has been used frequently in previous works for tidal turbines (Ai et al., 2020; Batten et al., 2007; Kundu, 2020; Tunio et al., 2020). In this series, X is maximum camber, Y is camber position, and ZW is the value of thickness. Among the NACA 4-digit series airfoils (Asr et al., 2016) symmetric NACA0015 is selected. The basic terminology of an airfoil (or hydrofoil) is shown in Figure 5.1. The effect of a hydrofoil on the performance of the turbine depends on four parameters, chord length, blade thickness, camber position, and maximum camber.

Table 5.1 Initial parameters of VAT Turbine

Parameter	Value
Blade height (H)	0.4 m
Chord length (D1)	0.06 m
Radius of the turbine (R)	0.2 m
Type of baseline hydrofoil	NACA 0015
Twist angle	0^{o}
Number of blades	3

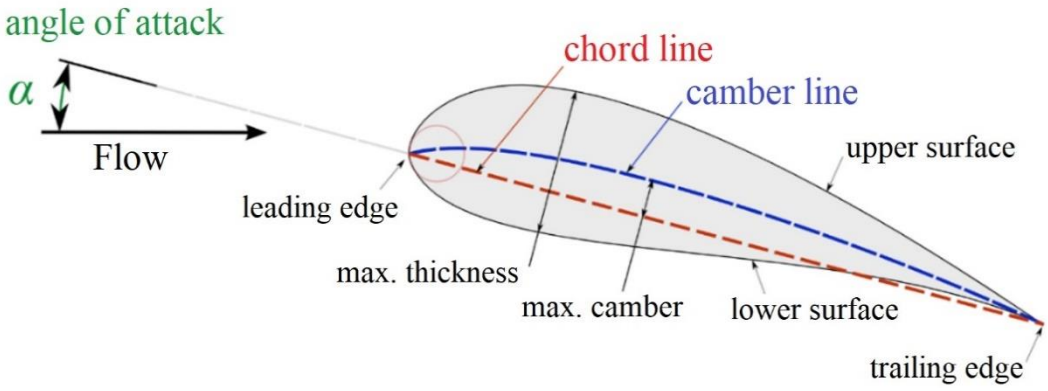

Figure 5.1 Basic hydrofoil terminology (Kishore, Stewart, & Priya, 2018).

Figure 5.2 illustrates the general configuration of the straight-blade VAT turbine (baseline case) submerged in horizontal water flow. The inlet velocity is considered 1.0 m/s.

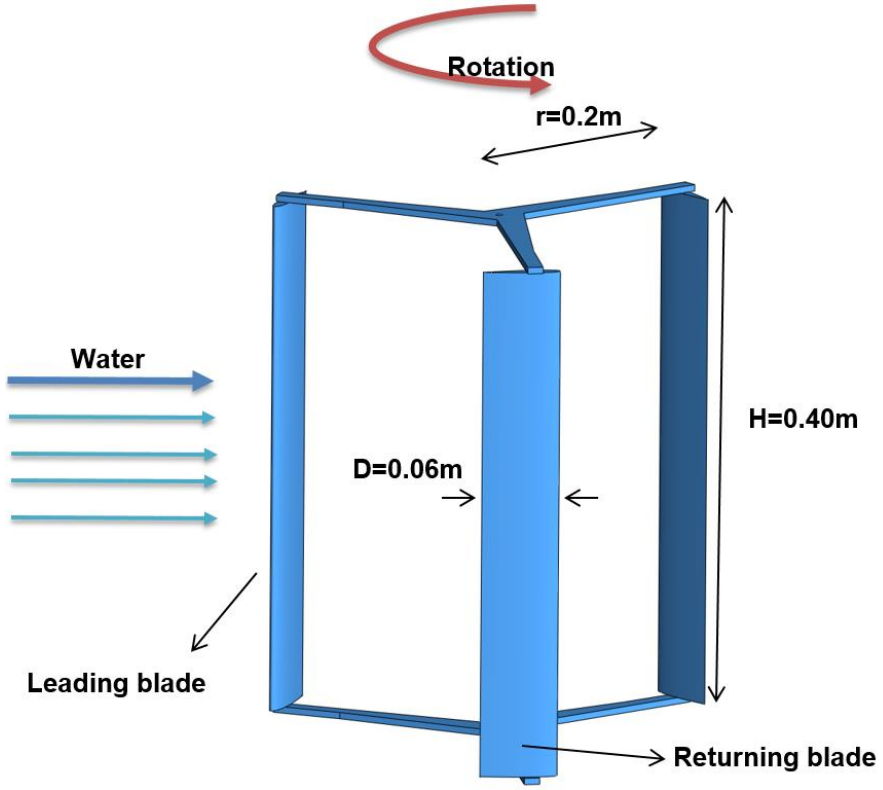

Figure 5.2 Schematic of the baseline VAT turbine.

Figure 5.3 summarises the computational domain and boundary conditions. Optimisation of this domain is extremely important in order to decrease the time needed for computational runs and to provide sufficient space for suitable meshing. The computational domain is considered as a cubic domain of 1.5m*2.5m*7.0m for CFD modelling (Nabavi, 2008). An unstructured mesh is built around the blades, whilst the rest of the domain is discretised using a structured mesh. A finer mesh is considered around the VAT turbine blade (Figure 5.3). A grid sensitivity test is performed with 9 different grids for convergence analysis to find the optimal mesh size. The number of cells is increased consistently from 524,329 to 2,097,316, whilst the y+ (dimensionless wall distance) is 1 in all the tested grids. Considering that the torque of the turbine is not constant, the average output torque is used to measure the mean moment coefficient (C_m). The value of C_t for each of the 9 cases is determined using Eq. 5.3 (Laín & Osorio, 2010). The results show that the relative standard deviation (RSD) of C_t for 1,048,658 cells is around 0.98 %. As in CFD, analysis the computational cost increases rapidly with the number of cells, 1,048,658 cells is selected for the rest of the CFD simulations of the baseline model. A similar approach is used for all CFD tests in this chapter.

A 3D transient and sliding mesh model is developed, using the ANSYS Fluent 19 software, for CFD analysis of the VAT turbine. The turbulence model of the Shear Stress Transport (SST) k-ω and the PISO (Pressure Implicit with Splitting of Operator) algorithm (coupling of the velocity and pressure equations) are adopted for the CFD simulation (Yang et al., 2011).

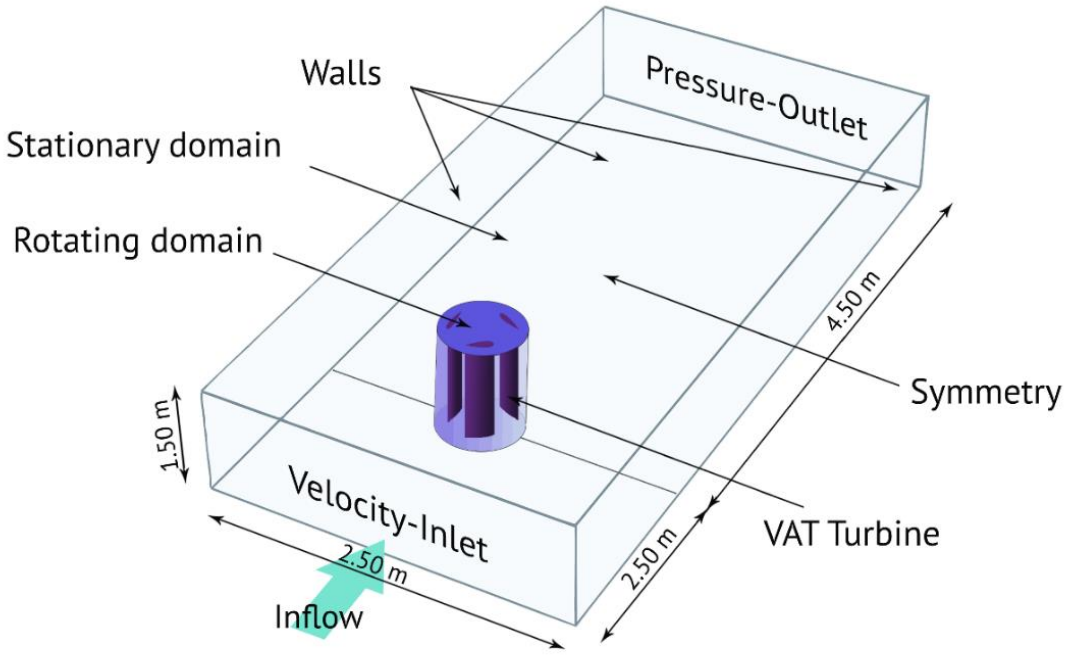

Figure 5.3 Computational domain and boundary conditions.

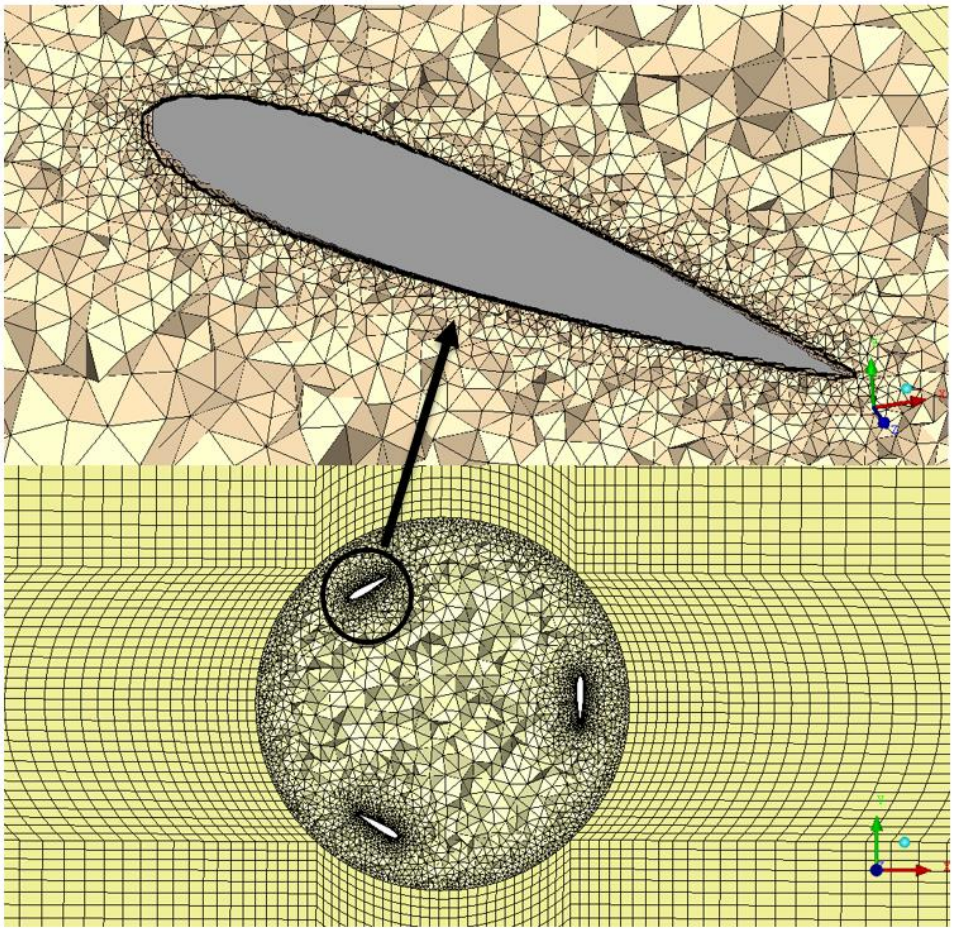

Figure 5.4 Intensive mesh around the blades.

One of the most common ways for validating CFD model for simulation of turbines is based on the power coefficient (C_p) (which is an indicator of the performance of turbines) and tip speed ratio (TSR) (which is defined as the ratio of the water velocity to the velocity at the turbine blade tips) (Chowdhury et al., 2016). The baseline VAT turbine was fabricated by a 3D printer in the Engineering Department of the University of Exeter according to the selected dimensions (Table 5.1). An experimental model is developed to validate the CFD model. Figure 5.5 shows the fabricated turbine that is submerged in a large flume. For measuring the power coefficient (C_p) according to Eq. 5.4, the power output (P) of the baseline turbine is measured using an energy meter, a resistance panel, and a small electromotor. The energy meter's sensitivity for voltage and current is ±0.5%

which was a different model used in previous section. Moreover, different tip speed ratios (*TSR*) are provided by changing the water velocity based on Eq. 5.4. An Acoustic Doppler Velocimeter (ADV) is used to monitor the current stream patterns in the channel.

Figure 5.5 Experimental set up in a large flume at the Hydraulic Laboratory.

Figure 5.6 shows the variations of C_p with *TSR* for both the numerical and experimental results, calculated using Eqs. 5.3 & 5.4 (Liu et al., 2016). The moment coefficient (C_m) of vertical turbines can be calculated by following equations:

$$C_m = \frac{T}{0.5\rho A U^2} \tag{5.3}$$

The power coefficient (C_p) can be determined by substituting the moment coefficient into Eq. 4.4 as follows:

$$C_p = \frac{P}{0.5\rho A U^3} = (TSR)C_m \tag{5.4}$$

It can be seen from Figure 5.6 that, in general, the CFD results are in good agreement with the experimental results. However, there is some difference between CFD and experimental values. The main reason for this difference is that the CFD simulations assume rigid body geometries which overlook turbine blade hydroelastic behaviour (Asghar et al., 2017; Badshah et al., 2019). Vibration and deformation can adversely influence the performance of the turbines. In reality, the blades of the tidal turbine bend due to the pressure of the edge. The power output of the deforming blade is lower than the rigid blade. The power reduction is because of the change of the pressure distribution on the blade caused by de-twisted blade sections. In addition, vibration causes increasing vorticity generated in blade tip which reduces the torque of turbine (Sewan et al., 2016). Accordingly, the difference between C_P values in the CFD and experimental analyses is less than 13% (with TSR=1.25 which is used in all tests in this chapter). However, the results indicate that this error is much greater at high tip speed ratios, which can emphasise that the effects are higher at high speeds.

A review of previous research on turbines indicates that C_p: *TSR* curves for all turbines have a peak point; i.e., the power coefficient increases with increasing *TSR* up to a point beyond which, further increase in *TSR* leads to reduction in C_p. For wind turbines, the maximum amount of power coefficient is limited to 16/27 (~0.59) according to the Betz Limit (De Lellis et al., 2018). The maximum power coefficient of the baseline model is computed numerically as 0.16 at a tip speed ratio of 1.2.

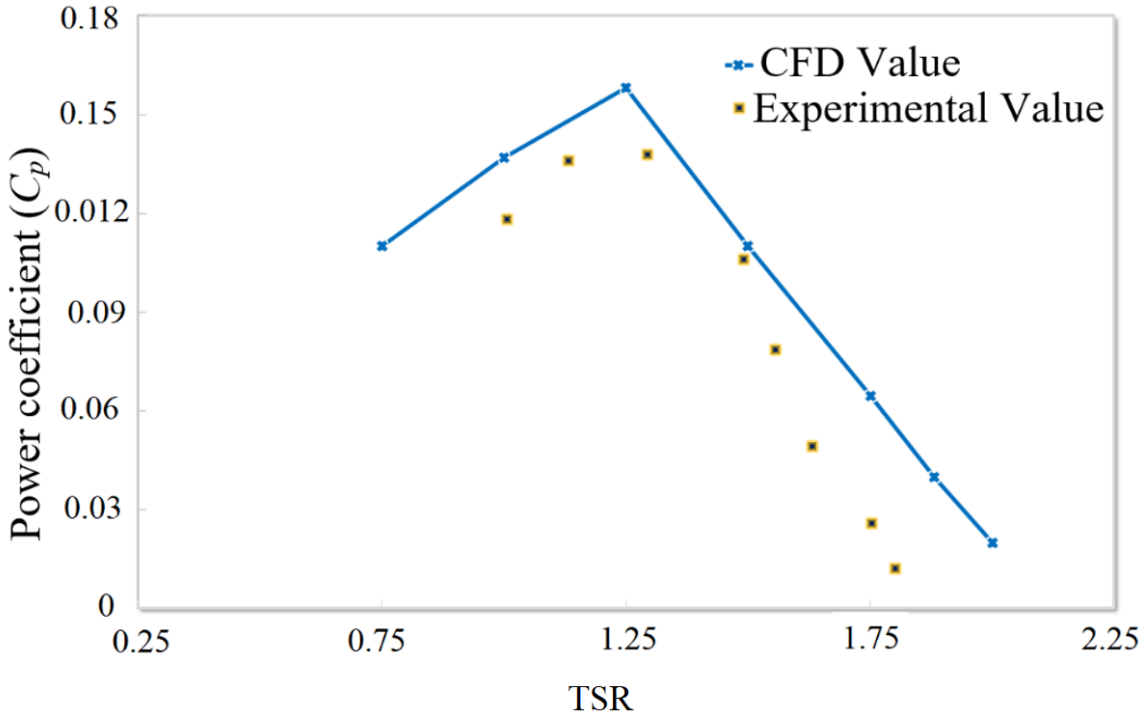

Figure 5.6 Comparison of CFD and experimental results for validation of the bassline case.

5.5 Optimal design using Taguchi method and ANOVA

The Taguchi method provides an inexpensive and efficient way to find optimised geometry of devices by minimum number of experiments (Chen et al., 2017). The process of identifying the optimal parameters can be summarised into seven steps (Bao et al., 2013). The block diagram of the whole process is illustrated in Figure 5.7.

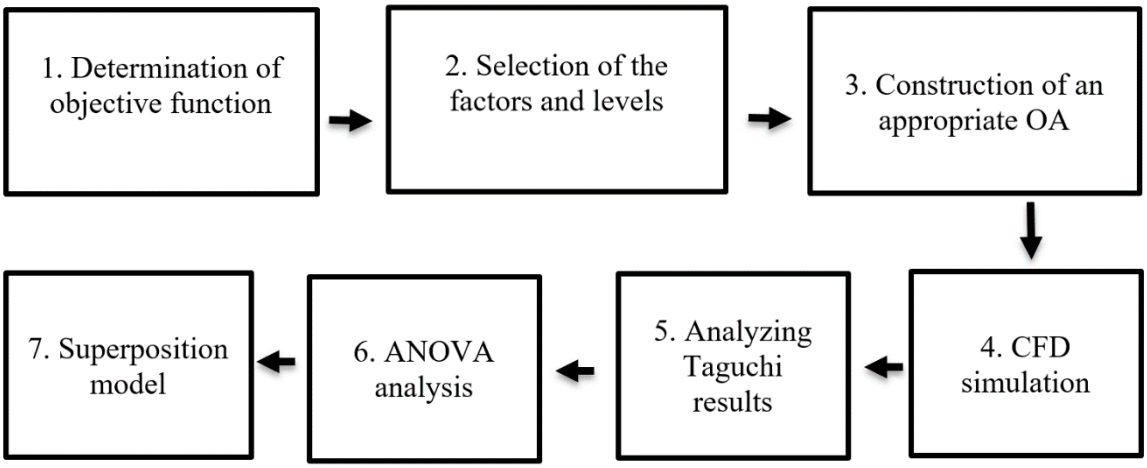

Figure 5.7 Block diagram of the process optimisation.

Step 1: Definition of the objective function

To calculate the output of the VAT turbine and determine the objective function, a Quality Loss (QL) function (Eq. 5.5) is determined to measure a parameter's deviation from its target quality (the maximum amount that can be obtained) (Phadke, 1995).

$$QL = K(V_e - V_t)^2 \tag{5.5}$$

where K is the quality loss factor, V_e is the calculated response, and V_t is the target quality.

The QL function can meaningfully approximate the reduction of quality (Pasha et al., 2018). In the current study, maximum power coefficient (C_p) is as the quality target. Vennell (Vennell, 2013) states that the power coefficient of tidal turbines can exceed the C_p of wind turbines. Accordingly in this research, the maximum C_p is considered as 16/27 (corresponding to wind turbine) based on the Betz Limit which is a safe assumption (De Lellis et al., 2018).

The Taguchi method uses a signal-to-noise (S/N) ratio to measure the output volatility of the chosen variables as the optimisation objective (Petit et al., 2020). In the Taguchi technique, the S/N ratio for each category of products can be determined as follows (Mandal et al., 2011):

Larger the better: $S/N_{LTB} = -10\log\frac{1}{\nu}\sum_{i=1}^{n}\frac{1}{(Y_i)^2}$ (5.6)

Nominal the best: $S/N_{NTB} = -10\log\frac{Y_m}{s^2}$ (5.7)

Smaller the better: $S/N_{STB} = -10\log\frac{1}{\nu}\sum_{i=1}^{n}(Y_i)^2$ (5.8)

where Y is the observed response, Y_m is the mean of the observed responses, s^2 is the variance, ν is the number of the observed responses.

The Quality Loss function belongs to the “smaller – the – better” type problem class. In this study, “small” refers to “QL function”. The QL function can generally be converted into an S/N ratio (Eq. 5.9) to measure the quality of a product (Phadke, 1995).

$$S/N_{STB} = -10\log(V_e - V_t) \quad (5.9)$$

As it can be seen from Eq. 5.10, the margin between maximum and optimum responses must be as small as possible for maximising the S/N ratio. Maximising V_e is equivalent to minimising quality loss in Eq. 5.10 which makes the noise sensitivity minimum (Freddi & Salmon, 2019). Therefore, by replacing maximum power coefficient and target quality, the objective function can be defined as:

$$S/N_{STB} = -10\log(C_p - 16/27)^2 \quad (5.10)$$

Step 2: Selection of the turbine factors and their levels

According to the parameter design tests, an optimal set of parameter response is defined as one that produces an inexpensive design while maintaining sufficient quality variation. Determining the optimal amount of each factor can be achieved by choosing the factor levels with the maximum S/N ratio. In the Taguchi method, the goal is to find the optimum combination of controlling factors. In this study, four standard factors which have significant effects on the hydrodynamic performance of vertical turbines (Danao et al., 2012; Naoi et al., 2006; Nicholls et al., 2008; Ouro et al., 2018; Sutikno et al., 2015; Urbina et al., 2019) are chosen, including twist angle (A), camber position (B), maximum camber (C), and chord/radius ratio (D).

The twist angle aims to minimise flow separation, making a positive lift at zero angle of attack (α) to allow self-start in ideal wind or water conditions. It also improves the performance of the turbine by increasing the blade's effective area (Gupta & Biswas, 2010). As the selected VAT turbine has three blades, the total twist angle of experiments can be increased up to 120°. 6 levels have been selected for the twist angle, including, 20^o, 40^o, 60^o, 80^o, 100^o, 120^o.

The camber position in the NACA family of airfoils can be varied from 0% to 90%. For investigating this factor, 70%, 45%, and 20% have been selected as levels of camber position (B). Moreover, the maximum camber in NACA airfoils can vary from 0 to 9.5%. There levels of 2.5%, 5.0%, and 7.5% are chosen for this factor. In the current study the thickness of hydrofoil is considered as constant.

Solidity ratio is among the most important factors that influence the efficiency of vertical tidal turbines (Dai & Lam, 2009). Solidity ratio is defined as the ratio of the swept area to total blade area of turbine (Figure 5.8) (Kumar et al., 2019).

The solidity ratio can be determined as (Bianchini et al., 2015):

$$\sigma = \frac{N_b D}{2R} \tag{5.11}$$

where σ is the solidity ratio, N_b is the number of blades, D is the length of blade chord, R is the radius of turbine.

Eq. 5.11 clearly shows that the solidity of a turbine can be changed by altering the turbine radius to blade chord ratio or the number of blades. The turbine's optimum running speed is determined by the solidity ratio (Armstrong et al., 2012) and the power coefficient of a turbine with the optimal solidity will be maximised, therefore the best value will depend on the operating conditions. According to the solidity ratio equation, a smaller solidity means the turbine converts low water (wind) energy. In other words, when solidity is low, the output power is also low. On the other hand, with increasing solidity, the maximum values of lift and drag coefficients decrease. According to Armstrong et al. (2012) the solidity ratio should not exceed 0.5 as the proximity of the blades degrades the turbine output. Since the number of the blades of the turbine is considered as three, a chord/radius ratio is considered to be optimised as a representative of the solidity ratio.

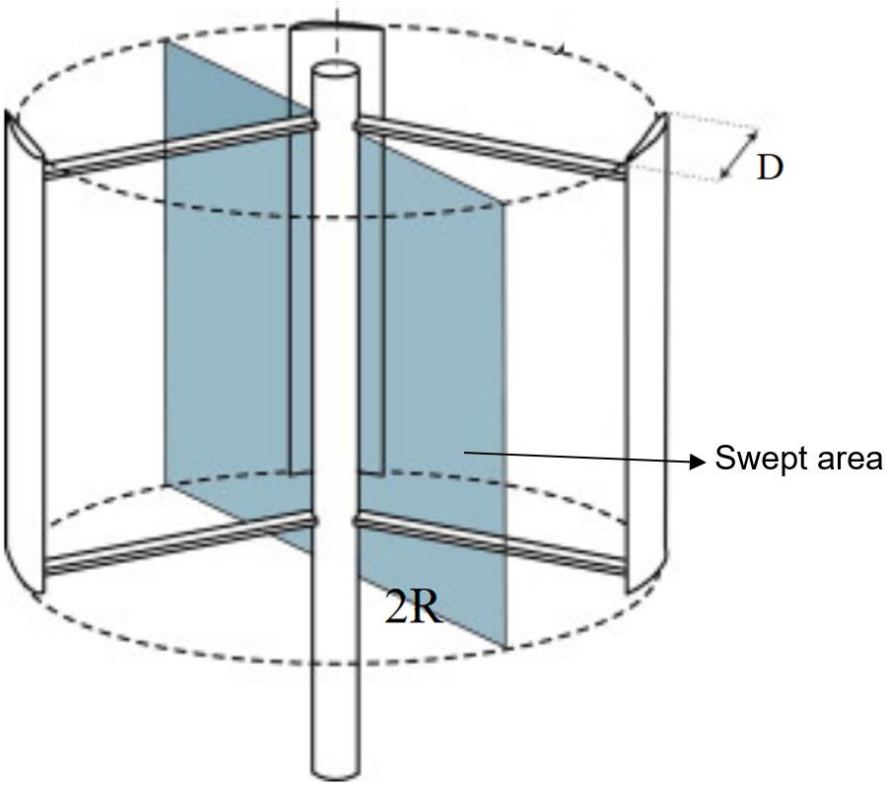

Figure 5.8 Illustration of solidity ratio of a VAT turbine (Bianchini et al., 2015).

Table 5.2 Specified factors and levels

Levels	1	2	3	4	5	6
A: Twist angle	20^0	40^0	60^0	80^0	100^0	120^0
Levels	1		2		3	
B: Camber position	0.70		0.45		0.20	
C: Maximum camber	0.025		0.050		0.075	
D: Chord/radius	0.10		0.20		0.30	

Step 3: Construction of an appropriate Orthogonal Array (OA)

In the Taguchi approach, only a certain number of experiments is needed to test according to the orthogonal (statistically independent) array rather than all feasible models. Generally, the selected optimisation approach needs a parameter matrix with a variety of levels that the parametric differences can be analysed. A type of general fractional factorial design is Orthogonal Array (OA). It is a fractional orthogonal design based on a design matrix which enables us to consider a subset of multiple factor combinations at multiple levels. OA are balanced to ensure that all levels of all variables are equally taken into account. The possible OA for the total number of selected parameters and levels is L_{18} (6^1*3^3) (mixed-level orthogonal array) which is constructed as shown in Table 5.3. Accordingly, based on the constructed orthogonal array, instead of 162 cases, 18 cases will be analysed to achieve maximum hydrodynamic performance of the turbine determined by the four factors, namely twist angle (6 levels), camber position (3 levels), maximum camber (3 levels), and chord/ radius ratio (3 levels).

Table 5.3 $L_{18}(6^1*3^3)$ Orthogonal array (OA)

No.	A	B	C	D
Run 1	1	1	1	1
Run 2	1	2	2	2
Run 3	1	3	3	3
Run 4	2	1	1	2
Run 5	2	2	2	3
Run 6	2	3	3	1
Run 7	3	1	2	1
Run 8	3	2	3	2
Run 9	3	3	1	3
Run 10	4	1	3	3
Run 11	4	2	1	1
Run 12	4	3	2	2
Run 13	5	1	2	3
Run 14	5	2	3	1
Run 15	5	3	1	2
Run 16	6	1	3	2
Run 17	6	2	1	3
Run 18	6	3	2	1

Step 4: CFD simulation

In this section, 18 different models (please see Appendix B), according to the dimensions listed in Table 5.2 and the constructed OA (Table 5.3), are designed using SOLIDWORKS 2017 and simulated by ANSYS Fluent 2019 software in order to quantify the hydrodynamic performance of the turbines. The moment coefficients (C_m) for a single revolution at *TSR*=1.25 for the baseline case and other 18 cases are calculated using Eq. 5.3 and the results of baseline and case 12 are presented in Figure 5.9 (for all cases please see Appendix C). Moreover, the power coefficients (C_p) are calculated using Eq. 5.4 and the results are presented in Table 5.4. From the results, it can be seen that the twist angle has an important effect on the output of the VAT turbine. The highest average moment coefficient (C_m) and power coefficient (C_p) correspond to case 12 which are 0.134 and 0.202 respectively. The value of C_p (0.202) obtained for case 12 is 26% higher than the C_p (0.16) for the baseline case, which was calculated in section 2.

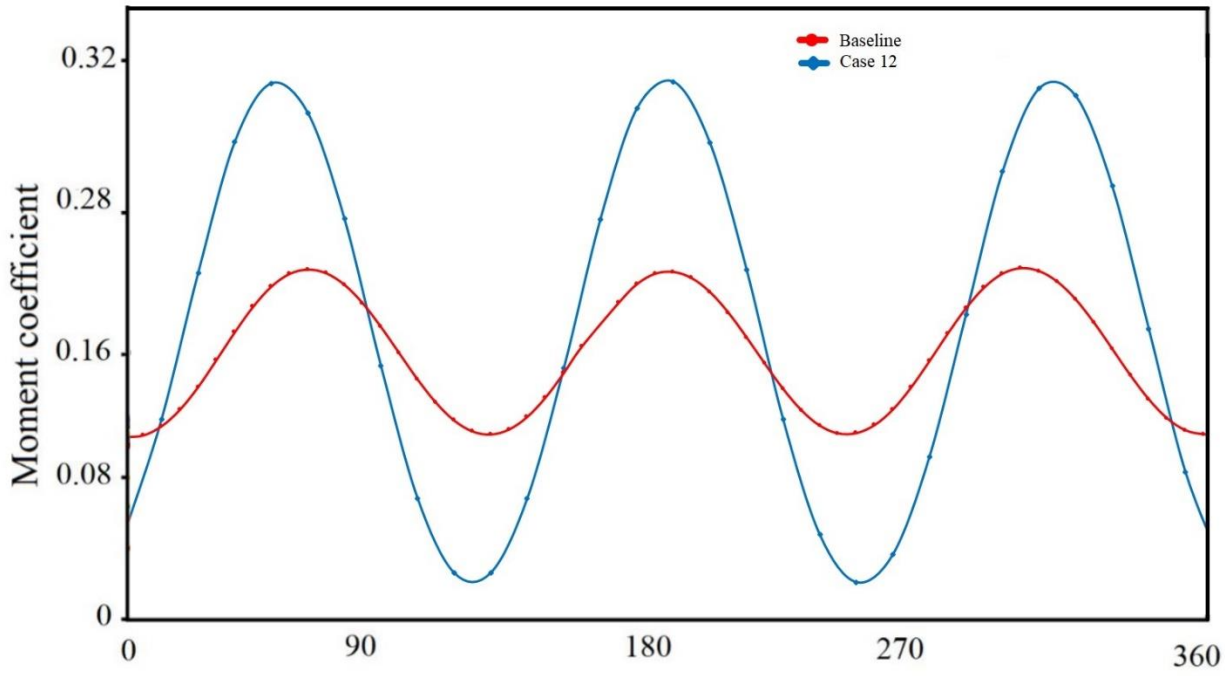

Figure 5.9 Variations in moment coefficient for single revolution, form 0° to 360° at water velocity of 1.0 m/s and *TSR*=1.25.

Step 5: Analysing Taguchi results

The S/N ratios of 18 different cases are calculated using Eq. 5.11 and the results are presented in Table 5.4. According to Eq. 5.11, the maximum S/N ratio occurs at the maximum power coefficient. The maximum S/N ratio is 8.232, which corresponds to case 12. In the next step, the Taguchi method is used to determine the order of impact and the optimal combination of the parameters to be selected for the design. The mean S/N ratios for parametric design are calculated using Eq. 5.11 and Table 5.4. For instance, the mean S/N ratio of A_6 is calculated from the average values of three level 6 factors $[(7.001 + 6.238 + 6.714)/3 = 6.651]$. Similarly, the S/N ratios are calculated for the rest of the factors with deferent levels and the results are plotted in Figure 5.10. The results show that the combination of A_4, B_3, C_2, and D_2 results in the maximum output. To find the order of the effect of each factor, a parameter (θ) is defined, which is the difference between the maximum and minimum responses of each factor. The values of this parameter for factors A, B, C, and D are 0.863, 0.136, 0.151, and 0.684 respectively. This implies that factor A, which is twist angle, is the most significant factor among the 4 tested factors, affecting the hydrodynamic performance of the turbine. Moreover, factors B (camber position) and C (maximum camber) have the least impact on the power output of the turbine.

Table 5.4 L_{18} Orthogonal array (OA)

No.	Twist angle	Camber position	Maximum camber	Chord/ Radius	C_p	S/N ratio
Run 1	20º	0.70	0.025	0.10	0.148	7.099
Run 2	20º	0.45	0.050	0.20	0.169	7.522
Run 3	20º	0.20	0.075	0.30	0.160	7.338
Run 4	40º	0.70	0.025	0.20	0.172	7.584
Run 5	40º	0.45	0.050	0.30	0.143	7.001
Run 6	40º	0.20	0.075	0.10	0.148	7.099
Run 7	60º	0.70	0.050	0.10	0.147	7.079
Run 8	60º	0.45	0.075	0.20	0.192	8.011
Run 9	60º	0.20	0.025	0.30	0.155	7.238
Run 10	80º	0.70	0.075	0.30	0.132	6.790
Run 11	80º	0.45	0.025	0.10	0.169	7.522
Run 12	80º	0.20	0.050	0.20	0.202	8.232
Run 13	100º	0.70	0.050	0.30	0.142	6.982
Run 14	100º	0.45	0.075	0.10	0.146	7.060
Run 15	100º	0.20	0.025	0.20	0.140	6.943
Run 16	120º	0.70	0.075	0.20	0.143	7.001
Run 17	120º	0.45	0.025	0.30	0.102	6.238
Run 18	120º	0.20	0.050	0.10	0.128	6.714
Baseline	0º	N/A	N/A	0.30	0.159	N/A

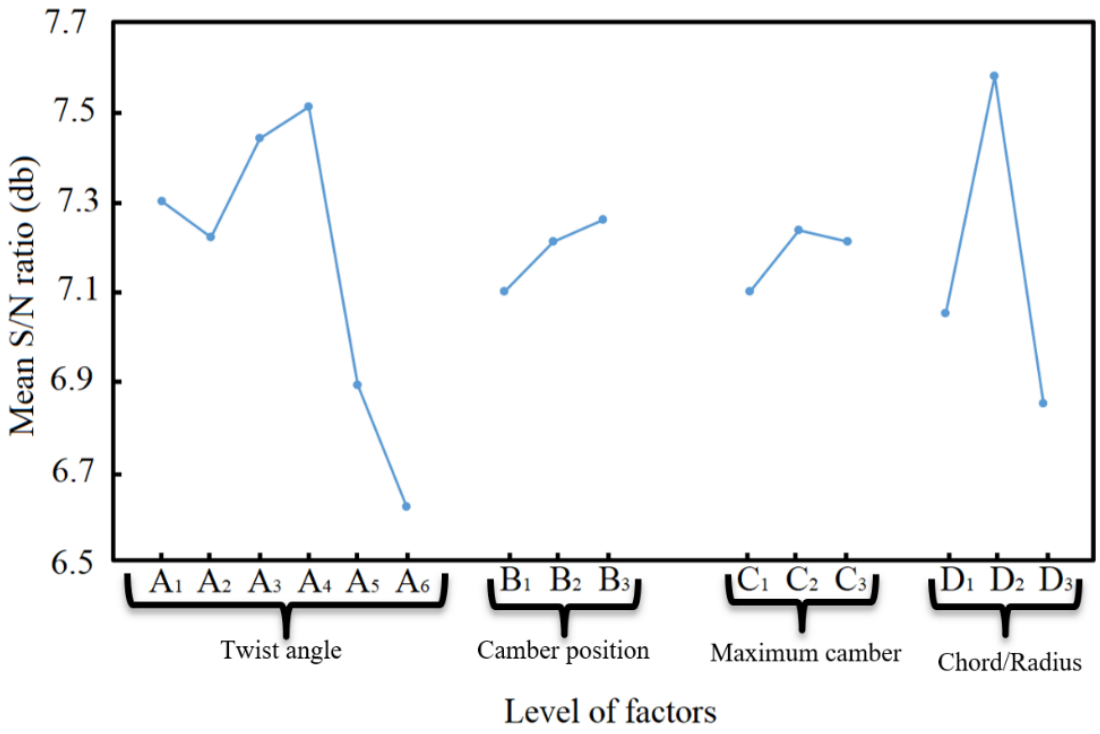

Figure 5.10 The mean S/N ratio for parametric design.

Step 6: Assessing the interactions between turbine parameters using ANOVA

Interactions between the turbine parameters are important and they should be considered in order to make the experiments and their analysis meaningful (Wang et al., 2018). The analysis of variance (ANOVA) technique can be used to provide a measure of reliability. ANOVA is an effective statistical method involving variance of the obtained responses in order to perform different confidence tests. Instead of analysing the data directly, this method determines the data variability and analyses the mean difference in quality of experiments conducted (Naik & Reddy, 2018; Roy, 2010). In ANOVA approach, all interactions in parameters can be assessed statistically important or negligible, by comparing them with the variance in the tests. This is why the method is called “analysis of variance”. A term of “total sum of squares" (TSS) is used in the framework of ANOVA, since it corresponds to the total variance of the measurements. There are different classical approaches for computing TSS in ANOVA for unbalanced data. In this study, to

evaluate the interaction of the turbine parameters, the two-way ANOVA technique is used for the S/N ratios in order to measure the interaction of each two independent factors. The (two-way) TSS of the variables can be calculated as follows (Ott & Longnecker, 2015; Ranganath & Vipin, 2013):

$$TSS = \sum_{i=1}^{n_y} (T_i - \bar{T})^2 \tag{5.12}$$

where n_y is the number of measurements, T_i is the ith measurements, and $\bar{T}$ is the mean of the n_y measurements.

ANOVA interaction plot can be used to visualise the relationship between the factors (Ott & Longnecker, 2015; Ranganath & Vipin, 2013). Figure 5.11 illustrates three different possible scenarios comprising two three-level factors according to the tested responses. This figure is provided as a general example to understand and assess Figure 5.11.In parallel trends, either interaction does not occur or is negligible while in non-parallel ones, the interaction between factors occurs and it must be considered (Abuthakeer et al., 2011). In this analysis, the interaction of each two factors is calculated according to the S/N ratios listed in Table 5.4 and plotted in Figure 5.12. The mean S/N ratio interaction graphs illustrate that the major influences the responses is due to the interaction of twist angle (A) with other factors. The parallel patterns in the lines of interaction between D and other factors clearly indicate negligible interaction and therefore in the following section A*D, B*D, and C*D will not be applied.

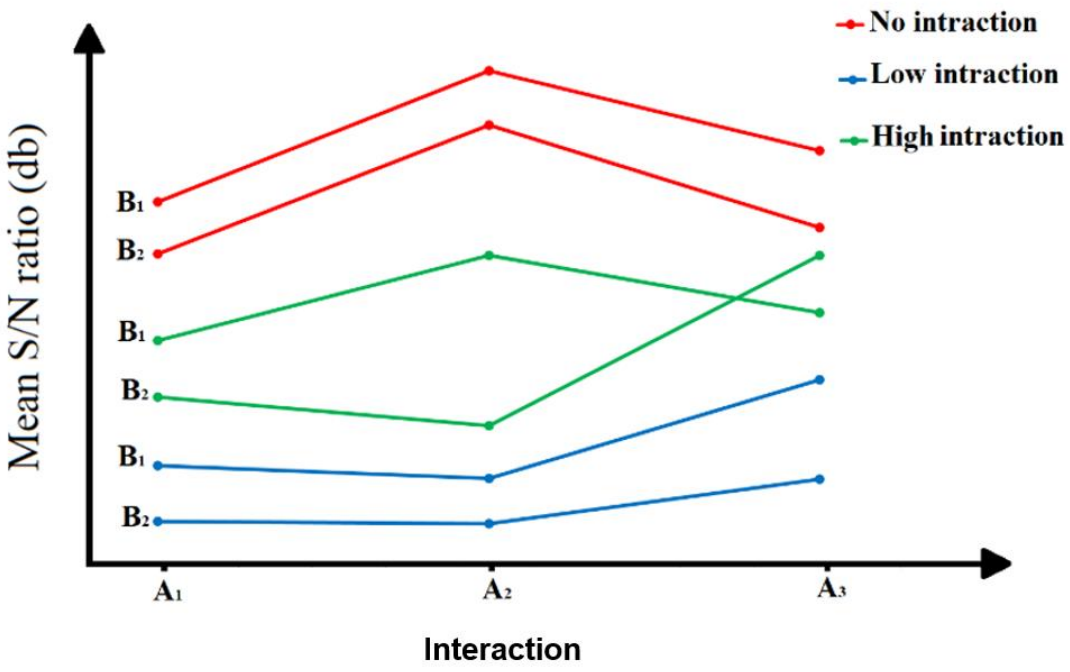

Figure 5.11 Interaction plot in three different possible scenarios.

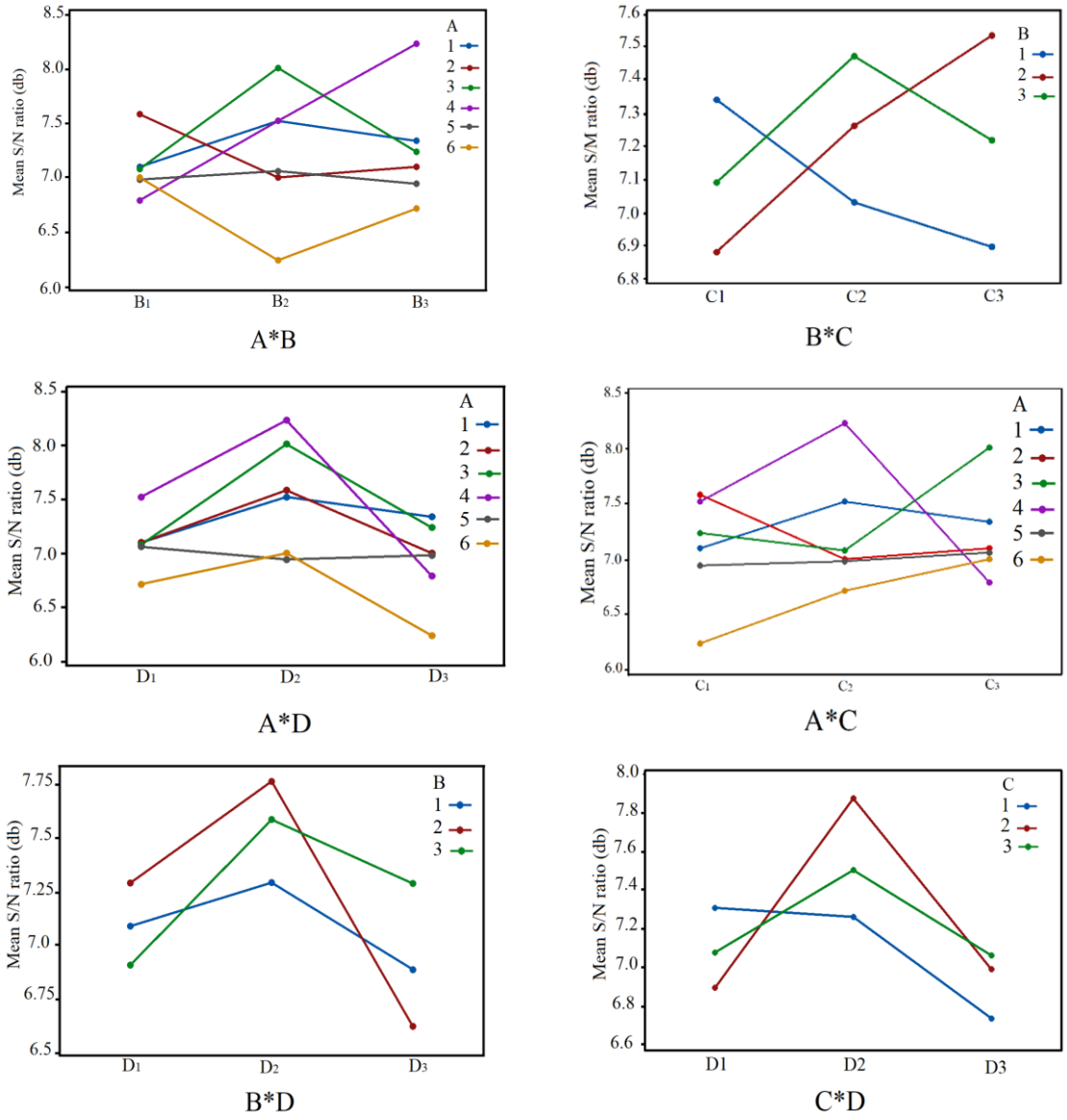

Figure 5.12 Interaction plot (ANOVA).

Step 7: Additive model (superposition model) for estimation all possible responses (S/N ratios) outside of orthogonal array

Superposition model can be used to estimate all possible responses (S/N ratios) outside of orthogonal array (OA). According to Phadke (1995), superposition model for the four factors, assuming that the amount of error is negligible, can be defines as:

$$\eta^{o}(A_i, B_j, C_k, D_l) = \eta + (\eta_{Ai} - \eta) + (\eta_{Bj} - \eta) + (\eta_{Ck} - \eta) + (\eta_{Dl} - \eta) \quad (5.13)$$

where η^o is the estimated S/N ratio, η is the average of total mean S/N ratios, η_{Ai}, η_{Bj}, η_{Ck}, and η_{Dl} are the S/N ratios with the factors A, B, C, and D at levels i, j, k, and l respectively.

The superposition equation should be updated to contain the interaction of factors by adding extra terms in order to provide the impacts of relationship between any two variables. Accordingly, additional term of A and B is determined as follows:

$$\eta^*(A_i, B_j) = (\eta_{AiBj} - \eta) - (\eta_{Ai} - \eta) - (\eta_{Bj} - \eta) \tag{5.14}$$

where η^* is the interaction term and η_{AiBj} is the average of total mean S/N ratios including both A_i and B_j.

This approach can be used for other interactions (A*B, A*C, and B*C) and by adding the interaction terms to the superposition equation, the modified superposition equation for calculating 162 (6*3*3*3) possible cases can be written as follows:

$$\begin{aligned}
&\eta^*(A_i, B_j, C_k, D_l) = \eta + (\eta_{Ai} - \eta) + (\eta_{Bj} - \eta) + (\eta_{Ck} - \eta) + (\eta_{Dl} - \eta) \\
&+(\eta_{AiBj} - \eta) - (\eta_{Ai} - \eta) - (\eta_{Bj} - \eta) + (\eta_{AiCk} - \eta) - (\eta_{Ai} - \eta) \\
&-(\eta_{Ck} - \eta) + (\eta_{CkBj} - \eta) - (\eta_{Ck} - \eta) - (\eta_{Bj} - \eta) = -(\eta_{Ai}) - (\eta_{Bj}) \\
&-(\eta_{Ck}) + (\eta_{Dl}) + (\eta_{AiBj}) + (\eta_{AiCk}) + (\eta_{CkBj})
\end{aligned} \tag{5.15}$$

To solve Eq. 5.15, a program is written in MATLAB and by using the data in Table 5.4, the total possible S/N ratios for 162 cases are calculated and the results are presented in Table 5.5.

The leave-one-out cross-validation method (Sammut and Webb, 2010) was used to validate the superposition model (Eq. 4.15). In this method, the S/N ratio values in Table 5.4 (18 different data points) were considered as a ground truth which can be trusted since they were obtained based on ANSYS Fluent simulations. Starting from the top of the Table 5.4 (Run 1), in each step one of the S/N ratios was taken out and its value was

predicted using the superposition method (Eq. 5.15). The results are listed in Table 5.5. The RMSE (root of the mean squared error) (Eq. 5.16) of the superposition model was calculated as 0.32, which indicates a good prediction according to Ritter & Muñoz-Carpena (2012). It should be noted that the values of S/N ratio in Table 5.6 were predicted with 18 data points, while in Table 5.5 each was predicted with 17 data points. Therefore, it can be said that S/N ratios in Table 5.6 have lower RMSE than 0.32.

$$RMSE=\left[\frac{1}{n}\sum_{i}^{n}(W_i-Z_i)^2\right]^{\frac{1}{2}} \tag{5.16}$$

where W_i is the i_{th} obtained data based on CFD, Z_i is the i_{th} predicted data with superposition model, n is the number of observations (Akpinar & Akpinar, 2005).

Table 5.5 Leave-one-out cross-validation of superposition model

No.	A	B	C	D	Exact S/N ratio (CFD)	Predicted S/N ratio (Superposition)
Run 1	1	1	1	1	7.099	7.4605
Run 2	1	2	2	2	7.522	7.2603
Run 3	1	3	3	3	7.338	6.9113
Run 4	2	1	1	2	7.584	7.4827
Run 5	2	2	2	3	7.001	6.7039
Run 6	2	3	3	1	7.099	7.4127
Run 7	3	1	2	1	7.079	7.1936
Run 8	3	2	3	2	8.011	7.816
Run 9	3	3	1	3	7.238	7.2812
Run 10	4	1	3	3	6.790	7.213
Run 11	4	2	1	1	7.522	7.7554
Run 12	4	3	2	2	8.232	7.903
Run 13	5	1	2	3	6.982	7.1818
Run 14	5	2	3	1	7.060	6.3502
Run 15	5	3	1	2	6.943	6.6424
Run 16	6	1	3	2	7.001	6.5375
Run 17	6	2	1	3	6.238	6.5281
Run 18	6	3	2	1	6.714	6.5489

Table 5.6 Estimated S/N ratios for all possible combinations

No.	A	B	C	D	Estimated S/N ratio	No.	A	B	C	D	Estimated S/N ratio	No.	A	B	C	D	Estimated S/N ratio
1	1	1	1	1	7.123	55	3	1	1	1	7.119	109	5	1	1	1	7.174
2	1	1	1	2	7.576	56	3	1	1	2	7.572	110	5	1	1	2	7.628
3	1	1	1	3	6.958	57	3	1	1	3	6.955	111	5	1	1	3	7.01
4	1	1	2	1	7.084	58	3	1	2	1	6.498	112	5	1	2	1	6.751
5	1	1	2	2	7.537	59	3	1	2	2	6.952	113	5	1	2	2	7.204
6	1	1	2	3	6.919	60	3	1	2	3	6.334	114	5	1	2	3	6.587
7	1	1	3	1	6.803	61	3	1	3	1	7.333	115	5	1	3	1	6.733
8	1	1	3	2	7.257	62	3	1	3	2	7.787	116	5	1	3	2	7.186
9	1	1	3	3	6.639	63	3	1	3	3	7.169	117	5	1	3	3	6.568
10	1	2	1	1	6.948	64	3	2	1	1	7.452	118	5	2	1	1	6.655
11	1	2	1	2	7.401	65	3	2	1	2	7.906	119	5	2	1	2	7.108
12	1	2	1	3	6.784	66	3	2	1	3	7.288	120	5	2	1	3	6.49
13	1	2	2	1	7.602	67	3	2	2	1	7.524	121	5	2	2	1	6.924
14	1	2	2	2	8.055	68	3	2	2	2	7.978	122	5	2	2	2	7.377
15	1	2	2	3	7.437	69	3	2	2	3	7.36	123	5	2	2	3	6.759
16	1	2	3	1	7.73	70	3	2	3	1	8.768	124	5	2	3	1	7.314
17	1	2	3	2	8.183	71	3	2	3	2	9.221	125	5	2	3	2	7.767
18	1	2	3	3	7.565	72	3	2	3	3	8.604	126	5	2	3	3	7.149
19	1	3	1	1	6.939	73	3	3	1	1	6.855	127	5	3	1	1	6.713
20	1	3	1	2	7.392	74	3	3	1	2	7.308	128	5	3	1	2	7.166
21	1	3	1	3	6.775	75	3	3	1	3	6.69	129	5	3	1	3	6.549
22	1	3	2	1	7.594	76	3	3	2	1	6.928	130	5	3	2	1	6.983
23	1	3	2	2	8.047	77	3	3	2	2	7.381	131	5	3	2	2	7.437
24	1	3	2	3	7.43	78	3	3	2	3	6.764	132	5	3	2	3	6.819
25	1	3	3	1	7.194	79	3	3	3	1	7.643	133	5	3	3	1	6.846
26	1	3	3	2	7.648	80	3	3	3	2	8.097	134	5	3	3	2	7.299
27	1	3	3	3	7.03	81	3	3	3	3	7.479	135	5	3	3	3	6.681
28	2	1	1	1	8.185	82	4	1	1	1	7.042	136	6	1	1	1	6.833
29	2	1	1	2	8.638	83	4	1	1	2	7.495	137	6	1	1	2	7.286
30	2	1	1	3	8.021	84	4	1	1	3	6.877	138	6	1	1	3	6.668
31	2	1	2	1	7.14	85	4	1	2	1	7.289	139	6	1	2	1	6.847
32	2	1	2	2	7.593	86	4	1	2	2	7.743	140	6	1	2	2	7.3
33	2	1	2	3	6.975	87	4	1	2	3	7.125	141	6	1	2	3	6.682
34	2	1	3	1	7.141	88	4	1	3	1	5.751	142	6	1	3	1	7.037
35	2	1	3	2	7.594	89	4	1	3	2	6.204	143	6	1	3	2	7.49
36	2	1	3	3	6.977	90	4	1	3	3	5.587	144	6	1	3	3	6.873
37	2	2	1	1	7.004	91	4	2	1	1	7.176	145	6	2	1	1	5.472
38	2	2	1	2	7.457	92	4	2	1	2	7.63	146	6	2	1	2	5.925
39	2	2	1	3	6.84	93	4	2	1	3	7.012	147	6	2	1	3	5.307
40	2	2	2	1	6.651	94	4	2	2	1	8.116	148	6	2	2	1	6.178
41	2	2	2	2	7.105	95	4	2	2	2	8.57	149	6	2	2	2	6.632
42	2	2	2	3	6.487	96	4	2	2	3	7.952	150	6	2	2	3	6.014
43	2	2	3	1	7.061	97	4	2	3	1	6.987	151	6	2	3	1	6.777
44	2	2	3	2	7.515	98	4	2	3	2	7.44	152	6	2	3	2	7.231
45	2	2	3	3	6.897	99	4	2	3	3	6.822	153	6	2	3	3	6.613
46	2	3	1	1	7.277	100	4	3	1	1	8.061	154	6	3	1	1	6.123
47	2	3	1	2	7.73	101	4	3	1	2	8.515	155	6	3	1	2	6.576
48	2	3	1	3	7.113	102	4	3	1	3	7.897	156	6	3	1	3	5.959
49	2	3	2	1	6.925	103	4	3	2	1	9.003	157	6	3	2	1	6.831
50	2	3	2	2	7.379	104	4	3	2	2	9.456	158	6	3	2	2	7.284
51	2	3	2	3	6.761	105	4	3	2	3	8.838	159	6	3	2	3	6.666
52	2	3	3	1	6.807	106	4	3	3	1	7.345	160	6	3	3	1	6.902
53	2	3	3	2	7.261	107	4	3	3	2	7.798	161	6	3	3	2	7.355
54	2	3	3	3	6.643	108	4	3	3	3	7.18	162	6	3	3	3	6.737

The results in Table 5.5 show that, the case 104 provides the maximum signal-to-noise ratio (9.456) in the combination of A_4, B_3, C_2, and D_2.

5.6 Fluid Dynamics of the baseline and optimised VAT turbines

A new turbine is designed based on the obtained optimised dimensions in the previous section. Figure 5.13 shows a comparison of the new design and the baseline case design. The optimised design is simulated numerically, as described in section 2. By using Eq. 5.4 and the data obtained from the CFD model, the power coefficient (C_p) is calculated as 0.210, which is 26% higher than the baseline case.

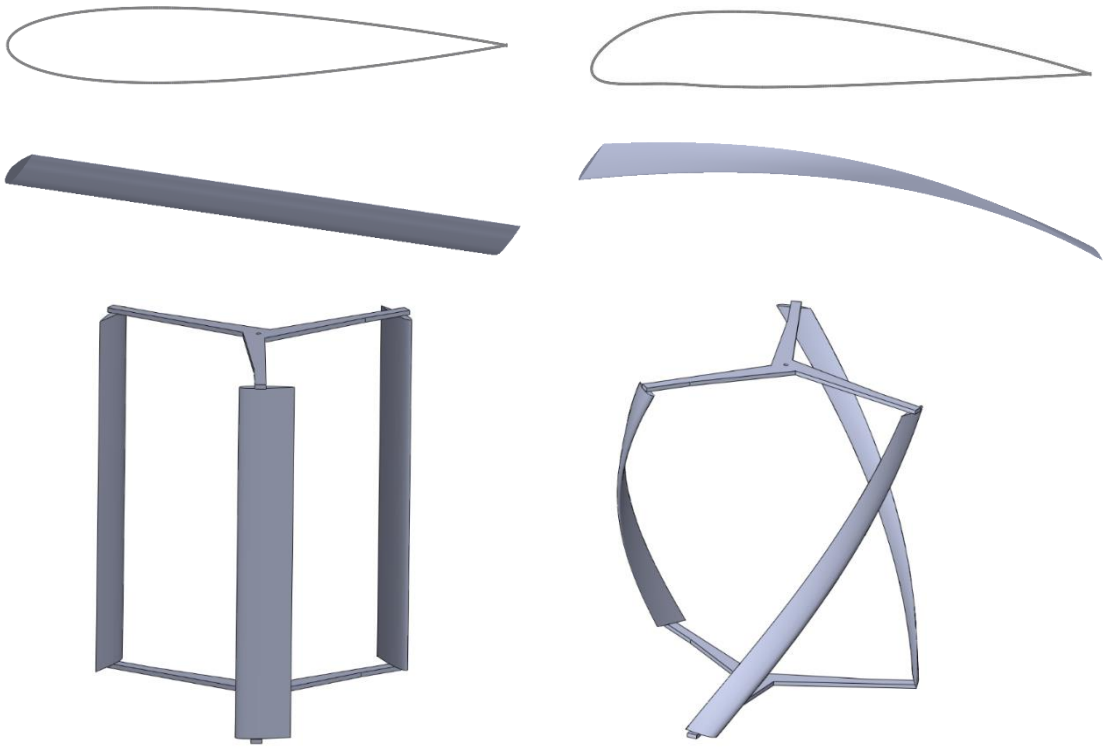

a b

Figure 5.13 (a) Baseline and (b) optimised configurations.

Although the updated superposition in the Taguchi approach enables to determine the optimal configuration of the VAT turbine to gain a significant increase in hydrodynamic

output, the fundamental fluid dynamics of this development still remains unknown. The pressure coefficient (Q_p) and the moment coefficient (C_m) around a single blade (leading blade) are calculated using the CFD data and the results show that the optimised turbine produces a promising improvement in power output.

The variations of moment coefficient (C_m) with azimuth angle for the baseline and optimised models at TSR= 1.25 are calculated and the results are presented in Figure 5.14. The results show that in the first half rotation, a significant part of positive moment contributions is located in the region between 40 ° and 180° and this is a very general characteristic demonstrated in several previous research (Chen & Lian, 2015; Ma et al., 2019). Although the maximum (C_m) in some parts of the graph (40-100^o) of the baseline model is higher than that in the optimised model, however the combination of the cambered-blade and twisted model has advantages when the whole region is considered.

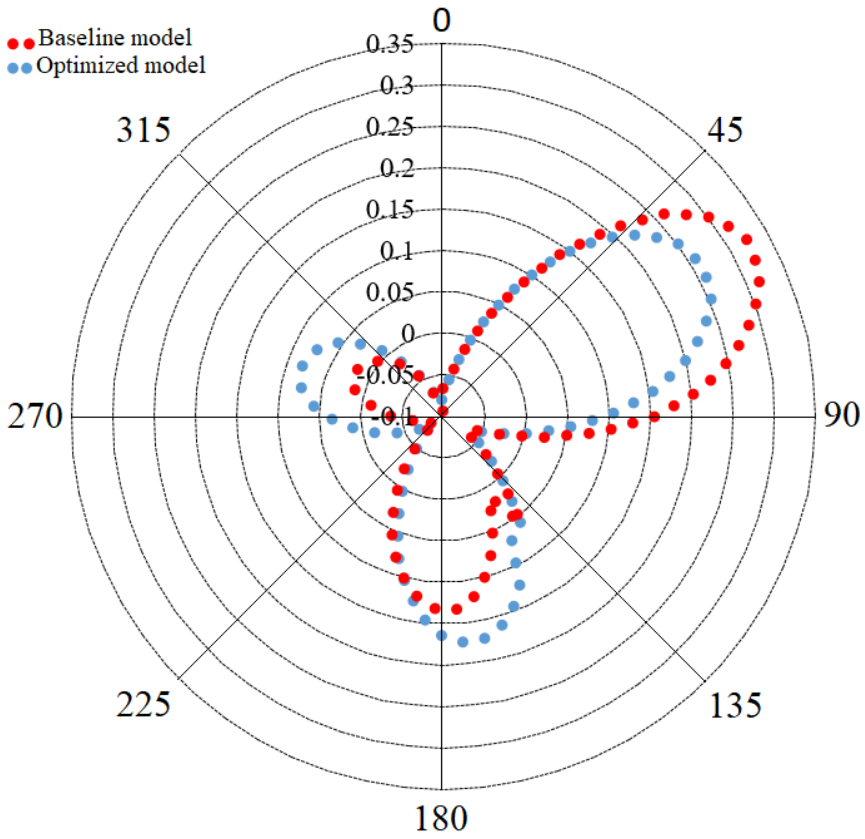

Figure 5.14 Moment coefficient (C_m) versus azimuth angle (0-360 degree) for a single blade of the baseline and optimised models at *TSR* = 1.25.

Since the efficiency of a VAT turbine is quite sensitive to the particular shape used for the hydrofoil (Walker et al., 2014), a qualitative assessment for the pressure coefficient for the baseline (symmetric) and cambered hydrofoils is performed to obtain a deeper understanding of this impact. The pressure coefficient over a hydrofoil can be determined by the pressure and stream properties as follows (Li et al., 2018):

$$Q_p = \frac{p - p_i}{0.5\rho A U^2} \tag{5.17}$$

where Q_p is the pressure coefficient, P is the pressure, and P_i is the freestream pressure.

Figure 5.15 demonstrates the distribution of the pressure coefficient (Q_p) over leading blade for the baseline and optimised models at *TSR* = 1.25 with the corresponding length of the chord. Q_p is negative at the bottom (lower surface) of hydrofoil and positive on its top (upper surface), and the hydrofoil's lift is heading upward. The suction peak is described as the highest suction value across the airfoil's bottom surface (Jawahar et al., 2020). The suction peak of Q_p for the cambered hydrofoil is greater than the baseline hydrofoil. Moreover, the margin (the difference between suction and pressure levels) of Q_p at the cambered hydrofoil is much greater than the symmetric hydrofoil, indicating a greater lifting force in the cambered hydrofoil.

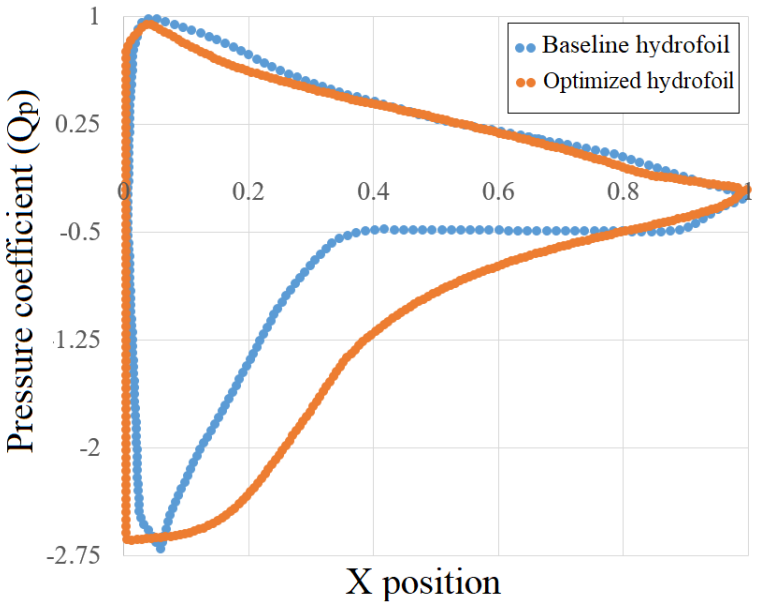

Figure 5.15 Pressure coefficient (Q_p) distribution for baseline and optimised hydrofoils at azimuth angle: 45°.

One of the fluid dynamics phenomena which can be used to compare and analyse the baseline and optimised turbines is dynamic-stall. To visualise the flow around the turbine, vorticity contours at 4 azimuth angles and 3 planes (I, II, and III) are plotted using CFD-Post ANYS 2019 (Figure 5.16). To analyse the performance of the turbine, a blade is

indicated as IB (see Figure 5.16) so that azimuth angle could be measured. The azimuth angle for the baseline model is shown with the location of the indicated blade (IB) illustrated in the contours and this angle for the optimised model is defined and measured in plane II. Examining the vorticity contour plots indicates that the stream separation in the optimised model is greatly reduced compared to the baseline model, suggesting that the twisted and cambered blade will be effective in regulating the spraying vortices over blades by suppressing dynamic-stall. According to Figure 5.16, in the baseline model, dynamic-stall on the turbine blade increases as the angle of attack increases by turbine rotation. Significant stream separation is seen at azimuth angle of 45^{o} and this is expanded until azimuth angle of 90^{o}. On the other hand, the optimised turbine which takes advantage of twisted and cambered blades, can suppress dynamic-stall by interacting with water in a different angle of attack at each azimuth angle. In the baseline model, which has straight-blades, the turbine interacts with water with constant angle of attack; however, twisted blades interact with water with different angles of attack at different points on the blade. To illustrate this effect, in Figure 5.16 all contours are plotted in three different planes. For instance, at azimuth angle of 45^{o} (plane I) of the optimised model, the separation is almost negligible in comparison with the same plane for the baseline model. This can be explained by considering the moment coefficient (C_m) and pressure coefficient (Q_p) curves of both turbines. According to Figure 5.14, the average moment coefficient of the optimised turbine is 30% higher than the baseline one from azimuth angles of 45^{o} to 90^{o}. Moreover, based on Figure 5.15, the moment that the positive cambered blade generates is consistently higher than the moment produced by the symmetric blade (baseline) due to greater lifting force. In addition, the wake (the span labelled "W" in Figure 5.16) generated by the baseline model stretches to a large region of the turbine blade, while for the optimised turbine it is a smaller region. The maximum region of wake for the baseline model is between 45^{o} to 90^{o}. In all contours plots displayed in the 4 azimuth angles, the span of produced wake in the baseline model is more than

the optimised one, which results in decrease in kinetic energy and in effect, lowers the performance of the turbine.

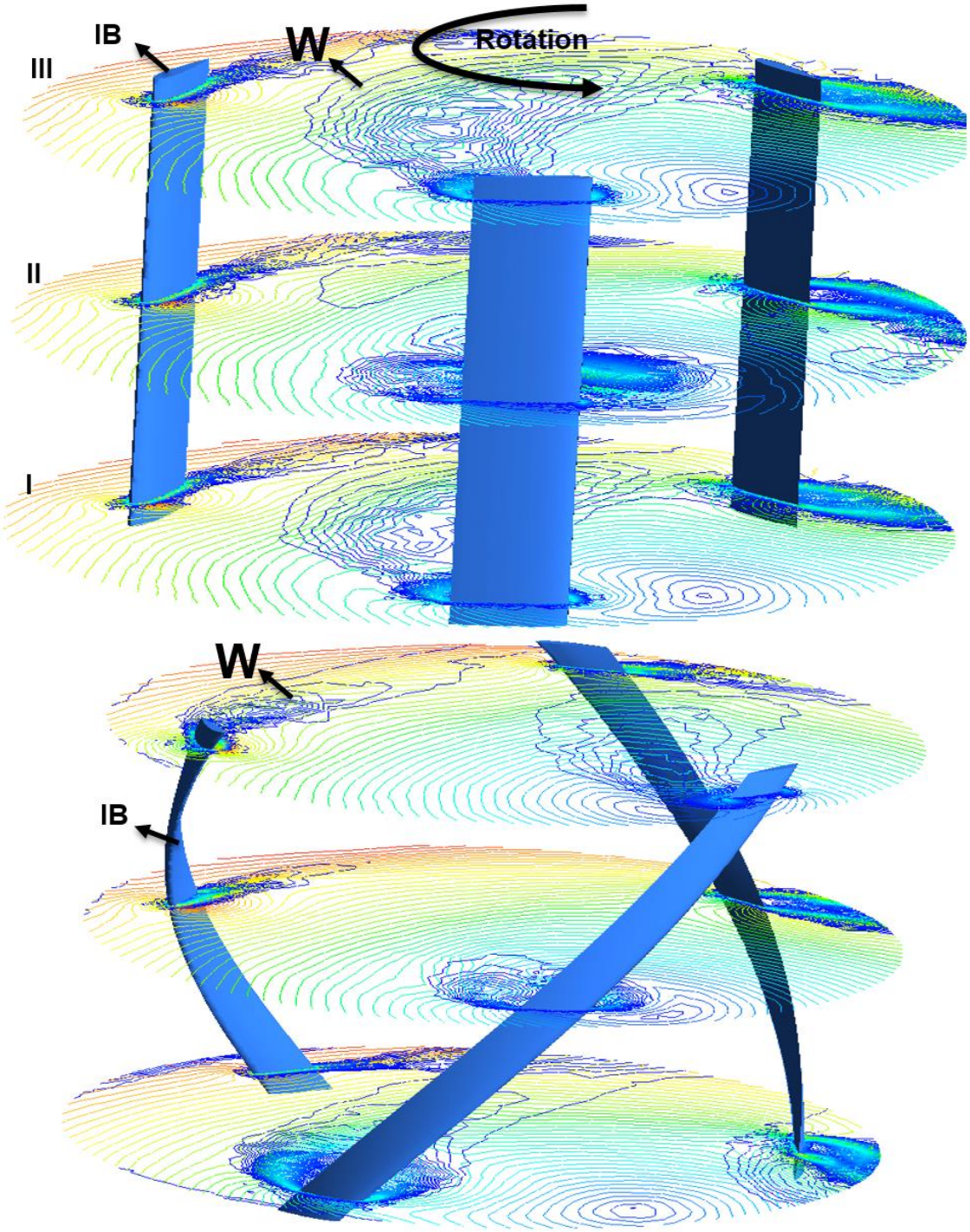

Azimuth angle: 45°

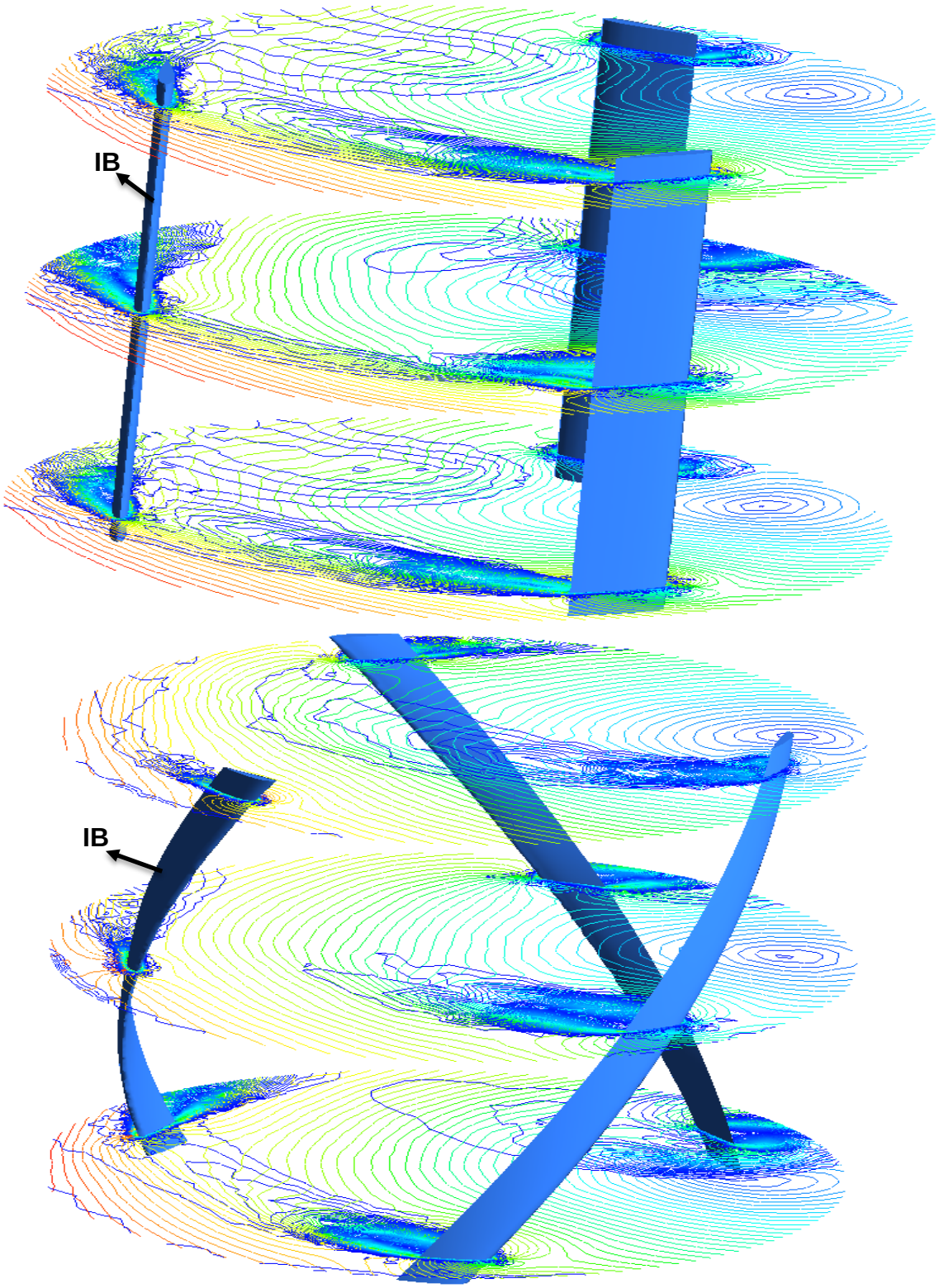
IB
IB
Azimuth angle: 90°
0.0 0.1 0.3 0.4 0.6 0.7 0.8 1.0 1.1 1.3 1.4 1.5 1.7 1.8 2.0 2.1 2.2 [m/s]

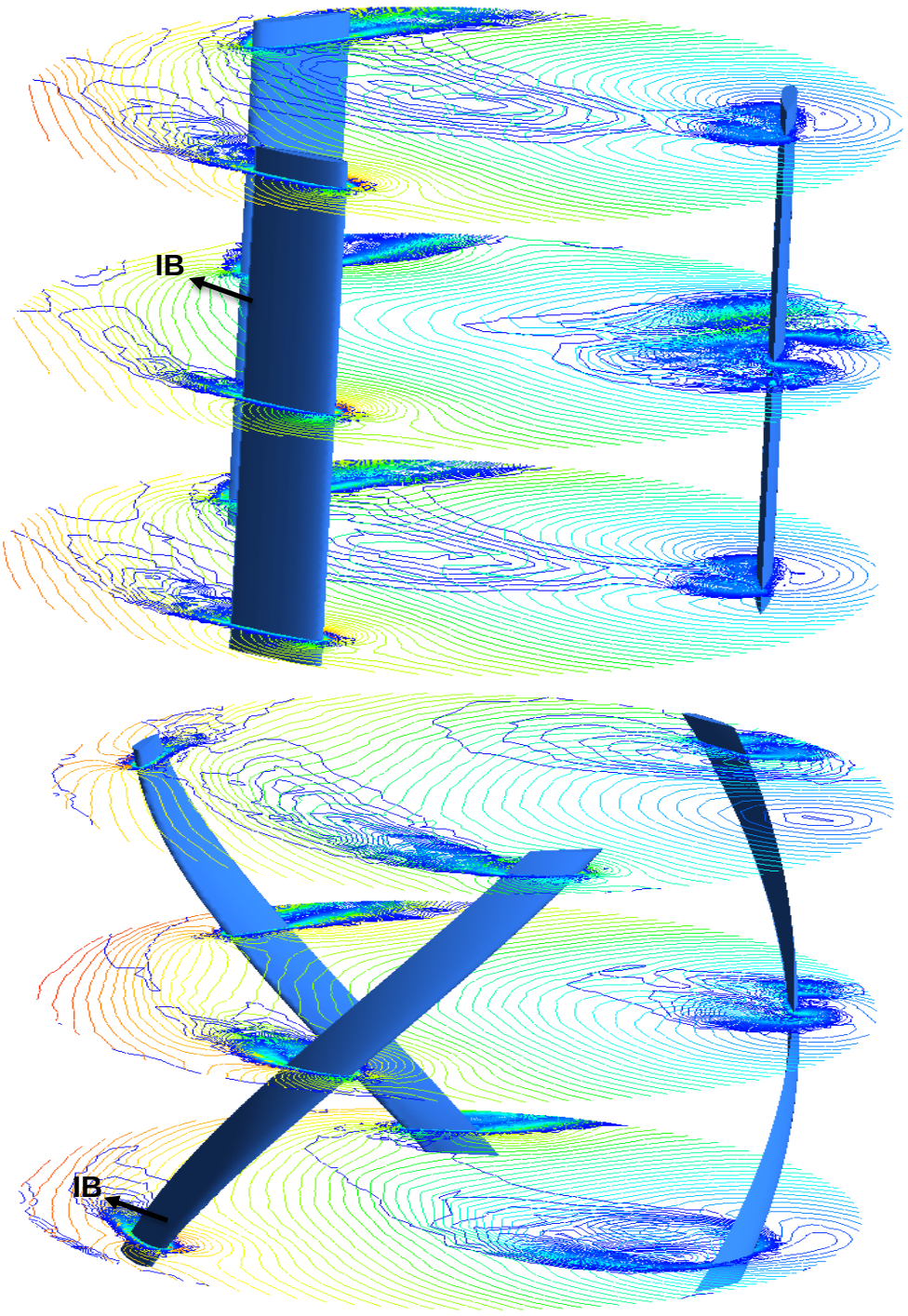

Azimuth angle: 135°

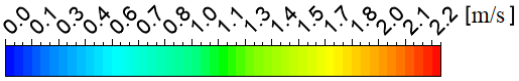

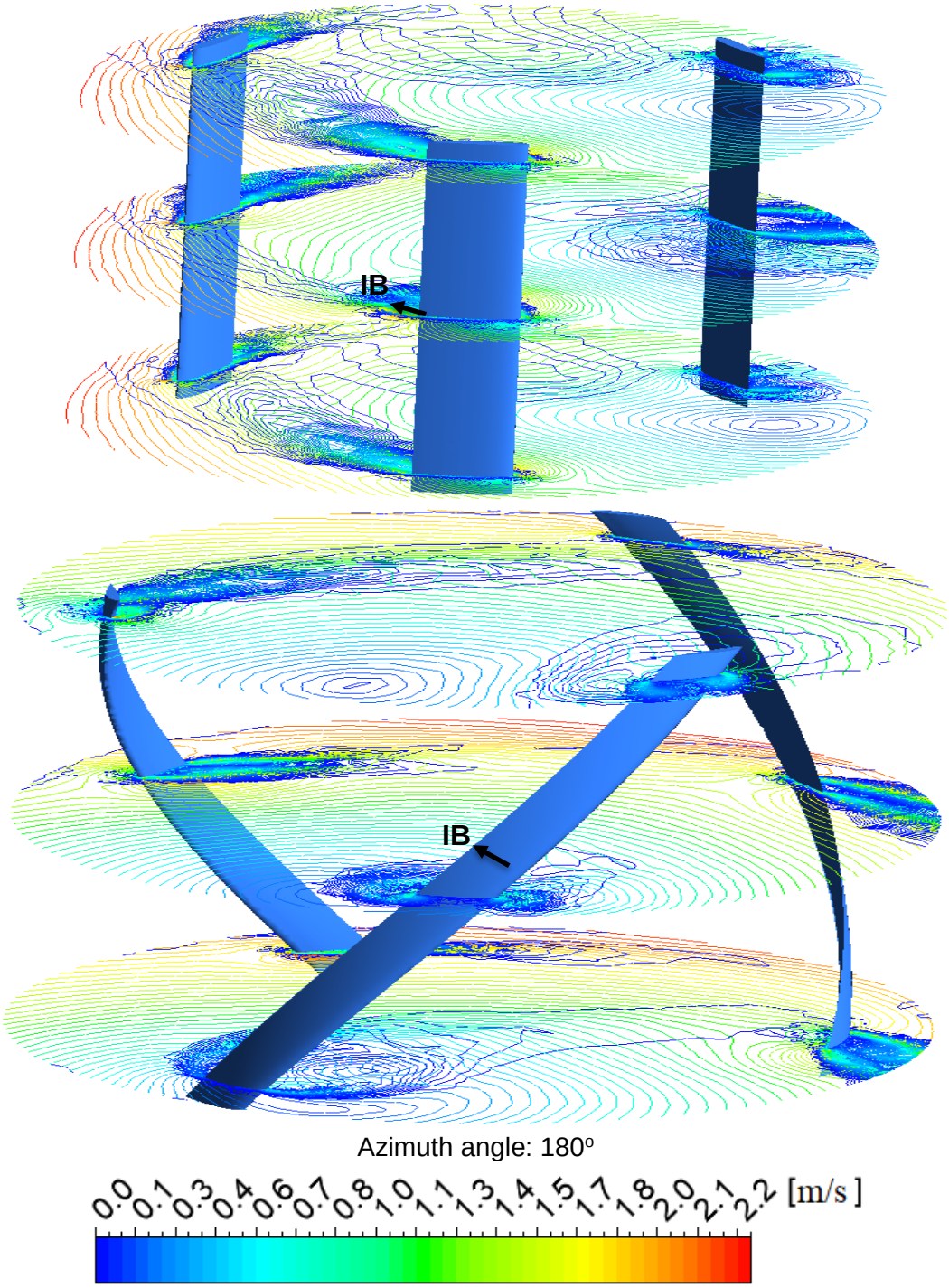

Figure 5.16 Vorticity distribution for the baseline and optimised models on 3 different planes.

To investigate the effects of surface roughness on the optimised turbine, the obtained optimised turbine with 500 μm roughness and no roughness was simulated using ANSYS Fluent 2019. The velocity contours obtained using the CFD Post software are illustrated in Figure 5.17. One part of the contours near the blade is magnified to highlight the destructive effects of roughness on the water flow. It can be seen that the turbine with surface roughness can create turbulence in the stream flow. And the turbulence of all three blades accumulate and interact and cause the stream flow to change. Fluid turbulence always reduces the kinetic energy, which in turn, reduces the total turbine efficiency. Using Eq. 4.13 and the obtained data from the simulations in ANSYS Fluent, the amount of power loss for a roughness of 500 μm was calculated to be 11%.

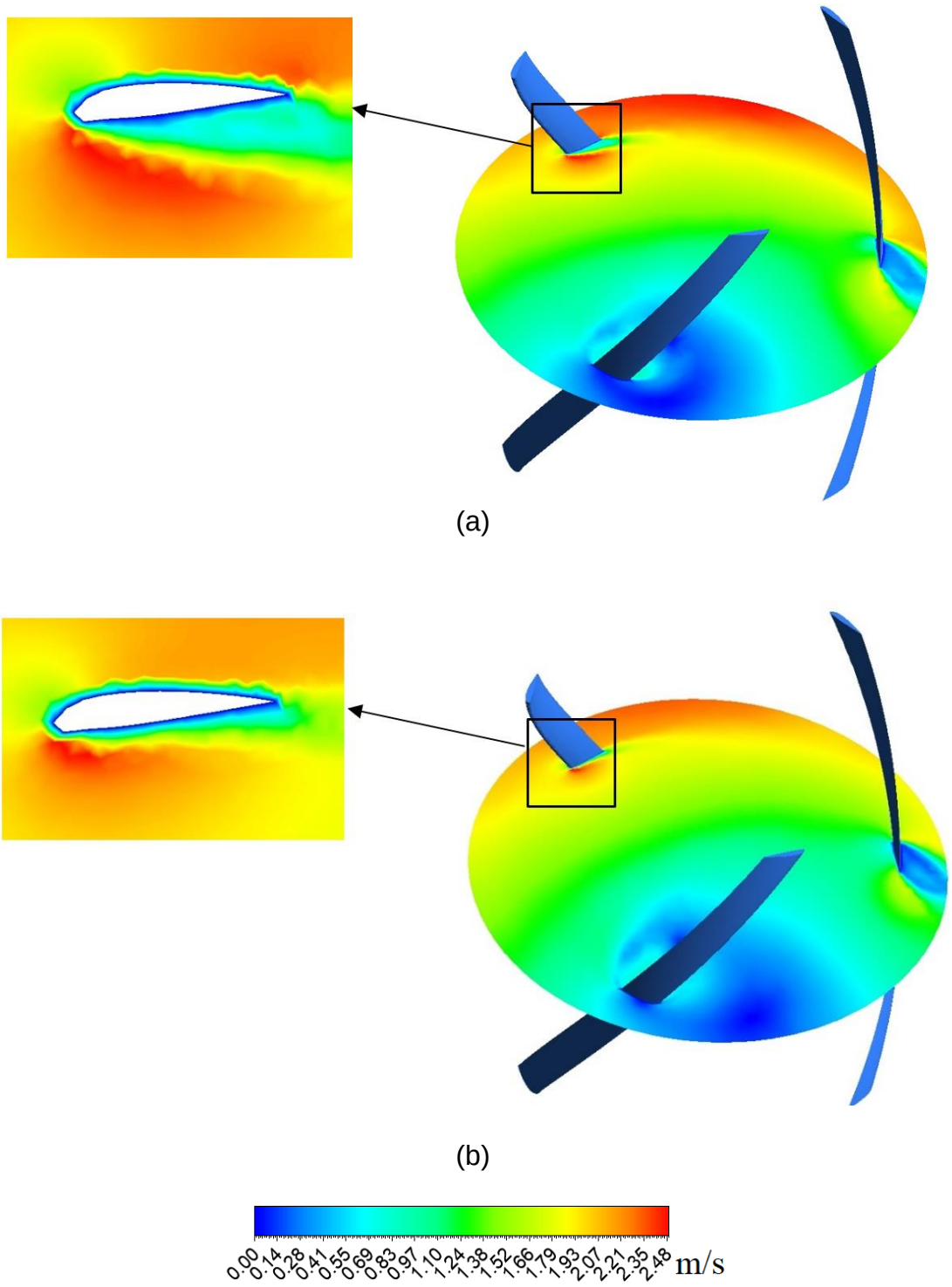

Figure 5.17 Velocity distribution for the optimised turbine (a) with and (b) without roughness (500 μm).

5.7 Conclusion

In this chapter, a mixed-level Taguchi approach and comprehensive CFD simulations were employed to optimise the main parametric factors that affect the hydrodynamic performance of a VAT turbine. The following conclusions can be drawn from the results presented in this chapter:

(1) The highest average moment coefficient (C_m) and power coefficient (C_p) correspond to case 12 which are 0.134 and 0.202 respectively. The S/N ratios of the 18 different cases were calculated. The maximum S/N ratio occurred at the maximum power coefficient. The maximum S/N ratio is 8.232 which corresponds to case 12.

(2) The results of the Taguchi method show that the combination of A_4, B_3, C_2, and D_2 results in the maximum output. The values of θ for factors A, B, C, and D are 0.863, 0.136, 0.151, and 0.684 respectively. This implies that twist angle is the most significant factor among the 4 tested factors, affecting the hydrodynamic performance of the turbine.

(3) Superposition was used to estimate all possible responses (S/N ratios) outside orthogonal array (OA). The superposition results showed that, the case 104 provides the maximum signal-to-noise ratio (9.456) with the combination A_4, B_3, C_2, and D_2 that is considerably greater than the optimal case (case 12), calculated by 18 cases in the Taguchi orthogonal array.

(4) The power coefficient (C_p) of the optimised turbine was calculated as 0.210, which is 26% higher than the baseline case. In addition, the optimised model reduced the required material by 57% compared with the baseline model, indicating that the new model needs less material. Moreover, the size of the wake generated in the baseline model was greater than the optimised model, resulting in a decrease in kinetic energy and a reduction in turbine output.

Chapter Six: Optimisation of a Horizontal Axis Tidal turbine for powering a RO desalination system

6.1 Abstract

Horizontal Axis Tidal (HAT) turbines can be used to power RO desalination systems. The greatest weakness of these turbines (http://tidalpower.co.uk, 2020) is the high price of design, development, and manufacturing. Traditionally, optimisation of turbine geometry is achieved by running several numerical models of the turbine which can become computationally expensive. The Taguchi-CFD (Computational Fluid Dynamics) approach has recently been introduced as an inexpensive and rapid tool for optimising industrial devices. This technique can be used as a straightforward solution for optimisation of geometry of HAT turbines. In this research, by adding a water storage tank for stabilising the driving energy and a PV panel for powering the booster pump, a new design of desalination system is introduced which can be powered by a HAT turbine. Subsequently, the geometry of the HAT turbine is optimised with combination of only 16 CFD simulations using the Taguchi method. The effects of blade size, number of blades, hub radius, and hub shape are studied and optimised. The Taguchi results reveal that the most important parameters influencing the power output of HAT turbine are the number of blades, size of blade, hub radius, and hub shape respectively. Moreover, the superposition model shows that the minimum signal-to-noise (S/N) ratio is 5% less than the amount achieved in the Taguchi approach. The power coefficient (C_p) of the optimised HAT turbine is 0.44 according to the results of CFD simulations, which is 10% higher than that of the baseline model (0.40) at tip speed ratio (*TSR*) of 5. The weight of the optimised model is less than the baseline model by 17%. The results of this study provide a comprehensive guidance for horizontal turbine optimisation process.

6.2 Introduction

The main objective of this chapter is to design and optimise the geometry of a HAT turbine for powering a desalination system. Review of the previous research shows that the influence of combinations of size of blade, number of blades, hub radius, and hub shape on the power output of HAT turbines has not been investigated. The goal of optimisation of these factors is to find a lighter, cheaper and smaller turbine which can be used in shallow water. For this purpose, the Taguchi method is used to optimise the turbine in order to identify a cost-effective geometry for use in a RO desalination system. By using the Taguchi method and only 16 CFD simulations, the effects of size of blades, number of blades, hub radius, and hub shape on power output of HAT turbine are studied. Finally, a new range of optimised variables is defined and evaluated. In addition, the dynamics of the fluid flow across the optimised and initial turbines is studied and compared.

6.3 Conceptual design of the HATRO desalination system

A schematic of the conceptual design of HATRO (Horizontal axis tidal turbine RO) desalination system using HAT turbine is illustrated in Figure 6.1. The main components of the design are similar to the HATRO desalination design (see section 4.5) and only HAT turbine is used in this design.

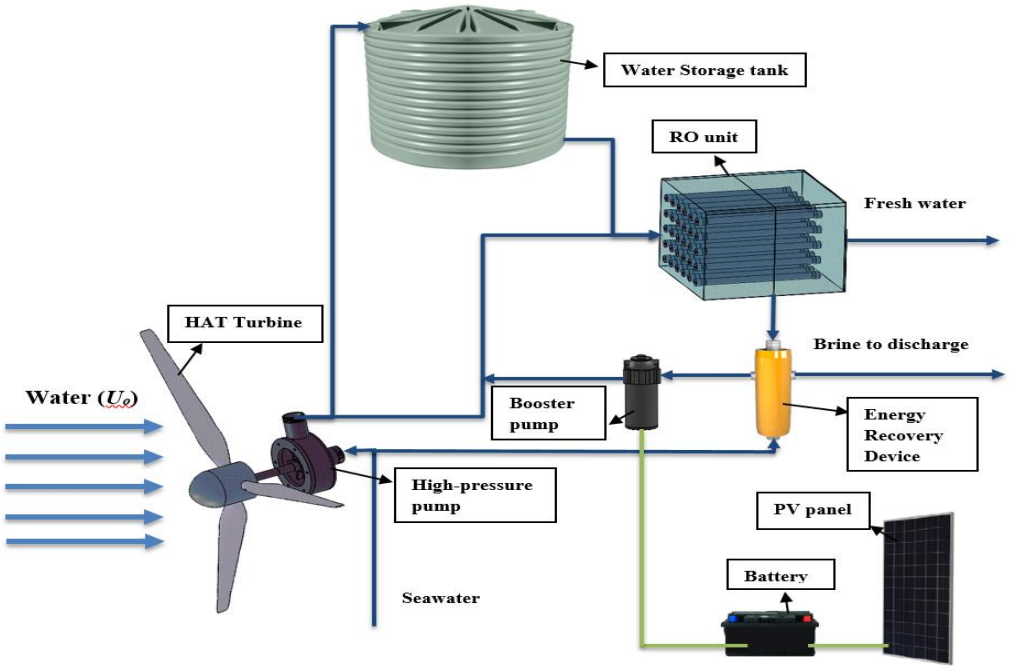

Figure 6.1 Schematic of the RO desalination system using a HAT turbine.

6.4 Preliminary design of the baseline HAT turbine

As mention in section 4.2.4., the turbine must provide 3440 W to power RO desalination system for producing 1 m^3/h freshwater. The real power output is described as the power coefficient (C_p) multiplied by nominal power output (P_n) (Eq. 5.1) (Meng et al., 2020). This nominal power output can be calculated by the turbine geometry as well as the flow characteristics based on the particular application (Li, 2014). According to the experimental work by Bahaj et al. (2007) the maximum amount of C_p of 0.3 is considered for the tidal turbine.

The nominal power of HAT turbine can be calculated as (De Lellis et al., 2018):

$$P_n = \frac{\rho \pi r^2 U^3}{2} \tag{6.1}$$

where r is the HAT turbine radius (distance between the centre of hub to the blade tip).

With the mentioned values for the power output and maximum power coefficient, and considering the inlet water velocity as 1 m/s, the initial parameters of the baseline HAT turbine are determined as summarised in Table 6.1.

Table 6.1 Initial parameters of HAT Turbine (b)

Parameter	Value
Total length of blade	1.2 m
Root length	0.24 m
Type of hydrofoil	NACA 0018
Hub radius	0.2 m
Number of blades	3

The related literature (Finnegan et al., 2020; Mehmood et al., 2012; Zhu et al., 2020) has been reviewed to design an efficient blade in order to achieve highest hydrodynamic performance. Accordingly, a model blade of 1.2 m is designed for the baseline turbine with SOLIDWORKS 2017, using the methodology outlined in (Kulkarni, 2016). The blade is designed by using NACA 0018 with different distances from the hub circle and different twist angles. According to previous publications, the distance from the hub circle to the root airfoil chord is selected as 0.24 m, which is 20 % of the total blade length and the twist angles for root and tip sections are varied from 18^{o} to 3^{o}. Details of the NACA 0018 stations and designed blade are illustrated in Table 6.2 and Figure 6.2. Using the values in Table 6.1 and the designed blade, the baseline HAT turbine is designed in the SOLIDWORKS software, the details of which are shown in Figure 6.3.

Table 6.2 Blade parameter

Section	Twist angle (º)	L (m)
Root	18	0.24
Station 1	14	0.36
Station 2	12	0.48
Station 3	10	0.60
Station 4	8	0.72
Station 5	7	0.84
Station 6	5	1.01
Station 7	4	1.12
Tip	3	1.20

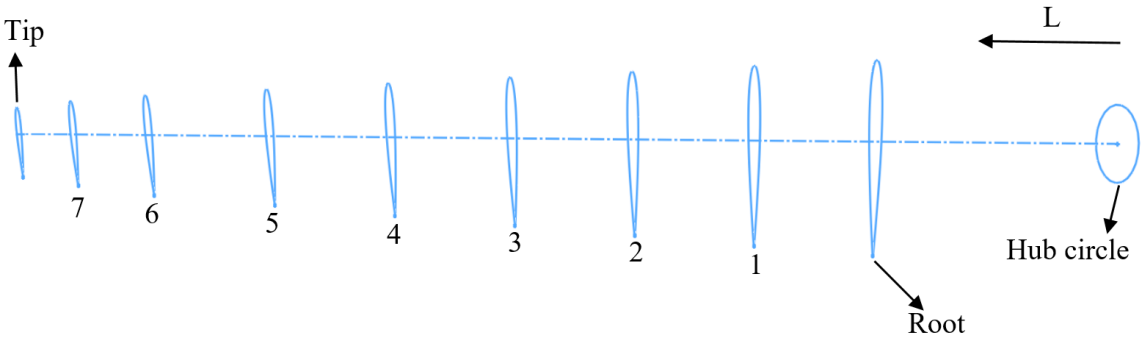

(a)

(b)

Figure 6.2 (a) Definition of the NACA 0018 stations and (b) designed blade.

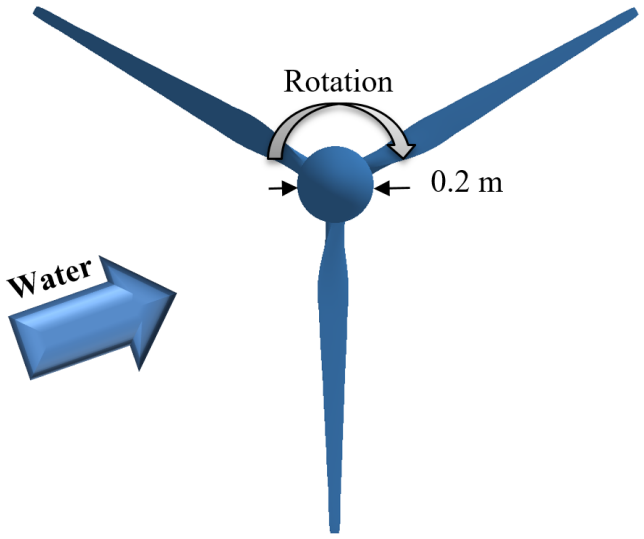

Figure 6.3 3D design of the baseline HAT turbine.

6.5 CFD simulation and validation of the baseline turbine

Figure 6.4 shows the details of the computational domain, mesh intensity around the turbine, and boundary conditions. An unstructured mesh is built around the turbine and a structured one over the entire computational domain by using the ICEM 2019 software. A three-dimensional transient model is built for CFD simulations of the HAT turbine using ANSYS Fluent. In addition, a sliding mesh method is used for simulating the movement of the fluid around the turbine. For the CFD simulations in ANSYS Fluent, the Shear Stress Transport (SST) k-ω turbulence method and the Pressure Implicit with Splitting of Operator (PISO) algorithm are implemented (Ghasemian & Nejat, 2015). A computer with 28-core Intel CPU E5-2680 v4 Processors, 256GB RAM is used to run the CFD simulation.

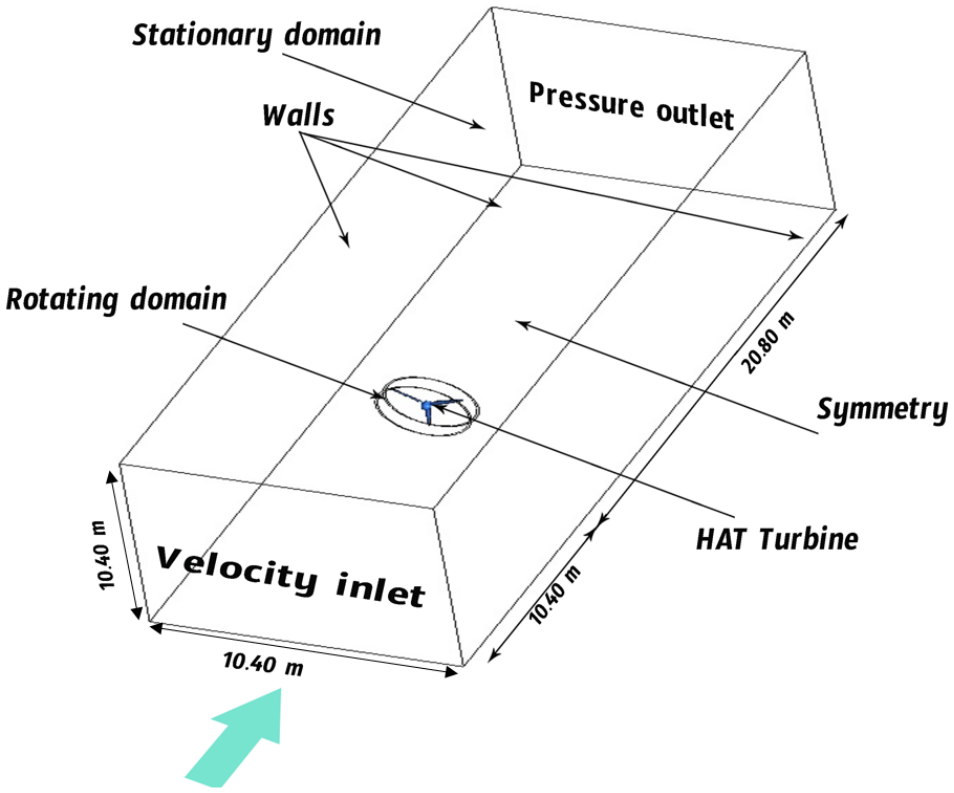

(a)

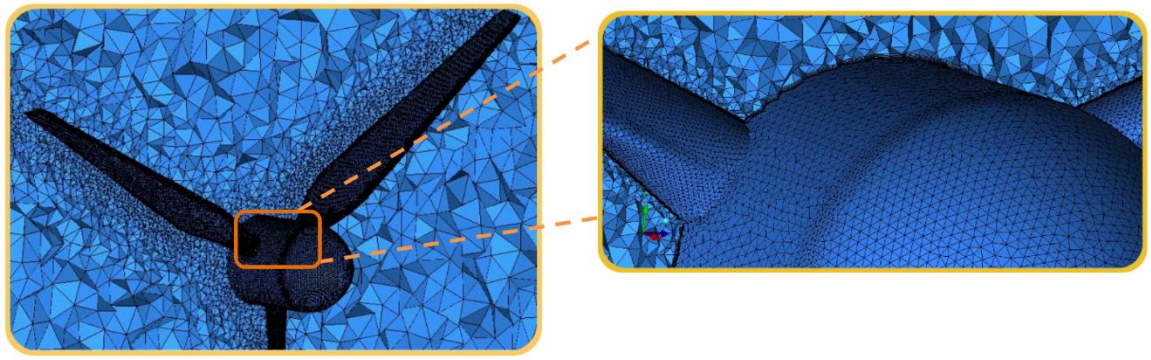

(b)

Figure 6.4 (a) Computational domain and boundary conditions and (b) mesh intensity over the turbine.

A grid sensitivity analysis is carried on by generating eight different meshes (from 598,771 cells to 6,981,342) for the baseline design using ICEM CFD software. Using Eq. 6.2 and the CFD simulation results, the moment coefficient (C_m) for is determined each case with varying amount of cells and the results are presented in Figure 6.5. The study revealed

that beyond 2,395,084 cells, the standard deviation of the moment coefficient is around 1.0%. As the computational time of the numerical analysis increases dramatically with the number of cells, 2,395,084 is selected for the rest of the CFD simulations.

$$C_m = \frac{T}{0.5\rho A_h U^3} \tag{6.2}$$

where C_m is the moment coefficient, T is the moment, and A_h is the area of the HAT turbine.

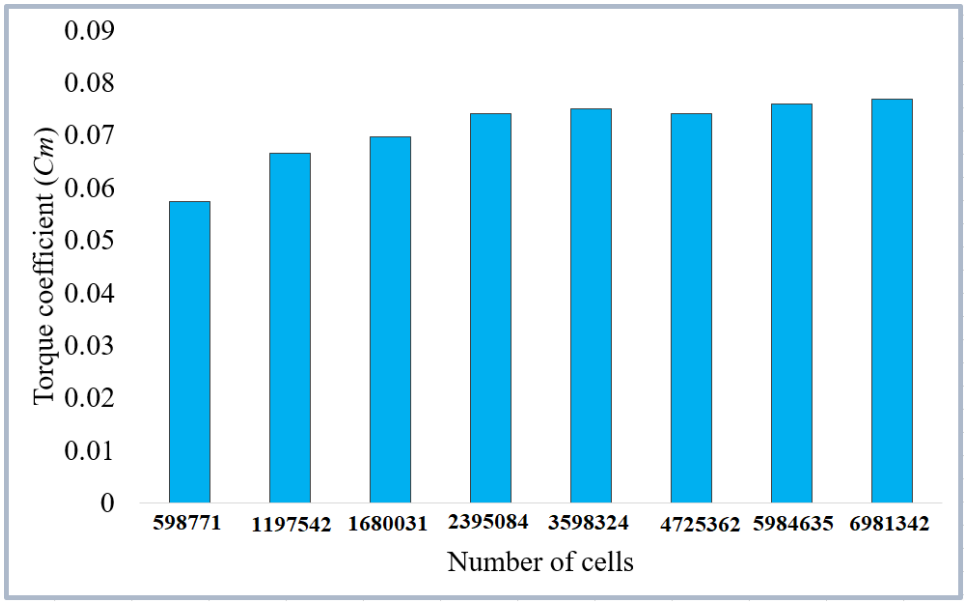

Figure 6.5 Moment coefficient (C_m) vs. number of cells for grid sensitivity analysis.

One of the common methods to validate CFD model for turbines simulation is assessing C_p against TSR. The power coefficient (C_p) of a HAT turbine can be determined as follows (Finnegan et al., 2020):

$$C_p = (TSR)C_m \tag{6.3}$$

Using Eqs. 6.2 & 6.3 and the CFD results, the values of power coefficient at various *TSR*s are determined and the results are shown in Figure 6.6. Also, the variations of C_p with *TSR* for an experimental work reported by Bahaj et al. (2007) and a CFD study by Kulkarni (Kulkarni, 2016) are provided in Figure 6.6 in order to validate the current CFD model. According to Figure 6.6, the results of the current CFD model are in good agreement with the experimental and CFD results of (Bahaj, Batten, & McCann, 2007; Kulkarni, 2016), both in terms of values and patterns.

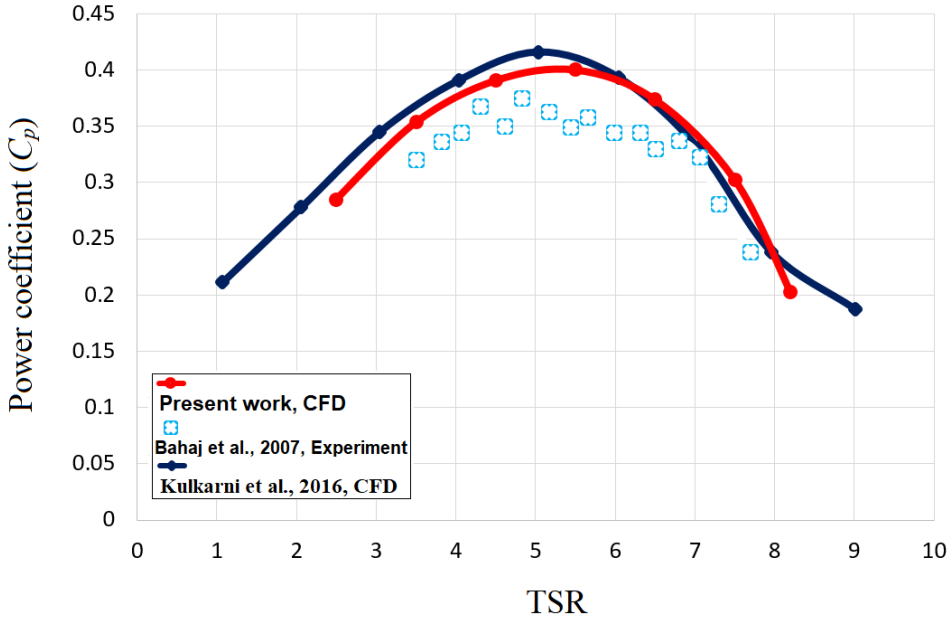

Figure 6.6 Variation of C_p with Tip speed ratio (*TSR*), used for model validation.

6.6 Taguchi method

The Taguchi method offers an affordable and effective way for minimal series of experiments to find optimal parameters of different systems (Chen et al., 2017). It uses a signal-to-noise (S/N) ratio to quantify the difference in responses. The identification of the optimum factors and levels can be divided into 7 stages (Bao et al., 2013).

Stage 1: Determination of an objective function

To determine the objective function, a quadratic loss (QL) function (Eq. 5.9) is used to calculate the divergence of a variable from its target quality (Pinar et al., 2009).

The QL function can estimate quality loss in a meaningful way (Wang et al., 2018) . In this study, power output is considered as the quality target for identifying the objective function. As mentioned in section 4.6, for calculating S/N ratio, there are three categories in the Taguchi method: Larger is the better, Nominal is the Best, and Smaller is the better (Mandal et al., 2011). Because the aim of this analysis is to minimise the QL function, in this chapter Smaller the better S/N ratio formula is used as follows:

According to the results presented in section 2.4, by replacing power output and target quality, the objective function can be redefined as:

$$S/N = 10\log(P-3440)^2 \tag{6.4}$$

Stage 2: Definition of factors and levels

The Taguchi approach is employed to analyse the impacts of different variables, so-called factors (or control factors), in order to optimise the main parameters of a system. The objective of this method is to estimate the optimal combination of control factors and their levels. In this work, four factors are considered to be optimised including size of blade (A), number of blades (B), hub radius (C), and hub shape (D). In addition, for each factor four levels are considered.

The solidity ratio, which is the most important factor affecting turbine performance (Dai & Lam, 2009; Maeda et al., 2016), is described as the ratio of the total turbine blade area over the swept area (Mohan Kumar et al., 2019). The solidity ratio for HAT turbine can be calculated as (Brusca et al., 2014; Rezaeiha et al., 2018):

$$\alpha = \frac{n_b A_h}{\pi r^2} \tag{6.5}$$

where α is the solidity ratio of HAT turbine, n_b is the number of HAT turbine blades, and A_h is the area of a blade.

According to Eq. 6.5, the solidity ratio varies greatly with the blade size and the number of blades. Thus, optimisation of this ratio is accomplished by changing these two factors. On the other hand, the type of hub can be changed based on the hub radius and shape of the hub.

In this work, four factors are considered to be optimised including size of blade (A), number of blades (B), hub radius (C), and hub shape (D). In addition, for each factor four levels are considered. Due to the submergence of the tidal turbines in water, the working conditions vary from the wind power region; HAT turbines face higher moment and pressure than horizontal axis wind (HAW) turbines. Therefore, tidal turbines must have smaller blades to avoid vibration and deformation which unfavourably affect the turbine efficiency (Park et al., 2016). Accordingly, four sizes of blade including 0.7b, 0.8b, 0.9b, and 1.0b (b is the size of blade according to Tables 5.1 and 5.2) for HAT turbine are chosen as four levels of factor A. The levels of number of blades (B) are selected as 3, 4, 5, and 6.

For the hub radius (C) (the third factor), 0.125, 0.175, 0.150, and 0.200 m are chosen as the levels. In addition, for factor the hub shape (D) four different levels (I, II, III, and IV) with four parabola equations are considered in order to test and find the optimum configuration. The selected shapes of hub and their corresponding parabolic equations

are showed in Figure 6.7. The hub shapes vary from a conical shape with equation of y=x^0.8 to a hemisphere with equation of y=x^0.2.

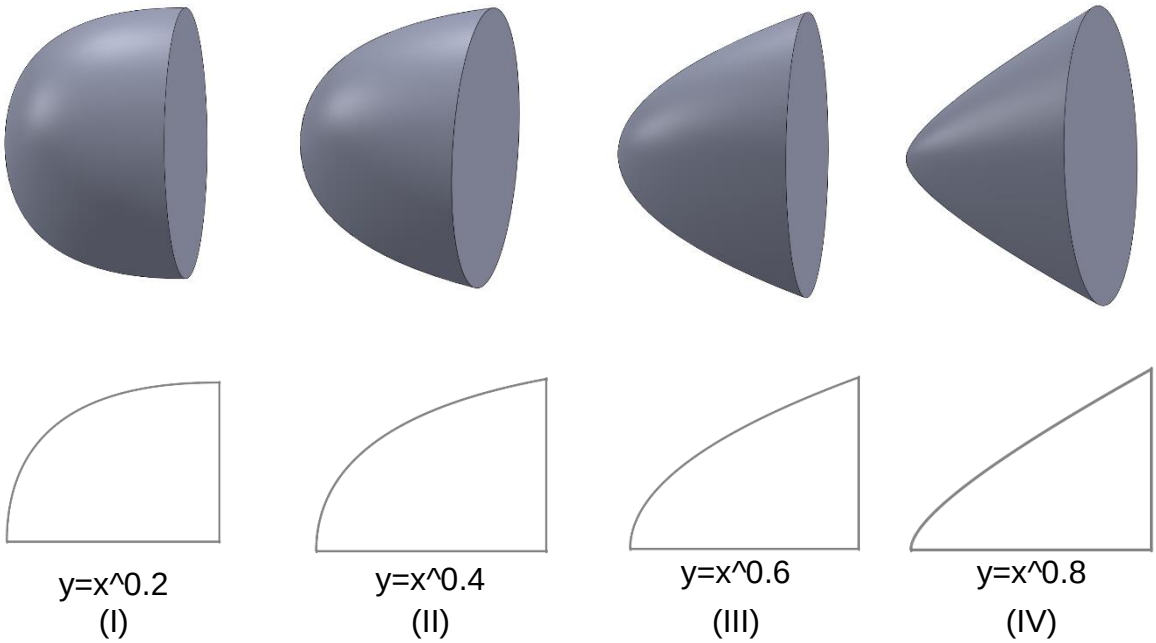

Figure 6.7 Four different hub shapes.

All the factors and levels are summarised in Table 6.3.

Table 6.3 Specified factors and levels

	Coded levels			
	1	2	3	4
A: Size of blade	0.7b	0.8b	0.9b	1.0b
B: Number of blades	3	4	5	6
C: Hub radius (m)	0.125	0.175	0.150	0.200
D: Hub shape	I	II	III	IV

Stage 3: Orthogonal Array

The data of the constructed experiment can be examined using both the Taguchi and analysis of variance (ANOVA) methods (Sohrabi et al., 2017). According to the previous stage, the OA should be adapted for the four factors at the four-level experiment design. For all identified factors and their levels, the feasible orthogonal array is L16 (4^4) which is built as seen in Table 6.4. According to Table 6.4, instead of 256 possible cases (4*4*4*4=256), 16 CFD simulations are evaluated to minimise the geometry of the designed HAT turbine with the four factors, including blade size, number of blades, hub radius, and hub shape, each in four levels.

Table 6.4 Selected $L_{16}(4^4)$ OA of the set factors and levels

No.	A	B	C	D
Test 1	1	1	1	1
Test 2	1	2	2	2
Test 3	1	3	3	3
Test 4	1	4	4	4
Test 5	2	1	2	3
Test 6	2	2	1	4
Test 7	2	3	4	1
Test 8	2	4	3	2
Test 9	3	1	3	4
Test 10	3	2	4	3
Test 11	3	3	1	2
Test 12	3	4	2	1
Test 13	4	1	4	2
Test 14	4	2	3	1
Test 15	4	3	2	4
Test 16	4	4	1	3

Stage 4: Computational Fluid Dynamics (CFD) analysis

16 different cases which have been modelled with SOLIDWORKS software, in accordance with the specifications described in Table 6.4 and the designed orthogonal array (Table 6.5) (please see appendix B). As described in stage 1 of the Taguchi approach, in this work, power output (P) is used as the objective function (OF). The power output of each case can be measured by moment coefficients (C_m) using Eq. 6.6. Accordingly, all the moment coefficients at different azimuth angles and *TSR*=5 are determined from the CFD simulations and the results of baseline and case 8 are presented in Figure 6.8 (for all cases please see Appendix C).

The power output (P) of each case is calculated using Eq. 4.3 and the results are presented in Table 6.5. From the results, it can be seen that the number of blades has a major effect on the performance of the turbine and it is directly related to the increase of power output. For example, two of the highest values of power output (4002 and 3600 W corresponding to deigns 4 and 16 respectively) are related to turbines with 6 blades and the two lowest power outputs (2809 and 2907 W corresponding to deigns 9 and 13 respectively) are related to 3-blade turbine. Increasing the number of blades provides greater moment; however, the maximum power output of a turbine must have a finite number of blades (Okulov & Sorensen, 2008). According to Armstrong et al. (2012) the solidity ratio should not exceed 0.5 as the proximity of the blades degrades the turbine output. Accordingly, because the amount of solidity cannot be more than this upper limit, the number of blades which is the main factor of solidity ratio is also limited. Considering this upper limit, in this study 3, 4, 5 and 6 blades were considered.

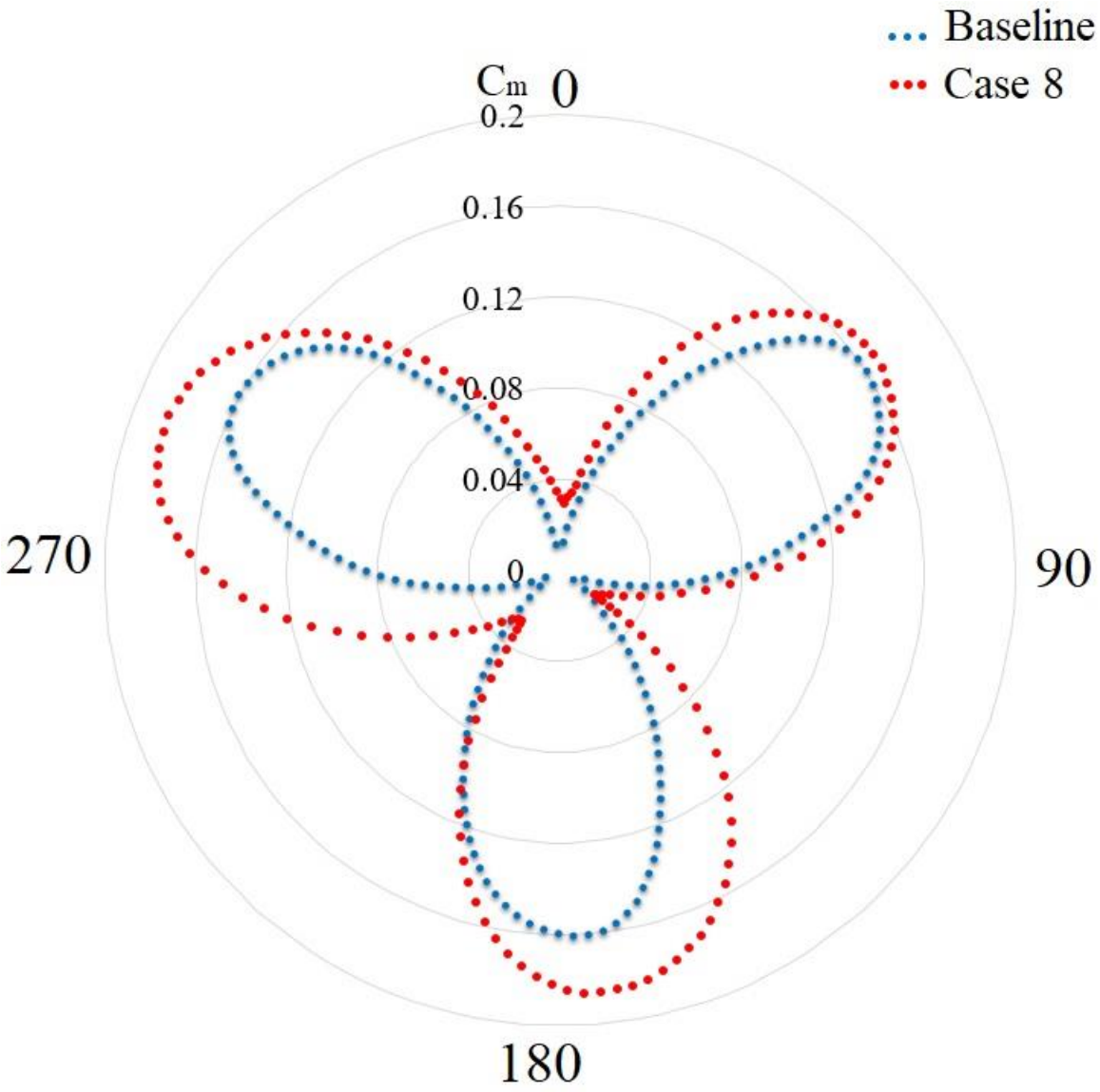

Figure 6.8 Changes in moment coefficient (C_m) of all cases for one revolution (0-360^o) at *TSR*=5.

Figure 6.8 demonstrates the variations of instantaneous torque coefficient (C_m) in one revolution at TSR=5 for 16 HAT turbine cases as well as the baseline turbine after the steady state condition is attained. The maximum and minimum average torque coefficients (C_m) correspond to cases 4 and 9, which are 0.125 and 0.08 respectively. The value of C_m (0.125) obtained for case 4 is 25% higher than that of the baseline case, which is 0.10.

Stage 5: Identification of the optimum factors and their levels

Eq. 5.7 is used to calculate the S/N ratio of 16 different designs, according to the data shown in Table 6.3, and the results are set out in Table 6.4. According to Eq. 5.7, the smallest value of S/N ratio occurs when there is the smallest difference between the power output and the target quality. From Table 6.5, it can be seen that the lowest S/N ratio (32) corresponds to design 6, which has the smallest difference between the power output (3476 W) and the target quality (3440 W). The Taguchi method is utilised in the next step to evaluate the order of effect and the optimum combination of the factors to be achieved in the optimised model. For the all factors and their levels, the mean S/N ratio is calculated and plotted in Figure 6.9. For example, the mean S/N ratio of A1 is computed from the mean values of four level 1 factor A [(53+ 43.5+ 39.7+55)/4=47.8]. The results show that power output of the combination A2, B3, C2, and D3 can provide the target quality with smallest geometry. An indicator (β) is determined to identify the order of influence of all four factors, which is the distance between each factor's top and bottom mean S/N ratios in Figure 6.9. For variables A, B, C, and D, the values of this indicator are 11.32, 12.2, 6.1 and 5.72 respectively. This clearly indicates that factor B, which is the number of blades, is the main factor amongst all evaluated factors, influencing the turbine's power output. On the other hand, factors C (hub radius) and D (hub shape) have the smallest effect on hydrodynamic performance of the HAT turbine.

Table 6.5 L_{16} OA

No.	Size of blade (A)	Number of blades (B)	Hub radius (C)	Hub shape (D)	P (W)	S/N ratio
Baseline	b	3	0.200	III	3417	N/A
Test 1	0.7b	3	0.125	I	2993	53
Test 2	0.7b	4	0.150	II	3589	43.5
Test 3	0.7b	5	0.175	III	3536	39.7
Test 4	0.7b	6	0.200	IV	4002	55
Test 5	0.8b	3	0.150	III	3537	39.8
Test 6	0.8b	4	0.125	IV	3479	32
Test 7	0.8b	5	0.200	I	3338	40.1
Test 8	0.8b	6	0.175	II	3490	34
Test 9	0.9b	3	0.175	IV	2809	56
Test 10	0.9b	4	0.200	III	3298	43
Test 11	0.9b	5	0.125	II	3349	39.1
Test 12	0.9b	6	0.150	I	3589	43.5
Test 13	1.0b	3	0.200	II	2907	54.5
Test 14	1.0b	4	0.175	I	2998	52.9
Test 15	1.0b	5	0.150	IV	3500	35.6
Test 16	1.0b	6	0.125	III	3600	44.1

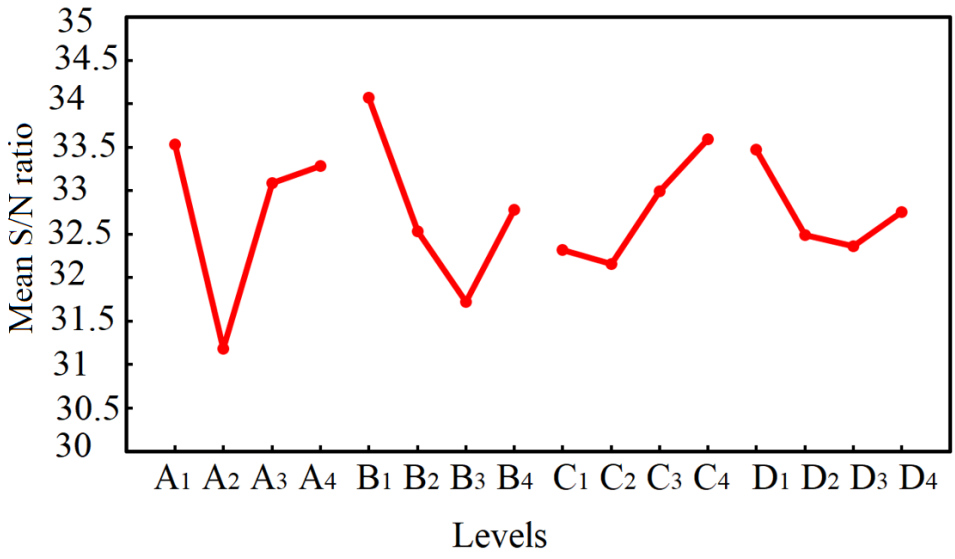

Figure 6.9 Graph of mean S/N ratio (smaller is the better).

Stage 6: Analysis of Variance (ANOVA)

In this stage, the interaction of all factors and with their levels is analysed by using ANOVA. The objective of ANOVA analysis is to evaluate the interaction between factors, with respect to the overall variation of all variables. There are different classical approaches for ANOVA analysis for unbalanced data. In this chapter, two-way interaction is used. In general, the difference between two-way, three-way, and four-way interaction is negligible and most of the relevant literature have used two-way interaction (Banerjee et al., 2019; Kechagias et al., 2020; Ogunbiyi et al., 2020). The relationship plot of ANOVA can be used to display the interaction between the factors in different levels (Ott & Longnecker, 2015; Ranganath & Vipin, 2013). According to the obtained interaction plots, two different potential options (a: parallel and b: non-parallel) can be considered (Figure 6.10). In parallel patterns, a certain interaction will not happen and can be ignored, whilst the interaction in non-parallel trends is important and should be considered. By using the S/N ratios listed in Table 6.5, the relationship between each of two variables is measured and presented in Figure 6.11 (Wang et al., 2018). By assessing the obtained graphs, it

can be seen that there is an interaction between all two factors due to non-parallel lines. Between the assessed variables, the relationship between factor B (number of blades) and other factors is very strong. This is also highlighted in the results of Taguchi method, where factor B has the greatest effect on power output of the HAT turbine (stage 5).

In the interpretation of ANOVA interaction plots, when interaction exists amongst the factors, the lines will be non-parallel (Alikhani, Ebadi, Karami, Shahanipour, & Razzaghi-Asl, 2020). By assessing the obtained ANOVA interaction plots (Figure 6.11), it can be seen that there is an interaction between each pair of factors due to non-parallel lines. Between the assessed variables, the interaction between number of blades (factor B) and other factors is very strong due to the number of non-parallel lines in comparison to other interactions. This is also highlighted in the results of the Taguchi method, where factor B has the greatest effect on the power output of the HAT turbine (stage 5).

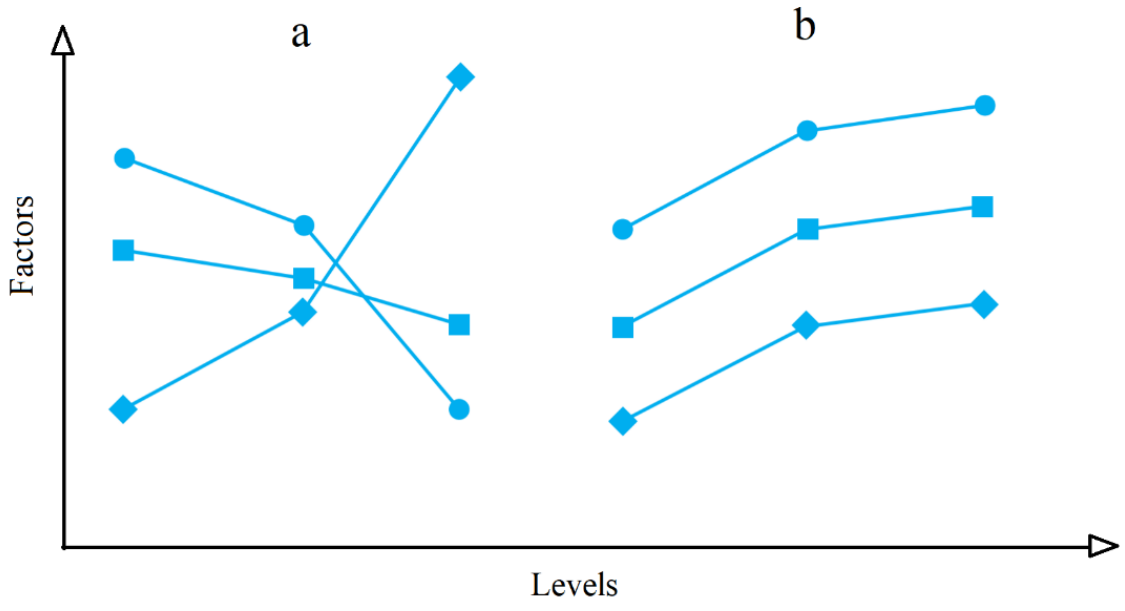

Figure 6.10 (a) Interaction and (b) no interaction plot (Ott & Longnecker, 2015).

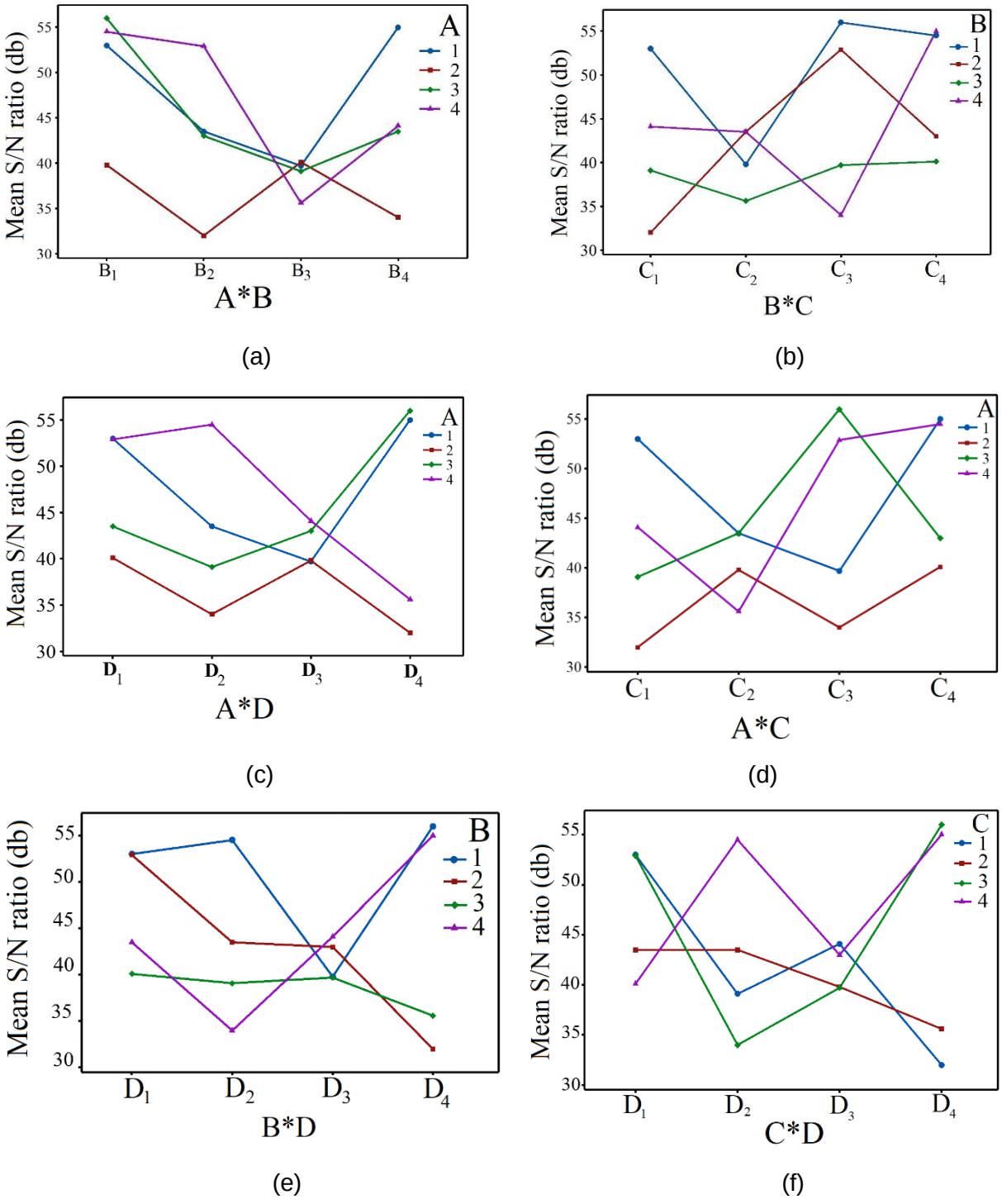

Figure 6.11 Interaction graph with analysis of variance.

Stage 7: Superposition model

As outlined in the stage 7 of section 4.6, the superposition model is used to predict the S/N ratios of all possible responses. The results are shown in Table 6.6. The Taguchi method was used on 16 cases with different combinations of 4 factors and 4 levels for each factor. The minimum S/N ratio was calculated as 32 for case 6, which corresponds to combination A2 (Size of blade: 0.8b), B2 (Number of blades: 4), C1 (Hub radius: 0.125), and D4 (Hub shape: IV). With 4 factors and 4 levels for each factor, the number of possible combinations was 256 (4*4*4*4= 256). Eq. 5.4 (superposition model - which was cross validated in Chapter 5) was used to obtain the S/N ratios of all possible combinations of factors and levels (Table 6.6). The results of the superposition model show that the S/N ratio of the same combination (case 6 of the Taguchi model: Size of blade: 0.8b; Number of blades: 4; Hub radius: 0.125; and Hub shape: IV) was 33.38 (Table 5.6; case 84) which shows 5% difference. It can also be seen from this table that the lowest S/N ratio is for case 103 and its value is 25.01. This value is for combination of factors A2 (0.8b), B3 (5), C2 (0.175), and D3 (III). Therefore, combination of factors A2, B3, C2, and D3 that is provided by the superposition model, is used to build a HAT turbine as the final optimised model and it is simulated using the CFD method described in section 4.

Table 6.6 Prediction of signal-to-noise (S/N) ratio of all achievable combinations

No.	A	B	C	D	S/N	NO.	A	B	C	D	S/N	No.	A	B	C	D	S/N	No.	A	B	C	D	S/N
1	1	1	1	1	55.71	65	2	1	1	1	44.38	129	3	1	1	1	53.31	193	4	1	1	1	54.68
2	1	1	1	2	51.11	66	2	1	1	2	39.78	130	3	1	1	2	48.71	194	4	1	1	2	50.08
3	1	1	1	3	49.98	67	2	1	1	3	38.66	131	3	1	1	3	47.58	195	4	1	1	3	48.96
4	1	1	1	4	52.98	68	2	1	1	4	41.66	132	3	1	1	4	50.58	196	4	1	1	4	51.96
5	1	1	2	1	54.26	69	2	1	2	1	42.93	133	3	1	2	1	51.86	197	4	1	2	1	53.23
6	1	1	2	2	49.66	70	2	1	2	2	38.33	134	3	1	2	2	47.26	198	4	1	2	2	48.63
7	1	1	2	3	48.53	71	2	1	2	3	37.21	135	3	1	2	3	46.13	199	4	1	2	3	47.51
8	1	1	2	4	51.53	72	2	1	2	4	40.21	136	3	1	2	4	49.13	200	4	1	2	4	50.51
9	1	1	3	1	59.31	73	2	1	3	1	47.98	137	3	1	3	1	56.91	201	4	1	3	1	58.28
10	1	1	3	2	54.71	74	2	1	3	2	43.38	138	3	1	3	2	52.31	202	4	1	3	2	53.68
11	1	1	3	3	53.58	75	2	1	3	3	42.26	139	3	1	3	3	51.18	203	4	1	3	3	52.56
12	1	1	3	4	56.58	76	2	1	3	4	45.26	140	3	1	3	4	54.18	204	4	1	3	4	55.56
13	1	1	4	1	61.81	77	2	1	4	1	50.48	141	3	1	4	1	59.41	205	4	1	4	1	60.78
14	1	1	4	2	57.21	78	2	1	4	2	45.88	142	3	1	4	2	54.81	206	4	1	4	2	56.18
15	1	1	4	3	56.08	79	2	1	4	3	44.76	143	3	1	4	3	53.68	207	4	1	4	3	55.06
16	1	1	4	4	59.08	80	2	1	4	4	47.76	144	3	1	4	4	56.68	208	4	1	4	4	58.06
17	1	2	1	1	47.73	81	2	2	1	1	36.41	145	3	2	1	1	45.33	209	4	2	1	1	46.71
18	1	2	1	2	43.13	82	2	2	1	2	31.81	146	3	2	1	2	40.73	210	4	2	1	2	42.11
19	1	2	1	3	42.01	83	2	2	1	3	30.68	147	3	2	1	3	39.61	211	4	2	1	3	40.98
20	1	2	1	4	45.01	84	2	2	1	4	33.68	148	3	2	1	4	42.61	212	4	2	1	4	43.98
21	1	2	2	1	46.28	85	2	2	2	1	34.96	149	3	2	2	1	43.88	213	4	2	2	1	45.26
22	1	2	2	2	41.68	86	2	2	2	2	30.36	150	3	2	2	2	39.28	214	4	2	2	2	40.66
23	1	2	2	3	40.56	87	2	2	2	3	29.23	151	3	2	2	3	38.16	215	4	2	2	3	39.53
24	1	2	2	4	43.56	88	2	2	2	4	32.23	152	3	2	2	4	41.16	216	4	2	2	4	42.53
25	1	2	3	1	51.33	89	2	2	3	1	40.01	153	3	2	3	1	48.93	217	4	2	3	1	50.31
26	1	2	3	2	46.73	90	2	2	3	2	35.41	154	3	2	3	2	44.33	218	4	2	3	2	45.71
27	1	2	3	3	45.61	91	2	2	3	3	34.28	155	3	2	3	3	43.21	219	4	2	3	3	44.58
28	1	2	3	4	48.61	92	2	2	3	4	37.28	156	3	2	3	4	46.21	220	4	2	3	4	47.58
29	1	2	4	1	53.83	93	2	2	4	1	42.51	157	3	2	4	1	51.43	221	4	2	4	1	52.81
30	1	2	4	2	49.23	94	2	2	4	2	37.91	158	3	2	4	2	46.83	222	4	2	4	2	48.21
31	1	2	4	3	48.11	95	2	2	4	3	36.78	159	3	2	4	3	45.71	223	4	2	4	3	47.08
32	1	2	4	4	51.11	96	2	2	4	4	39.78	160	3	2	4	4	48.71	224	4	2	4	4	50.08
33	1	3	1	1	43.51	97	2	3	1	1	32.18	161	3	3	1	1	41.11	225	4	3	1	1	42.48
34	1	3	1	2	38.91	98	2	3	1	2	27.58	162	3	3	1	2	36.51	226	4	3	1	2	37.88
35	1	3	1	3	37.78	99	2	3	1	3	26.46	163	3	3	1	3	35.38	227	4	3	1	3	36.76
36	1	3	1	4	40.78	100	2	3	1	4	29.46	164	3	3	1	4	38.38	228	4	3	1	4	39.76
37	1	3	2	1	42.06	101	2	3	2	1	30.73	165	3	3	2	1	39.66	229	4	3	2	1	41.03
38	1	3	2	2	37.46	102	2	3	2	2	26.13	166	3	3	2	2	35.06	230	4	3	2	2	36.43
39	1	3	2	3	36.33	103	2	3	2	3	25.01	167	3	3	2	3	33.93	231	4	3	2	3	35.31
40	1	3	2	4	39.33	104	2	3	2	4	28.01	168	3	3	2	4	36.93	232	4	3	2	4	38.31
41	1	3	3	1	47.11	105	2	3	3	1	35.78	169	3	3	3	1	44.71	233	4	3	3	1	46.08
42	1	3	3	2	42.51	106	2	3	3	2	31.18	170	3	3	3	2	40.11	234	4	3	3	2	41.48
43	1	3	3	3	41.38	107	2	3	3	3	30.06	171	3	3	3	3	38.98	235	4	3	3	3	40.36
44	1	3	3	4	44.38	108	2	3	3	4	33.06	172	3	3	3	4	41.98	236	4	3	3	4	43.36
45	1	3	4	1	49.61	109	2	3	4	1	38.28	173	3	3	4	1	47.21	237	4	3	4	1	48.58
46	1	3	4	2	45.01	110	2	3	4	2	33.68	174	3	3	4	2	42.61	238	4	3	4	2	43.98
47	1	3	4	3	43.88	111	2	3	4	3	32.56	175	3	3	4	3	41.48	239	4	3	4	3	42.86
48	1	3	4	4	46.88	112	2	3	4	4	35.56	176	3	3	4	4	44.48	240	4	3	4	4	45.86
49	1	4	1	1	49.03	113	2	4	1	1	37.71	177	3	4	1	1	46.63	241	4	4	1	1	48.01
50	1	4	1	2	44.43	114	2	4	1	2	33.11	178	3	4	1	2	42.03	242	4	4	1	2	43.41
51	1	4	1	3	43.31	115	2	4	1	3	31.98	179	3	4	1	3	40.91	243	4	4	1	3	42.28
52	1	4	1	4	46.31	116	2	4	1	4	34.98	180	3	4	1	4	43.91	244	4	4	1	4	45.28
53	1	4	2	1	47.58	117	2	4	2	1	36.26	181	3	4	2	1	45.18	245	4	4	2	1	46.56
54	1	4	2	2	42.98	118	2	4	2	2	31.66	182	3	4	2	2	40.58	246	4	4	2	2	41.96
55	1	4	2	3	41.86	119	2	4	2	3	30.53	183	3	4	2	3	39.46	247	4	4	2	3	40.83
56	1	4	2	4	44.86	120	2	4	2	4	33.53	184	3	4	2	4	42.46	248	4	4	2	4	43.83
57	1	4	3	1	52.63	121	2	4	3	1	41.31	185	3	4	3	1	50.23	249	4	4	3	1	51.61
58	1	4	3	2	48.03	122	2	4	3	2	36.71	186	3	4	3	2	45.63	250	4	4	3	2	47.01
59	1	4	3	3	46.91	123	2	4	3	3	35.58	187	3	4	3	3	44.51	251	4	4	3	3	45.88
60	1	4	3	4	49.91	124	2	4	3	4	38.58	188	3	4	3	4	47.51	252	4	4	3	4	48.88
61	1	4	4	1	55.13	125	2	4	4	1	43.81	189	3	4	4	1	52.73	253	4	4	4	1	54.11
62	1	4	4	2	50.53	126	2	4	4	2	39.21	190	3	4	4	2	48.13	254	4	4	4	2	49.51
63	1	4	4	3	49.41	127	2	4	4	3	38.08	191	3	4	4	3	47.01	255	4	4	4	3	48.38
64	1	4	4	4	52.41	128	2	4	4	4	41.08	192	3	4	4	4	50.01	256	4	4	4	4	51.38

6.7 Fluid dynamics study

With the obtained combinations from the superposition model and Table 6.4, the optimised turbine is designed in SOLIDWORKS 2017. The initial design with SOLIDWORKS shows that the weight of optimised design is 17% less than the baseline design; hence it requires less material and it can be manufactured cheaper. A comprehensive CFD simulation of the baseline and the optimised designs is carried out using ANSYS Fluent 2019 (as described in section 2) and the results are presented in this section. Using Eq. 5.10 and the CFD results, the power output of the optimised turbine is calculated to be 3830 W, which is suitable for the mentioned desalination system to produce 1 m^3/h freshwater (see section 2.4).

Figure 6.12 shows a comparison of the variations of power coefficient (C_p) with *TSR* for the baseline and optimised HAT turbines. When comparing the performance of the presented HAT turbines at various tip speed ratios (*TSR*s), the change of the blade size and number of blades helps to increase the power coefficient (C_p), however, after a particular *TSR*, the power output of the turbines decreases due to the increased turbulence. According to the obtained results, C_p of the optimised model is 0.44, while for baseline design it is 0.40 at *TSR*=5 (i.e., it is 10% more for the optimised model). Moreover, the optimised 5-bladed HAT turbine performs better at lower *TSR* (3-5.5) and the baseline 3-bladed HAT turbine works better at higher *TSR* (5.5-6.5) in both designs. To further investigate this, it is necessary to simulate both turbines at different *TSR*s.

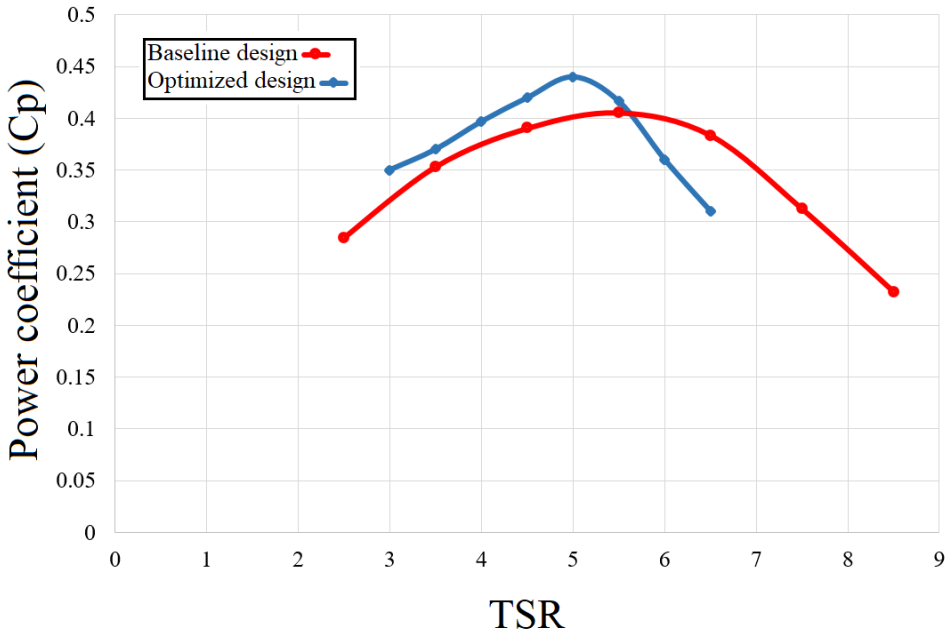

Figure 6.12 Variation of power coefficient (C_p) with tip speed ratio (TSR) of baseline and optimised designs.

Figure 6.13 shows the streamline contours across the revolving turbine in four different tip speed ratios (*TSR*s). These contour plots explicitly illustrate that the velocity deficiency is dependent on the *TSR*s which are provided by different inlet velocities. The water rotates the HAT turbine and the passing stream rotates in an inverse direction of the turbine. While water moves through the turbine, the turbine absorbs the energy of the water and that is why there is a difference in the velocity of upstream and downstream. The higher the inlet velocity, the greater is the difference in velocity. In both turbines, the flow runs normally at low *TSR*s and from upstream and downstream. In the baseline turbine, according to Figure 6.13, there is a heavy turbulence in the streamline distributions when the *TSR* changes from 5.5 to 6.0. However, in the optimised turbine this occurs after *TSR*=5.0 and the streamlines of downstream face a huge turbulence. These results provide further evidence for the findings in Figure 6.13, which show the optimised turbine has better performance at lower *TSR*s.

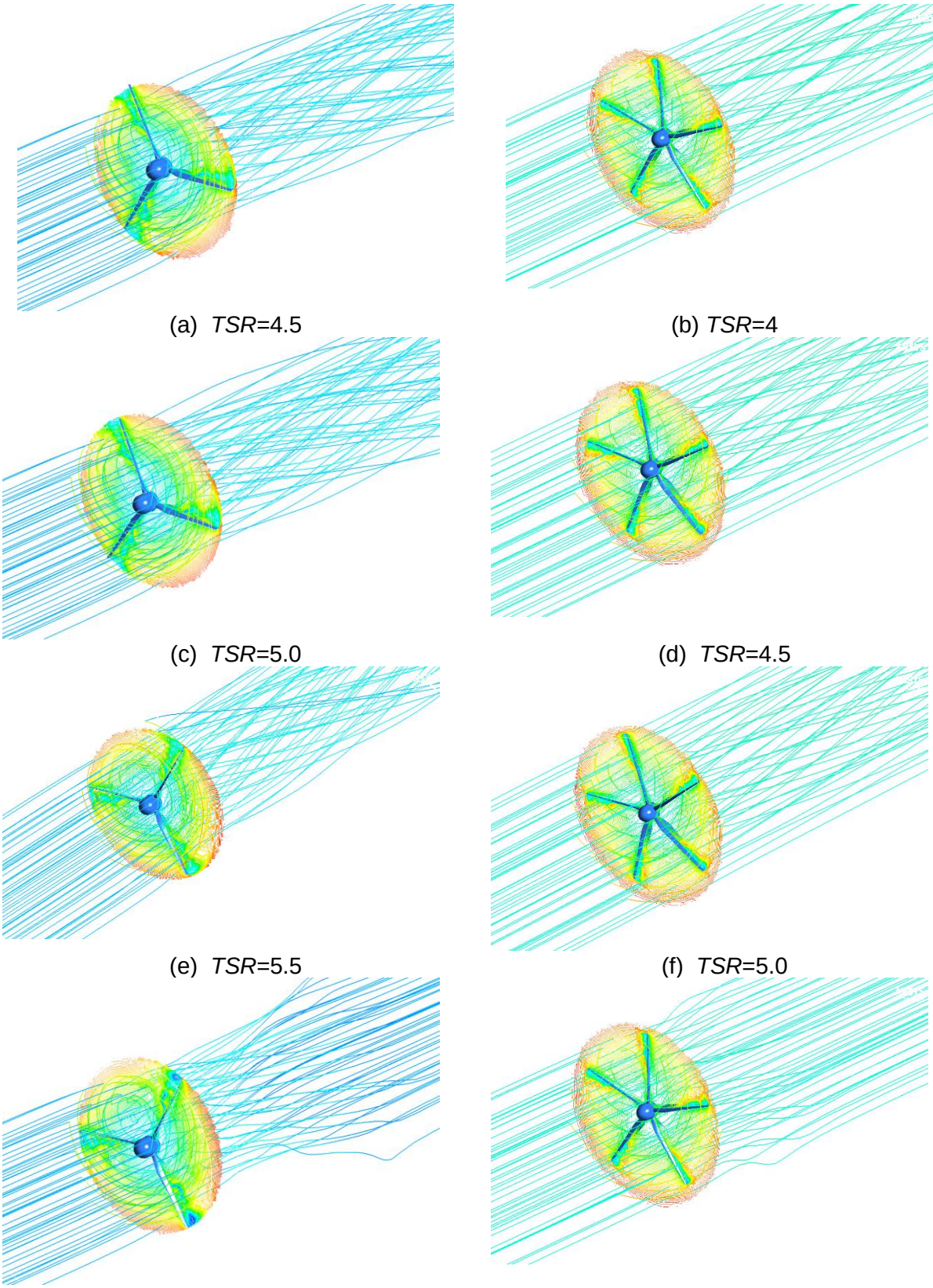

(a) *TSR*=4.5 (b) *TSR*=4

(c) *TSR*=5.0 (d) *TSR*=4.5

(e) *TSR*=5.5 (f) *TSR*=5.0

(g) *TSR*=6.0 (h) *TSR*=5.5

Figure 6.13 Streamline distributions in 4 different tip speed ratios (*TSR*).

The vorticity contours of the CFD simulations of both turbines through a cross section (YZ plane) at azimuth angles of 40°, 80°, and 120° are presented in Figure 6.14. For these contours to be comparable, one of the turbine blades is marked with letter Q (indicator blade) and the value of azimuth angle is defined according to this indicator blade. The results show that the baseline turbine (three-bladed turbine) experiences greater vortex and wake in comparison with the optimised turbine (five-bladed turbine), which results in better performance. The vorticity is indeed greater on the top of the blades due to rotational impact of the turbine blades, and the velocity gradient is much wider. The lower magnitude of vorticity at the bottom of the blades can be attributed to the separation of the flow on the blade surface, and it is very visible at the proximity of turbine hub. The energy contribution of both HAT turbine's blades near the hub is also less than the section near the tip portion. Since CFD simulation in ANSYS Fluent considers the solid parts as rigid body and it does not consider the deformation and vibration, in reality, this increase in the vortex at the end of the turbine blades causes an increase in vibration as well as deformation, which reduces the lifetime and the efficiency of the turbine. This is another reason that confirms the superiority of the optimised turbine, which has smaller blades (20% smaller) than the baseline turbine.

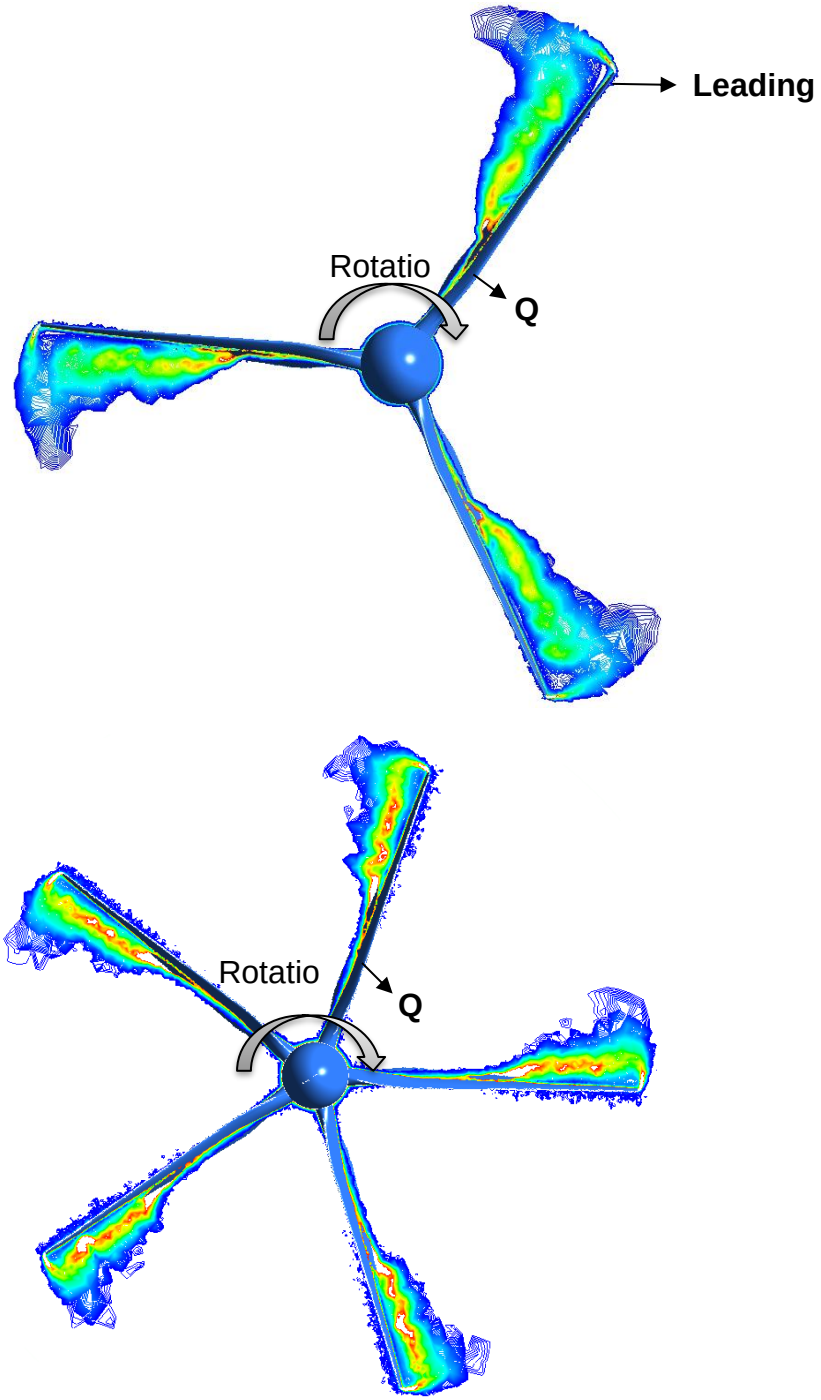

Azimuth angle: 40º

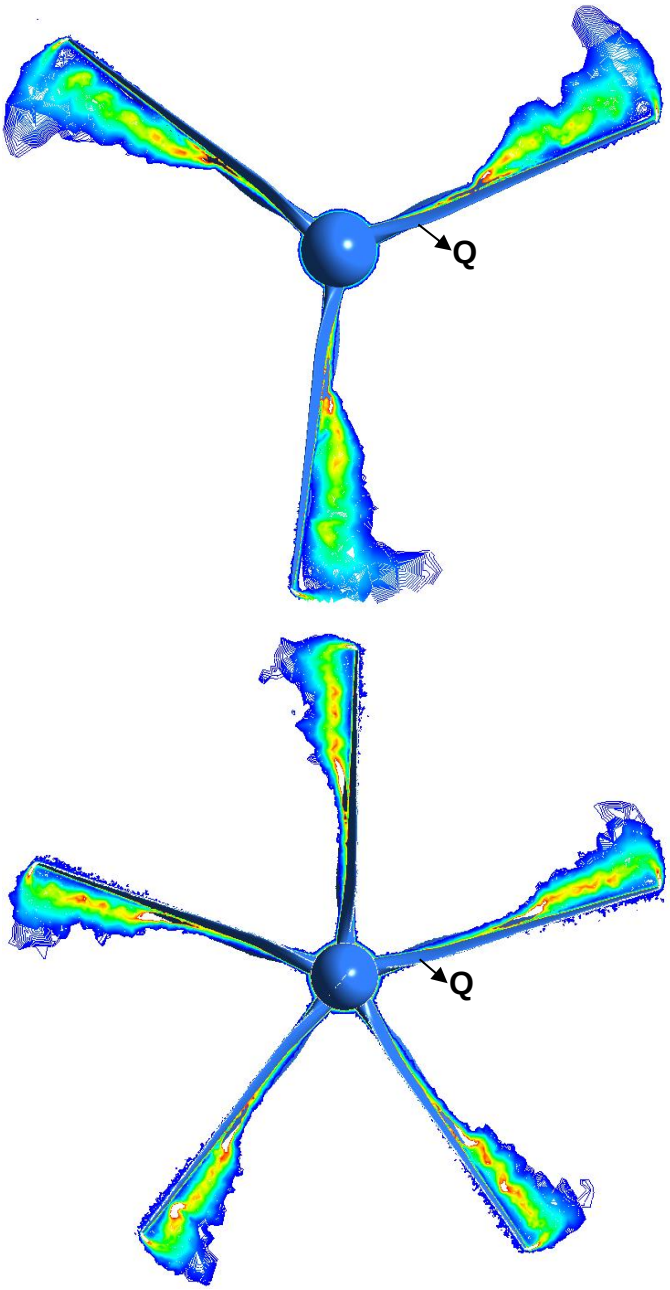

Azimuth angle: 80º

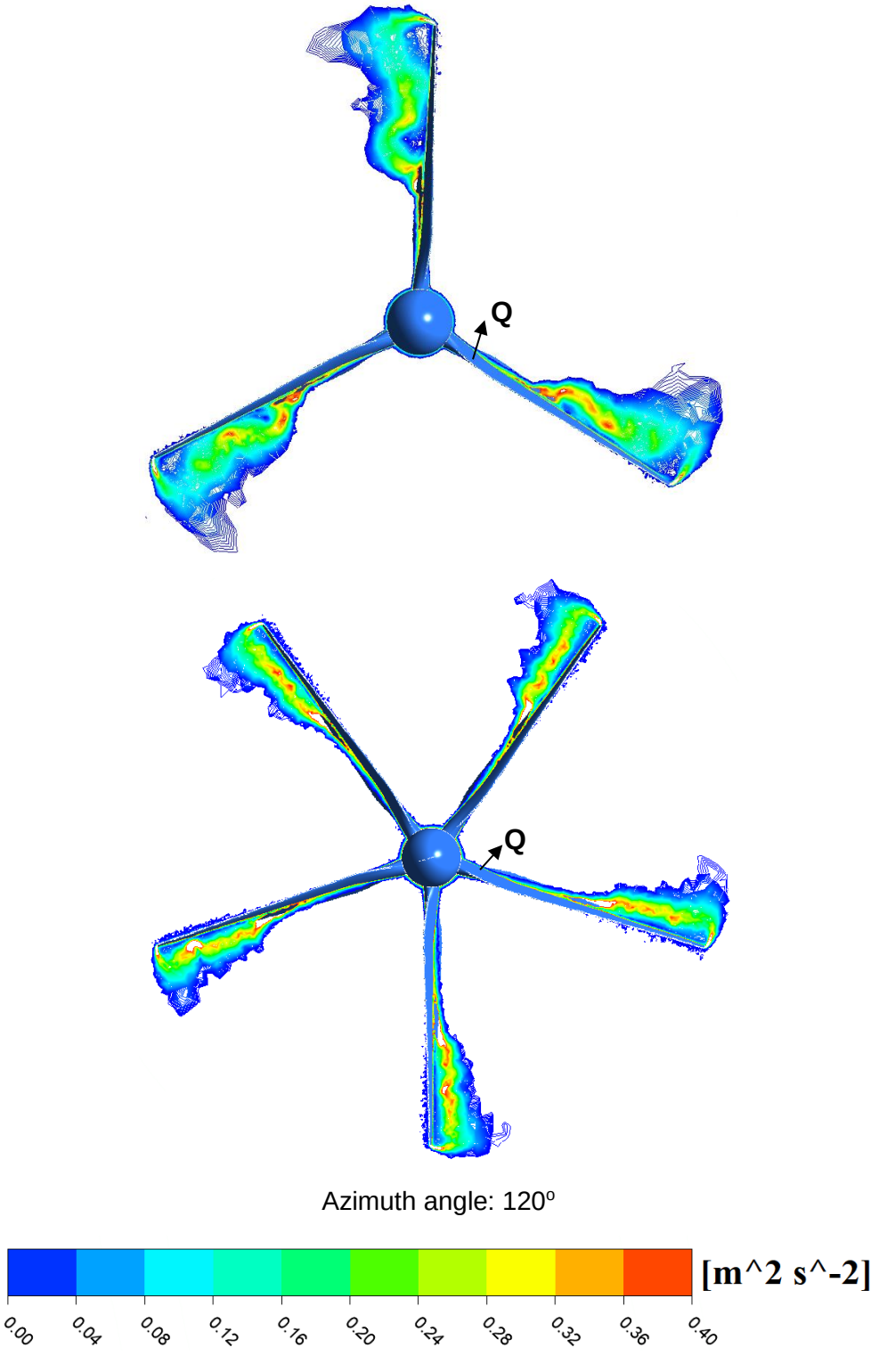

Figure 6.14 Vorticity contours at azimuth angles of 40°, 80°, and 120°. For these contours to be comparable, one of the turbine blades is marked with letter Q.

Finally, to better understand and compare the effect of different hubs on hydrodynamic performance of the HAT turbines, the velocity contours at three different azimuth angles on the ZX plane are shown in Figure 6.15. All contours are plotted at *TSR* of 5.0. As can be seen from this Figure, type III hub, which is used in the optimised model (compared to the type I (baseline model)), can be used to suppress the flow separation at different azimuth angles. On the other hand, in the baseline model, after water hits the nose of the hub, it causes separation and turbulence immediately, which can reduce the kinetic energy of water and the efficiency of the turbine. It can be concluded that the combination of the number of turbine blades and the type of hub can affect the performance of the turbine, as predicted in the previous section by the ANOVA method.

The obtained optimised turbine with rough (500 μm) and smooth blades was simulated at TSR= 5 using ANSYS Fluent 2019 to investigate the effects of surface roughness on the optimised turbine. Figure 6.16 shows the velocity contours using the CFD Post programme. As expected and previously observed for vertical turbines, surface roughness increases the turbulence in the flow, which reduces the output torque and ultimately reduces the output power of the turbine. The power loss for the turbine with a roughness of 500 mμ was calculated as 13% using Eq. 4.13 and the data obtained from the simulations in ANSYS Fluent.

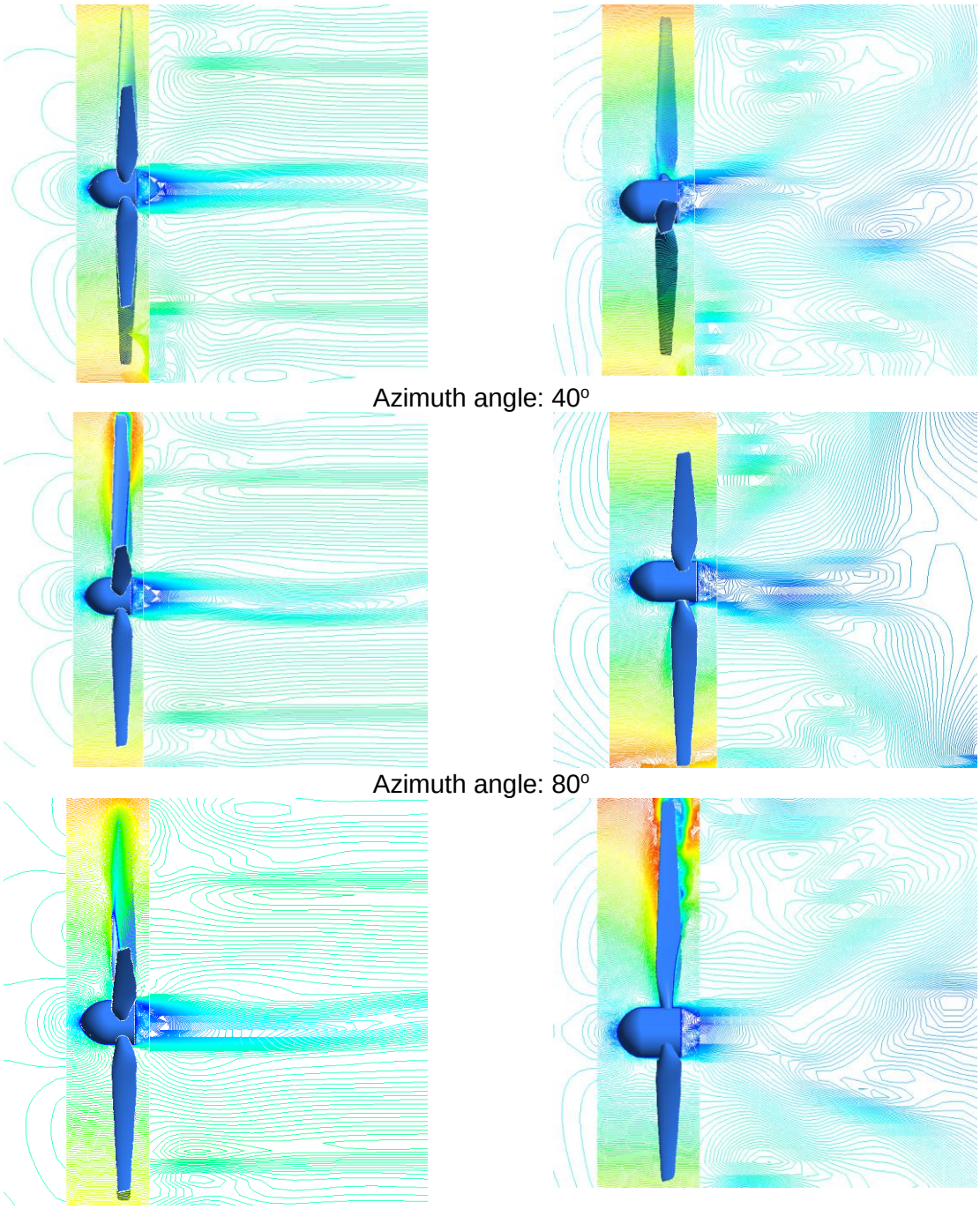

Figure 6.15 Velocity distribution at azimuth angles of 40°, 80°, and 120° (ZX plane) (left: optimised model and right: baseline model).

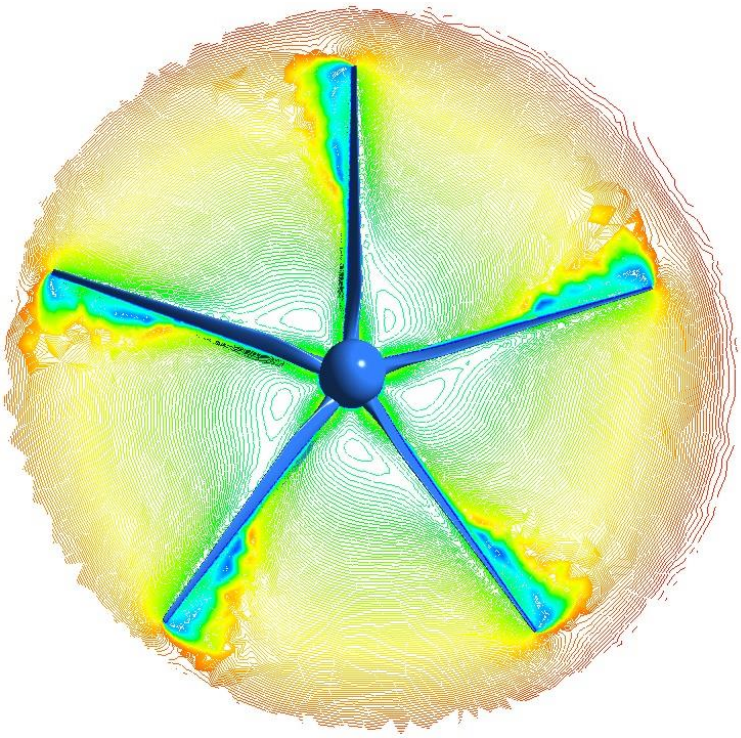

(a)

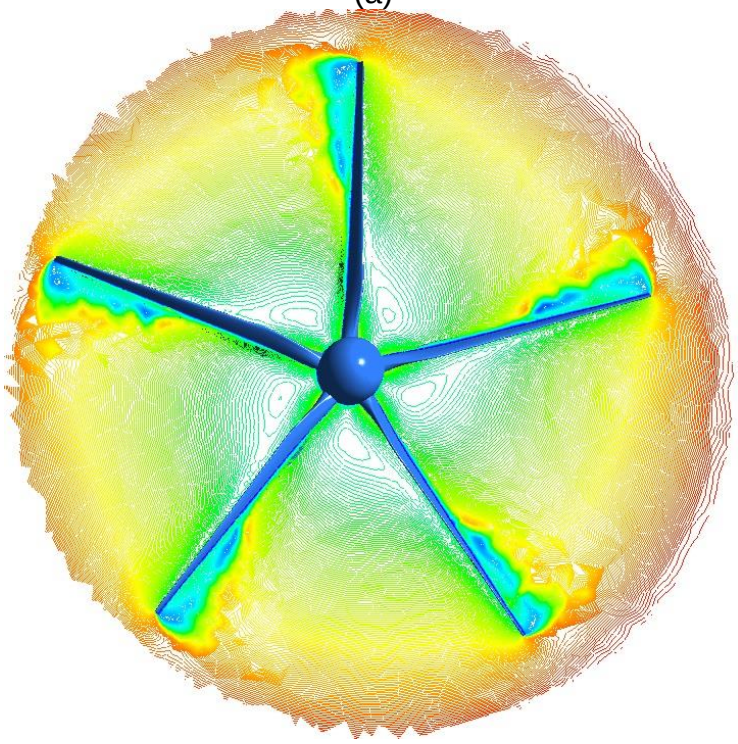

(b)

Figure 6.16 Distribution of velocity of optimised turbine with (a) smooth and (b) roughed blades and (a) at TSR= 5.5

6.8 Conclusion

The Taguchi method and extensive CFD simulations were utilised in this study to minimise the geometry of a HAT turbine, which can be used to power a desalination system. The results show that the Taguchi method is an effective tool for complex HAT turbine optimisation by using only few experiments. The main conclusions of this chapter can be summarised as follows:

(1) The optimum combination of the tested factors by the Taguchi method was achieved as (design 6): size of blade: 0.8b; number of blades: 4; hub radius: 0.125 m; and hub shape: type IV. The β indicator of variables A, B, C, and D, was calculated as 11.32, 12.2, 6.1 and 5.72 respectively. This indicates that number of blades (B), is main influential factor among the four assessed factors. The hub radius (C) and hub shape (D) have the least influence on the HAT turbine's hydrodynamic output.

(2) The results from ANOVA analysis show that all four parametric variables have a visible interaction with each other. Among the analysed factors, the relationship between number of blades (B) and other variables is very strong.

(3) The results of the superposition model show that the minimum S/N ratio is 25.01 for design 103. This value is for the combination of size of blade: 0.8b; number of blades: 5; hub radius: 0.150 m; and hub shape: type III. The weight of optimised model is 17% less than the baseline model, indicating that the optimised model would require less material and can be made cheaper.

(4) According to the CFD simulations, C_p of the optimised model is 0.44, which is 10% higher than the baseline model (0.40) at tip speed ratio (*TSR*) of 5. The optimised HAT turbine works better at lower *TSR* (3-5.5) and the baseline HAT turbine performs better at higher *TSR* (5.5-6.5).

Chapter Seven: Conclusions and Recommendations

7.1 Abstract

A literature review of ocean-powered desalination systems and optimisation of tidal turbines was conducted in Chapter 2. Moreover, the effects of surface roughness on hydrodynamic performance of tidal turbine were reviewed. Also the history of optimisation of vertical and horizontal axis tidal turbines was reviewed. For optimisation of a turbine with genetic algorithm or similar optimisation algorithms, hundreds of numerical simulations are needed. One of the limitations of 3D CFD is that it is highly time consuming, since for obtaining reliable results, different parameters must converge simultaneously. Computational time of combination of the genetic algorithm with the 3D CFD would be extremely expensive. However, the Taguchi method and superposition approach can provide a reasonable estimate of optimised parameters with a limited number of numerical simulations, and current PhD thesis is a valid example of this claim. It should be mentioned that the superposition model is a kind of simple of surrogate model and was used in this work.

7.2 Main conclusion remarks

A review of research on VAT turbines indicates that three parameters, namely twist angle, camber, and chord/radius ratio could have significant effect on turbine performance. The impacts of these three parameters on performance of VAT turbines have not been investigated in detail and their combined effects are unknown thus far. In this research, the effects of these three parameters on turbine performance were studied simultaneously. A horizontal turbine consists of two main parts: the hub and the blades. The solidity ratio, which is the ratio of the total turbine blade area over the swept area, is

the most important factor affecting turbine performance. The solidity ratio varies greatly with the blade size and the number of blades. Thus, optimisation of this ratio is accomplished by changing these two factors. On the other hand, the type of hub can be changed based on the hub radius and shape of the hub. In this work, four factors were considered to be optimised including size of blade, number of blades, hub radius, and hub shape.

Chapter 3 presented design of a RO desalination system. Combination of RO desalination system with clean energy sources decreases the environmental effect of carbon emissions by fossil fuels. The general objective of optimising the renewable energy powered RO desalination system is to reduce overall system costs and energy needs while still maintaining system performance. In this work, by adding a storage tank and a PV panel to a previous design of RO desalination system, a new design was introduced which can be powered with tidal turbines. In this chapter, conventional RO desalination systems were reviewed which showed the energy consumption for modern RO desalination systems is between 2-4 kWh/m^3. The most similar RO desalination system with this work, that used tidal energy, was reviewed. In the current research, a new design of desalination system was introduced (by adding a water storage tank for stabilising the driving energy and a PV panel for powering the booster pump), which can be powered by HAT or VAT turbines. Since in the proposed design, the most important part is the tidal turbine, the focus was placed on optimisation of the turbines and then, an appropriate Location of the desalination system was identified.

The coastline of South East England is suitable for installation of a tidal power devices for RO desalination system; not only it has low salinity and high current speed, but also in future it will have a higher demand for water. The mean tidal current velocity and salinity of water were assumed as 1 m/s and 30 ppt respectively. The energy required for the produced RO desalination system was determined. Therefore, the total energy required

for RO desalination system for desalinating 1 m^3/h freshwater system was determined as 2.7 kWh/m^3.

In Chapter 4, the effects of surface roughness on hydrodynamic performance of a tidal turbine were investigated in detail. Although improving the hydrodynamic performance is a key objective in the design of ocean-powered turbines, some factors affect the efficiency of the device during its operation. In this study, the impacts of a wide range of surface roughness, as a tribological parameter, on stream flow around a hydro turbine and its power loss were investigated. A comprehensive program of 3D Computational Fluid Dynamics (CFD) modelling, as well as an extensive range of experiments were carried out on a tidal turbine in order to measure reduction in hydrodynamic performance due to surface roughness. It was shown that the surface roughness increases the turbulence and decreases the active fluid energy that is required for rotating the turbine, thereby reducing the performance of the turbine. The following conclusions can be drawn from the results obtained in this chapter:

1) Velocity distributions showed that turbulence will increase with increasing the surface roughness of DH turbine. Turbulence reduces the kinetic energy, which in turn, reduces the total turbine efficiency.

2) The surface roughness degraded the margin of pressure coefficient, especially at high values of roughness.

3) The drag coefficient increased as a second order polynomial function of Hr. When NACA 0015 airfoil was used in DH turbine, the drag coefficient was very sensitive to the variations of Hr. The drag coefficient of roughed turbine (with Hr=1000 μm) studied in this chapter was 20% higher than the smooth blade.

4) The average torque showed small changes at low flow velocities. The adverse impact of surface roughness was significantly greater at high inlet velocities (i.e., in high

Reynold numbers). In the CFD simulation, all parameters in the Re equation were constant except the velocity of water. It was shown that the negative impacts of roughness are much greater at high Reynolds numbers.

5) The decrease in torque due to surface roughness reduced the power output of the turbine. For the turbine studied in this chapter, for Hr=1000, the maximum reductions in power output in the numerical and experimental models were about 27% and 22% μm respectively.

In Chapter 5 optimisation of a VAT turbine for powering a RO desalination system was performed. Vertical Axis Tidal (VAT) turbines can be used as ocean-powered devices to power the RO desalination systems from movements in ocean as a renewable source of energy. The energy required for desalinating 1 m^3/h was determined. Accordingly, a VAT turbine was designed to fulfil this amount of energy. A number of CFD simulations were carried out using the mixed-level modified Taguchi technique to determine the optimal hydrodynamic performance of a VAT turbine. The influence of four parameters: twist angle, camber position, maximum camber, and chord/radius ratio were studied. The interaction of these parameters was investigated using the Variance of Analysis (ANOVA) approach. The findings of this chapter can provide guidelines for optimisation of vertical turbines. The following conclusions can be drawn from the results presented in this chapter:

(1) The highest average moment coefficient (C_m) and power coefficient (C_p) correspond to case 12 which are 0.134 and 0.202 respectively. The value of C_p (0.202) obtained for case 12 was 26% higher than the baseline case (0.16). The S/N ratios of the 18 different cases were calculated. The maximum S/N ratio occurred at the maximum power coefficient. The maximum S/N ratio is 8.232 which corresponds to case 12.

(2) The results of the Taguchi method showed that the combination of A4, B3, C2, and D2 results in the maximum output. The values of θ for factors A, B, C, and D are 0.863,

0.136, 0.151, and 0.684 respectively. This implies that twist angle is the most significant factor among the 4 tested factors, affecting the hydrodynamic performance of the turbine.

(3) Superposition was used to estimate all possible responses (S/N ratios) outside orthogonal array (OA). The superposition results showed that, the case 104 provides the maximum signal-to-noise ratio (9.456) with the combination A4, B3, C2, and D2 that is considerably greater than the optimal case (case 12), calculated by 18 cases in the Taguchi orthogonal array.

(4) The power coefficient (C_p) of the optimised turbine was calculated as 0.210, which is 26% higher than the baseline case. In addition, the optimised model reduced the required material by 57% compared with the baseline model, indicating that the new model requires less material. Moreover, the size of the wake generated in the baseline model was greater than the optimised model, resulting in a decrease in kinetic energy and a reduction in turbine output.

In Chapter 6, optimisation of a HAT turbine for powering a RO desalination system was carried out. Horizontal Axis Tidal (HAT) turbines also can be used to power RO desalination systems. The Taguchi-CFD (Computational Fluid Dynamics) approach was used as an inexpensive and rapid tool for optimising HAT turbine. The effects of blade size, number of blades, hub radius, and hub shape were studied and optimised. The Taguchi results revealed that the most important parameters influencing the power output of HAT turbine are the number of blades, size of blade, hub radius, and hub shape respectively.

The main conclusions of this chapter can be summarised as follows:

(1) The optimum combination of the tested factors by the Taguchi method was achieved as (design 6): size of blade: 0.8b; number of blades: 4; hub radius: 0.125 m; and hub shape: type IV. The θ indicator of variables A, B, C, and D, was calculated as

11.32, 12.2, 6.1 and 5.72 respectively. This indicates that number of blades (B), is the main influential factor among the four assessed factors. The hub radius (C) and hub shape (D) have the least influence on the HAT turbine's hydrodynamic output.

(2) The results from ANOVA analysis showed that all four parametric variables have a visible interaction with each other. Among the analysed factors, the relationship between number of blades (B) and other variables is very strong.

(3) The results of the superposition model showed that the minimum S/N ratio is 25.01 for design 103. This value is for the combination of size of blade: 0.8b; number of blades: 5; hub radius: 0.150 m; and hub shape: type III. The weight of the optimised model was 17% less than the baseline model, indicating that the optimised model would require less material and can be made cheaper.

(4) According to the CFD simulations, C_p of the optimised model is 0.44, which is 10% higher than the baseline model (0.40) at tip speed ratio (TSR) of 5. The optimised HAT turbine works better at lower TSR (3-5.5) and the baseline HAT turbine performs better at higher TSR (5.5-6.5).

The main contributions and achievements of the current research in this field are summarised as follows:

- A new conceptual desalination system was introduced which can be powered by HAT or VAT turbines.
- A comprehensive 3D CFD simulations and a number of laboratory experiments were carried out, covering a wide range of roughness values for a vertical hydro turbine, in order to quantify the impacts of roughness on the hydrodynamic performance of hydro turbines.
- The Taguchi method was developed and used to optimise a VAT turbine in order to maximise its hydrodynamic performance. The combined effects of twist angle,

cambered blades, and solidity on performance of the VAT turbine was investigated. Using the mixed-level modified Taguchi approach and comprehensive 3D CFD simulations, a new set of optimised factors were identified and tested.

- The geometry of the HAT turbine was optimised with combination of 3D CFD simulations using the Taguchi method. The effects of size of blades, number of blades, hub radius, and hub shape on power output of HAT turbine were studied and optimised.
- The results of this study provide a comprehensive guidance for tidal turbine optimisation process.

7.3 Contributions of the work

- The effects of roughness on performance of tidal turbine has been quantified over a wide range of roughness.
- For the first time, the combined effects of twist angle, camber position, maximum camber, and chord/radius ratio on performance of the VAT turbine were investigated.
- For the first time, the effects of size of blades, number of blades, hub radius, and hub shape on power output of HAT turbine were studied.
- It was shown that there is a great interaction between the type of the hubs and the size and number of blades of horizontal turbines, and they must be optimized together.

7.4 Recommendations for Further Research

1) In this work, the effects of vibration and deformation of turbine blades have not been considered. The interaction between water and structure and turbine frame is another factor that was not taken into consideration.

2) The blade roughness which is caused by erosion or/and dogged marine animals, affects the hydrodynamic performance of turbines and can be considered as a factor in the Taguchi method and its individual impacts as well as combination with other factors can be investigated in future work.

3) An economic analysis of HAT and VAT turbines based on different materials is a potential area for future work.

4) Research and feasibility study of different combinations of ocean power desalination systems, which are listed in Table1.1, could be another area of future research.

5) More work needs to be carried out to find an RO unit, which can desalinate seawater at a much lower energy.

6) Another possible field for future research is investigation on different methods to reduce corrosion and roughness of turbines.

7) The use of other turbines for desalination system, including Archimedes screw turbines, is also recommended.

8) Further research is required to investigate the impact of roughness on HAT turbine performance.

9) Construction and testing of turbines and RO unit on a laboratory scale can lead to practical results in this field.

10) Combination of Kriging method and CFD simulations can be employed to predict the optimised combinations of parameters. Furthermore, the RMSE (root of the mean squared error) and EI (expected improvement) also can be used to guide the next experiment until a good accuracy around the optimum is achieved with comparable number of runs.

11) The proposed RO desalination system work can be improved in design by adding a control system consisting of sensors and switches.

Appendix A: Experimental cases with different roughness values

H_r: 0 μm (smooth)

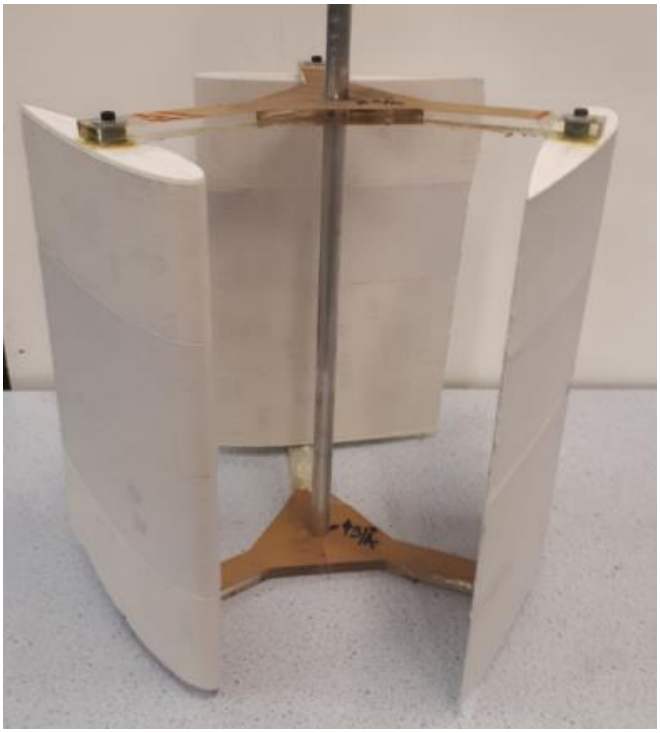

H_r: 50 μm

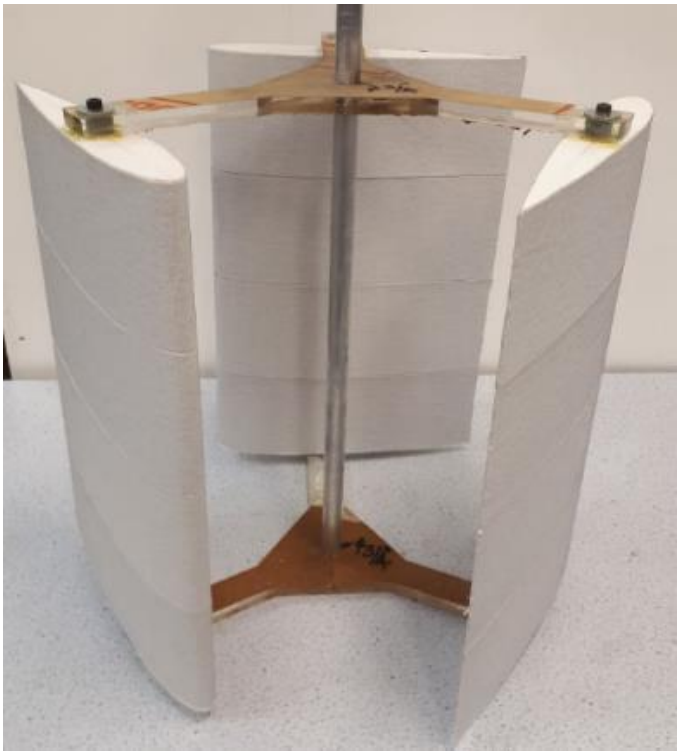

H_r: 100 µm

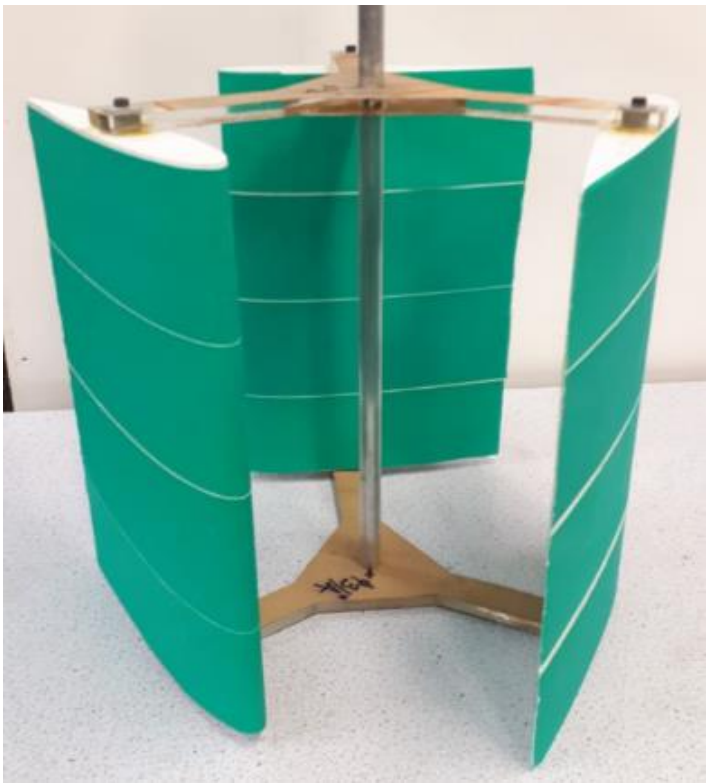

H_r: 250 µm

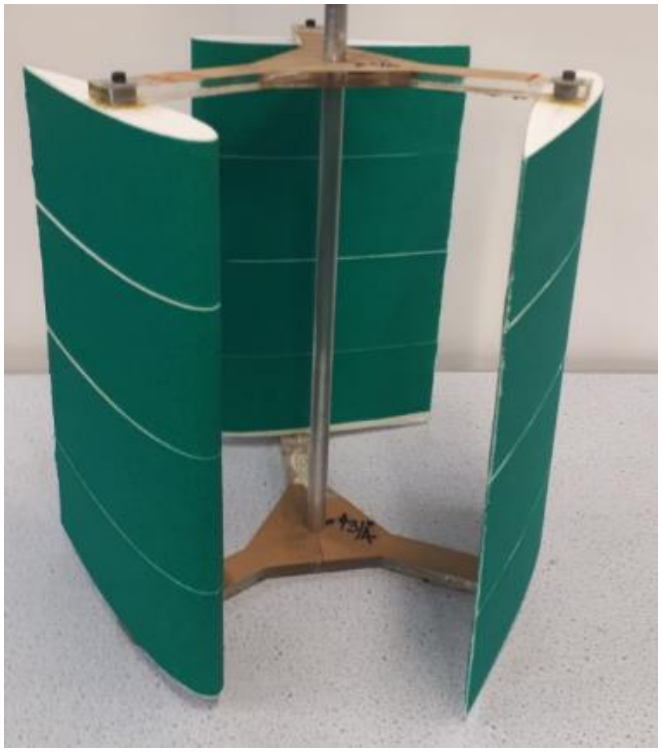

H_r: 500 μm

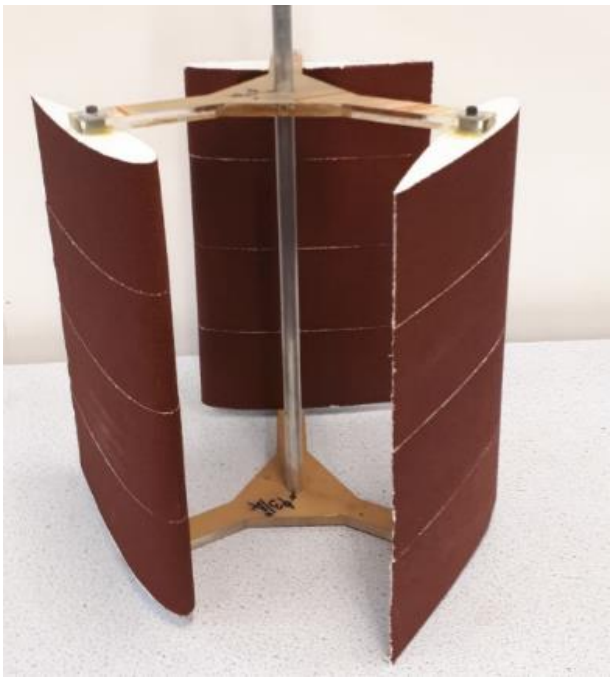

H_r: 1000 μm

Figure A.1 Experimental cases with different roughness values.

Appendix B: All turbine designs

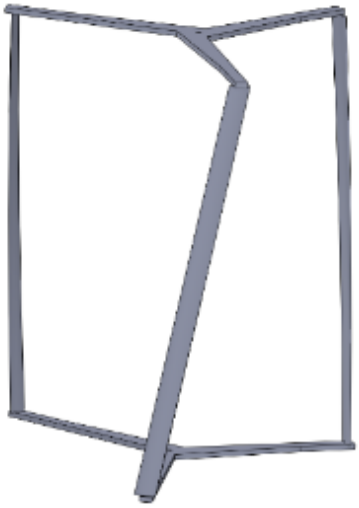

Case 1

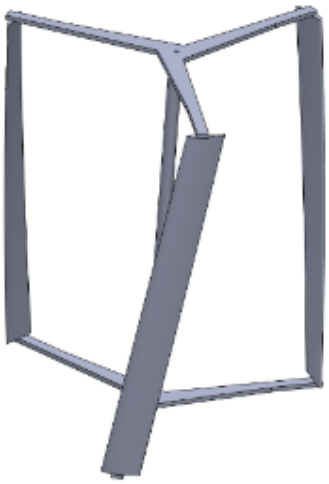

Case 2

Case 3

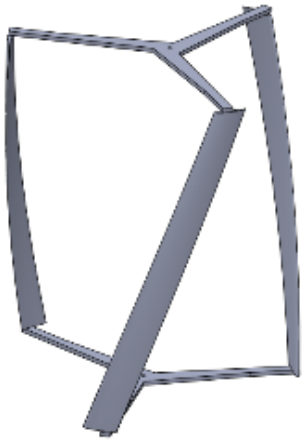

Case 4

Case 5

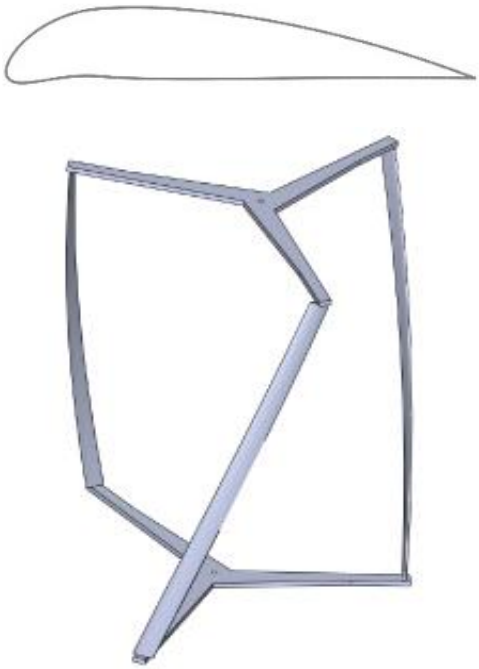

Case 6

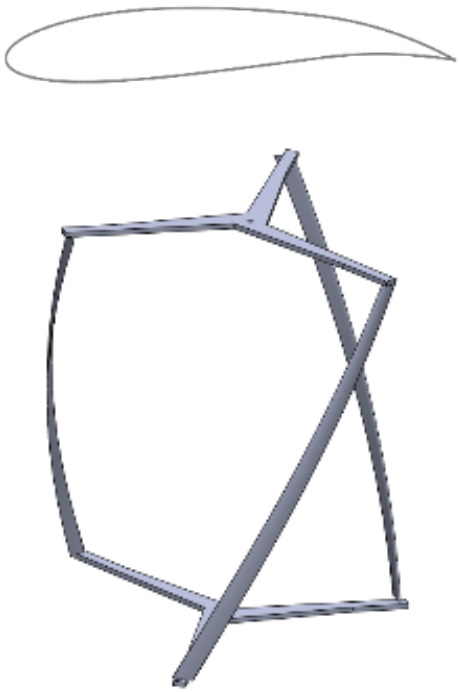

Case 7

Case 8

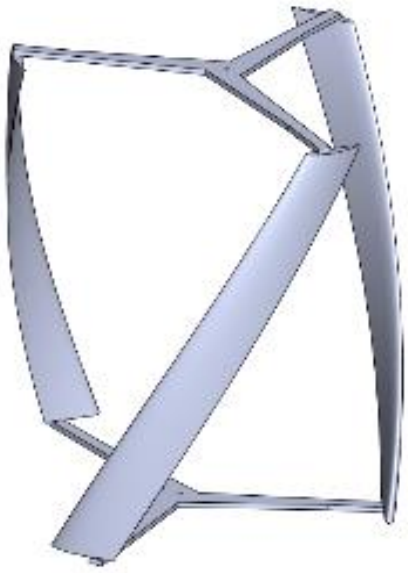

Case 9

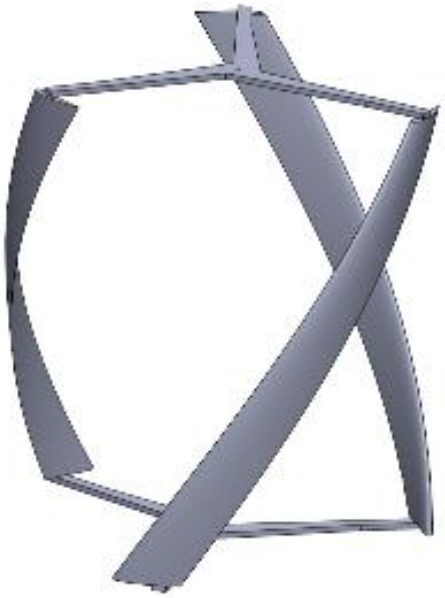

Case 10

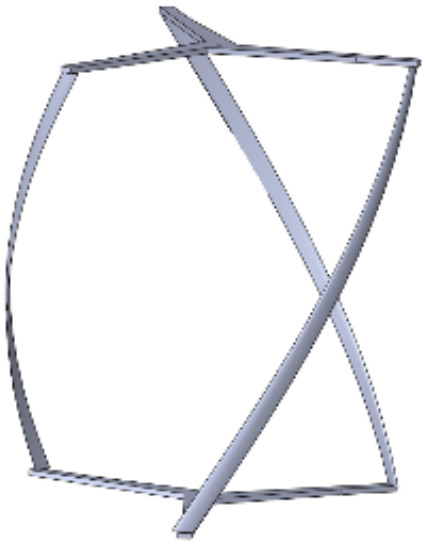

Case 11

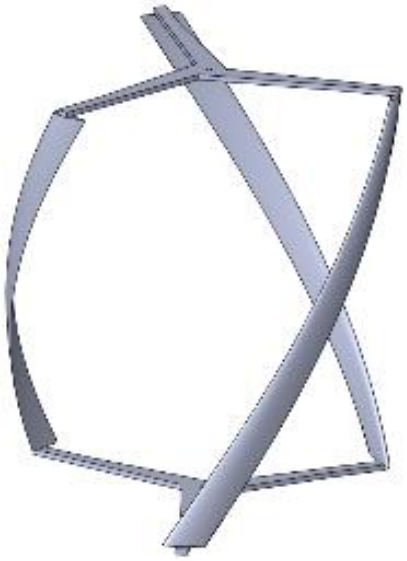

Case 12

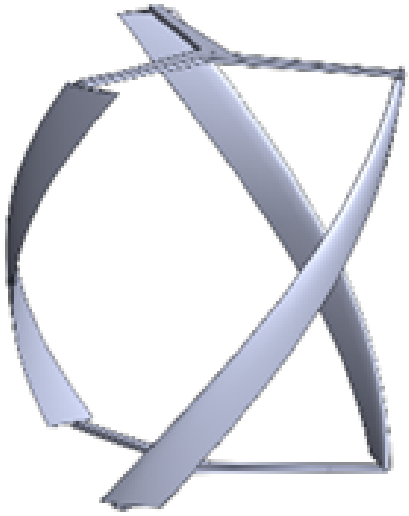

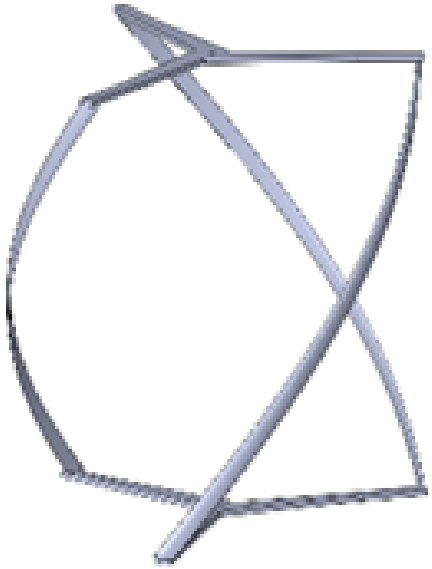

Case 13

Case 14

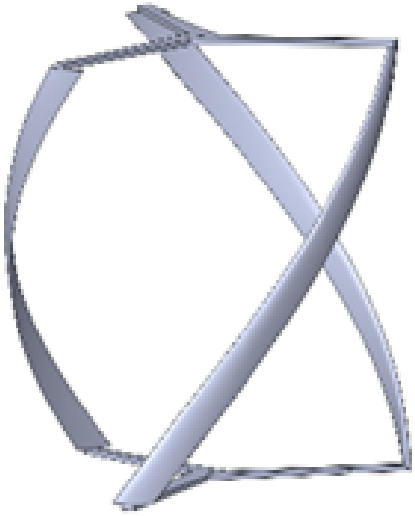

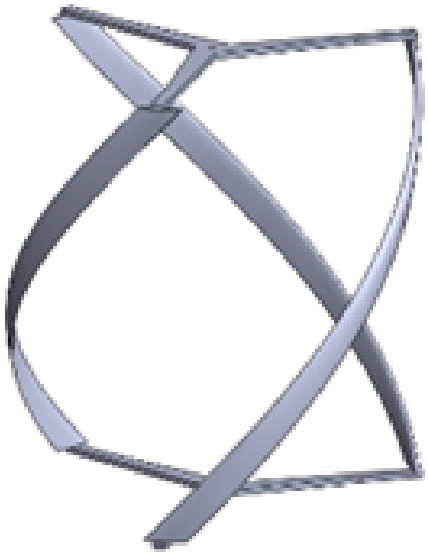

Case 15

Case 16

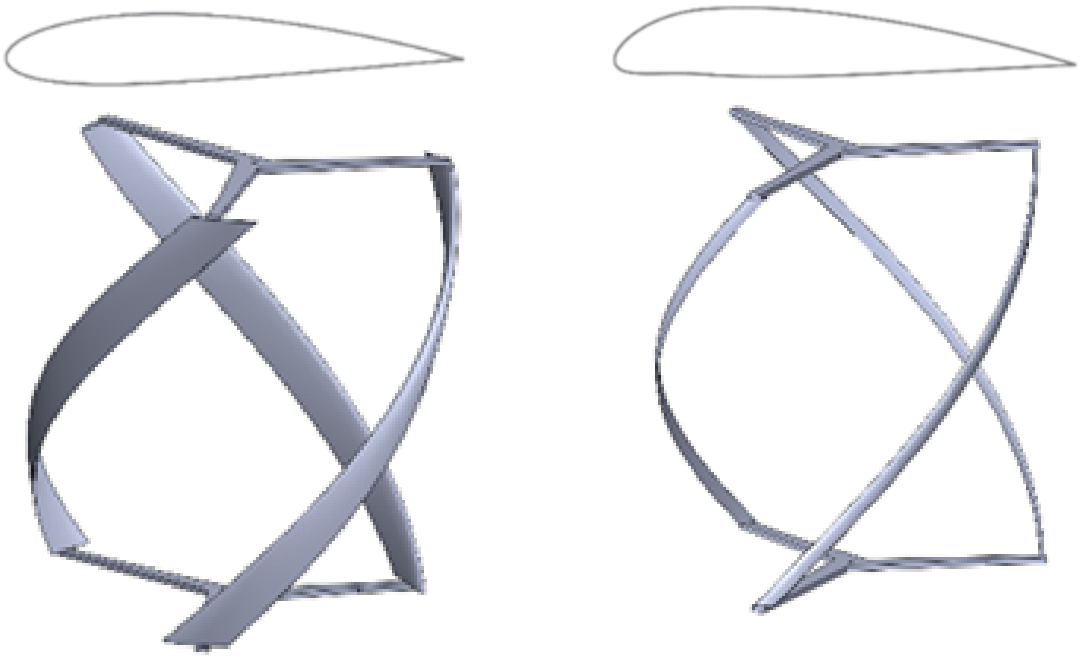

Case 17 Case 18

Figure B.1. All turbine designs according to the L_{18} Orthogonal array (OA).

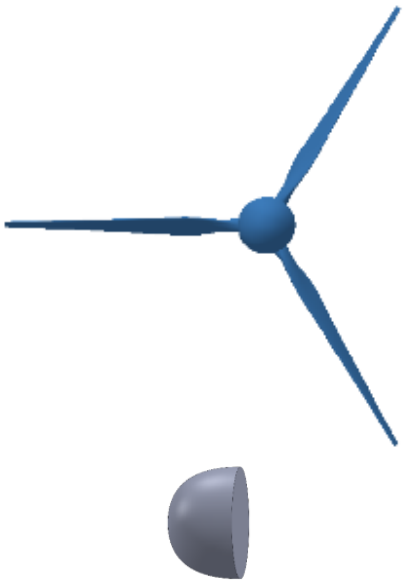

Case 1

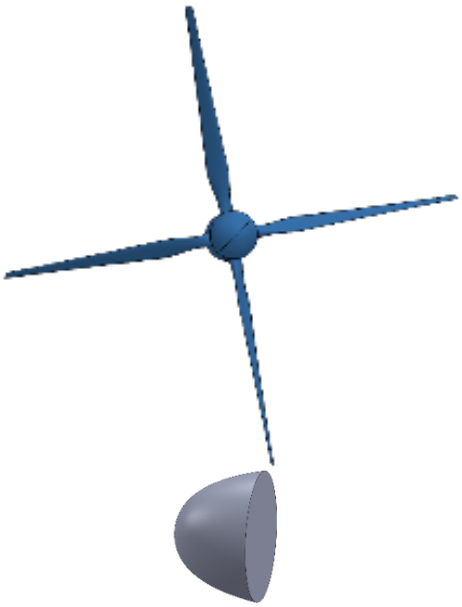

Case 2

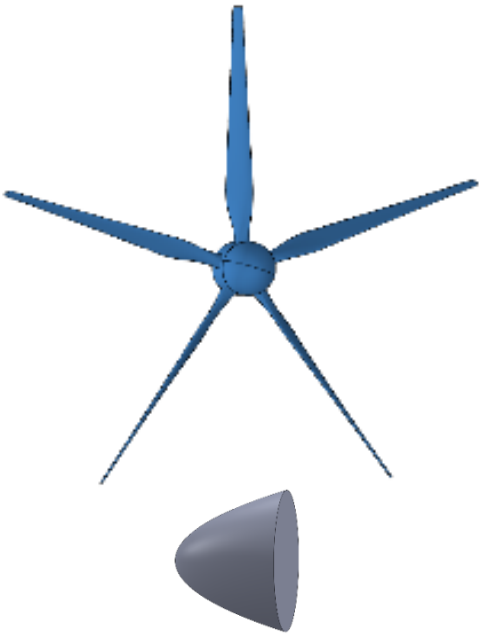

Case 3

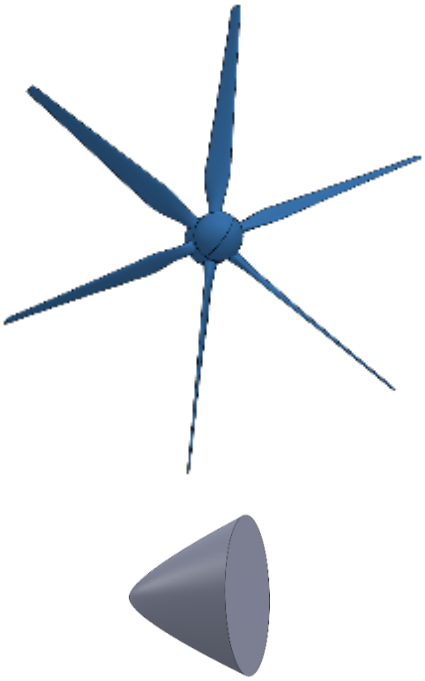

Case 4

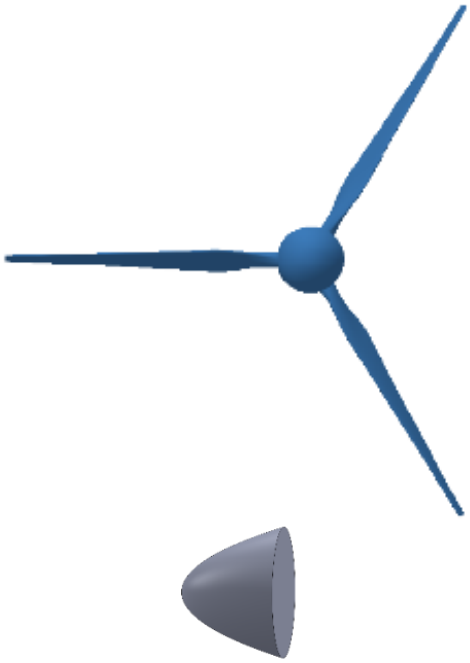

Case 5

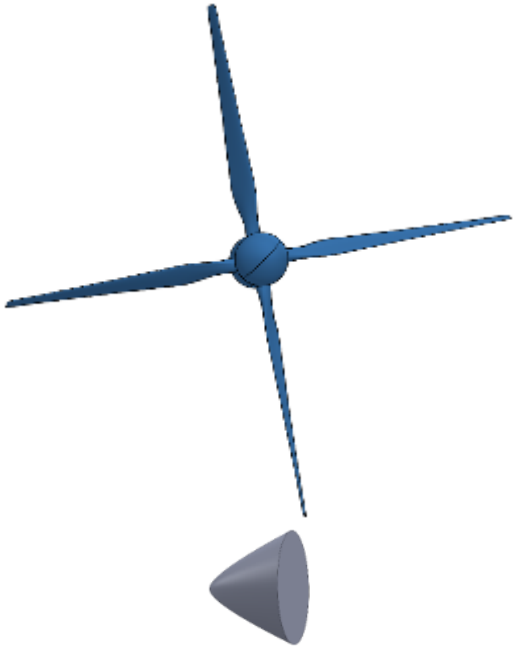

Case 6

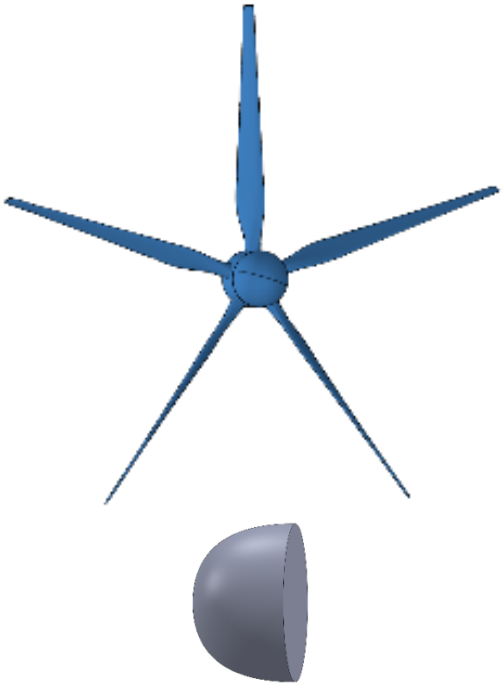

Case 7

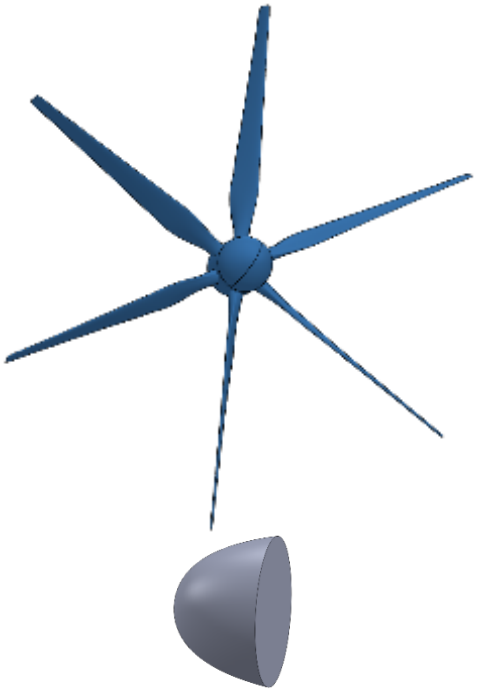

Case 8

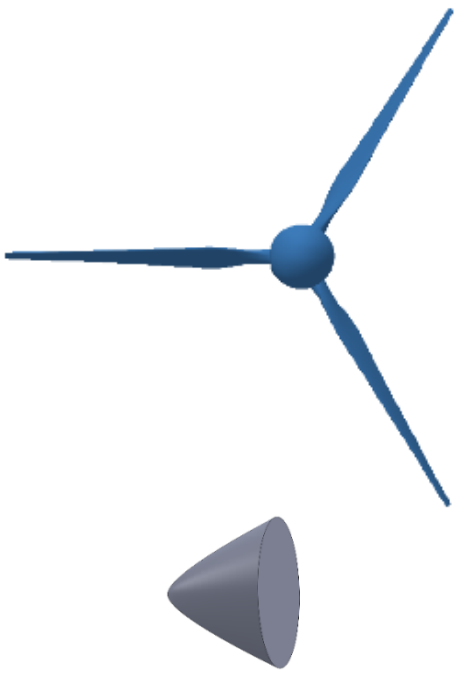

Case 9

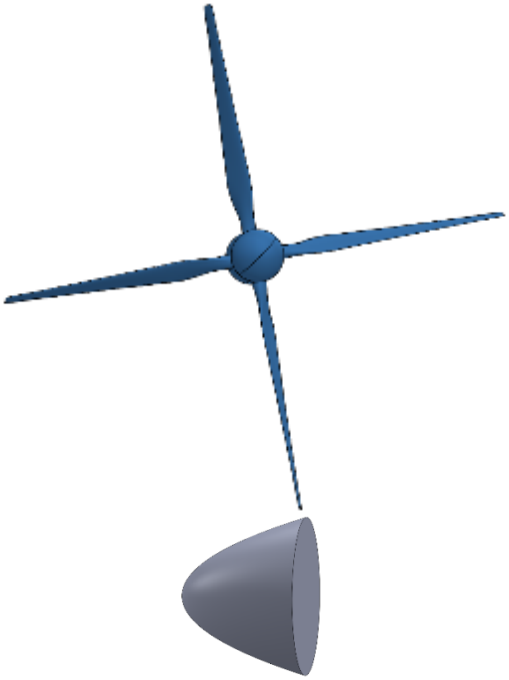

Case 10

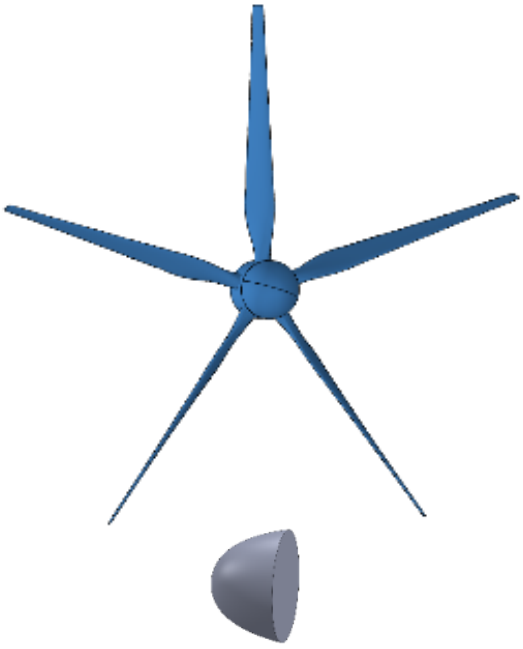

Case 11

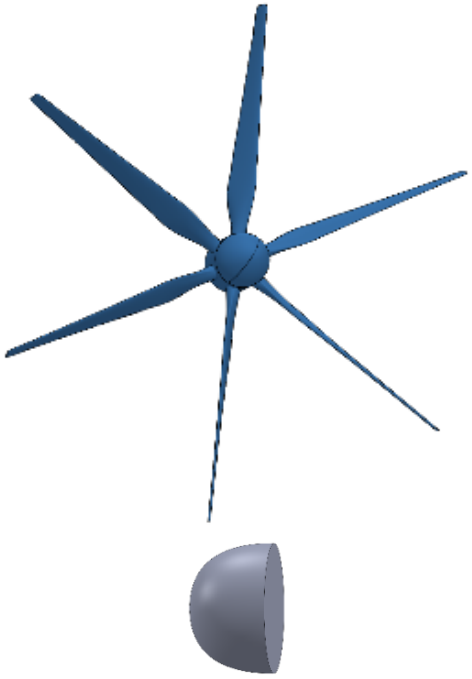

Case 12

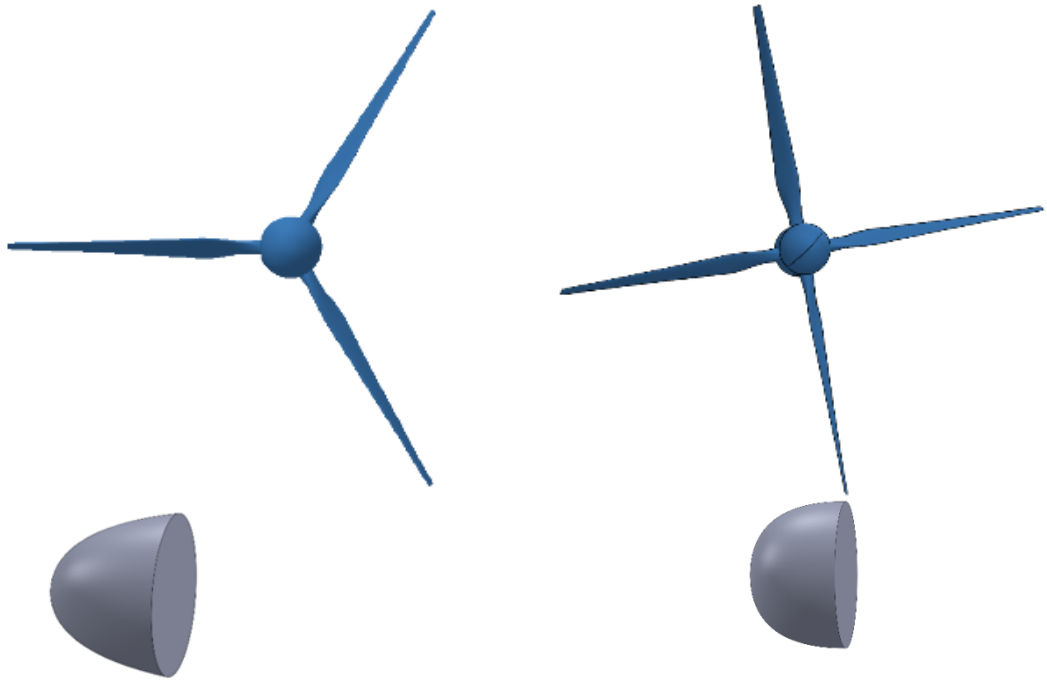

Case 13 Case 14

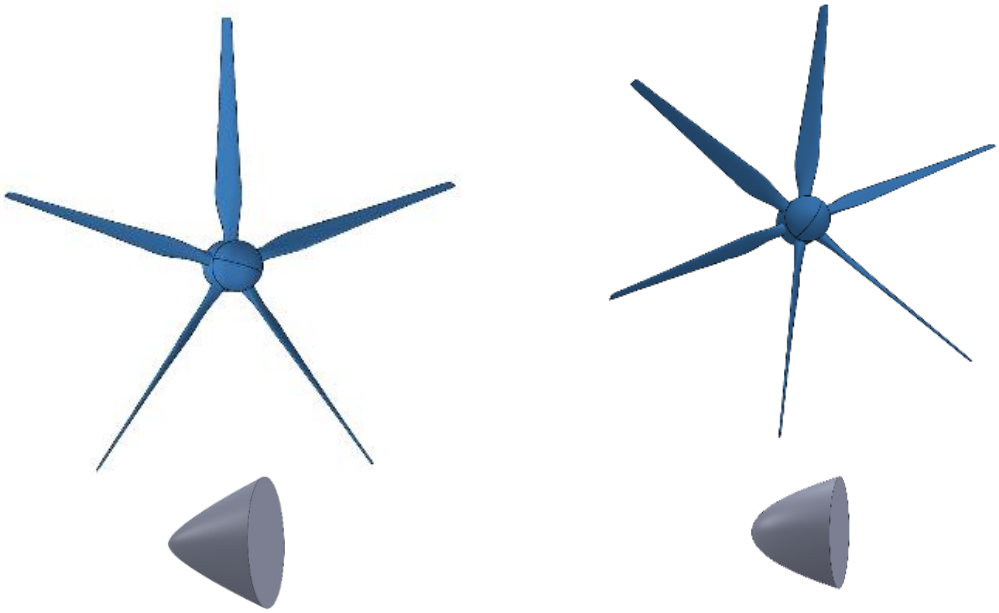

Case 15 Case 16

Figure B.2. All turbine designs according to the L_{16} Orthogonal array (OA).

Appendix C: Moment coefficients

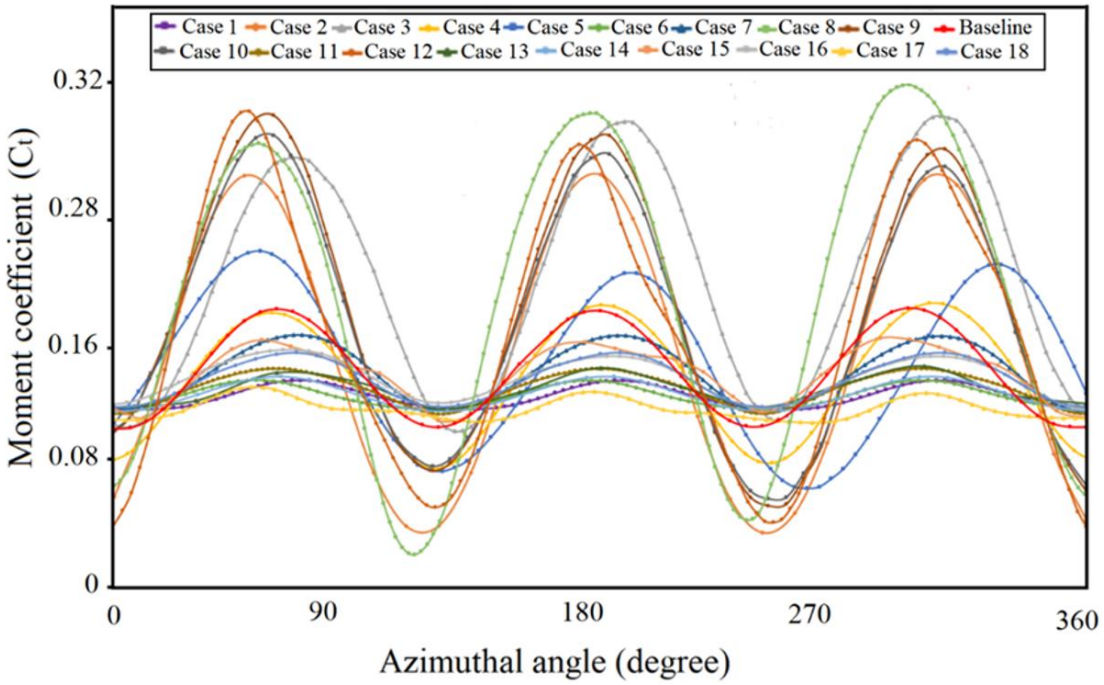

Figure C.1. Variations in moment coefficient for single revolution, form 0° to 360° at water velocity of 1.0 m/s and TSR=1.25.

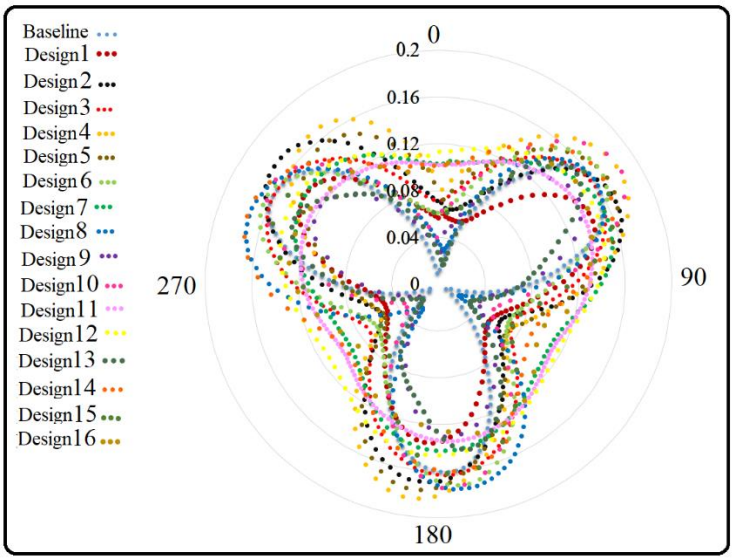

Figure C.2. Changes in moment coefficient (C_m) of all cases for one revolution (0-360º) at TSR=5.

References

Abuan, B. E., & Howell, R. J. (2019). The performance and hydrodynamics in unsteady flow of a horizontal axis tidal turbine. *Renewable Energy, 133*, 1338-1351.

Abuthakeer, S., Mohanram, P., & Kumar, G. M. (2011). Prediction and control of cutting Tool vibration in CNC Lathe with ANOVA and ANN. *International Journal of Lean Thinking, 2*(1), 1-23.

Adedeji, O. E., Yu, W., & Sanders, R. S. (2019). Analysis of local wear variables for high-precision erosion modelling in complex geometries. *Wear, 426*, 562-569.

Ahmadi, M. H., & Yang, Z. (2019). The evolution of turbulence characteristics in the wake of a horizontal axis tidal stream turbine. *Renewable Energy*.

Ahmed, M. R. (2012). Blade sections for wind turbine and tidal current turbine applications–current status and future challenges. *International journal of energy research, 36*(7), 829-844.

Ai, K., Cui, J., Wang, M., & Avital, E. (2020). Numerical modelling of a dual-rotor marine current turbine in a rectilinear tidal flow. *Ocean engineering, 200*, 107026.

Akinyele, D., & Rayudu, R. (2014). Review of energy storage technologies for sustainable power networks. *Sustainable Energy Technologies and Assessments, 8*, 74-91.

Akpinar, A.; and Akpinar, S., An assessment on seasonal analysis of wind energy characteristics and wind turbine characteristics, Energy Conversion and Management, Volume 46, Issues 11–12, 2005, Pages 1848-1867.

Al-Amshawee, S., Yunus, M. Y. B. M., Azoddein, A. A. M., Hassell, D. G., Dakhil, I. H., & Hasan, H. A. (2020). Electrodialysis desalination for water and wastewater: A review. *Chemical engineering journal, 380*, 122231.

Al-Karaghouli, A., & Kazmerski, L. L. (2013). Energy consumption and water production cost of conventional and renewable-energy-powered desalination processes. *Renewable and Sustainable Energy Reviews, 24*, 343-356.

Al-Nory, M. T., & Graves, S. C. (2013). *Water desalination supply chain modelling and optimization.* Paper presented at the 2013 IEEE 29th International Conference on Data Engineering Workshops (ICDEW).

Alidadi, M. (2009). *Duct optimization for a ducted vertical axis hydro current turbine.* University of British Columbia.

Alikhani, R., Ebadi, A., Karami, P., Shahanipour, S., & Razzaghi-Asl, N. (2020). Response Surface Study on Molecular Docking Simulations of Citalopram and Donepezil as Potent CNS Drugs. *Iranian Journal of Pharmaceutical Research*.

Alkaisi, A., Mossad, R., & Sharifian-Barforoush, A. (2017). A review of the water desalination systems integrated with renewable energy. *Energy Procedia, 110*, 268-274.

Alsarayreh, A. A., Al-Obaidi, M., Al-Hroub, A., Patel, R., & Mujtaba, I. (2020). Evaluation and minimisation of energy consumption in a medium-scale reverse osmosis brackish water desalination plant. *Journal of Cleaner Production, 248*, 119220.

Alsarayreh, A. A., Al-Obaidi, M. A., Al-Hroub, A. M., Patel, R., & Mujtaba, I. M. (2020). Performance evaluation of reverse osmosis brackish water desalination plant with different recycled ratios of retentate. *Computers & Chemical Engineering, 135*, 106729.

Amy, G., Ghaffour, N., Li, Z., Francis, L., Linares, R. V., Missimer, T., & Lattemann, S. (2017). Membrane-based seawater desalination: Present and future prospects. *Desalination, 401*, 16-21.

Ang, W. L., Mohammad, A. W., Hilal, N., & Leo, C. P. (2015). A review on the applicability of integrated/hybrid membrane processes in water treatment and desalination plants. *Desalination, 363*, 2-18.
Ang, W. L., Mohammad, A. W., Johnson, D., & Hilal, N. (2019). Forward osmosis research trends in desalination and wastewater treatment: A review of research trends over the past decade. *Journal of Water Process Engineering, 31*, 100886.
Antonio, F. d. O. (2010). Wave energy utilization: A review of the technologies. *Renewable and Sustainable Energy Reviews, 14*(3), 899-918.
Armstrong, S., Fiedler, A., & Tullis, S. (2012). Flow separation on a high Reynolds number, high solidity vertical axis wind turbine with straight and canted blades and canted blades with fences. *Renewable Energy, 41*, 13-22.
Asghar, U., Aziz, I., & Sher, F. (2017). *Modelling and simulation of flow induced vibrations in vertical axis wind turbine blade.* Paper presented at the 2017 14th International Bhurban Conference on Applied Sciences and Technology (IBCAST).
Asr, M. T., Nezhad, E. Z., Mustapha, F., & Wiriadidjaja, S. (2016). Study on start-up characteristics of H-Darrieus vertical axis wind turbines comprising NACA 4-digit series blade airfoils. *Energy, 112*, 528-537.
Atallah, M. O., Farahat, M. A., Lotfy, M. E., & Senjyu, T. (2020). Operation of conventional and unconventional energy sources to drive a reverse osmosis desalination plant in Sinai Peninsula, Egypt. *Renewable Energy, 145*, 141-152.
Badshah, M., Badshah, S., & Jan, S. (2019). Comparison of computational fluid dynamics and fluid structure interaction models for the performance prediction of tidal current turbines. *Journal of Ocean Engineering and Science*.
Badshah, M., Badshah, S., & Jan, S. (2020). Comparison of computational fluid dynamics and fluid structure interaction models for the performance prediction of tidal current turbines. *Journal of Ocean Engineering and Science, 5*(2), 164-172.
Bahaj, A. S., Batten, W. M. J., & McCann, G. (2007). Experimental verifications of numerical predictions for the hydrodynamic performance of horizontal axis marine current turbines. *Renewable Energy, 32*(15), 2479-2490.
Balduzzi, F., Bianchini, A., Maleci, R., Ferrara, G., & Ferrari, L. (2016). Critical issues in the CFD simulation of Darrieus wind turbines. *Renewable Energy, 85*, 419-435.
Balfaqih, H., Al-Nory, M. T., Nopiah, Z. M., & Saibani, N. (2017). Environmental and economic performance assessment of desalination supply chain. *Desalination, 406*, 2-9.
Banerjee, S., Poria, S., Sutradhar, G., & Sahoo, P. (2019). Design of Experiments Analysis of Friction Behavior of Mg-WC Nano-composites using Taguchi Methodology. *Materials Today: Proceedings, 18*, 4026-4033.
Bao, Z., Yang, F., Wu, Z., Nyamsi, S. N., & Zhang, Z. (2013). Optimal design of metal hydride reactors based on CFD–Taguchi combined method. *Energy conversion and management, 65*, 322-330.
Baratchi, F., Jeans, T., & Gerber, A. G. (2019). A modified implementation of actuator line method for simulating ducted tidal turbines. *Ocean engineering, 193*, 106586.
Batten, W., Bahaj, A., Molland, A., & Chaplin, J. (2006). Hydrodynamics of marine current turbines. *Renewable Energy, 31*(2), 249-256.
Batten, W., Bahaj, A., Molland, A., & Chaplin, J. (2008). The prediction of the hydrodynamic performance of marine current turbines. *Renewable Energy, 33*(5), 1085-1096.
Batten, W., Bahaj, A., Molland, A., Chaplin, J., & Group, S. E. R. (2007). Experimentally validated numerical method for the hydrodynamic design of horizontal axis tidal turbines. *Ocean Engineering, 34*(7), 1013-1020.
Bianchini A., Giovanni, F., Ferrari, L., Design guidelines for H-Darrieus wind turbines: Optimization of the annual energy yield, Energy Conversion and Management, Volume 89, 2015, Pages 690-707,

Blair, M. F. (1991). The effects of Reynolds number, rotor incidence angle and surface roughness on the heat transfer distribution in a large-scale turbine rotor passage.
Boström, C. (2011). *Electrical systems for wave energy conversion.* Acta Universitatis Upsaliensis.
Bouhal, T., Rajad, O., Kousksou, T., Arid, A., El Rhafiki, T., Jamil, A., & Benbassou, A. (2018). CFD performance enhancement of a low cut-in speed current Vertical Tidal Turbine through the nested hybridization of Savonius and Darrieus. *Energy conversion and management, 169*, 266-278.
Boyle, G. (2004). *Renewable energy*.
Bozzetto, A., & Tedeschi, E. (2014). *Wave power extraction with constrained power take-off: Single capture vs. double capture point absorbers.* Paper presented at the 2014 Ninth International Conference on Ecological Vehicles and Renewable Energies (EVER).
Brusca, S., Lanzafame, R., & Messina, M. (2014). Design of a vertical-axis wind turbine: how the aspect ratio affects the turbine's performance. *International Journal of Energy and Environmental Engineering, 5*(4), 333-340.
Burn, S., Hoang, M., Zarzo, D., Olewniak, F., Campos, E., Bolto, B., & Barron, O. (2015). Desalination techniques—A review of the opportunities for desalination in agriculture. *Desalination, 364*, 2-16.
Busch, M., & Mickols, W. (2004). Reducing energy consumption in seawater desalination. *Desalination, 165*, 299-312.
Carrel, S. (2016). World first for Shetlands in tidal power breakthrough. *The Guardian*.
Castelli, M., De Betta, S., & Benini, E. (2012). *Numerical investigation of the optimal spatial domain discretization for the 2-D analysis of a Darrieus vertical-axis water turbine.* Paper presented at the Proceedings of World Academy of Science, Engineering and Technology.
Cebeci, T., & Bradshaw, P. (1977). Momentum transfer in boundary layers. *Washington, DC, Hemisphere Publishing Corp.; New York, McGraw-Hill Book Co., 1977. 407 p.*
Chan, L. C., Akrami, M., Javadi, A., Tabor, G., Dibaj, M., & Khanjanpour, M. H. (2019). Optimisation of a conceptual aircraft model using a genetic algorithm and 3D Computational Fluid Dynamics (CFD).
Chen, D. (2015). Tidal energy seawater desalination system, power generation system and integral energy utilization system: Google Patents.
Chen, W.H., Chen, C.-Y., Huang, C.-Y., & Hwang, C.-J. (2017). Power output analysis and optimization of two straight-bladed vertical-axis wind turbines. *Applied energy, 185*, 223-232.
Chen, Y., & Lian, Y. (2015). Numerical investigation of vortex dynamics in an H-rotor vertical axis wind turbine. *Engineering Applications of Computational Fluid Mechanics, 9*(1), 21-32.
Chowdhury, A. M., Akimoto, H., & Hara, Y. (2016). Comparative CFD analysis of Vertical Axis Wind Turbine in upright and tilted configuration. *Renewable Energy, 85*, 327-337.
Chu, K. H., Lim, J., Kim, S.-J., Jeong, T.-U., & Hwang, M.-H. (2020). Determination of optimal design factors and operating conditions in a large-scale seawater reverse osmosis desalination plant. *Journal of Cleaner Production, 244*, 118918.
CohenTanugi, D., McGovern, R. K., Dave, S. H., Lienhard, J. H., & Grossman, J. C. (2014). Quantifying the potential of ultra-permeable membranes for water desalination. *Energy & Environmental Science, 7*(3), 1134-1141.
Coiro, D., Nicolosi, F., De Marco, A., Melone, S., & Montella, F. (2005). *Flow curvature effect on dynamic behaviour of a novel vertical axis tidal current turbine: numerical and experimental analysis.* Paper presented at the ASME 2005 24th International Conference on Offshore Mechanics and Arctic Engineering.

Connor, D., Gilliland, P., Golding, N., Robinson, P., Todd, D., & Verling, E. (2006). UKSeaMap: the mapping of seabed and water column features of UK seas. Joint Nature Conservation Committee, Peterborough.
Corten, G. P., & Veldkamp, H. F. (2001a). Aerodynamics: Insects can halve wind-turbine power. *Nature, 412*(6842), 41.
Corten, G. P., & Veldkamp, H. F. (2001b). *Insects cause double stall*: Netherlands Energy Research Foundation Petten.
Crerar, A. J., Low, R. E., & Pritchard, C. L. (1987). Wave powered desalination. *Desalination, 67*, 127-137.
Cruz, A. G. B. d., Mesquita, A. L. A., & Blanco, C. J. C. (2008). Minimum pressure coefficient criterion applied in axial-flow hydraulic turbines. *Journal of the Brazilian Society of Mechanical Sciences and Engineering, 30*(1), 30-38.
Cui, L., Zheng, S., Zhang, Y., Miles, J., & Iglesias, G. (2020). Wave power extraction from a hybrid oscillating water column-oscillating buoy wave energy converter. *Renewable and Sustainable Energy Reviews, 135*, 110234.
Cui, Y., & Liu, Z. (2015). Effects of solidity ratio on performance of OWC impulse turbine. *Advances in Mechanical Engineering, 7*(1), 121373.
Dai, Y., & Lam, W. (2009). Numerical study of straight-bladed Darrieus-type tidal turbine. *Proceedings of the Institution of Civil Engineers-Energy, 162*(2), 67-76.
Dalili, N., Edrisy, A., & Carriveau, R. (2009). A review of surface engineering issues critical to wind turbine performance. *Renewable and Sustainable Energy Reviews, 13*(2), 428-438.
Danao, L. A., Qin, N., & Howell, R. (2012). A numerical study of blade thickness and camber effects on vertical axis wind turbines. *Proceedings of the Institution of Mechanical Engineers, Part A: Journal of Power and Energy, 226*(7), 867-881.
David Boorman, E. D., Helen Houghton-Carr, Alan Jenkins, Virginie Keller, James Miller, Andrew Hughes, Majdi Mansour, Jonathan Mackay. (2012). *WATER SECURITY IN THE UK, A pilot model-based study of current and future water security in the UK*. Retrieved from Natural Environment Research Council: http://nora.nerc.ac.uk/id/eprint/19489/1/Water_Security_Report.pdf
Davies, P. (2005). Wave-powered desalination: resource assessment and review of technology. *Desalination, 186*(1-3), 97-109.
De Lellis, M., Reginatto, R., Saraiva, R., & Trofino, A. (2018). The Betz limit applied to airborne wind energy. *Renewable Energy, 127*, 32-40.
Delgado Torres, A. M., García-Rodríguez, L., & del Moral, M. J. (2020). Preliminary assessment of innovative seawater reverse osmosis (SWRO) desalination powered by a hybrid solar photovoltaic (PV)-Tidal range energy system. *Desalination, 477*, 114247.
Derakhshan, S., Ashoori, M., & Salemi, A. (2017). Experimental and numerical study of a vertical axis tidal turbine performance. *Ocean Engineering, 137*, 59-67.
Dunnett, D., & Wallace, J. S. (2009). Electricity generation from wave power in Canada. *Renewable Energy, 34*(1), 179-195.
Ehrmann, R. S. (2014). *Effect of Surface Roughness on Wind Turbine Performance.*
El-Dessouky, H. T., & Ettouney, H. M. (2002). *Fundamentals of salt water desalination*: Elsevier.
El-Ghonemy, A. (2012). Retracted: water desalination systems powered by renewable energy sources, Review: Elsevier.
Elimelech, M., & Phillip, W. A. (2011). The future of seawater desalination: energy, technology, and the environment. *science, 333*(6043), 712-717.
Elragei, O., Elshawesh, F., & Ezuber, H. M. (2010). Corrosion failure 90/10 cupronickel tubes in a desalination plant. *Desalination and water treatment, 21*(1-3), 17-22.
Elsaid, K., Sayed, E. T., Yousef, B. A., Rabaia, M. K. H., Abdelkareem, M. A., & Olabi, A. (2020). Recent progress on the utilization of waste heat for desalination: A review. *Energy conversion and management, 221*, 113105.

Esmaeilion, F. (2020). Hybrid renewable energy systems for desalination. *Applied Water Science, 10*(3), 1-47.
Etemadi, A., Emami, Y., AsefAfshar, O., & Emdadi, A. (2011). Electricity generation by the tidal barrages. *Energy Procedia, 12*, 928-935.
Falnes, J. (2007). A review of wave-energy extraction. *Marine Structures, 20*(4), 185-201.
Finnegan, W., Fagan, E., Flanagan, T., Doyle, A., & Goggins, J. (2020). Operational fatigue loading on tidal turbine blades using computational fluid dynamics. *Renewable Energy, 152*, 430-440.
Fluent, A. 19.2 Theory Guide.(2018), ANSYS: Inc.
Forstmeier, M., Mannerheim, F., D'Amato, F., Shah, M., Liu, Y., Baldea, M., & Stella, A. (2007). Feasibility study on wind-powered desalination. *Desalination, 203*(1-3), 463-470.
Freddi, A., & Salmon, M. (2019). Introduction to the Taguchi method *Design Principles and Methodologies* (pp. 159-180): Springer.
Freudenreich, K., Kaiser, K., Schaffarczyk, A., Winkler, H., & Stahl, B. (2004). Reynolds number and roughness effects on thick airfoils for wind turbines. *Wind Engineering, 28*(5), 529-546.
Fritzmann, C., Löwenberg, J., Wintgens, T., & Melin, T. (2007). State-of-the-art of reverse osmosis desalination. *Desalination, 216*(1-3), 1-76.
Ghasemian, M., & Nejat, A. (2015). Aerodynamic noise prediction of a Horizontal Axis Wind Turbine using Improved Delayed Detached Eddy Simulation and acoustic analogy. *Energy conversion and management, 99*, 210-220.
Ghermandi, A., & Messalem, R. (2009). Solar-driven desalination with reverse osmosis: the state of the art. *Desalination and water treatment, 7*(1-3), 285-296.
Gude, G. (2018). *Emerging technologies for sustainable desalination handbook*: Butterworth-Heinemann.
Gude, V. G., & Nirmalakhandan, N. (2010). Sustainable desalination using solar energy. *Energy conversion and management, 51*(11), 2245-2251.
Gunn, K., & Stock-Williams, C. (2012). Quantifying the global wave power resource. *Renewable Energy, 44*, 296-304.
Gupta, R., & Biswas, A. (2010). Computational fluid dynamics analysis of a twisted three-bladed H-Darrieus rotor. *Journal of Renewable and Sustainable Energy, 2*(4), 043111.
Hammons, T. J. (1993). Tidal power. *Proceedings of the IEEE, 81*(3), 419-433.
Han, D., He, W., Yue, C., & Pu, W. (2017). Study on desalination of zero-emission system based on mechanical vapor compression. *Applied energy, 185*, 1490-1496.
Hasan, E. (2015). Desalination integration with renewable energy for climate change abatement in the MENA region *Recent Progress in Desalination, Environmental and Marine Outfall Systems* (pp. 159-173): Springer.
Hasçalık, A., & Çaydaş, U. (2008). Optimization of turning parameters for surface roughness and tool life based on the Taguchi method. *The International Journal of Advanced Manufacturing Technology, 38*(9-10), 896-903.
Hau, E. (2013). *Wind turbines: fundamentals, technologies, application, economics*: Springer Science & Business Media.
Hay, H. C., Trinh, A., & Matsuyama, I. (2020). Powering the Galilean Satellites with Moon-Moon Tides. *Geophysical Research Letters, 47*(15), e2020GL088317.
Heavey, S. C., Leen, S. B., & McGarry, J. P. (2018). Hydrodynamic Design and Analysis of a Novel Vertical Axis Turbine. *International Journal of Offshore and Polar Engineering, 28*(04), 393-401.
Herold, D., Horstmann, V., Neskakis, A., Plettner-Marliani, J., Piernavieja, G., & Calero, R. (1998). Small scale photovoltaic desalination for rural water supply-demonstration plant in Gran Canaria. *Renewable Energy, 14*(1-4), 293-298.

Hodson, H., & Dominy, R. (1987). Three-dimensional flow in a low-pressure turbine cascade at its design condition.
Hong, Y.Y., Beltran Jr, A. A., & Paglinawan, A. C. (2018). A robust design of maximum power point tracking using Taguchi method for stand-alone PV system. *Applied Energy, 211*, 50-63.
Hong, Y.Y., & Satriani, T. R. A. (2020). Day-ahead spatiotemporal wind speed forecasting using robust design-based deep learning neural network. *Energy*, 118441.
Horne, N., Culloch, R. M., Schmitt, P., Lieber, L., Wilson, B., Dale, A. C., . . . Kregting, L. T. (2020). Collision risk modelling for tidal energy devices: A flexible simulation-based approach. *Journal of Environmental Management, 278*, 111484.
http://tidalpower.co.uk/disadvantages-of-tidal-power, (accessed november 2020).
https://tips.noveltis.com/, (accessed november 2020).
https://www.freshwatersystems.com/ (accessed november 2020).
https://www.pumpsandsystems.com/ (accessed november 2020).
Huang, B., & Kanemoto, T. (2015). Multi-objective numerical optimization of the front blade pitch angle distribution in a counter-rotating type horizontal-axis tidal turbine. *Renewable Energy, 81*, 837-844.
Hwang, I. S., Lee, Y. H., & Kim, S. J. (2009). Optimization of cycloidal water turbine and the performance improvement by individual blade control. *Applied Energy, 86*(9), 1532-1540.
Ibrahim, M. M., Mostafa, N. H., Osman, A. H., & Hesham, A. (2020). Performance analysis of a stand-alone hybrid energy system for desalination unit in Egypt. *Energy conversion and management, 215*, 112941.
Im, J.K., Cho, I.H., Kim, S.-K., & Zoh, K.D. (2012). Optimization of carbamazepine removal in O3/UV/H2O2 system using a response surface methodology with central composite design. *Desalination, 285*, 306-314.
Jahanshahi, M., Sanati, M., & Babaei, Z. (2008). Optimization of parameters for the fabrication of gelatin nanoparticles by the Taguchi robust design method. *Journal of Applied Statistics, 35*(12), 1345-1353.
James R Joubert, J. L. v. N., Josh Reinecke, Imke Meyer (2013). *Wave Energy Converters (WECs)*. Retrieved from https://www.crses.sun.ac.za/
Jawahar, H. K., Ali, S. A. S., Azarpeyvand, M., & da Silva, C. R. I. (2020). Aerodynamic and aeroacoustic performance of high-lift airfoil fitted with slat cove fillers. *Journal of Sound and Vibration*, 115347.
Kadaj, E., & Bosleman, R. (2018). Energy recovery devices in membrane desalination processes *Renewable energy powered desalination handbook* (pp. 415-444): Elsevier.
Karabelas, A. J., Koutsou, C. P., Kostoglou, M., & Sioutopoulos, D. C. (2018). Analysis of specific energy consumption in reverse osmosis desalination processes. *Desalination, 431*, 15-21.
Karagiannis, I. C., & Soldatos, P. G. (2008). Water desalination cost literature: review and assessment. *Desalination, 223*(1), 448-456.
Kechagias, J. D., Aslani, K.-E., Fountas, N. A., Vaxevanidis, N. M., & Manolakos, D. E. (2020). A comparative investigation of Taguchi and full factorial design for machinability prediction in turning of a titanium alloy. *Measurement, 151*, 107213.
Khan, J., & Bhuyan, G. (2009). Ocean energy: Global technology development status. *IEA-OES. Document, 104*.
Khan, M., Bhuyan, G., Iqbal, M., & Quaicoe, J. (2009). Hydrokinetic energy conversion systems and assessment of horizontal and vertical axis turbines for river and tidal applications: A technology status review. *Applied energy, 86*(10), 1823-1835.

Khan, M. J., Bhuyan, G., Iqbal, M. T., & Quaicoe, J. E. (2009). Hydrokinetic energy conversion systems and assessment of horizontal and vertical axis turbines for river and tidal applications: A technology status review. *Applied energy, 86*(10), 1823-1835.
Kiho, S., Shiono, M., & Suzuki, K. (1996). The power generation from tidal currents by Darrieus turbine. *Renewable Energy, 9*(1-4), 1242-1245.
Kim, J., Park, K., Yang, D. R., & Hong, S. (2019). A comprehensive review of energy consumption of seawater reverse osmosis desalination plants. *Applied energy, 254*, 113652.
Kirke, B., & Lazauskas, L. (2008). Variable pitch Darrieus water turbines. *Journal of Fluid Science and Technology, 3*(3), 430-438.
Kishore, R., Stewart, C., & Priya, S. (2018). *Wind Energy Harvesting: Micro-to-small Scale Turbines*: Walter de Gruyter GmbH & Co KG.
Koetsier, T., & Blauwendraat, H. (2004). *The Archimedean screw-pump: A note on its invention and the development of the theory.* Paper presented at the International symposium on history of machines and mechanisms.
Koutsou, C., Kritikos, E., Karabelas, A., & Kostoglou, M. (2020). Analysis of temperature effects on the specific energy consumption in reverse osmosis desalination processes. *Desalination, 476*, 114213.
Kurihara, M., Yamamura, H., Nakanishi, T., & Jinno, S. (2001). Operation and reliability of very high-recovery seawater desalination technologies by brine conversion two-stage RO desalination system. *Desalination, 138*(1-3), 191-199.
Kulkarni, S. S. (2016). *Design study of a horizontal axis tidal turbine blade.* Birmingham City University.
Kumar, A., & Saini, R. (2017). Techno-Economic Analysis of Hydrokinetic Turbines.
Kumar, P. M., Seo, J., Seok, W., Rhee, S. H., & Samad, A. (2019). Multi-fidelity optimization of blade thickness parameters for a horizontal axis tidal stream turbine. *Renewable Energy, 135*, 277-287.
Kundu, P. (2020). Numerical simulation of the effects of passive flow control techniques on hydrodynamic performance improvement of the hydrofoil. *Ocean engineering, 202*, 107108.
Laakso, T., Talhaug, L., Ronsten, G., Horbaty, R., Baring-Gould, I., Lacroix, A., & Peltola, E. (2005). Wind energy projects in cold climates. *International Energy Agency, 36*.
Laborde, H., Franca, K., Neff, H., & Lima, A. (2001). Optimization strategy for a small-scale reverse osmosis water desalination system based on solar energy. *Desalination, 133*(1), 1-12.
Lachmann, G. V. (1960). *Aspects of insect contamination in relation to laminar flow aircraft*: Ministry of Aviation, Aeronautical Research Council.
Laín Beatove, S., & Osorio, C. (2010). Simulation and evaluation of a straight-bladed Darrieus-type cross flow marine turbine.
Lain, S., & Osorio, C. (2010). Simulation and evaluation of a straight-bladed Darrieus-type cross flow marine turbine.
Lanzafame, R., Mauro, S., & Messina, M. (2013). Wind turbine CFD modeling using a correlation-based transitional model. *Renewable Energy, 52*, 31-39.
Lashofer, A., Hawle, W., & Pelikan, B. (2012). State of technology and design guidelines for the Archimedes screw turbine. *Univ. Nat. Resour. Life Sci. Vienna*, 1-8.
Leijon, J. (2020). *Wave Power for Desalination.* Acta Universitatis Upsaliensis.
Leijon, J., Anttila, S., Frost, A. E., Kontos, S., Lindahl, O., Engström, J., . . . Boström, C. (2020). Freshwater and Lithium from Desalination Powered by Marine Energy Sources. *International Journal of Offshore and Polar Engineering, 30*(03), 283-285.
Leijon, J., & Boström, C. (2018). Freshwater production from the motion of ocean waves–A review. *Desalination, 435*, 161-171.

Leijon, J., Forslund, J., Thomas, K., & Boström, C. (2018). Marine Current Energy Converters to Power a Reverse Osmosis Desalination Plant. *Energies, 11*(11), 2880.
Leijon, J., Salar, D., Engström, J., Leijon, M., & Boström, C. (2020). Variable renewable energy sources for powering reverse osmosis desalination, with a case study of wave powered desalination for Kilifi, Kenya. *Desalination, 494*, 114669.
Lemonis, G., & Cutler, J. (2004). Wave and Tidal Energy Conversion Encyclopedia of Energy: Elsevier journal.
Li, D., Li, R., Yang, C., & Wang, X. (2010). *Effects of surface roughness on aerodynamic performance of a wind turbine airfoil.* Paper presented at the 2010 Asia-Pacific Power and Energy Engineering Conference.
Li, S., Li, Y., Yang, C., Zhang, X., Wang, Q., Li, D., . . . Wang, T. (2018). Design and testing of a LUT airfoil for straight-bladed vertical axis wind turbines. *Applied Sciences, 8*(11), 2266.
Li, Y. (2014). On the definition of the power coefficient of tidal current turbines and efficiency of tidal current turbine farms. *Renewable Energy, 68*, 868-875.
Li, Y., & Calisal, S. M. (2010). Three-dimensional effects and arm effects on modeling a vertical axis tidal current turbine. *Renewable Energy, 35*(10), 2325-2334.
Li, Y., & Yu, Y.-H. (2012). A synthesis of numerical methods for modeling wave energy converter-point absorbers. *Renewable and Sustainable Energy Reviews, 16*(6), 4352-4364.
Li, Z., Siddiqi, A., Anadon, L. D., & Narayanamurti, V. (2018). Towards sustainability in water-energy nexus: Ocean energy for seawater desalination. *Renewable and Sustainable Energy Reviews, 82*, 3833-3847.
Ling, C., Lou, X., Li, J., & Zhang, Y. (2018). *Experimental investigation of a novel tidal supercharger driven by tidal energy for reverse osmosis seawater desalination.* Paper presented at the Advances in Renewable Energies Offshore: Proceedings of the 3rd International Conference on Renewable Energies Offshore (RENEW 2018), October 8-10, 2018, Lisbon, Portugal.
Ling, C., Wang, Y., Min, C., & Zhang, Y. (2018). Economic evaluation of reverse osmosis desalination system coupled with tidal energy. *Frontiers in Energy, 12*(2), 297-304.
Liponi, A., Wieland, C., & Baccioli, A. (2020). Multi-effect distillation plants for small-scale seawater desalination: thermodynamic and economic improvement. *Energy conversion and management, 205*, 112337.
Liu, Z., Qu, H., & Shi, H. (2016). Numerical Study on Self-Starting Performance of Darrieus Vertical Axis Turbine for Tidal Stream Energy Conversion. *Energies, 9*(10), 789.
López, I., Andreu, J., Ceballos, S., De Alegría, I. M., & Kortabarria, I. (2013). Review of wave energy technologies and the necessary power-equipment. *Renewable and Sustainable Energy Reviews, 27*, 413-434.
Lourenço, A. B., & Carvalho, M. (2020). Exergy, exergoeconomic and exergy-based emission cost analyses of a coconut husk-fired power and desalination plant. *International Journal of Exergy, 32*(3), 267-291.
Luo, Q.-J., Sheng, Q.-H., Zhang, L., & Han, R.-g. (2010). *Optimization of blade deflection angle of vertical-axis turbine for tidal current energy conversion.* Paper presented at the The Twentieth International Offshore and Polar Engineering Conference.
Ma, L., Wang, X., Zhu, J., & Kang, S. (2019). Dynamic Stall of a Vertical-Axis Wind Turbine and Its Control Using Plasma Actuation. *Energies, 12*(19), 3738.
Ma, Y., Zhang, L., Zhang, Z.-y., & Han, D.-f. (2016). Optimization of blade motion of vertical axis turbine. *China Ocean Engineering, 30*(2), 297-308.
Maeda, T., Kamada, Y., Murata, J., Shimizu, K., Ogasawara, T., Nakai, A., & Kasuya, T. (2016). Effect of solidity on aerodynamic forces around straight-bladed vertical axis wind turbine by wind tunnel experiments (depending on number of blades). *Renewable Energy, 96*, 928-939.

Mahmud, S., Sampebatu, L., & Kwang, S. C. (2017). *Mechanical power efficiency of modified turbine blades.* Paper presented at the AIP Conference Proceedings.
Mandal, N., Doloi, B., Mondal, B., & Das, R. (2011). Optimization of flank wear using Zirconia Toughened Alumina (ZTA) cutting tool: Taguchi method and Regression analysis. *Measurement, 44*(10), 2149-2155.
Mannion, B., Leen, S. B., & Nash, S. (2020). Development and assessment of a blade element momentum theory model for high solidity vertical axis tidal turbines. *Ocean engineering, 197*, 106918.
Maratos, D. (2003). Technical feasibility of wavepower for seawater desalination using the hydro-ram (Hydram). *Desalination, 153*(1-3), 287-293.
Maruzewski, P., Hasmatuchi, V., Mombelli, H.-P., Burggraeve, D., Iosfin, J., Finnegan, P., & Avellan, F. (2009). Surface roughness impact on Francis turbine performances and prediction of efficiency step up. *International Journal of Fluid Machinery and Systems, 2*(4), 353-362.
Mathioulakis, E., Belessiotis, V., & Delyannis, E. (2007). Desalination by using alternative energy: Review and state-of-the-art. *Desalination, 203*(1-3), 346-365.
Mazumder, R., & Arima, M. (2005). Tidal rhythmites and their implications. *Earth-Science Reviews, 69*(1-2), 79-95.
Mehmood, N. (2012). Study of naca 0015 for diffuser design in tidal current turbine applications. *International Journal of Engineering, 25*(4), 373-380.
Mehmood, N., Liang, Z., & Khan, J. (2012). CFD study of NACA 0018 for diffuser design of tidal current turbines. *Research Journal of Applied Science, Engineering and Technology, 4*(21), 4552-4560.
Meng, H., Ma, Z., Dou, B., Zeng, P., & Lei, L. (2020). Investigation on the performance of a novel forward-folding rotor used in a downwind horizontal-axis turbine. *Energy, 190*, 116384.
Menter, F. (2002). Two-equation eddy-viscosity turbulence models for engineering applications. *AIAA journal, 40*(2), 254-266.
Miller, S., Shemer, H., & Semiat, R. (2015). Energy and environmental issues in desalination. *Desalination, 366*, 2-8.
Mistry, K. H., & Lienhard, J. H. (2013). An economics-based second law efficiency. *Entropy, 15*(7), 2736-2765.
Mohamed, E. S., Papadakis, G., Mathioulakis, E., & Belessiotis, V. (2005). The effect of hydraulic energy recovery in a small sea water reverse osmosis desalination system; experimental and economical evaluation. *Desalination, 184*(1-3), 241-246.
Mohamed, M. (2012). Performance investigation of H-rotor Darrieus turbine with new airfoil shapes. *Energy, 47*(1), 522-530.
Mohan Kumar, P., Sivalingam, K., Lim, T.-C., Ramakrishna, S., & Wei, H. (2019). Strategies for Enhancing the Low Wind Speed Performance of H-Darrieus Wind Turbine—Part 1. *Clean Technologies, 2*(1), 32-51.
Mohsen, M. S., Akash, B., Abdo, A. A., & Akash, O. (2016). Energy options for water desalination in UAE. *Procedia Computer Science, 83*, 894-901.
Montomoli, F., Hodson, H., & Haselbach, F. (2010). Effect of roughness and unsteadiness on the performance of a new low pressure turbine blade at low Reynolds numbers. *Journal of Turbomachinery, 132*(3), 031018.
Nabavi, Y. (2008). *Numerical study of the duct shape effect on the performance of a ducted vertical axis tidal turbine.* University of British Columbia.
Nadel, B. (2008). Portable sea-powered electrolysis generator: Google Patents.
Naik, A. B., & Reddy, A. C. (2018). Optimization of tensile strength in TIG welding using the Taguchi method and analysis of variance (ANOVA). *Thermal Science and Engineering Progress, 8*, 327-339.

Nandagopal, R. A., & Narasimalu, S. (2020). Multi-objective optimization of hydrofoil geometry used in horizontal axis tidal turbine blade designed for operation in tropical conditions of South East Asia. *Renewable Energy, 146*, 166-180.
Naoi, K., Shiono, M., Katsuyuki, K., & Suzuki, S. (2006). *A Wind Power Generation System using the Vertical Axis Wind Turbine with Arc Camber Blades.* Paper presented at the The Sixteenth International Offshore and Polar Engineering Conference.
Nassrullah, H., Anis, S. F., Hashaikeh, R., & Hilal, N. (2020). Energy for desalination: A state-of-the-art review. *Desalination, 491*, 114569.
Nayar, K. G., Fernandes, J., McGovern, R. K., Dominguez, K., Al-Anzi, B., & Lienhard, J. (2017). Costs and energy needs of RO-ED hybrid systems for zero brine discharge seawater desalination. *Desalination (manuscript in progress, 2018 expected publication)*.
Ng, K. C., & Shahzad, M. W. (2018). Sustainable desalination using ocean thermocline energy. *Renewable and Sustainable Energy Reviews, 82*, 240-246.
Nicholls-Lee, R., Turnock, S., & Boyd, S. (2008). Performance prediction of a free stream tidal turbine with composite bend-twist coupled blades.
Nicholls-Lee, R. F. (2011). *Adaptive composite blades for horizontal axis tidal turbines.* University of Southampton.
Ning, D.-z., Zhou, Y., Mayon, R., & Johanning, L. (2020). Experimental investigation on the hydrodynamic performance of a cylindrical dual-chamber Oscillating Water Column device. *Applied energy, 260*, 114252.
Nobile, R., Vahdati, M., Barlow, J. F., & Mewburn-Crook, A. (2014). Unsteady flow simulation of a vertical axis augmented wind turbine: A two-dimensional study. *Journal of Wind Engineering and Industrial Aerodynamics, 125*, 168-179.
O Rourke, F., Boyle, F., & Reynolds, A. (2010). Tidal energy update 2009. *Applied energy, 87*(2), 398-409.
OECD, I. (2007). Renewables In Global Energy Supply-An IEA Fact Sheet.". *IEA. Retrieved on*, 12-29.
Ogunbiyi, O., Jamiru, T., Sadiku, R., Adesina, O., lolu Olajide, J., & Beneke, L. (2020). Optimization of spark plasma sintering parameters of inconel 738LC alloy using response surface methodology (RSM). *International Journal of Lightweight Materials and Manufacture, 3*(2), 177-188.
Okampo, E. J., & Nwulu, N. (2021). Optimisation of renewable energy powered reverse osmosis desalination systems: A state-of-the-art review. *Renewable and Sustainable Energy Reviews, 140*, 110712.
Okulov, V. L., & Sørensen, J. N. (2008). Refined Betz limit for rotors with a finite number of blades. *Wind Energy: An International Journal for Progress and Applications in Wind Power Conversion Technology, 11*(4), 415-426.
Ott, R. L., & Longnecker, M. T. (2015). *An introduction to statistical methods and data analysis*: Nelson Education.
Ouro, P., Stoesser, T., & Ramírez, L. (2018). Effect of blade cambering on dynamic stall in view of designing vertical axis turbines. *Journal of Fluids Engineering, 140*(6).
Owen, A. (2008). Tidal current energy: origins and challenges *Future energy* (pp. 111-128): Elsevier.
Paraschivoiu, I. (2002). *Wind turbine design: with emphasis on Darrieus concept*: Presses inter Polytechnique.
Park, K., Kim, J., Yang, D. R., & Hong, S. (2020). Towards a low-energy seawater reverse osmosis desalination plant: A review and theoretical analysis for future directions. *Journal of Membrane Science, 595*, 117607.
Park, S., Park, S., & Rhee, S. H. (2016). Influence of blade deformation and yawed inflow on performance of a horizontal axis tidal stream turbine. *Renewable Energy, 92*, 321-332.

Pasha, M., Moghadam, M. B., Fani, S., & Khadem, Y. (2018). Effects of quality characteristic distributions on the integrated model of Taguchi's loss function and economic statistical design of-control charts by modifying the Banerjee and Rahim economic model. *Communications in Statistics-Theory and Methods, 47*(8), 1842-1855.

Pattanapol, W., Wakes, S. J., Hilton, M. J., & Dickinson, K. J. (2008). Modeling of surface roughness for flow over a complex vegetated surface. *International Journal of Mathematical, Physical and Engineering Sciences, 2*(1), 18-26.

Pelc, R., & Fujita, R. M. (2002). Renewable energy from the ocean. *Marine Policy, 26*(6), 471-479.

Peñate, B., & García-Rodríguez, L. (2012). Current trends and future prospects in the design of seawater reverse osmosis desalination technology. *Desalination, 284*, 1-8.

Permanasari, A. A., Puspitasari, P., Utama, S. B., & Yaqin, F. A. (2019). *Experimental Investigation and Optimization of Floating Blade Water Wheel Turbine Performance Using Taguchi Method and Analysis of Variance (ANOVA).* Paper presented at the IOP Conference Series: Materials Science and Engineering.

Petit, H. A., Paulo, C. I., Cabrera, O. A., & Irassar, E. F. (2020). Modelling and optimization of an inclined plane classifier using CFD-DPM and the Taguchi method. *Applied Mathematical Modelling, 77*, 617-634.

Phadke, M. S. (1995). *Quality engineering using robust design*: Prentice Hall PTR.

Pinar, A. M., Uluer, O., & Kırmaci, V. (2009). Optimization of counter flow Ranque–Hilsch vortex tube performance using Taguchi method. *International journal of refrigeration, 32*(6), 1487-1494.

Polagye, B. (2009). *Hydrodynamic effects of kinetic power extraction by in-stream tidal turbines*: University of Washington.

Pongduang, S., Kayankannavee, C., & Tiaple, Y. (2015). Experimental investigation of helical tidal turbine characteristics with different twists. *Energy Procedia, 79*, 409-414.

Ponta, F., & Jacovkis, P. (2008). Marine-current power generation by diffuser-augmented floating hydro-turbines. *Renewable Energy, 33*(4), 665-673.

Priegue, L., & Stoesser, T. (2017). The influence of blade roughness on the performance of a vertical axis tidal turbine. *International journal of marine energy, 17*, 136-146.

Qi, S., Wang, R., Chaitra, G. K. M., Torres, J., Hu, X., & Fane, A. G. (2016). Aquaporin-based biomimetic reverse osmosis membranes: Stability and long term performance. *Journal of Membrane Science, 508*, 94-103.

Ranganath, M., & Vipin, R. (2013). Optimization of Process Parameters in Turning Operation of Aluminium (6061) with Cemented Carbide Inserts Using Taguchi Method and Anova. *International Journal, 1*(1), 13-21.

Rao, S. S. (2015). *Robust Design of Horizontal Axis Wind Turbines Using Taguchi Method.* Paper presented at the ASME 2015 International Mechanical Engineering Congress and Exposition.

Rasool, G., Johnstone, C., & Stack, M. M. (2016). *Tribology of tidal turbine blades: impact angle effects on erosion of polymeric coatings in sea water conditions*.

Ren, N., & Ou, J. (2009). *Numerical simulation of surface roughness effect on wind turbine thick airfoils.* Paper presented at the 2009 Asia-Pacific Power and Energy Engineering Conference.

Rezaeiha, A., Montazeri, H., & Blocken, B. (2018). Towards optimal aerodynamic design of vertical axis wind turbines: Impact of solidity and number of blades. *Energy, 165*, 1129-1148.

Ritter, A., Muñoz-Carpena, R., Performance evaluation of hydrological models: Statistical significance for reducing subjectivity in goodness-of-fit assessments, Journal of Hydrology, Volume 480, 2013, Pages 33-45, ISSN 0022-1694.

Roberts, A., Thomas, B., Sewell, P., Khan, Z., Balmain, S., & Gillman, J. (2016). Current tidal power technologies and their suitability for applications in coastal and marine areas. *Journal of Ocean Engineering and Marine Energy, 2*(2), 227-245.

Roy, R. K. (2010). *A primer on the Taguchi method*: Society of Manufacturing Engineers.

Ruiz-García, A., Melián-Martel, N., & Mena, V. (2018). Fouling characterization of RO membranes after 11years of operation in a brackish water desalination plant. *Desalination, 430*, 180-185.

Sadrzadeh, M., & Mohammadi, T. (2008). Sea water desalination using electrodialysis. *Desalination, 221*(1-3), 440-447.

Sagol, E., Reggio, M., & Ilinca, A. (2013). Issues concerning roughness on wind turbine blades. *Renewable and Sustainable Energy Reviews, 23*, 514-525.

Sammut C., Webb G.I. (Eds.), Leave-One-Out Cross-Validation, Springer US, Boston, MA (2010), pp. 600-601.

Samo, K. A., Rigit, A. R. H., & Baharun, A. (2017). Mapping of tidal energy potential based on high and low tides for Sabah and Sarawak. Paper presented at the MATEC Web of Conferences.

Sapakal, S., & Telsang, M. (2012). Parametric optimization of MIG welding using Taguchi design method. Int J Adv Eng Res Stud, 1(4), 28-30.

Sawyer, R. A., & Maratos, D. F. (2001). An investigation into the economic feasibility of unsteady incompressible duct flow (waterhammer) to create hydrostatic pressure for seawater desalination using reverse osmosis. Desalination, 138(1), 307-317.

Schallenberg-Rodríguez, J., Veza, J. M., & Blanco-Marigorta, A. (2014). Energy efficiency and desalination in the Canary Islands. Renewable and Sustainable Energy Reviews, 40, 741-748.

Segura, E., Morales, R., Somolinos, J. A., & López, A. (2017). Techno-economic challenges of tidal energy conversion systems: Current status and trends. *Renewable and Sustainable Energy Reviews, 77*, 536-550.

Setiawan, A. A., Zhao, Y., & Nayar, C. V. (2009). Design, economic analysis and environmental considerations of mini-grid hybrid power system with reverse osmosis desalination plant for remote areas. *Renewable Energy, 34*(2), 374-383.

Shaheen, M., & Abdallah, S. (2017). Efficient clusters and patterned farms for Darrieus wind turbines. *Sustainable Energy Technologies and Assessments, 19*, 125-135.

Shahzad, M. W., Burhan, M., Ang, L., & Ng, K. C. (2017). Energy-water-environment nexus underpinning future desalination sustainability. *Desalination, 413*, 52-64.

Shao, S., Ji, C., Graham, D. I., Reeve, D. E., James, P. W., & Chadwick, A. J. (2006). Simulation of wave overtopping by an incompressible SPH model. *Coastal Engineering, 53*(9), 723-735.

Sharmila, N., Jalihal, P., Swamy, A., & Ravindran, M. (2004). Wave powered desalination system. *Energy, 29*(11), 1659-1672.

Shekari Namin, A., Rostamzadeh, H., & Nourani, P. (2020). Thermodynamic and thermoeconomic analysis of three cascade power plants coupled with RO desalination unit, driven by a salinity-gradient solar pond. *Thermal Science and Engineering Progress, 18*, 100562.

Shrivastava, A., Rosenberg, S., & Peery, M. (2015). Energy efficiency breakdown of reverse osmosis and its implications on future innovation roadmap for desalination. *Desalination, 368*, 181-192.

Simmons, S., & Lubitz, W. (2017). *Archimedes screw generators for sustainable energy development.* Paper presented at the 2017 IEEE Canada International Humanitarian Technology Conference (IHTC).

Singh, S. (2020). *TIDAL STREAM RESOURCE CLASSIFICATIONS.* Georgia Institute of Technology.

Singh, T., Atieh, M. A., Al-Ansari, T., Mohammad, A. W., & McKay, G. (2020). The Role of Nanofluids and Renewable Energy in the Development of Sustainable Desalination Systems: A Review. *Water, 12*(7), 2002.
Siti Khodijah, A., Shiba, M., & Obara, S. y. (2021). Design of compensation battery for tidal power-photovoltaics-SOFC microgrids in Ternate and Pulau-Tidore Islands. *International Journal of Energy Research, 45*(2), 2100-2115.
Sobana, S., & Panda, R. C. (2011). Identification, modelling, and control of continuous reverse osmosis desalination system: a review. *Separation Science and Technology, 46*(4), 551-560.
Sohrabi, M. R., Khavaran, A., Shariati, S., & Shariati, S. (2017). Removal of Carmoisine edible dye by Fenton and photo Fenton processes using Taguchi orthogonal array design. *Arabian Journal of Chemistry, 10*, S3523-S3531.
Soleimani, K., Ketabdari, M. J., & Khorasani, F. (2015). Feasibility study on tidal and wave energy conversion in Iranian seas. *Sustainable Energy Technologies and Assessments, 11*, 77-86.
Sommerfeld, M., & Huber, N. (1999). Experimental analysis and modelling of particle-wall collisions. *International journal of multiphase flow, 25*(6-7), 1457-1489.
Sornes, K. (2010). Small-scale water current turbines for river applications. *Zero Emission Resource Organisation (ZERO)*, 1-19.
Sutikno, P., Nurdin, Y. S., Risqi, D., Mardani, E., & Sihombing, E. (2015). *Experimental of Three Parallel Water Current Turbine with Optimized Straight Blades and Using Flow Concentrator Channeling Device to Augmented Performance and Self-Starting Capability.* Paper presented at the Applied Mechanics and Materials.
Tahani, M., Babayan, N., Astaraei, F. R., & Moghadam, A. (2015). Multi objective optimization of horizontal axis tidal current turbines, using Meta heuristics algorithms. *Energy conversion and management, 103*, 487-498.
Tan, M. g., LIU, H.-l., WU, X. f., WANG, Y., WANG, K., & FU, M. (2011). The Effect of Roughness on the Numerical Prediction of the Characteristics of Centrifugal Pumps [J]. *China Rural Water and Hydropower, 2*.
Tekade, R. K., & Chougule, M. B. (2013). Formulation development and evaluation of hybrid nanocarrier for cancer therapy: Taguchi orthogonal array based design. *BioMed research international, 2013*.
Thiébot, J., Du Bois, P. B., & Guillou, S. (2015). Numerical modeling of the effect of tidal stream turbines on the hydrodynamics and the sediment transport–Application to the Alderney Race (Raz Blanchard), France. *Renewable Energy, 75*, 356-365.
Thompson, S. A. (2017). *Hydrology for water management*: CRC Press.
Tidemap/Tidetech-Maps/https://maps.tidetech.org. (2020).
Timmer, W., & Schaffarczyk, A. (2004). The effect of roughness at high Reynolds numbers on the performance of aerofoil DU 97-W-300Mod. *Wind Energy: An International Journal for Progress and Applications in Wind Power Conversion Technology, 7*(4), 295-307.
Thomas K., Low speed energy conversion from marine currents, Ph.D. thesis, Dept. Eng. Sci., Acta Univ. Upsaliensis, Sweden, 2007.
Tong, X., Liu, S., Chen, Y., & Crittenden, J. (2020). Thermodynamic analysis of a solar thermal facilitated membrane seawater desalination process. *Journal of Cleaner Production, 256*, 120398.
Tunio, I. A., Shah, M. A., Hussain, T., Harijan, K., Mirjat, N. H., & Memon, A. H. (2020). Investigation of duct augmented system effect on the overall performance of straight blade Darrieus hydrokinetic turbine. *Renewable Energy, 153*, 143-154.
Turek, M., & Bandura, B. (2007). Renewable energy by reverse electrodialysis. *Desalination, 205*(1-3), 67-74.

Tzen, E., & Morris, R. (2003). Renewable energy sources for desalination. *Solar energy, 75*(5), 375-379.
Ullman, P. W. (2002). Offshore Tidal Power Generation—A new approach to power conversion of the oceans' tides. *Marine Technology Society Journal, 36*(4), 16-24.
UN-Water, F. Coping with Water Scarcity: Challenge of the Twenty-First Century (2007).
Urbina, R., Epps, B. P., Peterson, M. L., & Kimball, R. W. (2019). A dynamic stall model for analysis of cross-flow turbines using discrete vortex methods. *Renewable Energy, 130*, 1130-1145.
Vakili-Nezhaad, G., Mishra, S. B., Mousa, H., & Ziaiefar, H. (2021). Simulation and optimization of hybrid green energy systems for desalination purposes. *Environmental Progress & Sustainable Energy, 40*(2), e13515.
Van Dam, J. C. (2003). *Impacts of climate change and climate variability on hydrological regimes*: Cambridge University Press.
Vennell, R. (2013). Exceeding the Betz limit with tidal turbines. *Renewable Energy, 55*, 277-285.
Villalpando, F., Reggio, M., & Ilinca, A. (2012). Numerical study of flow around iced wind turbine airfoil. *Engineering Applications of Computational Fluid Mechanics, 6*(1), 39-45.
Virk, M. S., Homola, M. C., & Nicklasson, P. J. (2010). Effect of rime ice accretion on aerodynamic characteristics of wind turbine blade profiles. *Wind Engineering, 34*(2), 207-218.
Voutchkov, N., Lazarova, V., Choo, K., & Cornel, P. (2012). *Energy use of seawater desalination–current status and future trends*: IWA Publishing, London.
Vukajlovic, N., Katie, V., Milicevic, D., Dumnic, B., & Popadic, B. (2018). *Active control of Induction Generator in Ocean Wave Energy Conversion System.* Paper presented at the 2018 IEEE 18th International Power Electronics and Motion Control Conference (PEMC).
Walker, J. M., Flack, K. A., Lust, E. E., Schultz, M. P., & Luznik, L. (2014). Experimental and numerical studies of blade roughness and fouling on marine current turbine performance. *Renewable Energy, 66*, 257-267.
Wang, S., & Huang, G. H. (2015). A multi-level Taguchi-factorial two-stage stochastic programming approach for characterization of parameter uncertainties and their interactions: An application to water resources management. *European Journal of Operational Research, 240*(2), 572-581.
Wang, Z., Wang, Y., Xu, G., & Ren, J. (2019). Sustainable desalination process selection: Decision support framework under hybrid information. *Desalination, 465*, 44-57.
Wang, Z., Wang, Y., & Zhuang, M. (2018). Improvement of the aerodynamic performance of vertical axis wind turbines with leading-edge serrations and helical blades using CFD and Taguchi method. *Energy conversion and management, 177*, 107-121.
Warsinger, D. M., Mistry, K. H., Nayar, K. G., Chung, H. W., & Lienhard, J. H. (2015). Entropy generation of desalination powered by variable temperature waste heat. *Entropy, 17*(11), 7530-7566.
Watchorn, M., & Trapp, T. (2000). *Tidal stream renewable offshore power generation (TS-Ropg).* Paper presented at the World renewable energy congress VI.
Waters, S. (2015). *Analysing the performance of the Archimedes Screw Turbine within tidal range technologies.* Lancaster University.
Westwood, A. (2004). Ocean power: Wave and tidal energy review. *Refocus, 5*(5), 50-55.
Wilf, M., & Awerbuch, L. (2007). *The guidebook to membrane desalination technology: reverse osmosis, nanofiltration and hybrid systems: process, design, applications and economics*: Balaban Desalination Publications.
Xiao, Q., & Zhu, Q. (2014). A review on flow energy harvesters based on flapping foils. *Journal of fluids and structures, 46*, 174-191.

Xie, J., & Zuo, L. (2013). Dynamics and control of ocean wave energy converters. *International Journal of Dynamics and Control, 1*(3), 262-276.
Xu, D., Ren, J., Dong, L., & Yang, Y. (2020). Portfolio selection of renewable energy-powered desalination systems with sustainability perspective: A novel MADM-based framework under data uncertainties. *Journal of Cleaner Production, 275*, 124114.
Yang, W., Wu, Y., & Liu, S. (2011). An optimization method on runner blades in bulb turbine based on CFD analysis. *Science China Technological Sciences, 54*(2), 338-344.
Youssef, P., Al-Dadah, R., & Mahmoud, S. (2014). Comparative analysis of desalination technologies. *Energy Procedia, 61*, 2604-2607.
Zhang, D.h., Ding, L., Huang, B., Chen, X.-m., & Liu, J.-t. (2019). Optimization study on the blade profiles of a horizontal axis tidal turbine based on BEM-CFD model. *China Ocean Engineering, 33*(4), 436-445.
Zhang, T., Wang, Z., Huang, W., Ingham, D., Ma, L., & Pourkashanian, M. (2020). A numerical study on choosing the best configuration of the blade for vertical axis wind turbines. *Journal of Wind Engineering and Industrial Aerodynamics, 201*, 104162.
Zhang, X.W., Wang, S.-Q., Wang, F., Zhang, L., & Sheng, Q.-H. (2012). The hydrodynamic characteristics of free variable-pitch vertical axis tidal turbine. *Journal of hydrodynamics, 24*(6), 834-839.
Zhang, X.-w., Zhang, L., Wang, F., Zhao, D.-y., & Pang, C.-y. (2014). Research on the unsteady hydrodynamic characteristics of vertical axis tidal turbine. *China ocean engineering, 28*(1), 95-103.
Zhang, Y., Fernandez-Rodriguez, E., Zheng, J., Zheng, Y., Zhang, J., Gu, H., . . . Lin, X. (2020). A Review on Numerical Development of Tidal Stream Turbine Performance and Wake Prediction. *IEEE Access, 8*, 79325-79337.
Zhang, Y., Igarashi, T., & Hu, H. (2011). *Experimental investigations on the performance degradation of a low-Reynolds-number airfoil with distributed leading edge roughness.* Paper presented at the 49th AIAA Aerospace Sciences Meeting Including the New Horizons Forum and Aerospace Exposition.
Zhang, Y., Zhang, J., Lin, X., Wang, R., Zhang, C., & Zhao, J. (2020). Experimental investigation into downstream field of a horizontal axis tidal stream turbine supported by a mono pile. *Applied Ocean Research, 101*, 102257.
Zhao, K., & Liu, Y. (2009). Theoretical study on multi-effect solar distillation system driven by tidal energy. *Desalination, 249*(2), 566-570.
Zheng, S., Antonini, A., Zhang, Y., Miles, J., Greaves, D., Zhu, G., & Iglesias, G. (2020). Hydrodynamic performance of a multi-Oscillating Water Column (OWC) platform. *Applied Ocean Research, 99*, 102168.
Zhu, F.w., Ding, L., Huang, B., Bao, M., & Liu, J.-T. (2020). Blade design and optimization of a horizontal axis tidal turbine. *Ocean engineering, 195*, 106652.